Multi-Physics Smoothed Particle Hydrodynamics Implementation to Enhance Vertebral Fracture Prediction in a Finite Element Model of a Lower Cervical Spine Segment Under Compression

by

Sophia Ngan

A thesis

presented to the University of Waterloo

in fulfillment of the

thesis requirement for the degree of

Master of Applied Science

in

Mechanical and Mechatronics Engineering

Waterloo, Ontario, Canada, 2024

© Sophia Ngan 2024

Author's Declaration

This thesis consists of material all of which I authored or co-authored: see Statement of Contributions included in the thesis. This is a true copy of the thesis, including any required final revisions, as accepted by my examiners.

I understand that my thesis may be made electronically available to the public.

Statement of Contributions

Some of the material in this thesis has been published in a journal article:

“Smoothed particle hydrodynamics implementation to enhance vertebral fracture finite element model in a cervical spine segment under compression”

DOI: 10.1016/j.jmbbm.2024.106412

SN: Writing – review & editing, Writing – original draft, Visualization, Software, Methodology, Investigation, Formal analysis.

CR: Writing – review & editing, Software, Methodology, Formal analysis.

AR: Writing – review & editing, Software, Methodology.

DC: Writing – review & editing, Supervision, Resources, Project administration, Methodology, Funding acquisition, Formal analysis, Conceptualization.

Some of the material in this thesis has been published in a conference paper:

“Smoothed Particle Hydrodynamics to Model Spinal Canal Occlusion of a Finite Element Functional Spinal Unit Model under Compression”

DOI: 10.4271/09-11-02-0015

SN: Writing – review & editing, Writing – original draft, Visualization, Software, Methodology, Investigation, Formal analysis.

CR: Writing – review & editing, Software, Methodology, Formal analysis.

JC: Writing – review & editing, Experimental work and analysis of experimental data

DC: Writing – review & editing, Supervision, Resources, Project administration, Methodology, Funding acquisition, Formal analysis, Conceptualization.

Abstract

Events such as vehicle rollovers can lead to compression of the spine and vertebral fractures. Bone fragments from vertebral fracture displace, or occlude, the spinal canal, deforming the spinal cord and leading to the potential of a spinal cord injury (SCI). Finite element (FE) human body models (HBMs) provide an opportunity to predict vertebral fractures and investigate SCIs. Models such as the Global Human Body Models Consortium (GHBMC) model use strain-based element erosion to model hard tissue fracture by removing elements from the simulation upon reaching threshold strains. While strain-based element erosion allows for the prediction of fracture initiation, the method results in the loss of hard tissue material. Under compression, the loss of hard tissue material limits the post-fracture predictive ability of the model due to the loss of structural support and absence of fractured material that may occlude the spinal canal. The objective of the work in this thesis was the implementation of a multi-physics modelling approach to combine strain-based element erosion with smoothed particle hydrodynamics (SPH) to preserve hard tissue material and simulate the movement of fractured material under central compression in a C5-C6-C7 cervical segment FE model. The implementation of SPH was then assessed by comparing the response of the segment model to experimental results and by evaluating SPH particle dependency. Finally, a parametric study was conducted using the model with the SPH implementation to investigate the response of the FE segment model under varied impact severities, aged hard tissue material parameters, and eccentric loading.

The model with the SPH implementation was numerically stable and was found to improve the prediction of the trend and magnitude of the force-displacement response, with the area under the curve compared to the experimental response improving from a 34% difference to a 4% difference. Additionally, the implementation of SPH allowed for modelling the flow of hard tissue material and, consequently, occlusion of the spinal canal. The prediction of maximum occlusion in the model compared to the experiments improved from a 137% difference to a 5% difference. Increasing the number of SPH particles generated for each solid element showed numerical instability, illustrating a need for compatibility between the size of the solid element and the number of SPH particles. Varying the impact severity of the central compression load showed that the occlusion in the FE segment model appeared to have a greater dependency on the maximum displacement applied in compression rather than the maximum velocity of the impact due to the amount of fractured material in the simulation. Applying hard tissue material parameters representative of an older age group resulted in higher occlusion and a lower force-displacement response, in agreement with experimental data. The resulting multi-physics approach improved the model predictive capabilities in all cases. Future research will include a spinal cord in the FE segment model to more accurately assess changes in the spinal canal geometry and potential for SCI.

Acknowledgements

I would like to gratefully acknowledge funding from the Natural Sciences and Engineering Research Council of Canada, Stellantis Canada, General Motors of Canada, Honda Development and Manufacturing of America, and the Global Human Body Models Consortium. This research was undertaken, in part, thanks to funding from the Canada Research Chairs Program. The human model was provided by the Global Human Body Models Consortium. Computing resources were provided by Digital Research Alliance of Canada.

I would also like to sincerely thank my supervisor, Duane Cronin, for all the opportunities he provided throughout my degree and for allowing me to work on this project. I am also grateful for his support, guidance, and patience throughout my degree.

Thank you to Claire Rampersadh for all our meetings, for her technical guidance with trabecular bone and getting the model to work, and for her mentorship.

Thank you to Aleksander Rycman for his guidance with the journal paper, getting started on this project, learning about different software, and getting the SPH implementation working.

Thank you to Jeffrey Barker for his help and support with the model, running simulations, and beginning my degree online.

I would also like to thank everyone in the IMMC group for providing help and feedback with my project work and presentations during meetings and through emails.

I would also like to thank my family for always being so supportive and for having my back. Thank you to my parents for raising me and giving me the foundation and security to continue studying. Thank you to my sister for being my advisor and confidant.

Table of Contents

Author's Declaration ii

Statement of Contributions iii

Abstract iv

Acknowledgements v

List of Figures xi

List of Tables xx

List of Abbreviations xxi

Chapter 1 Introduction 1

1.1 Motivation for Research 1

1.2 Research Objective and Approach 2

1.3 Thesis Outline 3

Chapter 2 Background 4

2.1 Anatomy 4

2.1.1 Anatomy of the Cervical Spine 5

2.1.2 Cervical Vertebrae Anatomy 7

2.2 Bone Composition 7

2.2.1 Cortical Bone 9

2.2.2 Trabecular Bone 9

2.3 Hard Tissue Injury in the Spinal Column 11

2.4 Experimental Studies to Measure Occlusion in the Spinal Canal Under Axial Compressive Loading 12

2.4.1 Measuring Occlusion in the Spinal Canal with a Fluid-Filled Tube 12

2.4.2 Measuring the Occlusion in the Spinal Canal Using a Strain Gauge Transducer 15

2.4.3 Measuring Occlusion in the Spinal Canal Using a Camera 16

2.4.4 Measuring Occlusion in the Spinal Canal Using the Spinal Canal Occlusion Transducer 17

2.5 Computational Human and Neck Models to Investigate Vertebral Fracture 20

2.5.1 Duke University Head and Neck Model (DUHNM) 21
2.5.2 Human Model for Safety (HUMOS) 21
2.5.3 Total Human Model for Safety (THUMS) 22
2.5.4 VIVA+ Model 23
2.5.5 Global Human Body Models Consortium (GHBMC) Model 23
2.6 Smoothed Particle Hydrodynamics (SPH) Method to Model Large Deformations 30
2.6.1 SPH in Bone and Spine Applications 31
2.6.2 Eroded Finite Elements Converted to SPH, Implementation in FE Code 32
2.6.3 Examples of Applications Implementing SPH to Convert Solid Elements to SPH Particle Elements 34
Chapter 3 Methods 35
3.1 Model Enhancements to the FE Motion Segment Model: GHBMC Segment to SPH Implementation 36
3.1.1 Plastic Kinematic Material Model for Hard Tissues: CC_{PlK} Model 40
3.1.2 Anisotropic Material Model for Hard Tissues: CC_{Ani} Model 41
3.1.3 Added Contact Definitions to Account for Erosion and to Allow for Ligament to Intervertebral Disc Contact: CC_{Con} Model 43
3.1.4 Addition of Minimum Principal Strain to Erosion Criterion of Trabecular Bone: CC_{MPS} Model 48
3.1.5 Implementation of SPH to Trabecular Bone: CC_{SPH} Model 49
3.2 Evaluation of the SPH Implementation in the CC_{SPH} Model Against Experimental Targets 52
3.2.1 Force-Displacement Response 52
3.2.2 Hard Tissue Failures Predicted in FE Model Compared to Reported Tissue Damage from Experiments 54
3.2.3 Spinal Canal Occlusion 55
3.3 Investigation of the Effect on the Force-Displacement Response with Varied Number of SPH Particles Generated Upon Erosion 57

3.4 Parametric Study: Investigating Model Response Under Varied Impact Severity, Material Parameters, and Eccentric Loading 58
3.4.1 Investigating the Effect of Varying Maximum Velocity and Maximum Displacement on Spinal Canal Occlusion 60
3.4.2 Comparison of Occlusion and Force-Displacement Response Using Aged Material Parameters for the Hard Tissues 63
3.4.3 Investigating the Effect of Eccentric Boundary Conditions on Spinal Canal Occlusion 67
Chapter 4 Results 70
4.1 Model Enhancements to the FE Motion Segment Model: GHBMC Segment to SPH Implementation 70
4.1.1 Plastic Kinematic Material Model for Hard Tissues: CC_{PlK} Model 70
4.1.2 Anisotropic Material Model for Hard Tissues: CC_{Ani} Model 72
4.1.3 Added Contact Definitions to Account for Erosion and to Allow for Ligament to Intervertebral Disc Contact: CC_{Con} Model 74
4.1.4 Addition of Minimum Principal Strain to Erosion Criterion of Trabecular Bone: CC_{MPS} Model 76
4.1.5 Implementation of SPH to Trabecular Bone: CC_{SPH} Model 79
4.2 Evaluation of the SPH Implementation in the CC_{SPH} Model Against Experimental Targets 81
4.2.1 Force-Displacement Response 81
4.2.2 Hard Tissue Failures Predicted in FE Model Compared to Reported Tissue Damage from Experiments 84
4.2.3 Spinal Canal Occlusion 85
4.3 Investigation of the Effect on the Force-Displacement Response with Varied Number of SPH Particles Generated Upon Erosion 89
4.4 Parametric Study: Investigating Model Response Under Varied Impact Severity, Material Parameters, and Eccentric Loading 91
4.4.1 Investigating the Effect of Varying Maximum Velocity and Maximum Displacement on Spinal Canal Occlusion 91

4.4.2 Comparison of Occlusion and Force-Displacement Response Using Aged Material Parameters for the Hard Tissues 94
4.4.3 Investigating the Effect of Eccentric Boundary Conditions on Spinal Canal Occlusion 99
Chapter 5 Discussion 101
5.1 Model Enhancements to the FE Motion Segment Model: GHBMC Segment to SPH Implementation 101
5.1.1 Plastic Kinematic Material Model for Hard Tissues: CC_{PlK} Model 101
5.1.2 Anisotropic Material Model for Hard Tissues: CC_{Ani} Model 103
5.1.3 Added Contact Definitions to Account for Erosion and to Allow for Ligament to Intervertebral Disc Contact: CC_{Con} Model 105
5.1.4 Addition of Minimum Principal Strain to Erosion Criterion to Trabecular Bone: CC_{MPS} Model 106
5.1.5 Implementation of SPH for Trabecular Bone: CC_{SPH} Model 106
5.2 Evaluation of the SPH Implementation in the CC_{SPH} Model Against Experimental Targets ... 107
5.2.1 Force-Displacement Response 107
5.2.2 Hard Tissue Failures Predicted in FE Model Compared to Reported Tissue Damage from Experiments 112
5.2.3 Spinal Canal Occlusion 113
5.3 Investigation of the Effect on the Force-Displacement Response with Varied Number of SPH Particles Generated Upon Erosion 115
5.4 Parametric Study: Investigating Model Response Under Varied Impact Severity, Material Parameters, and Eccentric Loading 117
5.4.1 Investigating the Effect of Varying Maximum Velocity and Maximum Displacement on Spinal Canal Occlusion 118
5.4.2 Comparison of Occlusion and Force-Displacement Response Using Aged Material Parameters for the Hard Tissues 121
5.4.3 Investigating the Effect of Eccentric Boundary Conditions on Spinal Canal Occlusion .. 125
5.5 Limitations and Future Work 129
Chapter 6 Conclusion 131

Letter of Copyright Permission 134

References 136

List of Figures

Figure 2.1: Anatomic planes and directions. From: https://commons.wikimedia.org/wiki/File:Anatomical_Planes.svg (with labels added) 4
Figure 2.2: Human spine with labels indicating the names of each vertebra (left) and region (right). From: https://commons.wikimedia.org/wiki/File:Figure_38_01_07.jpg..... 5
Figure 2.3: Bony structures of the cervical vertebra. 7
Figure 2.4: Diagram showing the cortical and trabecular bone (From: https://commons.wikimedia.org/wiki/File:Bone_unit_-_Osteon_1_--_Smart-Servier.png, https://commons.wikimedia.org/wiki/File:Spongy_bone_-_Trabecular_bone_-_Normal_trabecular_bone_--_Smart-Servier.png, https://commons.wikimedia.org/wiki/File:Rheumatology_-_Newly_formed_bone_--_Smart-Servier.png) 8
Figure 2.5: Stress-strain response of trabecular bone under compression. 10
Figure 2.6: An example diagram of the set-up of the closed-loop fluid-filled system used to measure occlusion in the spinal canal of a specimen. Adapted from Chang et al., 1994. 13
Figure 2.7: An example diagram showing the profile of the strain gauge transducer (in blue) in the spinal canal of a vertebra. 15
Figure 2.8: Schematic of the experimental set-up measuring the spinal canal occlusion using mirrors and a high-speed video camera. The grey shaded shape shows an example specimen. The blue lines indicate the location of mirrors that are fixed in position. The orange arrows indicate the path of the light from the light source, through the spinal canal, and to the high-speed video camera. Adapted from Wilcox et al., 2002. 16
Figure 2.9: A schematic showing the SCOT. Adapted from Raynak et al. (1998). 17
Figure 2.10: A diagram of the central compression experimental set-up from Carter et al. (2002). 19
Figure 2.11: Examples of finite element neck models (Cronin, 2021). 20
Figure 2.12: Locations of the ligaments on the C5-C6-C7 segment model. The red lines indicate the beam elements of the ligaments. 25
Figure 2.13: Locations of the facet joint cartilage parts on the C5-C6-C7 segment model. The yellow parts represent the solid elements of the facet joint cartilages. 26
Figure 2.14: Locations of the intervertebral discs on the C5-C6-C7 segment model (left). The section view (right) cuts the C6-C7 intervertebral disc in the midsagittal plane to show the annulus fibrosis layers sitting in the annulus matrix. The translucent red part indicates the annulus matrix. The solid red part indicates the nucleus. 27

Figure 2.15: Locations of the endplates in the C5-C6-C7 segment model. The dark gray parts indicate the shell elements of the endplates..... 28
Figure 2.16: The locations of the vertebrae in the C5-C6-C7 segment model (left). The section view (right) cutting the C5 vertebra in the midsagittal plane shows the cortical and trabecular bone. The purple part indicates the shell elements of the cortical bone. The orange part indicates the solid elements of the trabecular bone..... 29
Figure 2.17: Simplified diagram showing the SPH particle elements for bone and spine simulations. 32
Figure 2.18: A diagram illustrating an example of the SPH implementation where solid Lagrangian continuum elements are transformed into SPH particle elements upon erosion of the solid element. The light green shaded squares represent solid elements. The yellow-orange shaded squares represent solid elements that reach their failure threshold. The grey shaded circles represent inactive SPH particle elements. The light green shaded circles represent active SPH particle elements. 33
Figure 3.1: Schematic of model development, assessment and evaluation. The section numbers and objectives are in bold. 36
Figure 3.2: Sagittal view of the GHBMC M50 head and neck model (left). The orange, light purple, and red parts circled in red indicate the functional spinal units extracted for the CC model (right). The labels on the CC model used for the central compression loading show parts of the loading apparatus and cervical spine segment parts. The green arrow shows the direction of the preload and displacement-controlled input applied to the top potting. 37
Figure 3.3: The displacement vs time graph showing the displacement in the downward direction (compression) of the top potting. A 40 N preload was applied from 0 ms to 250 ms in the simulation. At 250 ms, a displacement-controlled input was applied. The displacement input applied during the Loading Phase was based on the profile of a Haversine velocity pulse. The displacement was held constant during the Holding Phase. The displacement in the unloading phase corresponded to the upward motion of the top potting. 38
Figure 3.4: Progression of models to include changes to the cervical spine segments leading to the implementation of SPH. At each step, a change is added to the model from the preceding step. Each step of the schematic shows the name assigned to the model at each step of the progression as well as the new change implemented in the step. 39
Figure 3.5: Sagittal plane views showing an example of each contact added in the CC_{Con} model. 46
Figure 3.6: Stress-strain response of a single element simulation using the trabecular bone material model developed by Khor (Khor, 2018; Liu et al., 2013; Mosekilde et al., 1985; Sanyal et al., 2012). The *x*-axis shows the true strain in compression. The *y*-axis shows the true stress in compression..... 49

Figure 3.7: SPH implementation into the solid elements of the trabecular bone. The vertebra (top) shows the elements of the C6 vertebra. The schematic (bottom) shows the conversion of solid elements into SPH particle elements. The solid element is loaded. The solid element is transformed into an SPH particle element upon erosion of the solid element. 50
Figure 3.8: Sagittal view of the CC model with labels to indicate where the displacement and force values are measured. The displacement is measured as the displacement of the top potting. The green arrow indicates the direction of positive displacement. The force is measured at the load cell. The red arrow indicates to location of the section plane used to measure the force in the model. 53
Figure 3.9: Schematic of the steps in the Rectangle Method used to calculate percent occlusion in the model. The images of the C6 vertebra shown steps 4 to 7 are an examples of the percent occlusion calculation method for the last time step of the CC_{SPH} model. 56
Figure 3.10: Overview of simulation configuration names included in the investigation of increasing the number of SPH particles generated for each solid element. Each diagram shows a two-dimensional illustration of the configuration of SPH particles generated in LS DYNA. 58
Figure 3.11: Overview of parameters investigated for the parametric study using the cervical spine model as developed for the CC_{SPH} model. 59
Figure 3.12: Each black diamond point shows the maximum displacement and maximum velocity measured for a central compression experimental specimen. The orange circle points show the maximum displacement and maximum velocity for each case run in the impact severity investigation in the parametric study. 60
Figure 3.13: Case names for each combination of maximum displacement and maximum velocity run for the impact severity parametric study. 61
Figure 3.14: Stress-strain response of a single element simulation using the trabecular bone material model developed by Khor (Khor, 2018; Liu et al., 2013; Mosekilde et al., 1985; Sanyal et al., 2012). The *x*-axis shows the true strain in compression. The *y*-axis shows the true stress in compression. The “X” indicates where the erosion of the solid Lagrangian element occurs. 65
Figure 3.15: The displacement vs time graph shows the displacement of the top potting with maximum displacements of 15 mm in compression (CC_{A15}) and of 8 mm in compression (CC_{A08}). A 40 N preload was applied between 0 ms and 250 ms. After 250 ms, a displacement-controlled input was applied in the downward direction (compression). The grey dashed curve shows the displacement input with a maximum displacement of 15 mm. The light grey curve shows the displacement input with a maximum displacement of 8 mm. 67
Figure 3.16: Model setups used for the (a) anterior, (b) posterior, (c) low lateral, and (d) high lateral eccentric cases in the parametric study. The red dashed lines indicate the location of the geometric

centroid of the C6-C7 intervertebral disc. The green arrows indicate the location of the bearing where the displacement-controlled input was applied. The labels above the red arrows indicate the horizontal distance between the geometric centroid of the C6-C7 disc and the bearing where the displacement-controlled input was applied. The light and dark green parts indicate the loading apparatus. The blue parts indicate the bearing of the loading apparatus. The grey parts indication the load cell. 68
Figure 4.1: Force-displacement responses of the experimental specimen and of the CC_{PlK} model. The black dashed curves show the experimental responses (Carter et al., 2002; Rycman et al., 2023). The yellow curve shows the force-displacement response of the CC_{PlK} model. 71
Figure 4.2: Section views in the midsagittal plane (top) and hard tissue erosion patterns (bottom) for the CC_{PlK} model during loading. In the section views, the light orange parts represent the solid elements of the trabecular bone, the purple-grey parts represent the shell elements of the cortical bone, the red parts represent the intervertebral discs, and the green parts represent the potting. In the erosion pattern images, the blue shaded region indicates the eroded hard tissue elements. 72
Figure 4.3: Force-displacement responses of the experimental specimen and of the CC_{Ani} model. The black dashed curves show the experimental responses (Carter et al., 2002; Rycman et al., 2023). The light green curve shows the force-displacement response of the CC_{Ani} model. 73
Figure 4.4: Section views in the midsagittal plane (top) and hard tissue erosion patterns (bottom) for the CC_{Ani} model during loading. In the section views, the light orange parts represent the solid elements of the trabecular bone, the purple-grey parts represent the shell elements of the cortical bone, the red parts represent the intervertebral discs, and the green parts represent the potting. In the erosion pattern images, the blue shaded region indicates the eroded hard tissue elements. 74
Figure 4.5: Force-displacement responses of the experimental specimen and of the CC_{Con} model. The black dashed curves show the experimental responses (Carter et al., 2002; Rycman et al., 2023). The purple curve shows the force-displacement response of the CC_{Con} model. 75
Figure 4.6: Section views in the midsagittal plane (top) and hard tissue erosion patterns (bottom) for the CC_{Con} model during loading. In the section views, the light orange parts represent the solid elements of the trabecular bone, the purple-grey parts represent the shell elements of the cortical bone, the red parts represent the intervertebral discs, and the green parts represent the potting. In the erosion pattern images, the blue shaded region indicates the eroded hard tissue elements. 76
Figure 4.7: Force-displacement responses of the experimental specimen and of the CC_{MPS} model. The black dashed curves show the experimental responses (Carter et al., 2002; Rycman et al., 2023). The orange curve shows the force-displacement response of the CC_{MPS} model. 78
Figure 4.8: Section views in the midsagittal plane (top) and hard tissue erosion patterns (bottom) for the CC_{MPS} model during loading. In the section views, the light orange parts represent the solid elements of

the trabecular bone, the purple-grey parts represent the shell elements of the cortical bone, the red parts represent the intervertebral discs, and the green parts represent the potting. In the erosion pattern images, the blue shaded region indicates the eroded hard tissue elements. 79
Figure 4.9: Force-displacement responses of the experimental specimen and of the CC_{SPH} model. The black dashed curves show the experimental responses (Carter et al., 2002; Rycman et al., 2023). The light blue curve shows the force-displacement response of the CC_{SPH} model. 80
Figure 4.10: Section views in the midsagittal plane (top) and hard tissue erosion patterns (bottom) for the CC_{SPH} model during loading. In the section views, the light orange parts represent the solid elements of the trabecular bone, the purple-grey parts represent the shell elements of the cortical bone, the red parts represent the intervertebral discs, and the green parts represent the potting. In the erosion pattern images, the blue shaded region indicates the eroded hard tissue elements. 81
Figure 4.11: Force-displacement responses of the experimental specimen, the CC_{MPS} model and the CC_{SPH} model. The black dashed curves show the experimental responses (Carter et al., 2002; Rycman et al., 2023). The orange curve shows the force-displacement response of the CC_{MPS} model without the SPH implementation. The light blue curve shows the force-displacement response of the CC_{SPH} model with the SPH implementation. 82
Figure 4.12: Eroded elements and section views in the sagittal plane of the CC_{MPS} model without the SPH implementation (top) and the CC_{SPH} model with the SPH implementation (bottom). The points correspond to the points in Figure 4.11. Point A is at 2.0 mm, point B is at 5.2 mm, point C is at 9.3 mm, point D is at 9.5 mm, point E s at 12.0 mm, and point F is at 12.3 mm. The blue regions indicate eroded elements of the hard tissues in the vertebrae. In the sagittal plane section views, the orange parts indicate the solid elements of the trabecular bone, the cyan spheres indicate the SPH particle elements, the dark purple part indicate the shell elements of the cortical bone, the red parts indicate the intervertebral discs, and the light and dark green parts indicate the top and bottom potting. The light blue circles at points C and D indication the differences in the intrusion of the intervertebral discs into the C5 and C7 vertebral bodies. The light blue circles at points E and F indication the differences in displacement of hard tissue material into the spinal canal space..... 83
Figure 4.13: Eroded elements and superior views of the hard tissues of the whole C6 vertebra. In the images of eroded elements, the blue shaded regions indicate eroded solid and shell hard tissue elements. In the superior views of the hard tissues, the orange elements indicate the solid elements of the trabecular bone, the light purple elements indicate the shell elements of the cortical bone, and the cyan spheres indicate the SPH particle elements of the trabecular bone..... 85
Figure 4.14: Percent occlusion of the spinal canal at the level of the C6 vertebra as a function of time in the simulation. The orange curve shows the percent occlusion of the CC_{MPS} model without the SPH

implementation. The light blue curve shows the percent occlusion of the CC_{SPH} model with the SPH implementation. The light grey dotting lines indicate the beginning and ends of the loading phase, the holding phase, and the unloading phase. The letter labels correspond to the points in Figure 4.11. 86
Figure 4.15: Superior views of the hard tissues of the whole C6 vertebra. The black rectangles indicate the area used to measure the percent occlusion. The orange elements represent the solid elements of the trabecular bone. The light purple elements represent the shell elements of the cortical bone. The cyan spheres indicate the SPH particle elements of the trabecular bone. 88
Figure 4.16: Maximum percent occlusions of the experiments and models. The maximum percent occlusion and standard deviation (SD) for the Experimental Average are for the age and sex-matched experimental specimens. The maximum percent occlusion for the CC_{MPS} model is for the model without the SPH implementation. The maximum percent occlusion for the CC_{SPH} model is for the model with the SPH implementation. 89
Figure 4.17: Force-displacement responses of the experiments and models. The black dashed curves indicate the force-displacement responses of the central compression age and sex-matched specimen. The light blue curve indicates the force-displacement response of the CC_{SPH} model with the SPH implementation. The brown curve and dashed brown curve indicate the responses of the CC_{NQ2} model and the CC_{NQ3} model where the number of SPH elements generated for each eroded solid element in the trabecular bone is increased. 90
Figure 4.18: The maximum percent occlusions from the experiments and models with varying maximum displacements and maximum velocities. The maximum percent occlusion plotted as a function of (a) the maximum displacement and (b) maximum velocity. 92
Figure 4.19: The maximum percent occlusions from the experiments and models with varying maximum displacements and maximum velocities. The grey bars indicate the maximum percent occlusions for the four experimental specimens with maximum displacement and maximum velocity combinations that most closely match a maximum displacement and maximum velocity combination in a model. The groups of bars increase in maximum velocity along the x-axis. 93
Figure 4.20: Maximum percent occlusions for the experiments and models with matching maximum displacement and maximum velocity combinations. 94
Figure 4.21: Force-displacement responses of the experimental specimen and of the CC_{A08} model. The grey dotted curve shows the experimental response (Carter, 2002). The light purple dashed curve shows the force-displacement response of the CC_{A08} model. 95
Figure 4.22: Force-displacement responses of the experimental specimen and of the CC_{A15} model. The grey dotted curve shows the experimental response (Carter, 2002). The light purple curve shows the force-displacement response of the CC_{A15} model. 96

Figure 4.23: The maximum percent occlusions for the experimental and models with aged material parameters. 97
Figure 4.24: Superior views of the hard tissues of the whole C6 vertebra for the CC_{A15} model and CC_{A08} model with aged hard tissue material parameters. The black rectangles indicate the area used to measure the percent occlusion. The orange elements represent the solid elements of the trabecular bone. The light purple elements represent the shell elements of the cortical bone. The cyan spheres represent the SPH particle elements of the trabecular bone. 98
Figure 4.25: Maximum percent occlusion for the experiments and models under central compression and eccentric loading. The grey bars represent the average maximum values reported in the experiments for central compression and posterior eccentricity (Carter, 2002) and for low and high lateral eccentricity (Van Toen et al., 2014b). The blue bars represent the maximum percent occlusion from the models measured at the level of the C6 vertebra. 99
Figure 4.26: Superior views of the hard tissues of the whole C6 vertebra for eccentric loading. The black rectangles indicate the area used to measure the percent occlusion. The orange elements represent the solid elements of the trabecular bone. The light purple elements represent the shell elements of the cortical bone. The cyan spheres represent the SPH particle elements of the trabecular bone. 100
Figure 5.1: Midsagittal section view of the CC_{PlK} model showing the onset of erosion in the C6 vertebra, the abrupt loss in hard tissue material in the C6 vertebra, and the interpenetration between hard tissues and intervertebral discs. 102
Figure 5.2: Midsagittal section view of the CC_{Ani} model showing the interpenetration at the inferior C6 articular pillar and inferior C5 vertebral body with erosion. 104
Figure 5.3: Midsagittal section view of the CC_{Con} model showing the contacts preventing interpenetration at the inferior C6 articular pillar and inferior C5 vertebral body. 105
Figure 5.4: Midsagittal section view of the CC_{MPS} model showing the fracture initiation and propagation in the C6 vertebral body. 106
Figure 5.5: Midsagittal section view of the CC_{SPH} model showing the fracture initiation and propagation in the C6 vertebral body. 107
Figure 5.6: Energy from the force-displacement responses of the CC_{MPS} model and the CC_{SPH} model calculated before divergence (between 0.0 mm and 5.2 mm), before C6 fracture propagation (between 0.0 mm and 9.3 mm), at maximum displacement (between 0.0 mm and 15.0 mm). 110
Figure 5.7: Energy from the force-displacement responses of the experiments and models calculated between 0.0 mm and 15.0 mm. The experimental average and corresponding standard deviation (SD) are from the age and sex-matched experimental specimen showing improved correspondence between the CC_{SPH} model and experiment. 111

Figure 5.8: Midsagittal section plane views of the CC_{SPH} model and the CC_{NQ2} model. The models show similar fracture patterns with fracture at the pedicles at 4.5 mm, fracture propagation at 12.3 mm, and crushing of hard tissue material at the maximum displacement of 15.0 mm. 115
Figure 5.9: Midsagittal section plane views of the CC_{SPH} model, the CC_{NQ2} model, and the CC_{NQ3} model. At 5.6 mm, there was a sharp increase in the force-displacement response of the CC_{NQ3} model. At 9.3 mm, the CC_{NQ3} model reached an error termination. 116
Figure 5.10: The energy of the force-displacement responses of the models where the number of SPH particles generated for each solid element in the trabecular bone is increased. The energy was calculated between 0.0 mm and 9.3 mm and between 0.0 mm and 15.0 mm. 117
Figure 5.11: Midsagittal section views showing the models with varying maximum velocities and maximum displacements. Each image shows the model at the maximum displacement. The maximum displacements increase from left to right. The maximum velocities decrease from top to bottom. More visible SPH particles (cyan spheres) corresponds to larger amounts of damage. 119
Figure 5.12: Midsagittal section view of the $CC_{12/1.2}$ model, compressed to a maximum displacement of 12.6 mm at a maximum velocity of 1.2 m/s. The section views show the segment when the maximum occlusion was measured according to the Rectangle method (left) and the segment at the maximum displacement of 12.6 mm (right). Since the spinous process displaced in the posterior direction for the $CC_{12/1.2}$ model, the maximum occlusion occurred before reaching maximum displacement. 120
Figure 5.13: The energy of the aged experimental specimen (solid gray) and the CC_{A08} model (striped purple) with aged hard tissue material parameters compressed to a maximum displacement of 8.0 mm. 122
Figure 5.14: A midsagittal section view showing the CC_{A08} model at the maximum percent occlusion. The maximum occlusion was measured during the unloading phase. 122
Figure 5.15: The energy of the CCA08 model (stripped purple) with aged hard tissue material parameters compressed to a maximum displacement of 8.0 mm and the CC_{A15} model (solid purple)with the aged hard tissue material parameters compressed to a maximum displacement of 15.0 mm. 123
Figure 5.16: Midsagittal section views showing the CC_{SPH} model (top) and the CC_{A15} model (bottom) at 8.1 mm, 12.1 mm, and 15.0 mm of displacement. In the CC_{SPH} model with the young hard tissue material parameters, fracture initiated and propagated across the C6 vertebral body. In the CC_{A15} model with the aged hard tissue material parameters, hard tissue material failure progressed from the superior to inferior sides of the C6 vertebra..... 124
Figure 5.17: Midsagittal section views of a) the model with no loading and b) the CC_{SPH} model, c) the Ant_{SPH} model, d) the Pos_{SPH} model, e) the LLt_{SPH} model, and f) the HLt_{SPH} model at the maximum percent occlusion, as measured by the two-dimensional area from the superior view of the C6 vertebra. The black

vertical arrows indicate the regions of the C6 vertebra that would be considered to have occluded the spinal canal area using the Rectangle Method. 127

List of Tables

Table 3.1: Constitutive material model and key material parameters for the hard tissues of the cervical spine in the GHBMC M50 v6-0 model. 40
Table 3.2: Constitutive material models and key material parameters for the anisotropic hard tissue material models developed by Khor (Khor, 2018) 42
Table 3.3: Principal strains, in terms of true strain, of the strain-based erosion criterion applied to the hard tissue material models developed by Khor (Khor, 2018). 43
Table 3.4: Summary of new contacts added to the cervical spine segment model as part of the enhancements in the CC_{Con} model. The first column contains the names assigned to the new contact definition. The second column contacts the contact type used in LS-DYNA. The third column contains the part or part set whose surface is defined as the slave side of the contact. The fourth column contains the part or part set whose surface is defined as the master side of the contact. 45
Table 3.5: Constitutive material model and material parameters assigned to the SPH elements of the trabecular bone in the SPH Model. 51
Table 3.6: Constitutive material models and key material parameters for the anisotropic hard tissue material models developed by Khor for the aged age group of older than 70 years old (Khor, 2018). 63
Table 3.7: Principal strains, in terms of true strain, of the strain-based erosion criterion applied to the hard tissue material models with aged material parameters (Khor, 2018). 64
Table 3.8: Constitutive material models and key material properties assigned to the SPH elements of the aged trabecular bone. 66
Table 4.1: Reported injury patterns in the experimental specimens (Carter, 2002). The values in the Experimental Specimen row indicate the number of specimens out of the eight total central compression specimens with injury reported at each hard tissue location. The structures evaluated were the AVB (anterior vertebral body), PVB (posterior vertebral body), RPED (right pedicle), LPED (left pedicle), RAP (right articular pillar), LAP (left articular pillar), RLAM (right lamina), LLAM (left lamina), and SP (spinous process) 84

List of Abbreviations

ALL - anterior longitudinal ligament

CL - capsular ligaments

CT - computed tomography

DUHNM - Duke University Head and Neck Model

F50 - average female/50th percentile female

FE - finite element

FEM to SPH - finite element method to smoothed particle hydrodynamics

FSU - functional spinal unit

GHBMC - Global Human Body Models Consortium

HBM - human body model

HUMOS - Human Model for Safety

ISL - interspinous ligaments

IVD - intervertebral disc

LF - ligamenta flava

M50 - average male/50th percentile male

MRI - magnetic resonance imaging

PLL - posterior longitudinal ligament

SCI - spinal cord injury

SCOT - spinal canal occlusion transducer

SPH - smoothed particle hydrodynamics

THUMS - Total Human Model for Safety

Chapter 1
Introduction

1.1 Motivation for Research

It has been estimated that around 15.4 million people, globally, suffered from spinal cord injury (SCI) (WHO, 2024) with the most common causes being falls, motor vehicle accidents, and sports (Praxis Spinal Cord Institute, 2023). In 2021, it was estimated that approximately 30 000 of the 86 000 individuals living with an SCI in Canada had a traumatic spinal cord injury (Praxis Spinal Cord Institute, 2023). The estimated lifetime cost for each individual living with a traumatic SCI was ranged from 1.5 to 2 million dollars, while the healthcare cost in Canada due to SCIs was estimated to be around 2 billion dollars (Krueger et al., 2013; Praxis Spinal Cord Institute, 2023, 2021; Spinal Cord Injury BC, 2020). Between 2020 and 2023, the most common cause of SCI was found to be motor vehicle accidents, accounting for 36.4% of SCIs (National Spinal Cord Injury Statistical Center, 2023). The second most common cause of SCI was found to be falls (National Spinal Cord Injury Statistical Center, 2023). Although falls have been accounting for an increasing percentage of SCIs, motor vehicle accidents are still the most common cause leading to SCIs among younger age groups, while falls become a more prevalent cause in older age groups (Algahtany et al., 2021; Chiu et al., 2024; Jackson et al., 2004; Lenehan et al., 2009). The cervical spine was the most commonly injured level in the spine (Chiu et al., 2024; Jackson et al., 2004; Lenehan et al., 2009; Singh et al., 2014), with most cervical spine injuries occurring in the subaxial cervical spine (C3 to C7) (Hobson and Eisenberg, 2024; Tang et al., 2021). The most common injury to the cervical spine was reported to be vertebral fractures (Chiu et al., 2024), and rollovers were reported to be the most likely mechanism leading to injury of the cervical spine (Baigi et al., 2024; Müller et al., 2014; Stein et al., 2011; Thurman et al., 1995). Incidents such as rollovers can lead to compressive loading to the head, which in turn results in compressive loading to the spine causing vertebral fracture and soft tissue damage (Bambach et al., 2013; Mattucci et al., 2019). Injury to the spinal column can then result in fractured hard tissue occluding the spinal canal, deforming the spinal cord and potentially resulting in a SCI (Carter et al., 2002; Mattucci et al., 2019).

Researchers have used experimental and numerical methods to understand vertebral fractures resulting from compression loading. Experimental studies of compression tests have been done with various scales of the spine, including whole cadavers, isolated head-neck studies, isolated cervical spine studies, and cervical spine segment studies. Finite element (FE) Human Body Models (HBMs) have been developed with the aim to assess injury, but are limited in assessing hard tissue failure in the cervical spine and predicting post-fracture and occlusion response (DeWit and Cronin, 2012). FE models, such as the Global

Human Body Models Consortium (GHBMC) 50th percentile male (M50) model, use strain-based element erosion to model the failure of hard tissues in the cervical spine. While the strain-based element erosion method was a numerically stable method that allowed for fracture prediction, the material lost through the removal of elements from the simulation during compression resulted in a loss of both post-fracture structural support and fractured hard tissue to simulate the occlusion of bone fragments into the spinal canal. Thus, to be able to investigate vertebral fractures and the possibility of spinal cord injury, a model needs to be able to predict fracture initiation, post-fracture response, and flow of the fractured or comminuted hard tissues (DeWit and Cronin, 2012).

Smoothed particle hydrodynamics (SPH) is a meshless particle method that has been introduced in solid mechanics problems involving machining, wear, and impacts (de Vaucorbeil and Hutchinson, 2020; Gingold and Monaghan, 1977; Lucy, 1977). More recently, SPH has also been used in numerical simulation of the spinal cord (Arhiptsov and Marom, 2021; Russell et al., 2012; Rycman et al., 2022) and hard tissues such as bone (Basafa et al., 2012; Li et al., 2017, 2014). Furthermore, a recent method to convert Lagrangian elements into SPH particle elements (FEM to SPH) has been applied for simulations including debris modelling of concrete and aluminium (He et al., 2020; Kala and Husek, 2016; Tokura and Niwa, 2017) and in the impact of marine structures on ice (Chen et al., 2021), and could have potential benefits in addressing the challenge in traditional erosion of finite elements.

1.2 Research Objective and Approach

The overall aim of this work was to enhance the modelling of hard tissue fracture of a lower cervical spine finite element segment under compression using SPH implemented into the trabecular bone to preserve material and support load in the segment during fracture. The implementation of SPH in this work was a FEM to SPH approach, where solid Lagrangian elements were adapted into meshless SPH particles upon failure (erosion). The Lagrangian to SPH particle element implementation was applied to the trabecular bone and investigated as a means to improve the post-fracture response in the vertebra under central compression loading.

The first objective was to improve the post-fracture structural support in the FE segment model under central compression through the modelling of hard tissue fracture. Thus, a series of progressively implemented hard tissue model enhancements were added to the segment model, ultimately leading up to the implementation of SPH in the trabecular bone.

The second objective was to evaluate the implementation of SPH in the trabecular bone by evaluating the force-displacement response, occlusion, and hard tissue damage of the FE models against the results reported from experiments.

The third objective was to assess the force-displacement response when varying the number of SPH particles generated upon erosion of a solid trabecular element.

Finally, the fourth objective was to conduct a parametric study by varying the maximum velocity and displacement of a central compression load, implementing aged hard tissue material parameters, and varying the eccentricity of the compression load.

1.3 Thesis Outline

This thesis is organized into five chapters. The first chapter outlines the research problem and objectives. The second chapter of the thesis covers the relevant background starting with the anatomical terms used in the thesis. The chapter then describes cortical and trabecular bone, experimental work related to the compression and resulting occlusion of cervical segments, finite element human body models developed to investigate injury, and finite element studies that have used SPH. The third chapter covers the methods in four subsections. The first subsection comprises a series of progressively implemented model enhancements, leading up to and including the implementation of SPH to the trabecular bone. The second subsection evaluates the implementation of SPH by comparing the FE segment model response to experimental results. The third subsection covers an investigation of a comparison of the FE segment model response when increasing the number of SPH particles generated for each eroded solid element. Finally, the fourth subsection covers a parametric study using the FE segment model with the SPH implementation to investigate the changes in response to varying the impact severity, aging of the hard tissue material parameters, and applying eccentric compression loading. The fourth chapter covers the results of the work described in the method section, following the same order of subsections from the third chapter. Finally, the fifth chapter discusses the results presented in the fourth chapter, limitations of the work, and contributions of the study to improve fracture modeling of the spine.

Chapter 2
Background

The objective of this work was to implement SPH into the trabecular bone of a cervical spine finite element model to convert the solid trabecular bone elements into SPH particle elements upon erosion of the solid element. The background section will cover the anatomy relevant to the lower cervical spine, characteristics of the trabecular bone, mechanics of injury to the spinal column leading to spinal canal occlusion, examples of experimental work measuring spinal canal occlusion, examples of finite element human body models, and finally, SPH and examples of the SPH implementation in different applications.

2.1 Anatomy

There are three anatomic planes that indicate sections through a body (Figure 2.1). The midsagittal plane is a vertical plane that passes from the front to the back of the body, dividing the left and right sides of the body. The sagittal plane is any plane that is parallel to the midsagittal plane. The coronal plane is a vertical plane that passes from the left to the right sides of the body, dividing the anterior and posterior sides of the body. The transverse plane is a horizontal plane that sits at a right angle to both the sagittal plane and the coronal plane (Klenerman, 2015).

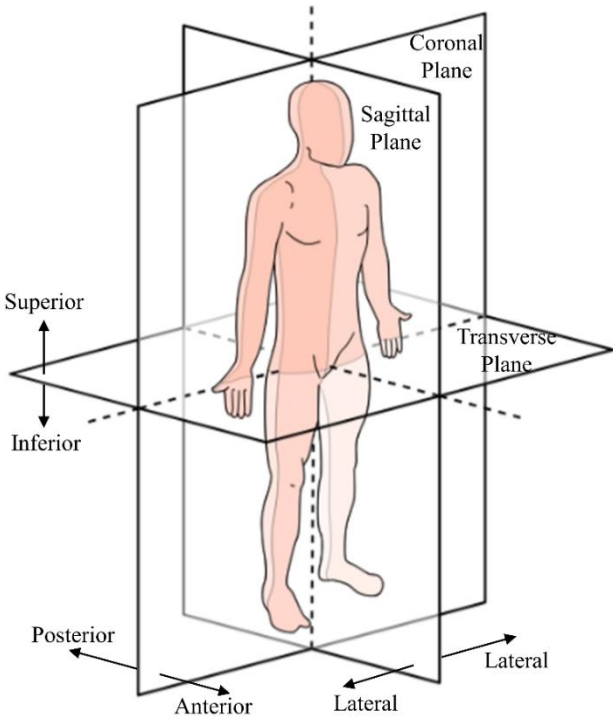


Figure 2.1: Anatomic planes and directions. From: https://commons.wikimedia.org/wiki/File:Anatomical_Planes.svg (with labels added)

In addition to anatomic planes, anatomic terms are also used to describe the relative positions or directions of structures (Klenerman, 2015). The anterior direction refers to the position or direction in front, while the posterior position or direction is behind. The superior direction is above, and the inferior direction is below. The lateral directions are to the sides.

2.1.1 Anatomy of the Cervical Spine

The human spine, or vertebral column, is made of thirty-three vertebrae that are grouped into five regions: the cervical, thoracic, lumbar, sacral, and coccygeal regions (Figure 2.2) (Gray, 1918). The cervical region has seven vertebrae, the thoracic region has twelve vertebrae, and the lumbar region has five vertebrae. The sacral region and coccygeal region are made of five and four vertebrae, respectively; however, the vertebrae in each region are fused together. The cervical region of the spine is the superior-most region.

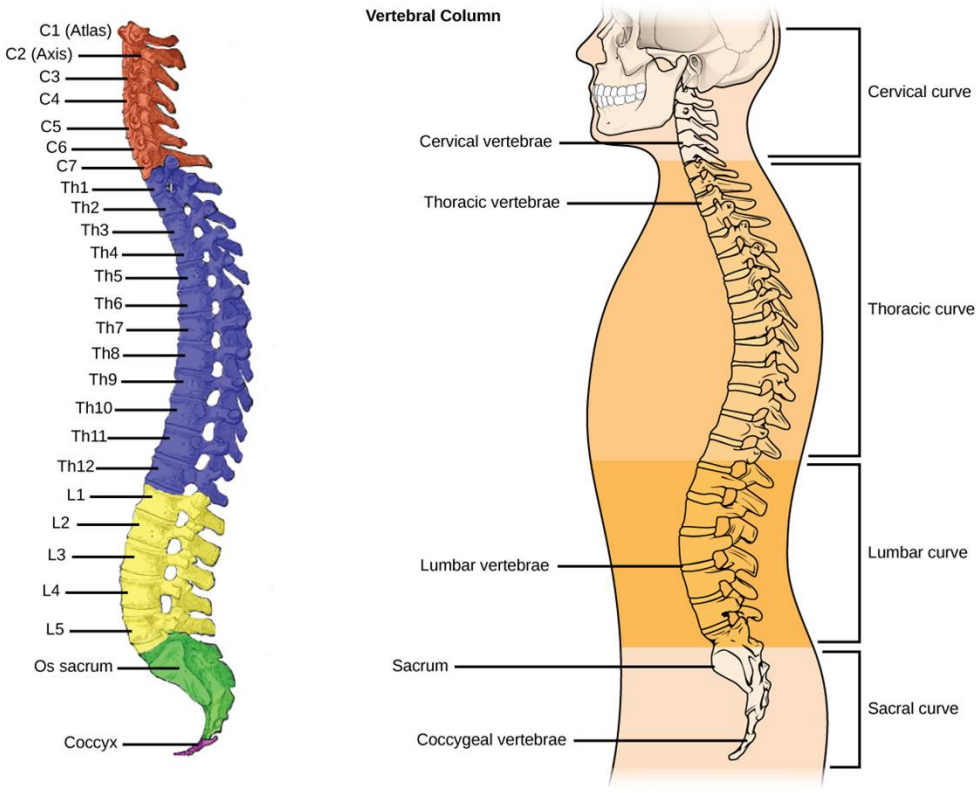


Figure 2.2: Human spine with labels indicating the names of each vertebra (left) and region (right). From: https://commons.wikimedia.org/wiki/File:Figure_38_01_07.jpg

The soft tissues of the ligamentous cervical spine include the intervertebral discs, cervical spine ligaments, and the facet joint cartilage. The hard tissues of the cervical vertebrae include the trabecular bone and the cortical bone. The lower cervical spine includes the C3 to C7 vertebrae, with the size of each vertebra increasing from the C3 vertebra down to the C7 vertebra. The vertebrae enclose the spinal canal, which contains the spinal cord.

The vertebral bodies of each vertebra are connected by an intervertebral disc (IVD). The intervertebral disc is made of the annulus fibrosis which surrounds the nucleus pulposus. The annulus fibrosis is a ring of fibrocartilage. The nucleus pulposus is a semifluid structure which can deform under vertical forces (Hamilton, 1976; Klenerman, 2015). The anterior longitudinal ligament (ALL) and the posterior longitudinal ligament (PLL) attach to the anterior and posterior sides, respectively, of adjacent vertebrae (Hamilton, 1976). The articular pillars of adjacent vertebrae form a synovial joint. Thus, the adjacent articular pillars are held together by capsular ligaments (CL) with a synovial membrane lining (Hamilton, 1976). The surface of the inferior articular pillar of one vertebra and the surface of the superior articular pillar of the adjacent vertebra are covered by a facet joint cartilage (Hamilton, 1976). The small cavity between the inferior and superior surfaces of the articular pillars contain synovial fluid (Hamilton, 1976). The joints between the adjacent vertebral bodies and adjacent articular pillars allows for motion between vertebrae. The ligamenta flava (LF) is a ligament connecting the laminae of adjacent vertebrae, and the interspinous ligament connects the spinous processes of adjacent vertebrae (Hamilton, 1976).

2.1.2 Cervical Vertebrae Anatomy

A typical vertebra in the cervical region of the spine comprises a vertebral body, pedicles, articular pillars, laminae, and a spinous process (Figure 2.3) (Gray, 1918). The space formed by the vertebral body and the pedicles, articular pillars, laminae, and spinous process is the spinal canal. The largest part of a vertebra is the vertebral body. The vertebral body is approximately cylindrical and is the anterior-most structure of the vertebra (Gray, 1918; Hamilton, 1976). The pedicles are two short and thick processes that extend from the sides of the vertebral body in the posterior direction. The pedicles attach to the articular pillars on the left and right. The laminae extend from the articular pillars and fuse together. The spinous process then extends from the junction where the laminae fuse, forming the posterior-most structure of the vertebra (Gray, 1918; Hamilton, 1976).

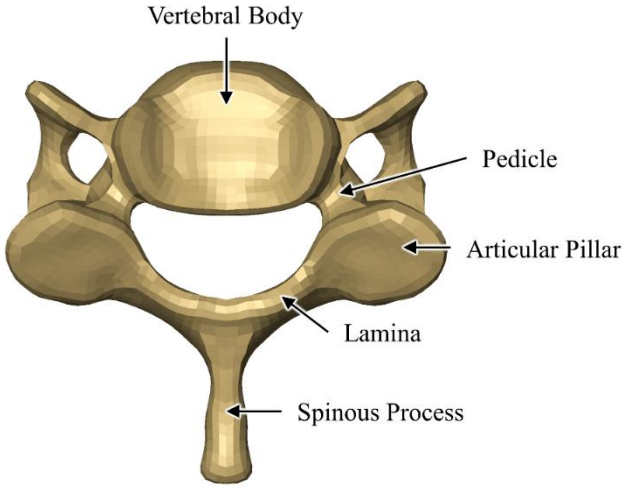


Figure 2.3: Bony structures of the cervical vertebra.

2.2 Bone Composition

The hard tissues in the cervical spine making up the vertebrae are the cortical bone and the trabecular bone (Figure 2.4). The cortical bone, also known as the compact bone, is the thinner, compact, outside layer of the vertebrae (Cooper et al., 2016). The trabecular bone, also known as the cancellous bone, is the spongy bone that accounts for most of the volume of the vertebrae. On a macroscale, trabecular bone is distinguished from cortical bone by being more porous and less dense. Since trabecular bone is more porous, it accounts for 20% of the total weight of bone despite have a greater volume and surface area than cortical bone (Ru et al., 2024). On a microscale, cortical bone is formed by osteons while trabecular bone is formed by trabeculae. Osteons and trabeculae are made of lamellae (Rho et al., 1998). The lamellae are layers of cells embedded a matrix consisting of collagen fibers, crystalline hydroxyapatite, and amorphous calcium phosphate (Gibson and Ashby, 1997; Huiskes and Rietbergen, 2005; Rho et al.,

1998). The composition of organic and inorganic materials contributes to the strength and stiffness of bone (Gibson and Ashby, 1997). Furthermore, bone has both structural and material properties (Rho et al., 1998). The structural properties of bone are determined from the macroscopic structure of bone and are influenced by factors such as the arrangement of osteons or trabeculae and the porosity (Rho et al., 1998). The material properties are determined by the osteons or trabeculae from the microstructure of the bone. Cortical and trabecular bone are both anisotropic materials and are generally stronger along their axis of loading, corresponding to the direction in which osteons and trabeculae are arranged (Rho et al., 1998).

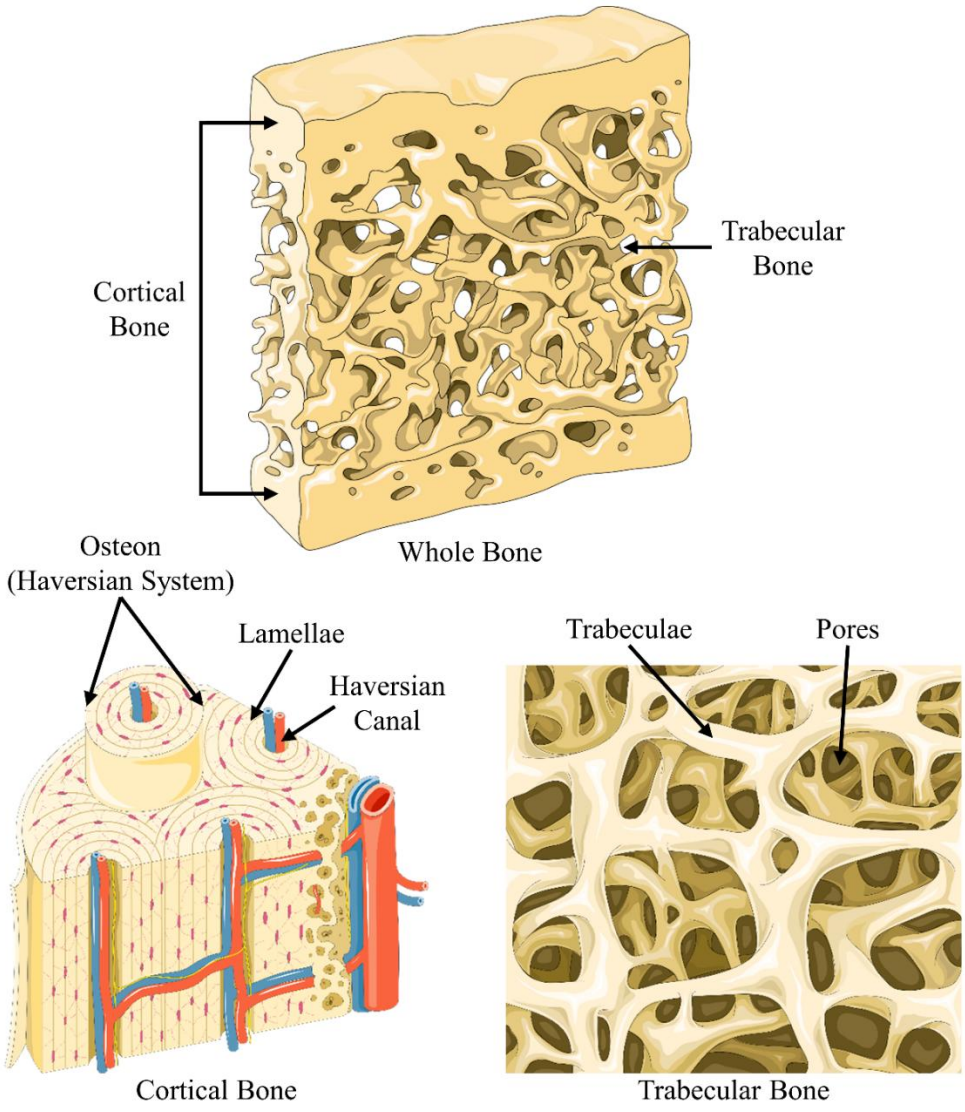


Figure 2.4: Diagram showing the cortical and trabecular bone (From: https://commons.wikimedia.org/wiki/File:Bone_unit_-_Osteon_1_--_Smart-Servier.png, https://commons.wikimedia.org/wiki/File:Spongy_bone_-_Trabecular_bone_-_Normal_trabecular_bone_--_Smart-Servier.png, https://commons.wikimedia.org/wiki/File:Rheumatology_-_Newly_formed_bone_--_Smart-Servier.png)

2.2.1 Cortical Bone

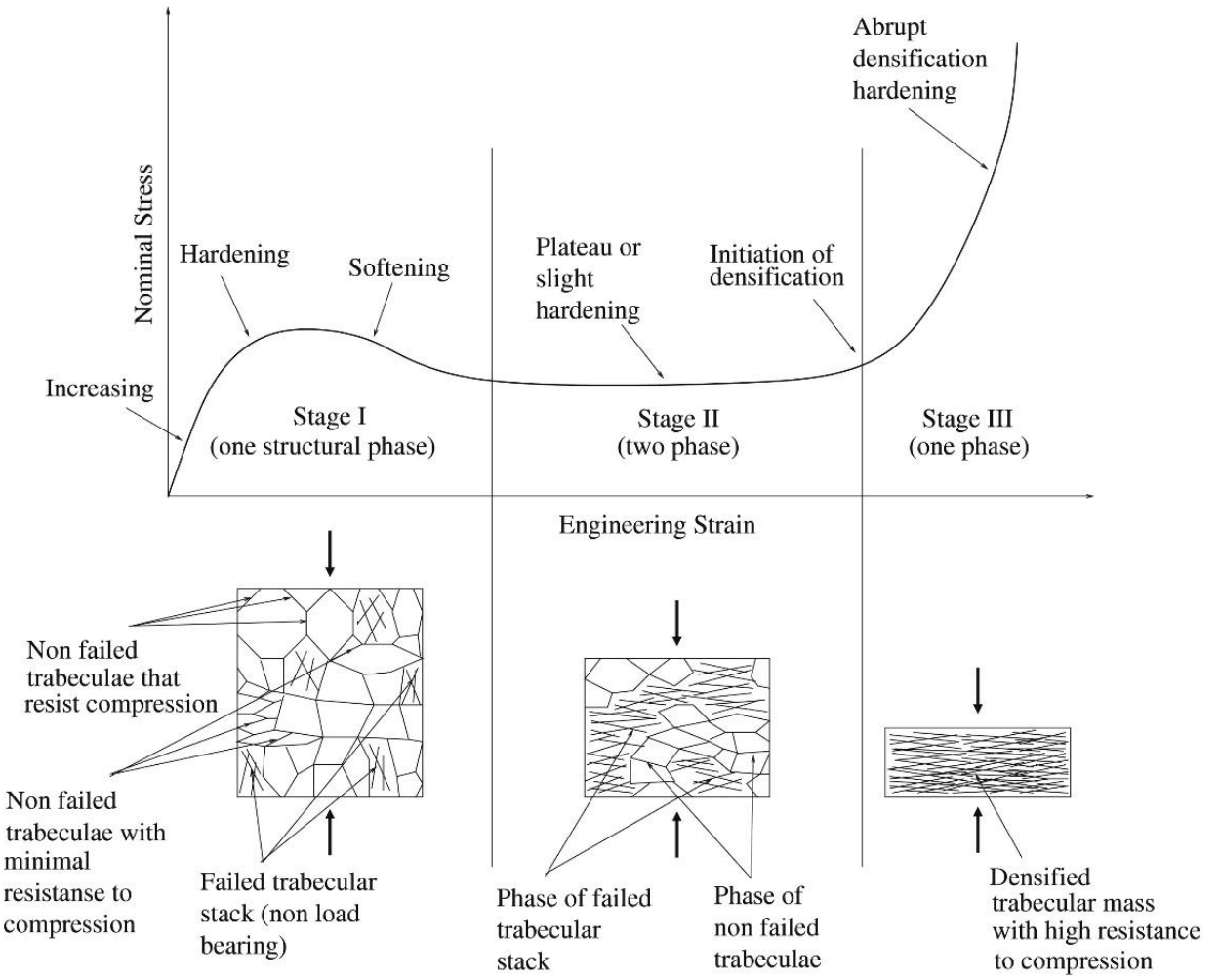
On a microscale, cortical bone is formed by cylindrical structures called osteons or Haversian systems (Gray, 1918; Hamilton, 1976; Ru et al., 2024). The Haversian canals are the holes that run down the center of the osteon. The lamellae, thin plates of bony tissue, are arranged in concentric rings around the Haversian canal. The packed arrangement of osteons gives the cortical bone its strength. The bone is then covered with a membrane known as the periosteum, except at the joints where it is covered by cartilage (Gray, 1918; Hamilton, 1976).

Experimental measurements of cortical bone in the human body also vary depending on factors such as anatomic location, loading direction, and age. Values between 11 GPa and 20 GPa have been reported for the Young's modulus, and values between 0.222 and 0.63 have been reported for the Poisson's ratio (Ashman et al., 1984; Currey, 1984; Gibson and Ashby, 1997; Reilly and Burstein, 1975).

2.2.2 Trabecular Bone

Trabecular bone is a heterogeneous structure with anisotropic mechanical behaviour (Keaveny and Hayes, 1993). Mechanical properties of bone can vary between individuals and between different anatomic locations within an individual (Goldstein, 1987). The strength and stiffness of bone are thought to vary based on the load it experiences and the direction the load is applied to the bone, leading to its anisotropy (Gibson and Ashby, 1997). One of the challenges characterizing the behaviour of trabecular bone arises due to the dependence of its material properties on the architecture of the bone (Goldstein, 1987). The architecture of trabecular bone is dependant on the shape, size, and organization of the trabeculae (Keaveny and Hayes, 1993).

Trabecular bone has a porous structure made of trabeculae (struts) that form a lattice (Carter and Hayes, 1977; Gibson, 1985; Gibson and Ashby, 1997). The lattice forms pores which are filled with red and yellow marrow (Carter and Hayes, 1977). Trabecular bone is often treated as a cellular solid (Keaveny et al., 2001; Keaveny and Hayes, 1993). Overall, the stress-strain response of the trabecular bone under compression can be characterized by three stages: a linear elastic region, a plateau region, and the densification region (Figure 2.5). In the linear elastic region, the initial increase in the stress-strain response is followed by strain hardening and then softening (Carter and Hayes, 1977; Kefalas and Eftaxiopoulos, 2012). The stress-strain response then plateaus as the pores of the trabecular bone collapse due to the failure of the trabeculae (Carter and Hayes, 1977; Kefalas and Eftaxiopoulos, 2012). As the collapsed pores consolidate, the stress rises abruptly in the densification region and the trabecular bone becomes more compact (Carter and Hayes, 1977; Kefalas and Eftaxiopoulos, 2012).



(Reprinted with permission from Elsevier, Kefalas and Eftaxiopoulos, 2012)

Figure 2.5: Stress-strain response of trabecular bone under compression.

In literature, the stress-strain response in the plateau region has been approximated with a straight line, while the densification region has been approximated with a linear stress-strain response (Carter and Hayes, 1977; Gibson and Ashby, 1997; Kefalas and Eftaxiopoulos, 2012; Keyak, 2001). Additionally, the three stages of the stress-strain response have been expressed in constitutive models based on foam-type response (DeWit and Cronin, 2012).

The porous structure of the trabecular bone results in differences between the macroscopic mechanical properties of trabecular bone and between the mechanical properties of the trabeculae. It has therefore been assumed that the mechanical properties of the trabeculae match those of the cortical bone (Gibson and Ashby, 1997).

The properties of trabecular bone can vary between individuals and anatomic locations. Experimental tests on trabecular bone have reported elastic moduli values ranging from 62 MPa to 13 GPa and ultimate strength values ranging from 1 MPa to 14 MPa (Gibson and Ashby, 1997; Goldstein, 1987; Keaveny et al., 2001; Keaveny and Hayes, 1993; Liu et al., 2013; Mosekilde et al., 1987). One experimental test measuring the properties of trabecular bone samples from male cervical vertebrae reported elastic moduli values between 62 MPa and 620 MPa, ultimate stress values between 1 MPa and 14 MPa, and ultimate strain values between 2% and 6% (Liu et al., 2013). The Poisson's ratio is challenging to measure due to the heterogeneous, anisotropic, and cellular nature of trabecular bone (Keaveny and Hayes, 1993). Structural analyses of trabecular bone often assume a Poisson's ratio value of 0.3, which may not be accurate (Keaveny and Hayes, 1993; Wu et al., 2018). Experimental measurements of trabecular bone in the human body have reported Poisson's ratio values of 0.152 to 0.28 (Dalstra et al., 1993; Hong et al., 2007).

2.3 Hard Tissue Injury in the Spinal Column

The spinal column can experience axial compressive loading from head-first impacts as the torso loads the spinal column (Saari et al., 2011). Spinal cord injuries can occur when surrounding tissue pushes on spinal cord, leading to deformation of the spinal cord (Mattucci et al., 2019). There are usually two events leading to the injury of the cervical spinal cord (Chang et al., 1994; Mattucci et al., 2019). The first event results in instability of the spinal column as the ligaments and bone are damaged (Chang et al., 1994; Mattucci et al., 2019). The instability of the spinal column results in a loss of the ability of the spinal column to protect the spinal cord (Mattucci et al., 2019). Damage to the bone of the spinal column can result in vertebral fractures such as compression fractures and burst fractures (Chang et al., 1994; Mattucci et al., 2019). If the instability of the spinal column leads to insult of the spinal column tissues onto the spinal cord, the second event will then involve the deformation of the spinal cord (Chang et al., 1994; Mattucci et al., 2019).

Compressive fractures are usually characterized by injury to the anterior half of the vertebral body (DeWit and Cronin, 2012). Burst fractures are usually characterized by injury to the anterior and posterior vertebral body, with damage also progressing into the laminae (DeWit and Cronin, 2012). Burst fractures are thought to occur as the endplate fractures and the nucleus is pushed into the vertebral body (Roaf, 1960; Tran et al., 1995). When the nucleus is pushed into the vertebral body faster than the fat and marrow within the vertebral body can exit the vertebral body, pressurization occurs inside the vertebral body resulting in a fracture pattern known as the burst fracture (Roaf, 1960; Tran et al., 1995). Bone fragments from the posterior vertebral body can be displaced into the spinal canal (Mattucci et al., 2019). Intrusion of the tissues of the spinal column into the spinal canal space is known as spinal canal

occlusion. Tissues that occlude the spinal canal may push on the spinal cord resulting in deformation of the spinal cord. Deformation of the spinal cord can lead to a potential spinal cord injury.

2.4 Experimental Studies to Measure Occlusion in the Spinal Canal Under Axial Compressive Loading

Axial compression experimental studies have been done on various levels and scales of the cervical spine to observe the kinematics and kinetics (forces, motion, impact conditions) leading to injury in the cervical spine column (fracture type/pattern, occlusion). Compression testing was done on specimens including full cervical spine specimens (Carter et al., 2000; Chang et al., 1994; Ching et al., 1997; Saari et al., 2011), cervical spine segment specimens (Carter et al., 2002; Nuckley et al., 2007), thoracolumbar spine segment specimens (Panjabi et al., 1995; Tran et al., 1995; Wilcox et al., 2003, 2002), and thoracic spine segment specimens (Zhu et al., 2008).

To investigate and understand the mechanics leading to spinal cord injuries resulting from compressive loading, experiments sought to first quantify the geometric changes in the spinal canal, in other words, the spinal canal occlusion. Since clinical neurological impairments from spinal cord injuries did not correlate to the computed tomography (CT) scans of the spinal cord and canal taken after the injury occurred, it was thought that the occlusion of the spinal canal during the impact causing the injury was what lead to the greatest neurological deficit on the spinal cord.

Thus, the experiments that measured occlusion typically measured both post-injury occlusion and transient occlusion. Post-injury occlusion was measured after the specimen had been loaded and fractured. A radiograph or CT scan, typically in the sagittal plane, was used to measure the occlusion of the spinal canal. Transient occlusion was measured during the experiment as loading was applied to the specimen. The changes in the spinal canal geometry were tracked using methods, such as the use of a transducer, to monitor the occlusion of the spinal canal during the impact as injury occurred.

2.4.1 Measuring Occlusion in the Spinal Canal with a Fluid-Filled Tube

One method to measure the occlusion in the spinal canal during impact used the pressure change in a closed-loop fluid-filled system (Figure 2.6) (Chang et al., 1994). A flexible plastic tube was fitted through the spinal canal. The tube was connected to a reservoir and a pump circulated water through the system (Chang et al., 1994). A pressure transducer upstream of the cervical specimen measured the change in pressure in the system (Chang et al., 1994). The system was calibrated to determine the tube diameter change associated with pressure change and the change in cross-sectional area associated with a change in tube diameter (Chang et al., 1994). The changes in the cross-sectional area could be used to calculate

percent occlusion. Thus, as bone fragments were pushed into the spinal canal, resulting in an increase in spinal canal occlusion, the pressure in the tube would decrease (Chang et al., 1994).

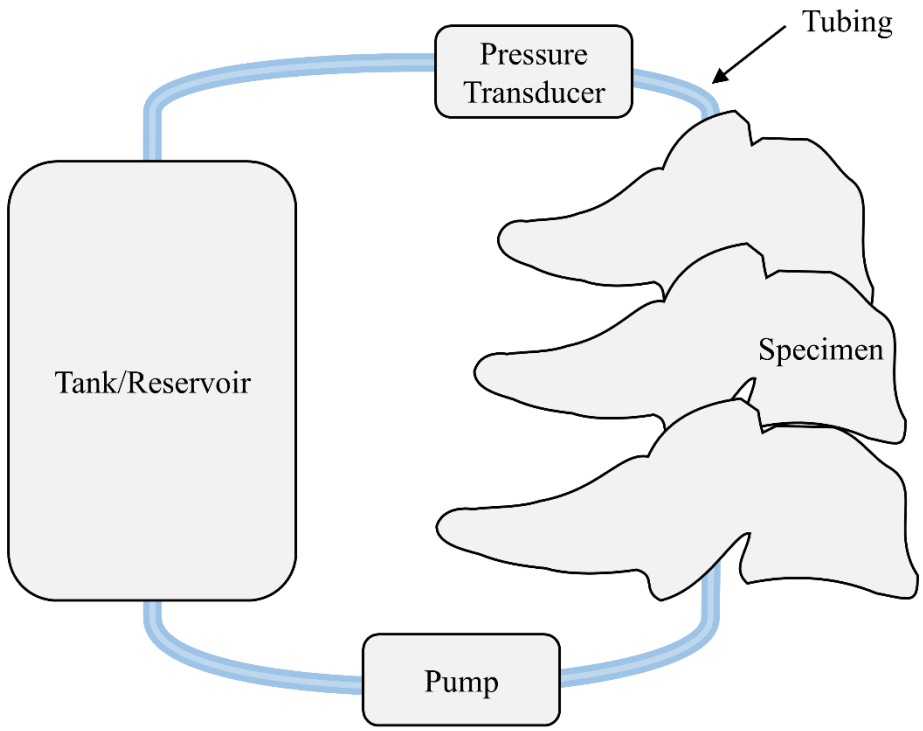


Figure 2.6: An example diagram of the set-up of the closed-loop fluid-filled system used to measure occlusion in the spinal canal of a specimen. Adapted from Chang et al., 1994.

Chang et al. (1994) used the pressure change in a fluid-filled tube to measure the occlusion in the spinal canal resulting from burst fractures in full cervical spine specimens. The aim of the experiment was to compare the transient and post-injury occlusions. Burst fractures in the vertebrae of the C1 to T10 specimens were produced by generating an axial compressive load from dropping a 5.95 kg weight from a height of 1.53 m (Chang et al., 1994). Muscle tissues and the spinal cord were removed from the specimen (Chang et al., 1994). The tube of the closed-loop pressure filled system was fitted through the spinal canal (Chang et al., 1994). The mean peak transient occlusion of 193.2 mm^2 was reported as the canal area in the region of maximum occlusion (Chang et al., 1994). The study found that only the largest occlusion would affect the pressure drop if bone pushed on the tube at multiple levels. Furthermore, the pressure measurement could not inform the level at which the occlusion occurred (Chang et al., 1994).

A different study using three-vertebra thoracolumbar segments used the closed-loop fluid-filled tube system to compare the canal occlusion resulting from low and high rates of loading (Tran et al., 1995). To create a low loading rate, a hydraulic ram was used to apply an axial compressive load over 400 ms. To

create a high loading rate, a weight was dropped on the specimen to apply the axial compressive load over 20 ms. The occlusion of the spinal canal was calculated from the pressure drop in the closed-loop fluid-filled system. The specimens loaded with a high loading rate had a higher percent occlusion of 47.62% compared the low loading rate group with a percent occlusion of 6.84%. The high loading rate generated burst fracture, while the low loading rate group generated compressive fractures with less bone protruding into the canal (Tran et al., 1995).

A third study using the closed-loop fluid-filled system measured the occlusion of the spinal canal in full cervical spine specimens subjected to high and low rate axial compression (Carter et al., 2000). The low rate compression was applied over 250 ms, while the high rate loading was applied over 20 ms by dropping a 4.5 kg mass from a height of 1.5 m. The high rate loading was found to generate burst fractures with a mean maximum percent occlusion during loading of 71%. The occlusion in the high rate group was also higher than in the low rate loading group. Two of the limitations identified in this study included the lack of active musculature and the age range represented by the specimen. The lack of active musculature to stabilize the spine was noted to have less importance due to the compressive, rather than tensile, loading. The age range of the specimen was also older and therefore outside the younger age group that typically experienced fractures due to axial compression impacts (Carter et al., 2000).

One of the identified limitations of the closed-loop fluid-filled tube system was the limited range of spinal canal occlusions the tube was capable of measuring (Chang et al., 1994; Tran et al., 1995). The inner to outer diameter relationship of the tubing and the fit of the tubing in the spinal canal were factors contributing to the range of spinal canal occlusions measurable by the system (Chang et al., 1994; Tran et al., 1995). For example, a smaller tube diameter might be able to measure up to a 61% canal occlusion, while a larger tube diameter might be able to measure up to an 81% canal occlusion (Tran et al., 1995). Additionally, a snugger fit of the tubing into the spinal canal was required to be able to measure partial or smaller occlusions in the canal (Tran et al., 1995). The tube dimensions and fit could therefore be selected to target a desired range of spinal canal occlusions (Chang et al., 1994). The Chang et al. (1994) experiments targeted a 25% to 55% canal occlusion range to measure (Chang et al., 1994). However, due to the variations in canal dimensions within the same vertebrae and in the different vertebrae along the spine, the fit of the tube in the spinal canal was not the same along the entire length of the spine and tube (Chang et al., 1994).

Another identified limitation of the closed-loop fluid-filled tube system was the oscillations of pressure in the system; however, the pressure oscillation was noted to be small relative to the operating pressure of the system (Tran et al., 1995).

2.4.2 Measuring the Occlusion in the Spinal Canal Using a Strain Gauge Transducer

Panjabi et al. (1995) used a transducer with a strain gauge positioned across the spinal canal to quantify the transient occlusion of the spinal canal resulting from burst fractures in three-vertebra thoracolumbar specimens (Figure 2.7). The burst fractures were produced using an incremental protocol. The weight of the mass dropped on the specimen was increased until a burst fracture was produced. The transducer measuring the canal occlusion consisted of a bent steel spring with a strain gauge in the middle portion (Panjabi et al., 1995). Wire feet at the ends secured the transducer to the anterior and posterior walls of the spinal canal (Panjabi et al., 1995). Thus, as the spinal canal narrowed due to the encroachment of bone into the canal, the strain gauge would measure the canal narrowing as the wire feet were brought together (Panjabi et al., 1995). The occlusion measured during the impact was greater than 33.3% (Panjabi et al., 1995). When compared to the closed-loop fluid-filled system, the strain gauge transducer allowed for determining the level in the spine at which occlusion occurred and also allowed for measuring smaller occlusions with a faster response time (Panjabi et al., 1995). Furthermore, the use of an incremental protocol to create burst fractures allowed for applying the minimum energy required to produce the desired fracture (Panjabi et al., 1995). In comparison, other studies applied a single impact to produce the desired fracture, which made it likely a greater energy than the minimum required was applied (Panjabi et al., 1995). The greater energy likely affected the percent occlusion, leading to a lower maximum occlusion value compared to other axial compression experiments (Panjabi et al., 1995).

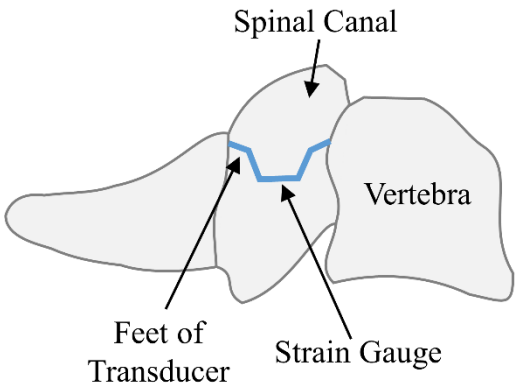


Figure 2.7: An example diagram showing the profile of the strain gauge transducer (in blue) in the spinal canal of a vertebra.

One of the limitations of the strain gauge transducer was a result of designing the transducer to not affect the motion of the segment and fragments and of the transducer itself (Panjabi et al., 1995). The transducer needed to be lightweight to avoid affecting the motion of the bony fragments and intervertebral disc, which contributed to allowing the transducer to dislodge when a bony fragment bounced off it.

Additionally, the wires leading from the transducers out of the canal needed to be thin, which contributed to the wires shorting due to fluid in the canal. Both these events resulted in some loss of data (Panjabi et al., 1995).

2.4.3 Measuring Occlusion in the Spinal Canal Using a Camera

A study by Wilcox et al. (2002) observed the occlusion inside the spinal canal of three-vertebra thoracolumbar bovine segments during burst fractures (Figure 2.8) (Wilcox et al., 2002). The burst fractures in the canal were produced by dropping a mass on the specimen. Mirrors located above and below the spinal canal were angled to allow high-speed video cameras outside the specimen to film the whole spinal canal. The video of the spinal canal was used to observe the inside of the canal and to measure the percent occlusion. It was seen that after initial fracture, fragments from the spinal column would displace into the spinal canal and then recoil due to soft tissue attachments, such as the PLL. For example, one specimen impacted by a 5.6 kg mass dropped from a height of 2 m had a percent occlusion which increased to a maximum of around 68% before decreasing and then plateauing (Wilcox et al., 2002).

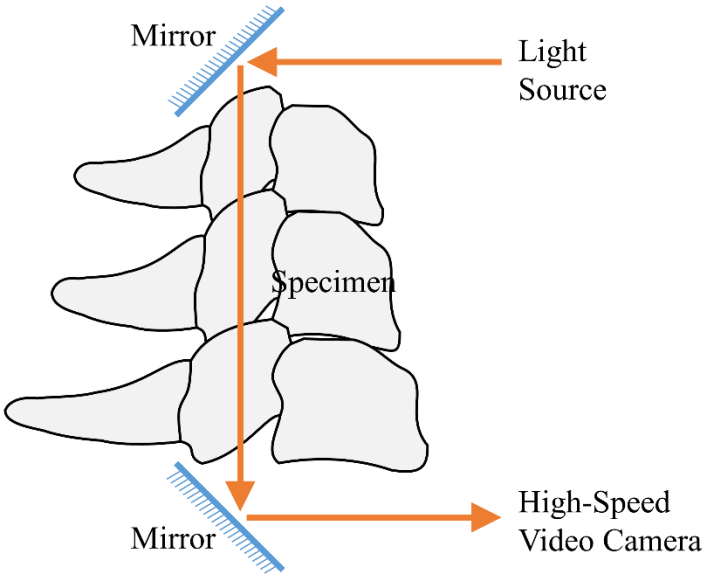


Figure 2.8: Schematic of the experimental set-up measuring the spinal canal occlusion using mirrors and a high-speed video camera. The grey shaded shape shows an example specimen. The blue lines indicate the location of mirrors that are fixed in position. The orange arrows indicate the path of the light from the light source, through the spinal canal, and to the high-speed video camera. Adapted from Wilcox et al., 2002.

Two limitations of this study were that measuring the occlusion of the canal using a camera was more suitable for axial compression of a straight segment where a single view of the camera would allow for viewing the entire canal space (Wilcox et al., 2002). Additionally, the method of measuring occlusion

would not consider the number of occlusions, length of occlusion, or level of occlusion (Wilcox et al., 2002).

2.4.4 Measuring Occlusion in the Spinal Canal Using the Spinal Canal Occlusion Transducer

The spinal canal occlusion transducer (SCOT) was another transducer used to measure spinal canal occlusion (Figure 2.9) (Raynak et al., 1998). The SCOT was comprised of a tube filled with a saline solution. The bottom of the tube was sealed, while the top was vented. Electrodes were placed at intervals along the tube, forming multiple sensing sections. An alternating, constant amplitude current was run through the tube. The potential at each electrode was measured relative to the ground. A change in the tube diameter in one of the sensing sections of the tube would result in a change in the voltage measured in the sensing section between two electrodes. Using Ohm's Law, the change in voltage would be used to find the change in resistance. From prior calibrations, this change in resistance would be used to find the change in the cross-sectional area of the tubing of the SCOT (Raynak et al., 1998). In the experimental work of Carter (Carter, 2002), a percent occlusion was reported as the change in mid-sagittal canal diameter as calculated from the measurements of the SCOT.

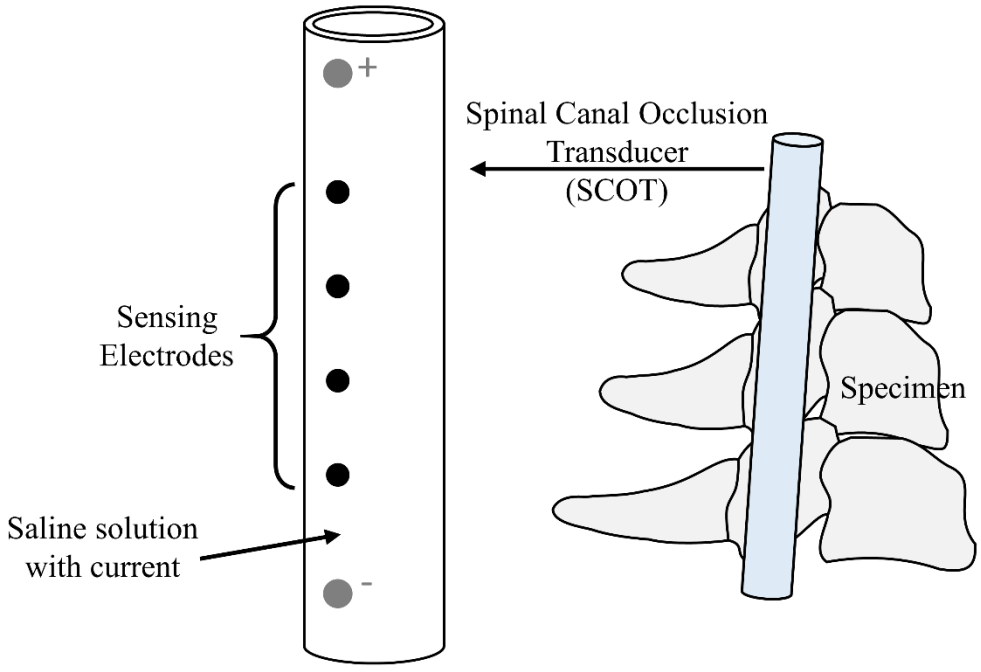


Figure 2.9: A schematic showing the SCOT. Adapted from Raynak et al. (1998).

The SCOT improved on the limitation of the pressure-filled tube by having multiple sensing sections along the tube, allowing for multiple occlusions to be detected along the canal.

One of the studies using the SCOT measured the occlusion in three-vertebrae T1 to T4 segments of the thoracic spine for central compression, posterior eccentric, and anterior eccentric boundary conditions (Zhu et al., 2008). For the central compression case, an incremental trauma protocol was used to apply displacements increasing by 5 mm increments from 5 mm in compression to 30 mm in compression at 0.5 m/s. The mean maximum occlusion increased from approximately 18% at 5 mm of displacement in compression to approximately 42% and 99% at 15 mm and 30 mm in compression, respectively. One of the limitations of the study was that the specimens were from an older population, and therefore, had lower bone densities and disc degeneration. Additionally, the loading cases were idealized, but this allowed for investigating the factors contributing to the spinal canal occlusion. Finally, the specimens did not include active musculature; however, the effect of the lack of active musculature was likely minimized since the impact and acute SCI occurred within 20 ms (Zhu et al., 2008).

Nuckley et al. (2007) used the SCOT to measure occlusion in the spinal canal of three-vertebra baboon cervical spine segment (Nuckley et al., 2007). The specimens were from a younger population since the objective of the study was to investigate the occlusion for developmental ages up to adulthood. Compression was applied using a hydraulic ram with a haversine displacement input profile to apply maximum displacements between 8 mm and 15 mm over a 15 ms pulse width. The average maximum occlusion was found to be 52%. Although the baboon animal model was smaller than human spine specimens, the specimens from the baboon were similar in terms of anatomy and mechanical behaviour (Nuckley et al., 2007).

Carter (2002) used the SCOT to measure the occlusion in the spinal canal of three-vertebra cervical spine specimens loaded under axial compression (Figure 2.10) (Carter, 2002; Carter et al., 2002). The loading groups were central, anterior, and posterior axial compression (Carter, 2002). In the central compression loading group, the specimens were subjected to a 40 N preload, followed by a displacement-controlled input load (Carter et al., 2002). The displacement-controlled input had a haversine velocity pulse profile with maximum displacements between 8 mm to 16 mm applied over a 15 ms pulse width (Carter et al., 2002). The average maximum occlusion was found to be 58.7% for central compression loading and 60.0% for posterior compression loading (Carter, 2002). Occlusion data for the anterior compression loading case was not reported since pulling of the SCOT made the data unreliable (Carter, 2002).

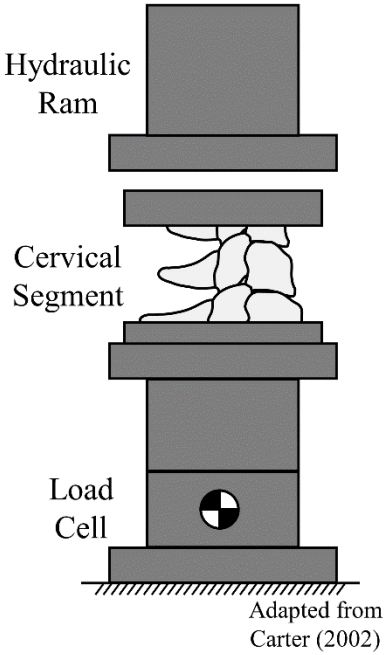


Figure 2.10: A diagram of the central compression experimental set-up from Carter et al. (2002).

A study by Van Toen et al. (2014) also used the SCOT to measure the occlusion in three-vertebra cervical spine segments under low and high lateral eccentric boundary conditions (Van Toen et al., 2014b). The low and high lateral eccentric boundary conditions consisted of lateral bending superimposed on an axial compression load. The specimens were compressed to 20% and 40% of the specimen height in the low and high lateral eccentric cases, respectively. For each eccentric boundary condition, a preload of 50 N was first applied. The preload was followed by the eccentric boundary condition load applied at 0.5 m/s. The specimen was held for 0.1 s before being unloaded at 0.05 m/s. The maximum percent occlusions measured by the SCOT was up to 76% for the low lateral eccentric cases and 33% for the high lateral eccentric cases (Van Toen et al., 2014b).

One of the limitations of the SCOT was that even when ensuring a snug fit of the tubing in the spinal canal, the tube did not fill the entire spinal canal, particularly in the lateral direction (Van Toen et al., 2014b; Zhu et al., 2008). A 100% percent occlusion of the SCOT was therefore equivalent to 64% occlusion of the spinal canal (Zhu et al., 2008). The effect of the SCOT not filling the lateral direction was considered minimized since the occlusion primarily occurred in the sagittal direction (Zhu et al., 2008).

Another limitation of the SCOT was that the transducer measured the changes in the occlusion of the spinal canal (Nuckley et al., 2007). The measured occlusion was therefore a measurement of the change in the space containing the spinal cord, and not a measurement of the cord deformation itself. Thus, the

measurement of spinal canal occlusion did not directly represent the neurologic impairment or injury of the spinal cord (Nuckley et al., 2007).

The presence of the tubing of the SCOT prevented motion of bony fragments into the spinal canal (Zhu et al., 2008). While the tube provided resistance to the displacement of tissues into the spinal canal, the stiffness of the tubing in the transverse direction was similar to that of an in vivo spinal cord (Hung et al., 1982; Zhu et al., 2008).

2.5 Computational Human and Neck Models to Investigate Vertebral Fracture

Various finite element (FE) human body models (HBMs) have been developed to assess and investigate tissue level injuries under various impact conditions (Figure 2.11). Examples of these models include head and neck models such as the Duke University Head and Neck Model (section 2.5.1) and full body human models developed in a seating position for driving (sections 2.5.2, 2.5.3, 2.5.4, and 2.5.5).

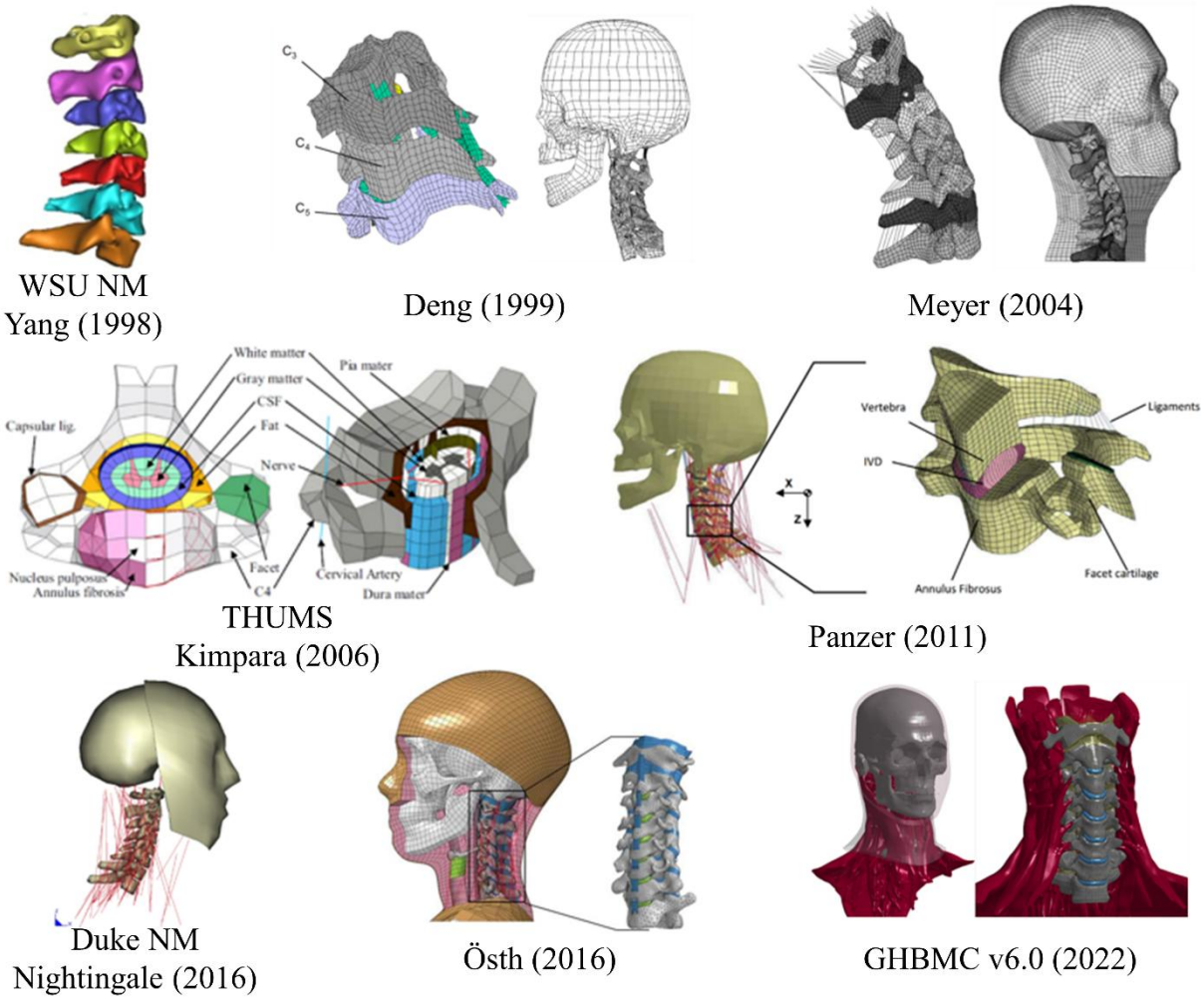


Figure 2.11: Examples of finite element neck models (Cronin, 2021).

2.5.1 Duke University Head and Neck Model (DUHNM)

The Duke University Head and Neck Model (DUHNM) is a hybrid finite element-multibody dynamics model consisting of a deformable head and a lumped parameter neck (Camacho et al., 1997; Nightingale et al., 2016). The geometry of the model was formed from CT scans of the 39-year-old male (Camacho et al., 1997). The vertebrae were modelled as rigid bodies connected by intervertebral joints modelled as Kelvin solids (Camacho et al., 1997). The intervertebral joints were therefore modelled with non-linear springs and linear dashpots (Camacho et al., 1997). The deformable head allowed for load transmission from the head into the spine. Representing the intervertebral joints as Kelvin solids allowed for the behaviour of the joints to be modelled. The DUHNM had been used to study the response of the head and neck under head-first impacts (Camacho et al., 1997; Nightingale et al., 2016). The model could be used to predict kinematics of the head and neck, and therefore, could be used to predict whether the cervical spine might be at risk of injury; however, failure was not modelled so the model could not predict post-injury response (Camacho et al., 1997).

One of the limitations of the model was that it was validated in the midsagittal plane under compressive impacts with the model in an anatomically neutral position (Eckersley et al., 2019; Nightingale et al., 2016).

While the DUHNM could be used to predict vulnerability of the cervical spine to fracture, it did not model hard tissue failure (Camacho et al., 1997). The lack of hard tissue failure modelling limited the model's ability to characterize or predict post-failure response (Camacho et al., 1997). As well, the kinematic and kinetics after the joint or material tolerances were exceeded might not have been realistic (Nightingale et al., 2016).

2.5.2 Human Model for Safety (HUMOS)

The Human Model for Safety (HUMOS) was developed with the aim of developing a three-dimensional finite element human body model in a driving seated position which could be widely used across different computer platforms such as MADYMO, RADIOSS, and PAM-CRASH (Robin, 2001; Tropiano et al., 2004). The geometry of the model was obtained from a cadaver close to the 50^{th} percentile European male (Robin, 2001; Tropiano et al., 2004). The vertebrae were modelled as rigid bodies with shell elements representing the cortical bone and solid elements representing the trabecular bone (Robin, 2001). The HUMOS model could be used to observe the movement of the spine and the stress distribution in the bone (Sun et al., 2012). The Von Mises stress was used to evaluate the risk of bone fracture in the vertebrae (Sun et al., 2012). Once the stress in the elements surpassed threshold stresses of 130 MPa for

the cortical bone and 50 MPa for the trabecular bone, the element was considered failed (Sun et al., 2012; Thollon et al., 2002).

One of the limitations was in the ability of the HUMOS model to describe injury (Thollon et al., 2002). Failure of the tissues was not directly modelled, instead the parts were evaluated during post-processing to see if tissues had exceeded failure thresholds (Sun et al., 2012). This provided a way to evaluate the risk or potential of injury; however, it limited the ability of the model to predict post-failure response (Sun et al., 2012). Improvements were therefore needed in modelling the failure properties of tissues (Thollon et al., 2002). The limitations in modelling material behaviour and injury mechanics were due to limited knowledge (Robin, 2001).

2.5.3 Total Human Model for Safety (THUMS)

The Total Human Model for Safety (THUMS) was developed to study the effect of vehicle impact conditions on the human body (Chawla et al., 2005). The anatomy of the THUMS model was based on the geometry from a commercial data package and anatomic texts, scaled to represent an average American male with a height of 175 cm and a weight of 77 kg (Iwamoto et al., 2015, 2002). The hard tissues of the cervical vertebrae were assigned elastic viscoplastic material models. Shell elements were used to mesh the cortical bone and solid elements were used to mesh the trabecular bone (Chawla et al., 2005; Cloake et al., 2021). Bone fracture in the cortical bone of the vertebrae was assessed based on the risk of fracture from the average peak principal strain (Mattos et al., 2015). 1.0% plastic strain in the vertebrae was used as the threshold to predict where injury would occur (Mattos et al., 2015). The model was able to be used to look at forces and moments of the head and neck, peak principal strains in the cortical bone of the vertebrae, and head and neck injury metrics such as N_{ij} and BrIC (Mattos et al., 2015).

Areas that had been identified for improvement included the material models, contact interfaces, level of detail in the neck and ligaments, and failure modelling (Chawla et al., 2005; Cloake et al., 2021). Material properties did not include both non-linear anisotropic characteristics and strain-rate dependency. Instead, they usually included one or the other (Iwamoto et al., 2002). More details in the model of the brain and organs might also benefit investigations of soft tissue injuries (Iwamoto et al., 2002). The hard tissue properties were based on literature data, but the hard tissues of the cervical vertebrae did not include modelling for simulating hard tissue failure and crack propagation (Cloake et al., 2021). Element erosion was implemented in hard tissues in locations such as the ribs and skull but was not in the vertebrae of the cervical spine (Iwamoto et al., 2002). Instead, peak strains in the cortical bone of the vertebrae were used as an indicator of the fracture risk (Mattos et al., 2015). The peak strains in the cortical bone allowed for evaluating the potential of hard tissue fracture and locations of potential fracture, but without a means to

model hard tissue failure, forces in the cervical spine would be overpredicted, and the model would be limited in its ability to predict post-failure response.

2.5.4 VIVA+ Model

The motivation for the development of the VIVA+ models was to create an average female (F50) model and a platform for the development of a female HBM (Östh et al., 2017b). Other derivatives of the human body model, such as the average male (M50) model, were derived from the F50 model. In the detailed VIVA+ detailed head-neck model, the vertebrae of the cervical spine were modelled with tetrahedral trabecular bone elements covered by a layer of triangular shell elements representing the cortical bone (Östh et al., 2017a, 2016). The elements of both hard tissues were assigned isotropic elastic-plastic material models (Östh et al., 2016). The cervical spine model also included intervertebral discs modelled with hexahedral bulk elements for the annulus ground substance and quadrilateral membrane elements for the annulus fibrosis layers (Östh et al., 2016). Cervical ligaments were meshed with quadrilateral membrane elements (Östh et al., 2016).

One of the limitations of the VIVA+ model was that parts such as the upper extremities, thoracic and lumbar vertebrae, feet, hands, and internal organs were simplified to balance between the overall model detail and computational time (John et al., 2022, 2020). While certain body regions were simplified, the regions identified as locations of interest for studying sex differences in crash impact scenarios included a higher level of detail in the model (John et al., 2022).

Another limitation of the VIVA+ model was that it did not include element erosion (John et al., 2022). Although strains in the cortical bone were used to evaluate injury risk, the absence of a method of modelling hard tissue failure meant the predicted peak forces in the model may be overpredicted (John et al., 2022). In addition, the model would be limited in its ability to model and predict hard tissue failure and post-failure response.

2.5.5 Global Human Body Models Consortium (GHBMC) Model

The Global Human Body Models Consortium (GHBMC) model was developed with the intention of creating a detailed finite element human body model for simulations of automotive crashes. The geometry of the GHBMC 50th percentile male (M50) model was based on CT and magnetic resonance imaging (MRI) scans of a 26-year-old individual with a height of 174.9 cm and a weight of 78.6 kg (Gayzik et al., 2011). Tissue material properties of the model were based on in vitro experiments (Barker et al., 2017).

The neck model, extracted from the GHBMC M50 full body model, had 284 734 elements (Barker and Cronin, 2022). The neck model has been validated against experiment data at the levels of the motion

segment, the ligamentous neck model, and the neck model with musculature (Barker and Cronin, 2022). In the cervical spine, motion segments, consisting of two adjacent vertebrae and an intervertebral joint, were validated against experimental data at various rates and level of the cervical spine (Barker et al., 2017). Validation for the quasi-static loading rates included flexion, extension, lateral bending, and axial rotation boundary conditions (Barker et al., 2017). Dynamic loading rates were applied for flexion and extension boundary conditions (Barker et al., 2017).

The ligaments of the GHBMC model were represented with one-dimensional tension-only truss elements (Figure 2.12) (Barker et al., 2017). The ligaments were assigned non-linear elastic force-displacement responses based on experimental ligament testing (Mattucci, 2011). The number of truss elements representing each cervical ligament was based on the ligament width (DeWit and Cronin, 2012). Failure of the ligaments was represented with a progressive failure criterion to represent the gradually tearing of ligaments (DeWit and Cronin, 2012). The failed truss elements would be deleted from the simulation upon reaching a threshold failure displacement (DeWit and Cronin, 2012). The cervical ligaments modelled were the anterior longitudinal ligaments (ALL), the posterior longitudinal ligaments (PLL), the ligamentum flavum (LF), the interspinous ligaments (ISL), and the capsular ligaments (CL).

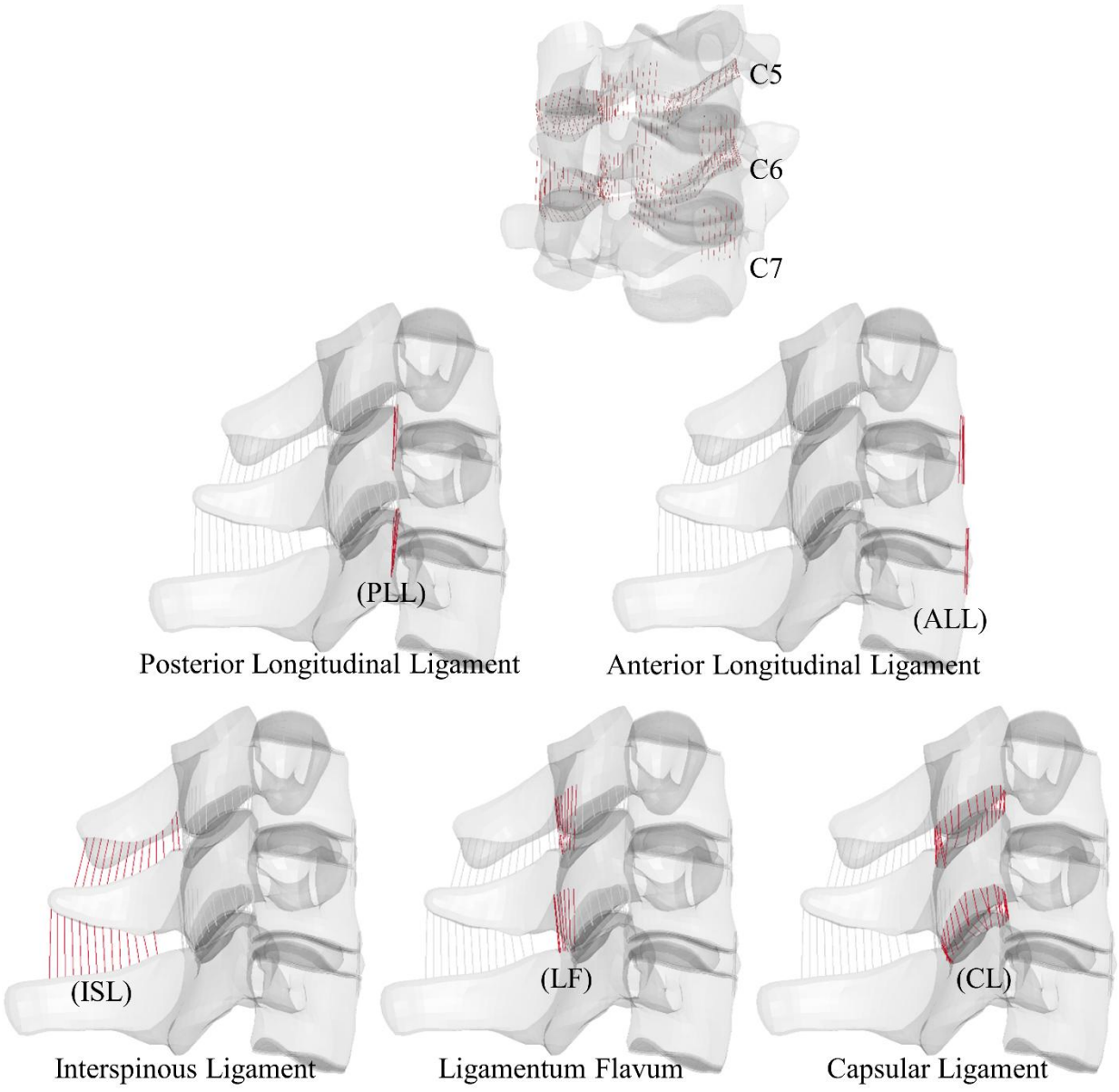


Figure 2.12: Locations of the ligaments on the C5-C6-C7 segment model. The red lines indicate the beam elements of the ligaments.

The cervical facet joint cartilage was meshed with hexahedral solid elements (Figure 2.13). The geometry was based on a “parametric representation of each facet surface” (Corrales and Cronin, 2021).

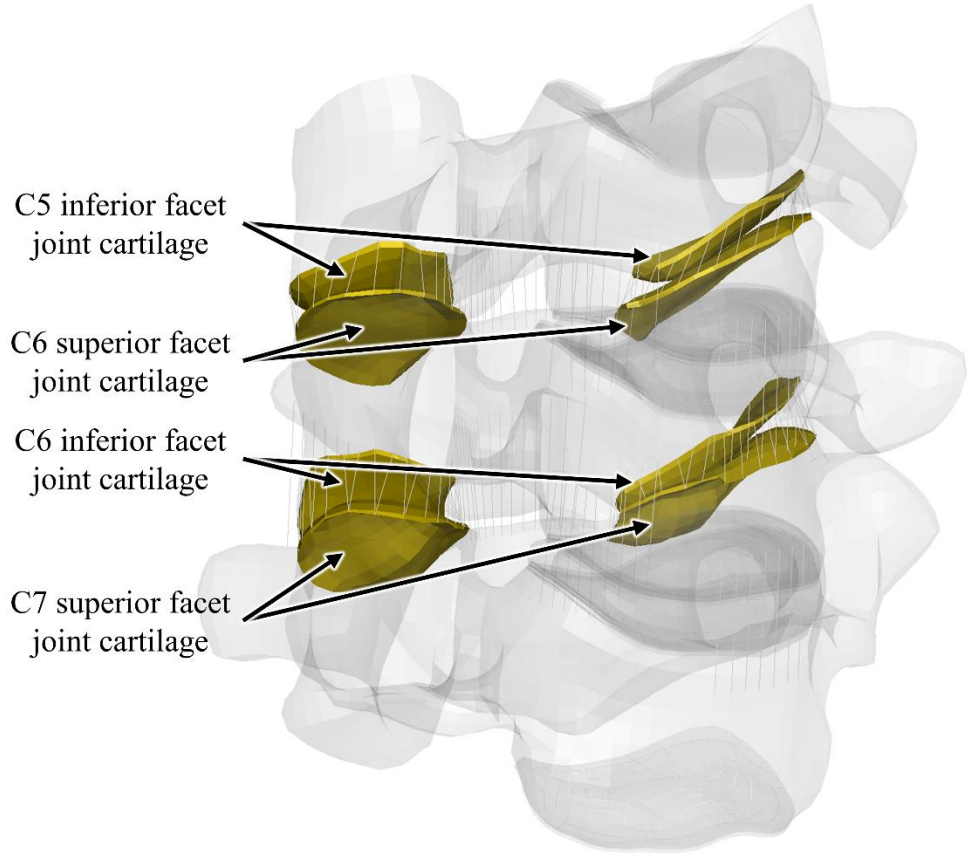


Figure 2.13: Locations of the facet joint cartilage parts on the C5-C6-C7 segment model. The yellow parts represent the solid elements of the facet joint cartilages.

The intervertebral disc was modelled as three parts: the annulus fibrosis layers, the annulus ground substance, and the nucleus pulposus (Figure 2.14). The annulus fibrosis layers were meshed with five pairs of quadrilateral shell element layers. Each pair of concentric shell elements had fibre orientations starting from ±25° on the innermost layer and increasing to ±45° on the outermost layer (Boakye-Yiadom and Cronin, 2018; Khor, 2018). The fibre orientation angles were measured from the transverse plane. The annulus ground substance and the nucleus pulposus were meshed with hexahedral solid elements. Disc avulsion between the intervertebral discs and adjacent vertebral bodies was modelled using a tied interface criterion (Barker et al., 2017).

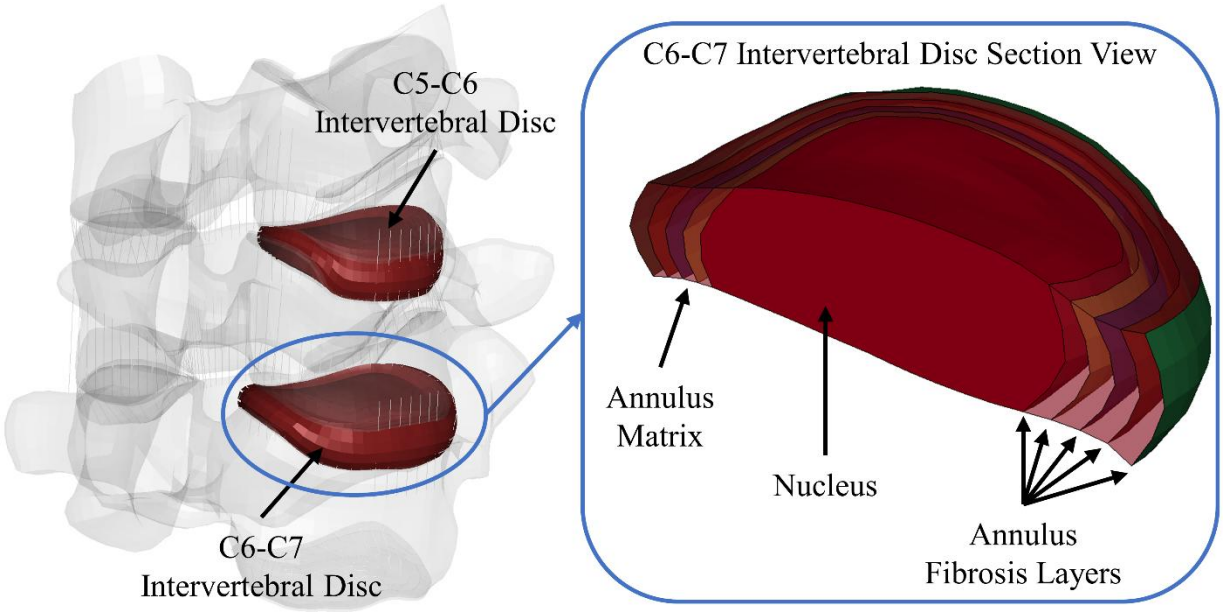


Figure 2.14: Locations of the intervertebral discs on the C5-C6-C7 segment model (left). The section view (right) cuts the C6-C7 intervertebral disc in the midsagittal plane to show the annulus fibrosis layers sitting in the annulus matrix. The translucent red part indicates the annulus matrix. The solid red part indicates the nucleus.

Quadrilateral shell elements were used to mesh the endplates (Figure 2.15). Each endplate, connecting the intervertebral disc and vertebral body, had a constant thickness.

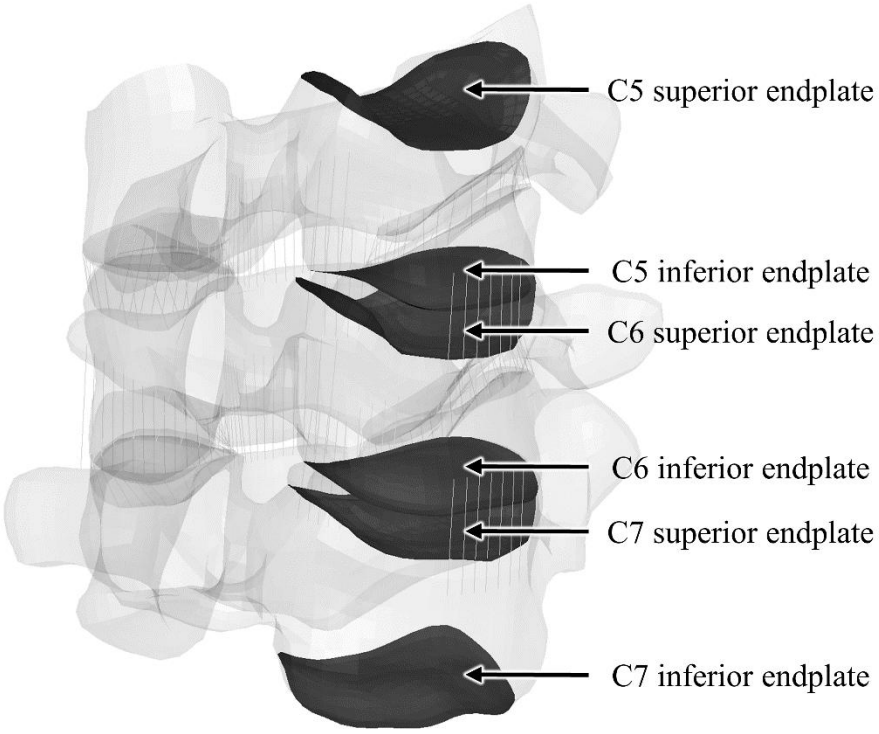


Figure 2.15: Locations of the endplates in the C5-C6-C7 segment model. The dark gray parts indicate the shell elements of the endplates.

Hard tissues of the vertebrae were modelled using quadrilateral shell elements for the cortical bone and hexahedral solid elements for the trabecular bone (Figure 2.16). The hard tissue failure in the GHBMC model was modelled using an element erosion criterion based on the plastic strain.

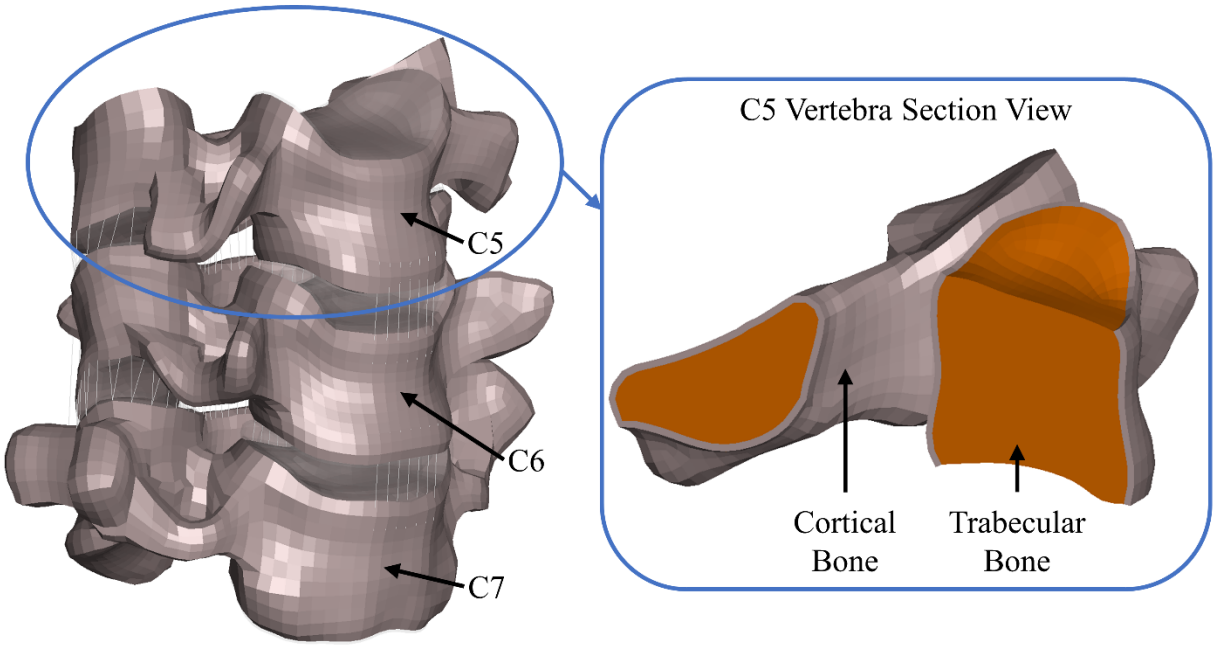


Figure 2.16: The locations of the vertebrae in the C5-C6-C7 segment model (left). The section view (right) cutting the C5 vertebra in the midsagittal plane shows the cortical and trabecular bone. The purple part indicates the shell elements of the cortical bone. The orange part indicates the solid elements of the trabecular bone.

Previous work by Khor (2018) developed anisotropic material models for the hard tissues of the vertebrae to improve the prediction of fracture initiation during compression of a cervical spine segment model (Khor, 2018). The boundary conditions and model setup were based on the central, posterior, and anterior compression experiments by Carter (2002) and the lateral compression experiments by Van Toen et al. (2014) (Khor, 2018). The cervical spine specimen used in the model was a C5-C6-C7 segment extracted from the GHBMC M50 neck model. Asymmetric and anisotropic material models were developed for the cortical and trabecular bone of the segment for young (less than 50 years old) and aged (older than 70 years old) age groups (Khor, 2018; Wishart et al., 1995). Upon comparison of the model response to experimental data, the anisotropic material models were recommended for both the cortical and trabecular bone to predict and model fracture initiation (Khor, 2018).

Failure of the hard tissues were modelled using strain-based element erosion based on thresholds of maximum and minimum principal strains (Khor, 2018). With a strain-based element erosion criterion, the shell or solid element would be deleted and removed from the simulation upon reaching the defined

threshold strain. The pattern of deleted, or eroded, elements was used as an indication of the fracture location and pattern. In the material models of Khor (2018), the erosion criterion for the cortical bone was defined with both a maximum and minimum principal strain. The erosion criterion for the trabecular bone was only defined with a maximum principal strain (Khor, 2018). The decision to not fail the elements of the trabecular bone based on a minimum principal strain was made to model the densification behaviour of trabecular bone under compression.

While the element erosion method allows for predicting the forces and locations of hard tissue fracture initiation, it also results in a loss of material as elements are removed from the simulation. The loss of material is particularly important under compression loading since fractured fragments of hard tissues still carry load with the continuation of compression in the segment after fracture initiation has begun. Thus, the loss of the fractured material during compression results in a loss of structural support and energy, particularly post fracture. In addition to the loss of structural support, the loss of material also limits the ability to simulate the motion of hard tissue during and after fracture in the segment. Experimental studies from axial compression loading on the spine segment specimens showed that bone fragments from fractured vertebrae were pushed into the spinal canal (Tran et al., 1995; Wilcox et al., 2002). Bone fragments that occlude the spinal canal have the potential to lead to transverse compression of the spinal cord and spinal cord injury. Retaining bone fragments in the simulation is therefore important in order to model occlusion to ultimately investigate spinal cord injury. Thus, to investigate spinal cord injury and model vertebral fractures, a model needs to be able to predict fracture initiation, post-fracture response, and the flow of fractured hard tissues (DeWit and Cronin, 2012).

2.6 Smoothed Particle Hydrodynamics (SPH) Method to Model Large Deformations

Smoothed particle hydrodynamics (SPH) is a meshless particle method with a Lagrangian formation. It was developed in 1997 for astrophysics problems, such as the fission of rotating stars, that result in large deformations (Gingold and Monaghan, 1977; Lucy, 1977).

The SPH method is an interpolation method that can be used to determine field parameters at discrete particle locations within a particle field (Basafa et al., 2012; Li et al., 2017). Field quantities are calculated at a central particle, and a smoothing kernel function is then used to calculate the field quantity at each adjacent particle within the area of influence around the central particle (Basafa et al., 2012; Fraser, 2014; Gingold and Monaghan, 1977; Lucy, 1977). The smoothing kernel function also determines the interaction of particles.

The meshless nature of SPH makes it suitable for simulating large deformations that may otherwise lead to a tangled or distorted mesh in traditional Lagrangian elements (Basafa et al., 2012; Li et al., 2017). SPH has therefore also been introduced in solid mechanics problems involving machining, wear, and impacts (de Vaucorbeil and Hutchinson, 2020).

2.6.1 SPH in Bone and Spine Applications

Numerical simulations in the spinal cord and of bone cement have used SPH to model fluid-like behaviour. In the spinal cord, the epidural fat (Arhiptsov and Marom, 2021) and cerebral spinal fluid (Arhiptsov and Marom, 2021; Russell et al., 2012; Rycman et al., 2022) have been modelled using SPH. The diffusion on bone cement trabecular bone for procedures such as femoroplasty has been modelled using SPH (Basafa et al., 2012). The study simulated an experiment where silicone, representing the bone cement, was injected into a foam block, representing the trabecular bone (Basafa et al., 2012). Navier-Stokes equations were built into the SPH formulation to model the fluid flow of the silicon into the foam block (Basafa et al., 2012).

Scenarios such as bone cutting and implant penetration have also used SPH to model hard tissues. Bone cutting and implant penetration tests into rectangular bone specimens have used SPH to model cortical and trabecular bone since these events result in large deformations during bone fracture. One study used SPH to simulate penetration tests of a bone cutting tool into cortical bone specimens from bovine femur (Li et al., 2017, 2014). The cortical bone specimen was modelled using both SPH particle elements and solid Lagrangian continuum elements (Li et al., 2017, 2014). The SPH particle elements were implemented in the middle section of a rectangular bone specimen in the model where the cutting tool would penetrate (Figure 2.17a) (Li et al., 2017, 2014). Penetration of a bone cutting tool into bone can occur during scenarios such as orthopaedic surgery (Li et al., 2017, 2014). SPH was also used to represent trabecular bone for simulating the penetration of indenter tips into trabecular bone specimens (Kulper et al., 2018). The entire specimen was modelled using SPH (Figure 2.17b).

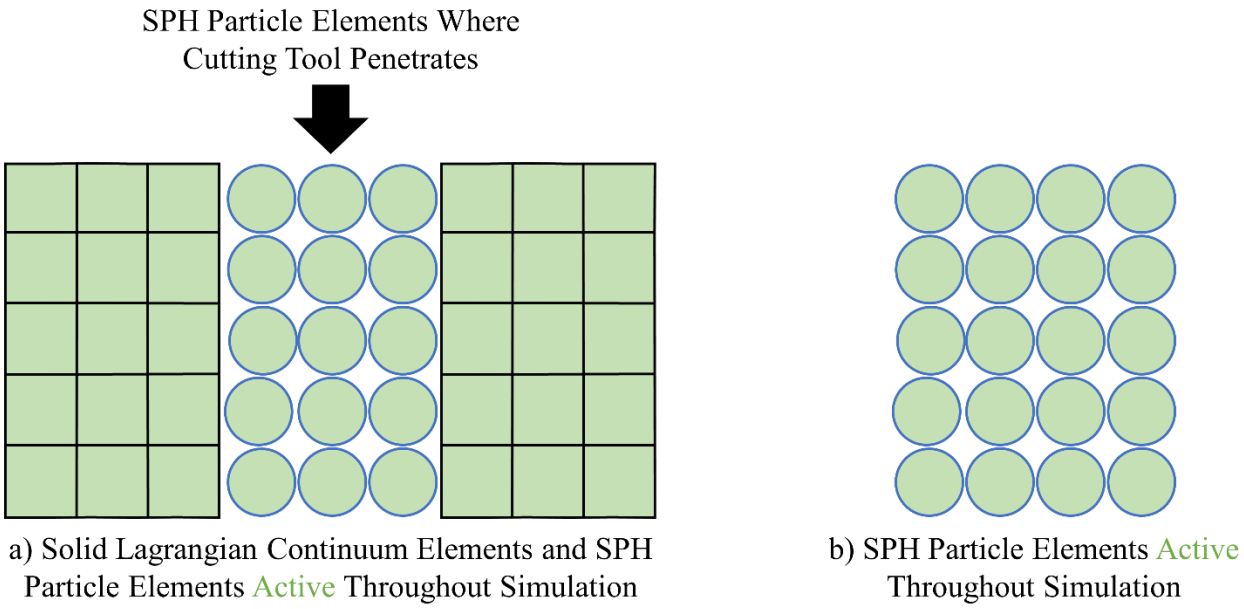


Figure 2.17: Simplified diagram showing the SPH particle elements for bone and spine simulations.

In these applications, all the SPH particle elements were active throughout the entire simulation.

2.6.2 Eroded Finite Elements Converted to SPH, Implementation in FE Code

The finite element method to SPH (FEM to SPH) implementation will be referred to as the SPH implementation in this work. In the FEM to SPH implementation, continuum elements are converted into SPH particle elements. The motivation for using a FEM to SPH approach was to extend the computation time by filtering out the elements with large deformations that would result in numerical issues while also mitigating the computation time from using a particle method (Johnson and Stryk, 2003; Kala and Husek, 2016). The main idea was to transform Lagrangian finite elements into SPH particle elements in order to take advantage of and minimize the shortcomings of each method (Chen et al., 2021).

At the beginning of the simulation, SPH particle elements are coupled to the finite elements; however, the SPH particle elements are inactive (Figure 2.18) (Chen et al., 2021; Kala and Husek, 2016). At each step in the calculation, the Lagrangian finite elements are checked to see if they meet the assigned failure criterion (He et al., 2020). Once the failure criterion is reached, the Lagrangian element erodes and is converted into the SPH particle element that becomes activated and inherits the Lagrangian finite element properties, such as mass, position, stress, and velocity (Chen et al., 2021; He et al., 2020). The newly activated SPH particle element is then added to the calculation and can interact with other SPH particle elements and other finite elements in the model (He et al., 2020). The SPH particle elements can, for example, represent the broken material in the simulation to withstand compressive stresses (He et al.,

2020). Newly activated SPH particle elements are not automatically coupled to the remaining Lagrangian elements, and so the interaction between SPH and Lagrangian elements are defined through contacts. Contact algorithms and other control parameters can be defined for the SPH particle elements (He et al., 2020).

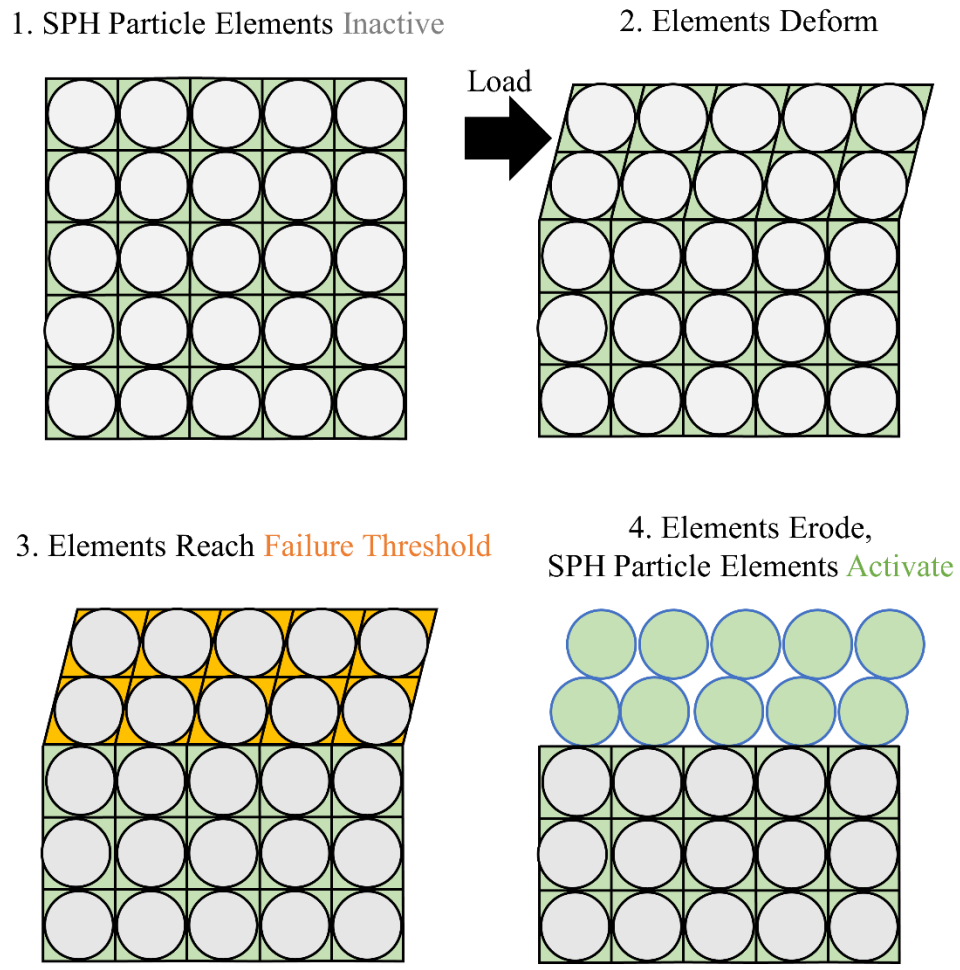


Figure 2.18: A diagram illustrating an example of the SPH implementation where solid Lagrangian continuum elements are transformed into SPH particle elements upon erosion of the solid element. The light green shaded squares represent solid elements. The yellow-orange shaded squares represent solid elements that reach their failure threshold. The grey shaded circles represent inactive SPH particle elements. The light green shaded circles represent active SPH particle elements.

2.6.3 Examples of Applications Implementing SPH to Convert Solid Elements to SPH Particle Elements

The implementation of SPH to convert solid Lagrangian continuum elements into SPH particle elements has been applied for scenarios outside simulations involving bone and the spinal cord.

The FEM to SPH method was used to model projectiles impacting concrete specimens (Kala and Husek, 2016). The SPH implementation was applied to the concrete specimens to allow the comminuted material of the concrete to interact with the rest of the model after fracture.

Tokura and Niwa (2017) also used a FEM to SPH approach to model debris for the failure of concrete (Tokura and Niwa, 2017). Failed solid elements of concrete were replaced with SPH particle elements to model the accumulation of debris when an impactor impacted concrete (Tokura and Niwa, 2017). The FEM to SPH approach was implemented for the concrete area around the location of the impactor (Tokura and Niwa, 2017). One of the parameters investigated was the number of SPH particles generated for each solid element (Tokura and Niwa, 2017). The FEM to SPH implementation was implemented in LS-DYNA and an eroding contact between the nodes and surface contact was defined between the SPH and the solid elements (Tokura and Niwa, 2017).

He et al. (2020) used the FEM to SPH approach to model the debris cloud in a high velocity impact problem where a space fragment impacted the wall of a spacecraft (He et al., 2020). The FEM to SPH implementation was implemented in the area of the space wall around the space fragment and was implemented through LS-DYNA (He et al., 2020).

Chen et al. (2021) used the FEM to SPH approach to model the accumulation of ice rubbles when a marine structure impacted ice (Chen et al., 2021). The solid elements of the ice would be converted into SPH particle elements, and the SPH particle elements of the ice would continue to interact with the ice and marine structure in the model (Chen et al., 2021). A validation was then performed to check the mesh sensitivity (Chen et al., 2021).

Chapter 3
Methods

The overall aim of this research was to improve the modelling of the post-fracture response of a cervical spine segment loaded under compression by enhancing the modelling of hard tissue fracture by implementing SPH into the trabecular bone to preserve fractured material.

This section describes the finite element model development, boundary conditions, model evaluation, and parametric study (Figure 3.1). Section 3.1 describes the progression of improvements, leading to the implementation of SPH into the cervical spine segment model. Section 3.2 describes the method of evaluating the SPH implementation. The results of the model with and without the SPH implementation were compared to the results from the experimental tests. Section 3.3 describes an investigation into the effect on the model response when the number of SPH particles generated for each eroded solid element was increased. Section 3.4 describes a parametric study using the cervical spine segment model with the SPH implementation to investigate the effect of varying impact severities, using aged material parameters for the hard tissues, and applying eccentric boundary conditions. The models were solved using a commercial finite element solver (LS-DYNA R13.1.1, LST, Livermore, CA).

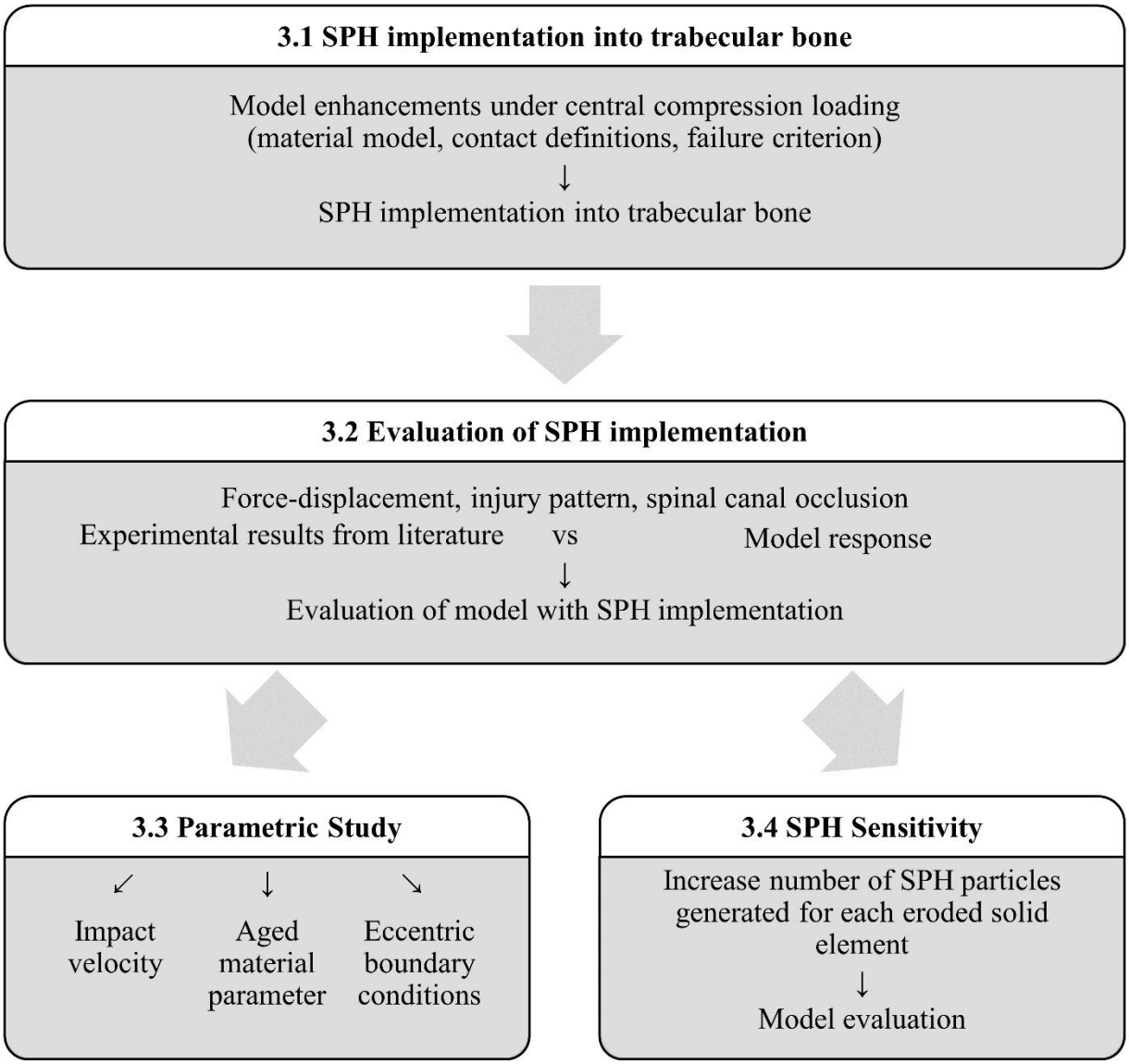


Figure 3.1: Schematic of model development, assessment and evaluation. The section numbers and objectives are in bold.

3.1 Model Enhancements to the FE Motion Segment Model: GHBMC Segment to SPH Implementation

The FE vertebral segment model for the central compression loading comprised two adjacent functional spinal units (FSUs) at the C5 to C7 vertebral levels. The C5-C6-C7 segment was extracted from the cervical spine of the GHBMC M50 neck model (C6-0, GHBMC, Elemance, Winston-Salem, NC) (Barker and Cronin, 2022, 2020). The extracted segment included the C5, C6, and C7 vertebrae with ligaments, intervertebral discs, endplates, and facet joints.

The boundary conditions of the model were based on the central compression experimental setup from Carter (Carter et al., 2002) described in section 2.4.4. To recreate the central compression experimental setup, the central compression FE model (CC model) included the C5-C6-C7 cervical segment and the loading apparatus (Figure 3.2) (Khor, 2018; Khor et al., 2018, 2017). The loading apparatus included the top potting, the bottom potting, and the load cell. The top and bottom potting in the model were meshed around the C5 vertebra and C7 vertebra, respectively. The load cell was located below the bottom potting.

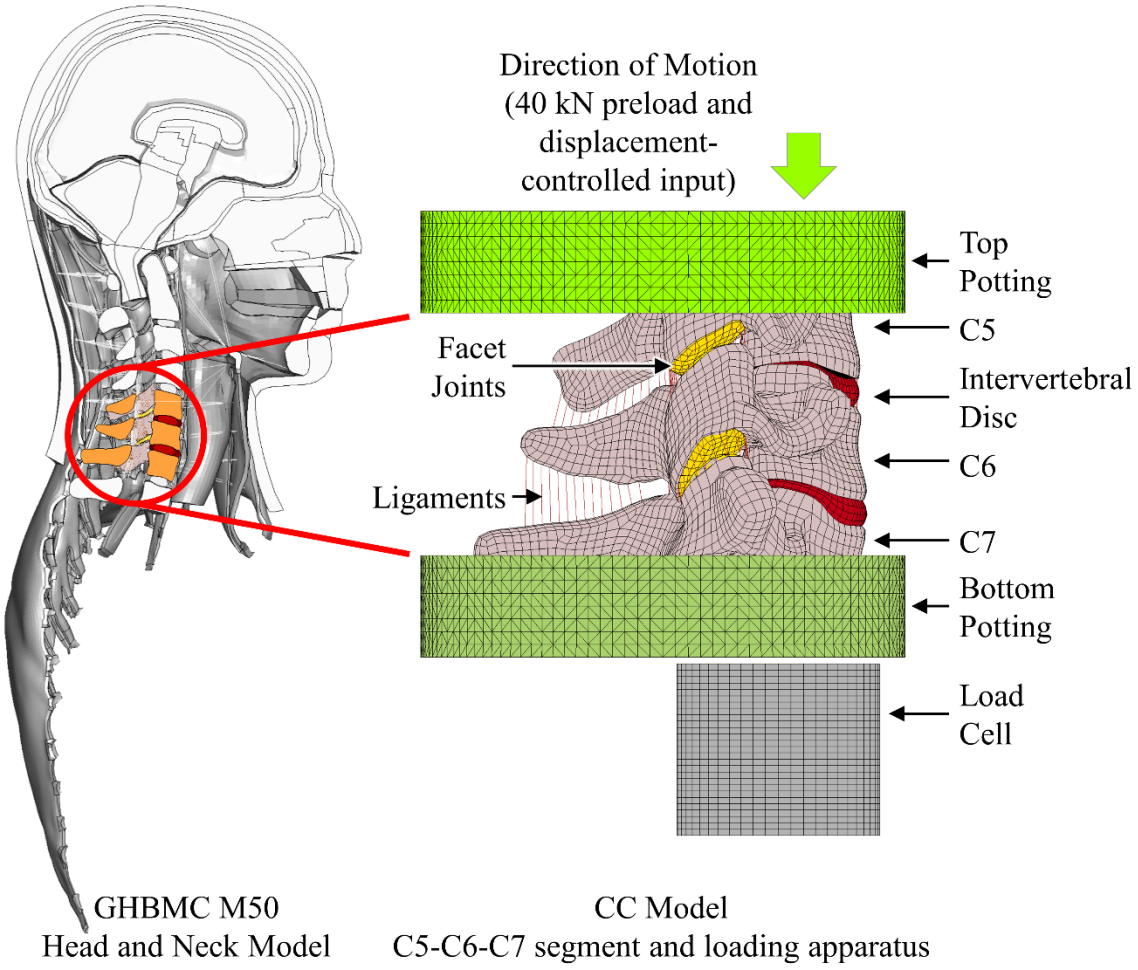


Figure 3.2: Sagittal view of the GHBMC M50 head and neck model (left). The orange, light purple, and red parts circled in red indicate the functional spinal units extracted for the CC model (right). The labels on the CC model used for the central compression loading show parts of the loading apparatus and cervical spine segment parts. The green arrow shows the direction of the preload and displacement-controlled input applied to the top potting.

The top potting was allowed to displace downward in the *z*-direction to apply a central compression load to the cervical spine segment model (Khor, 2018). The compression boundary condition applied to the top potting was an initial 40 N preload followed by a displacement-controlled input for a total simulation time of 550 ms. The 40 N preload was applied from 0 ms to 250 ms. From 250 ms to 550 ms, a displacement-controlled input consisting of a loading phase, a holding phase, and an unloading phase was applied to the top potting (Figure 3.3). The direction vector of the preload and displacement input was applied based on the geometric centroid of the superior C5 endplate. The location of the direction vector ensured a central, rather than eccentric, loading to the cervical spine segment.

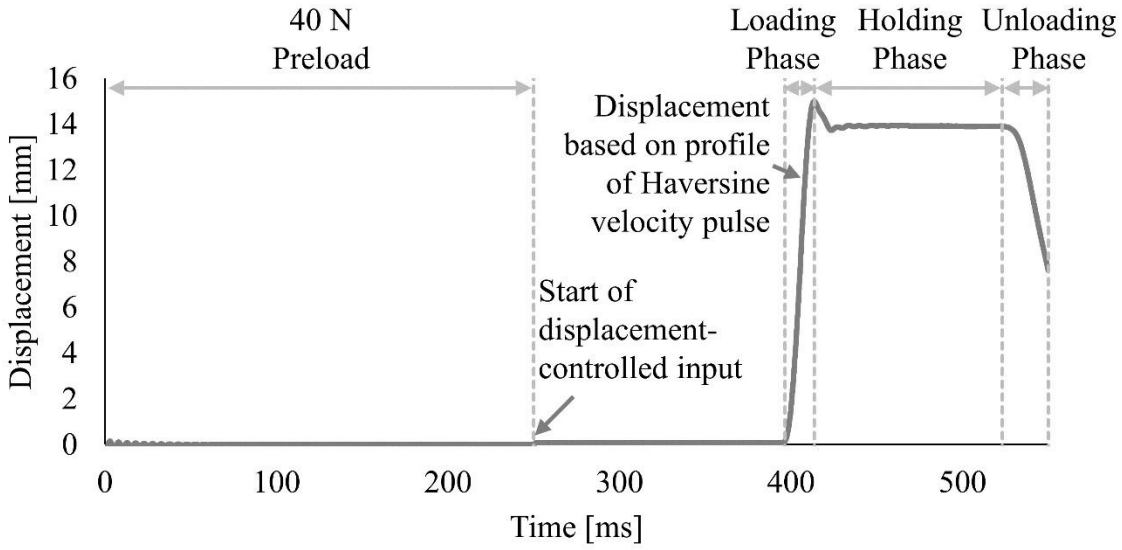


Figure 3.3: The displacement vs time graph showing the displacement in the downward direction (compression) of the top potting. A 40 N preload was applied from 0 ms to 250 ms in the simulation. At 250 ms, a displacement-controlled input was applied. The displacement input applied during the Loading Phase was based on the profile of a Haversine velocity pulse. The displacement was held constant during the Holding Phase. The displacement in the unloading phase corresponded to the upward motion of the top potting.

This section describes the development of the cervical spine segment in the CC model to lead to the implementation of SPH in the trabecular bone (Figure 3.4). The CC_{Plk} model in section 3.1.1 used the segment extracted from the GHBMC M50 model. The CC_{Ani} model in section 3.1.2 incorporated anisotropic material models for the hard tissues. The CC_{Con} model in section 3.1.3 built on the CC_{Ani} model by including modified and new contact definitions. The CC_{MPS} model in section 3.1.4 added a minimum principal strain to the erosion criterion of the trabecular bone. The CC_{SPH} model in section 3.1.5 added the implementation of SPH to the trabecular bone to the CC_{MPS} model.

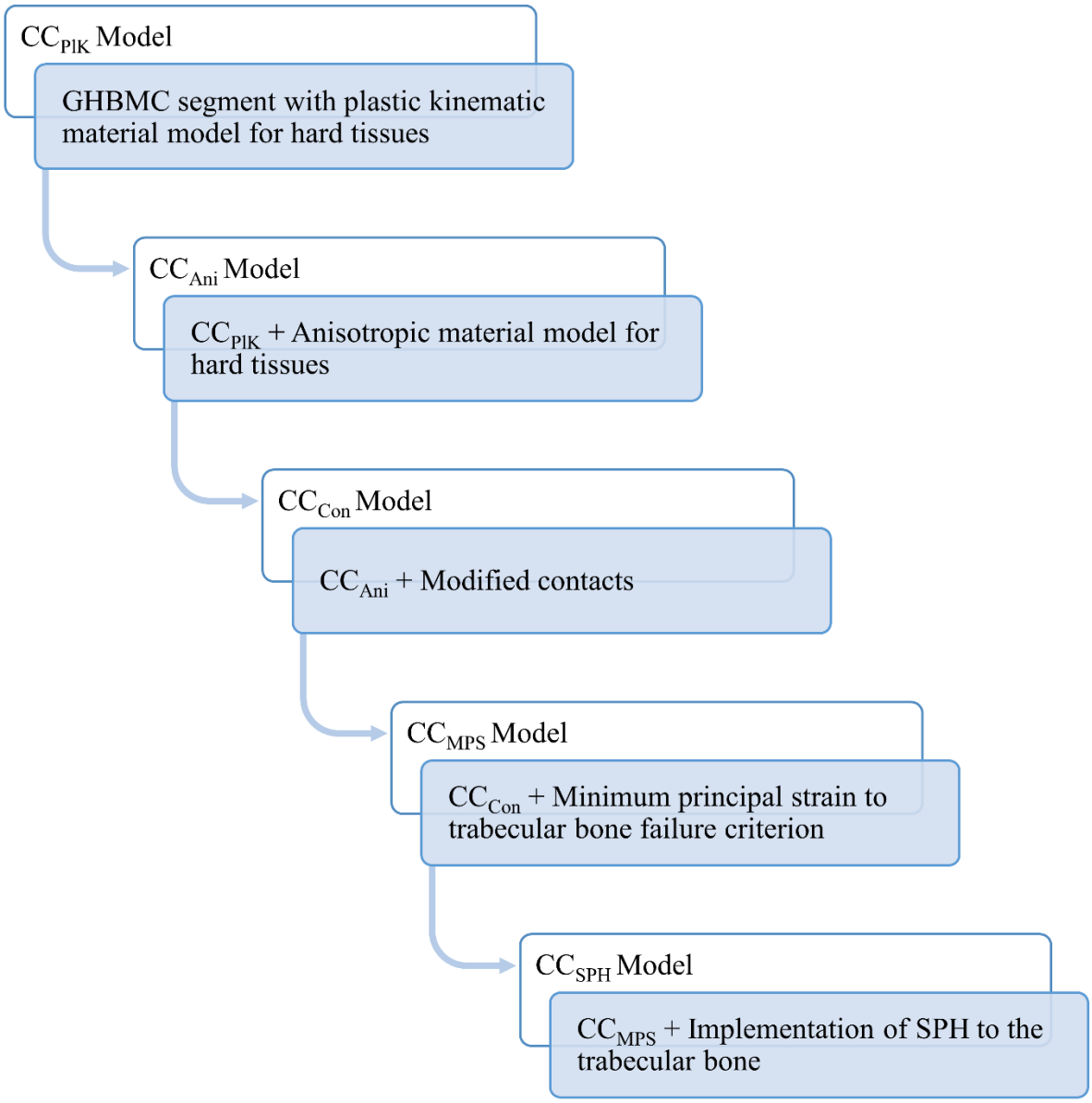


Figure 3.4: Progression of models to include changes to the cervical spine segments leading to the implementation of SPH. At each step, a change is added to the model from the preceding step. Each step of the schematic shows the name assigned to the model at each step of the progression as well as the new change implemented in the step.

3.1.1 Plastic Kinematic Material Model for Hard Tissues: CC_{PIK} Model

The cervical spine segment in the CC_{PIK} model used the segment from the GHBMC M50 v6-0 model with the default material models, parameters, and contacts. The hard tissues, therefore, had plastic kinematic material models with the parameters summarized in Table 3.1. The erosion failure criterion for the trabecular and cortical bone elements were based on an effective plastic strain (fs).

Table 3.1: Constitutive material model and key material parameters for the hard tissues of the cervical spine in the GHBMC M50 v6-0 model.

Tissue	Constitutive Material Model Description	LS-DYNA Material Model Name	Material Model Parameters	References
Trabecular Bone	Plastic Kinematic	*MAT_PLASTIC_KINEMATIC	ρ = 1000 kg/m^3 E = 442 MPa pr = 0.3 σ_y = 2.83 MPa E_{Tan} = 30.1 MPa β = 1 fs = 0.095	(Keaveny et al., 2001; Lindahl, 1976)
Cortical Bone	Plastic Kinematic	*MAT_PLASTIC_KINEMATIC	ρ = 2000 kg/m^3 E = 18.439 GPa pr = 0.28 σ_y = 189.8 MPa E_{Tan} = 1.249 GPa β = 1 fs = 0.0178	(McElhaney, 1966; Reilly et al., 1974)

3.1.2 Anisotropic Material Model for Hard Tissues: CC_{Ani} Model

In the CC_{Ani} model, the hard tissues of the previous CC_{PlK} model were assigned anisotropic material models (Khor, 2018). The trabecular bone parts for the C5, C6, and C7 vertebrae were assigned a transversely anisotropic low-density crushable foam material model. The cortical bone part of only the middle C6 vertebra was assigned an orthotropic elastic-plastic material model to account for the difference in support around the superior-most and inferior-most vertebrae of the segment present in the experiments and model. The potting in the experiments covered most of the vertebral bodies of the superior-most and inferior-most vertebrae. In contrast, the potting in the model covered approximately 40% of the C5 vertebral body height and 62% of the C7 vertebral body height. The C5 and C7 cortical bone parts in the models were, therefore, assigned the plastic kinematic material model from the CC_{PlK} model. The plastic kinematic material model was stiffer than the orthotropic elastic-plastic material model to mimic the stiffer support provided by the potting in the experiments around the superior-most and inferior-most vertebrae.

The material parameters for the anisotropic material models were representative of a young age group of younger than 50 years old (Table 3.2). The younger than 50 years old age range matched the average stature GHBMC M50 model representative of a 26-year-old (i.e. young) male (175.9 cm in height, 78.6 kg in weight, and 25.7 in BMI) (Gayzik et al., 2011).

Table 3.2: Constitutive material models and key material parameters for the anisotropic hard tissue material models developed by Khor (Khor, 2018).

Tissue	Constitutive Material Model Description	LS-DYNA Material Model Name	Material Model Parameters	References
Trabecular Bone	Transversely Anisotropic Low-Density Crushable Foam	*MAT_ TRANSVERSELY _ANISOTROPIC_ CRUSHABLE_ FOAM	E_1 = 689 MPa E_2 = 293 MPa ρ = 1000 kg/m^3 G = 265 MPa K = 574 MPa	(Khor, 2018; Liu et al., 2013)
Cortical Bone	Orthotropic Elastic-Plastic	*MAT_ORTHO_ ELASTIC_ PLASTIC	E_1 = 17.91 GPa E_2 = 10.44 GPa ρ = 2000 kg/m^3 σ_y = 200.86 MPa ν_{12} = 0.35 ν_{23} = 0.42 ν_{31} = 0.222	(Ashman et al., 1984; Hansen et al., 2008; Khor, 2018; Reilly and Burstein, 1975)

The anisotropic material models included a strain-based erosion criterion to model the failure of the hard tissues. The erosion criterion was defined with maximum and minimum principal strains, in terms of true strain. With a strain-based erosion criterion, once a shell or solid element of the cortical or trabecular bone eroded, the element would be deleted and removed from the simulation. The failure strains for the erosion criterion are summarized in Table 3.3. At this stage, a minimum principal strain was not defined for the trabecular bone since trabecular bone is a foam-like material which densifies under compression (Khor, 2018). The absence of a minimum principal strain criterion for erosion allowed the solid trabecular bone elements to remain in the simulation during the densification stage.

Table 3.3: Principal strains, in terms of true strain, of the strain-based erosion criterion applied to the hard tissue material models developed by Khor (Khor, 2018).

Tissue	Minimum Principal Strain	Maximum Principal Strain	References
Trabecular Bone	N/A	0.0917	(Khor, 2018; Liu et al., 2013)
Cortical Bone	-0.0206	0.0343	(Khor, 2018; Reilly and Burstein, 1975)

3.1.3 Added Contact Definitions to Account for Erosion and to Allow for Ligament to Intervertebral Disc Contact: CC_{Con} Model

In the CC_{Con} model, contact definitions between parts were revised to account for the erosion of hard tissue elements in the CC_{Ani} model. A contact definition was also added to mitigate interpenetration between the intervertebral disc and the ALL and PLL.

In LS-DYNA, contacts are defined between two surfaces. One surface is designated as the master side and the other as the slave side. At each time step of the simulation, LS-DYNA checks for and prevents penetration of the nodes from one side into the surface of the other side.

The following three contacts were default contacts from the GHBMC M50 model that were included in the CC_{PlK} model.

1. Automatic surface-to-surface contacts between the C5 and C6 trabecular bone and between the C6 and C7 trabecular bone: To prevent interpenetration between adjacent vertebrae.
2. Automatic surface-to-surface contacts between the C5 inferior and C6 superior facet joints and between the C6 inferior and C7 superior facet joints: To prevent interpenetration between adjacent facet joint cartilage parts.
3. Automatic one-way surface-to-surface tiebreak contacts between the intervertebral disc and the superior and inferior endplates: The disc avulsion criterion to prevent interpenetration of the intervertebral discs through the endplates, and to allow disc avulsion to occur during tension.

In the contact definitions of the CC_{PlK} model, the master and slave surfaces were defined as the outermost surface of a part or set of parts at the beginning of the simulation. The surface defined at the beginning of the simulation would be checked for penetration throughout the simulation. However, with the erosion criterion introduced as part of the CC_{Ani} model, elements on the outermost surface would erode, resulting in a change in the outermost elements of a part. Since the contact types from the CC_{PlK} model did not account for the changing of elements in the outermost surfaces, interpenetration between parts would occur. To resolve the interpenetration due to erosion, the CC_{Con} model added new eroding surface-to-surface contact definitions. The eroding surface-to-surface contact implementation in LS-DYNA allows the designated outermost surfaces to update at each time step to account for element erosion.

The last contact added to the CC_{Con} model was between the beam elements of the ALL and PLL and the outmost fibrosis layer of the intervertebral disc. The contact definition between the ligaments and intervertebral disc was added to mitigate penetration of the intervertebral disc through the ligaments as the compression of the segment led to outward deformation of the intervertebral disc.

The list of contacts added as part of the CC_{Con} model are summarized in Table 3.4.

Table 3.4: Summary of new contacts added to the cervical spine segment model as part of the enhancements in the CC_{Con} model. The first column contains the names assigned to the new contact definition. The second column contacts the contact type used in LS-DYNA. The third column contains the part or part set whose surface is defined as the slave side of the contact. The fourth column contains the part or part set whose surface is defined as the master side of the contact.

Contact Name	Contact Type	Parts for Surfaces of Slave Side in Contact	Parts for Surfaces of Master Side in Contact
Disc to Trabecular Contact	Eroding surface-to-surface	Set of Parts: Annulus matrix, the annulus fibrosis, and the nucleus of each disc	Part: Trabecular bone of each vertebra
Facet Joint to Trabecular Contact	Eroding surface-to-surface	Part: Facet joint at each intervertebral joint	Part: Trabecular bone of each vertebra
Vertebra to Vertebra Contact	Eroding surface-to-surface	Set of Parts: Endplate, cortical bone, trabecular bone	Set of Parts: Endplate, cortical bone, trabecular bone
Trabecular Self Contact	Eroding surface-to-surface	Part: Trabecular bone of each vertebra	
Ligament to Disc Contact	Automatic beams-to-surface	Set of Parts: Anterior longitudinal ligament, posterior longitudinal ligament	Set of Parts: Annulus fibrosis 1A (outermost fibrosis layer)

An example of the parts in each of the new contact definitions is shown in Figure 3.5.

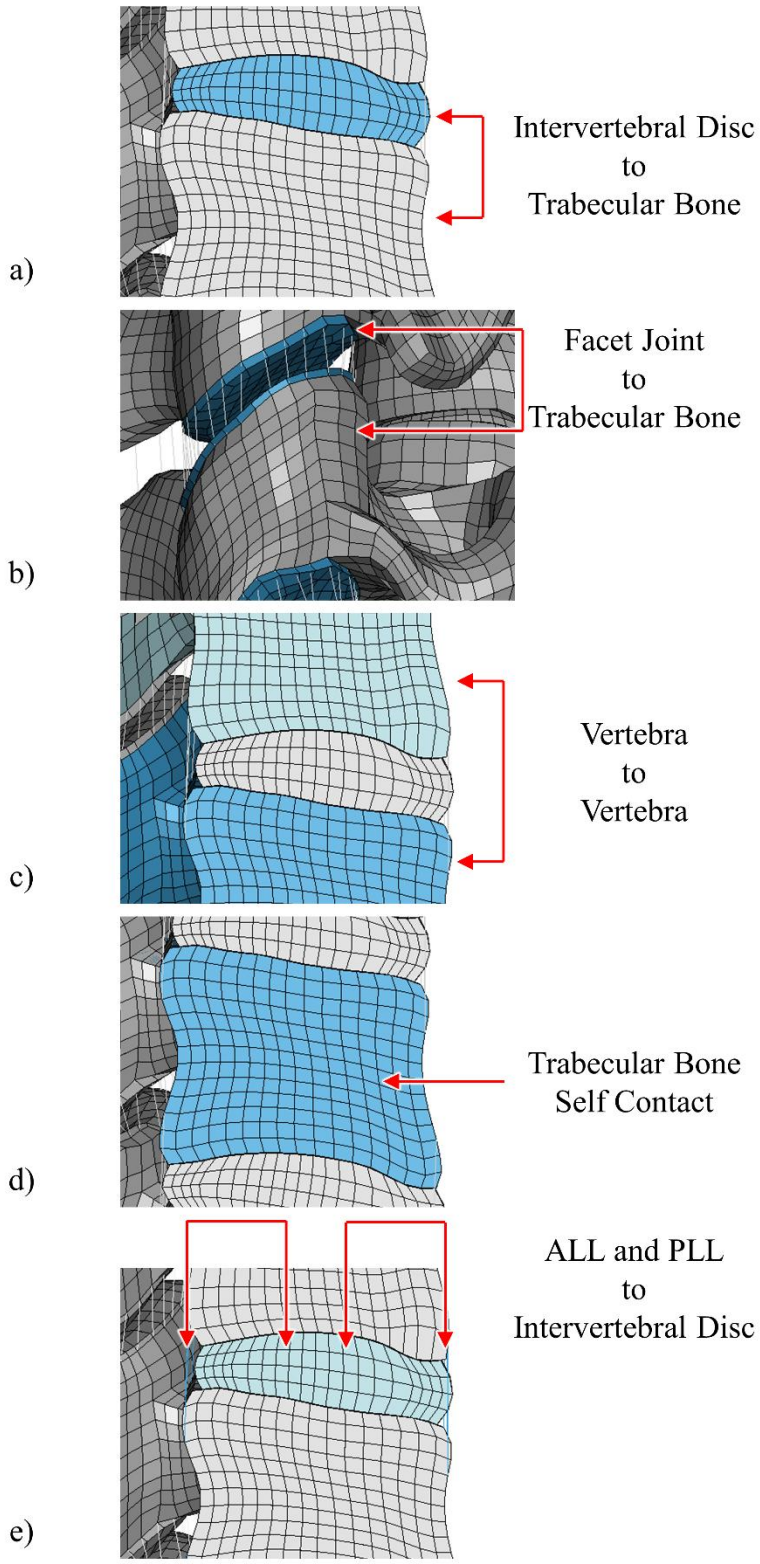


Figure 3.5: Sagittal plane views showing an example of each contact added in the CC_{Con} model.

The following is a description of each contact added to the CC_{Con} model.

Disc to Trabecular Contact (Figure 3.5a): The Disc to Trabecular Contact was added to prevent penetration between the intervertebral disc and the trabecular bone of the adjacent vertebra. The default tiebreak contact of the CC_{PlK} model between the intervertebral disc and adjacent endplate in the CC_{PlK} model prevented penetration before erosion. To prevent the intervertebral discs from penetrating through the vertebral bodies with erosion of the solid trabecular bone, the eroding contact was defined between each intervertebral disc and the trabecular bone part of the adjacent vertebrae. The tiebreak contact of the CC_{PlK} model was not removed in order to prevent interpenetration before the onset of erosion in the vertebral body and to maintain the disc avulsion criterion.

Facet Joint to Trabecular Contact (Figure 3.5b): The Facet Joint to Trabecular Contact was added between each facet joint and the trabecular bone in the adjacent vertebra. As the cervical segment was compressed, the facet joint cartilage could slide and be pushed into the adjacent vertebra. The added eroding contact would, therefore, prevent the facet joint from penetrating through the trabecular bone of the adjacent vertebra.

Vertebra to Vertebra Contact (Figure 3.5c): The Vertebra to Vertebra Contact replaced the automatic surface-to-surface contacts between the trabecular bone in the CC_{PlK} model. The Vertebra to Vertebra Contact prevented interpenetration between the endplates and trabecular bone of the same vertebra and between the trabecular bone of adjacent vertebrae. The endplates of the CC_{PlK} model were kept in place through shared nodes between the endplates and the trabecular bone. Thus, the endplates would be pushed through the solid trabecular bone elements with erosion of the trabecular bone. The interpenetration between the endplates and trabecular bone was resolved with the added eroding contact between vertebrae. Each vertebra in this contact definition was defined as a set of parts, where each set included the endplates, cortical bone, and trabecular bone of one vertebra. The contacts would then be defined to prevent penetration between the C5 and C6 and the C6 and C7 adjacent vertebrae. Grouping the endplates and trabecular bone parts in the contact definition prevented the endplate from pushing through the solid trabecular elements. Furthermore, the eroding contact between adjacent vertebrae replaced and improved the surface-to-surface contact of the CC_{PlK} model by preventing interpenetration between the hard tissue of adjacent vertebrae both before and after erosion.

Trabecular Self Contact (Figure 3.5d): The Trabecular Self Contact was an eroding contact added to prevent interpenetration of the solid trabecular elements within the same vertebra. Under central compression loading, vertebral fracture, occurring with erosion of the solid trabecular elements, propagated across the middle of the vertebral body. As compression of the cervical segment continued after fracture propagation, the top of the vertebral body would be pushed into the bottom of the vertebral

body. The addition of the eroding contact would, therefore, prevent the interpenetration of a vertebra into itself as new surfaces formed during hard tissue fracture.

Ligament to Disc Contact (Figure 3.5e): The Ligament to Disc Contact was the only added contact unrelated to the erosion of hard tissue elements. The Ligament to Disc Contact was an automatic beam-to-surface contact between the ALL and PLL and the outermost fibrosis layer. The ALL and PLL were defined as a set of parts. Since the ALL and PLL surround the anterior and posterior edges of the interverbal disc, the beam-to-surface contact was added with the intention of mitigating the additional penetration of the intervertebral discs through the ligaments with compression of the cervical segment.

3.1.4 Addition of Minimum Principal Strain to Erosion Criterion of Trabecular Bone: CC_{MPS} Model

In the CC_{MPS} model, a minimum principal strain (i.e. compression strain) was added to the existing erosion criterion of the trabecular bone in the CC_{Con} model. The trabecular bone erosion criterion first introduced in the CC_{Ani} model only included a maximum principal strain (Table 3.3). As stated in section 3.1.2, the absence of a minimum principal strain in the erosion criterion allowed for the densification of the foam-like trabecular bone elements under compression in the model. Since this work will implement SPH to model the densified trabecular bone element (section 3.1.5), a minimum principal strain was added to the erosion criterion of the trabecular bone material.

The value for the minimum principal strain was determined based on a single element simulation of the transversely anisotropic low-density crushable foam material model (Table 3.3). The minimum principal strain was selected to be -0.9 (true strain in compression) to correspond to where the densification region of the stress-strain response became linear (Figure 3.6).

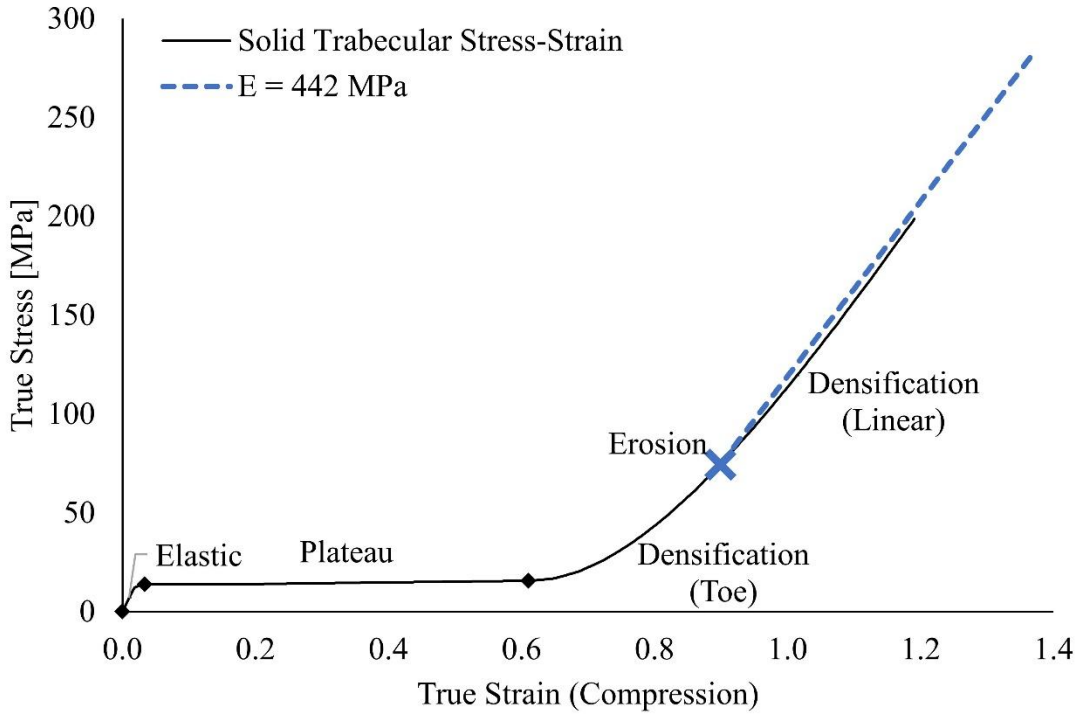


Figure 3.6: Stress-strain response of a single element simulation using the trabecular bone material model developed by Khor (Khor, 2018; Liu et al., 2013; Mosekilde et al., 1985; Sanyal et al., 2012). The *x*-axis shows the true strain in compression. The *y*-axis shows the true stress in compression.

3.1.5 Implementation of SPH to Trabecular Bone: CC_{SPH} Model

In the CC_{SPH} model, an implementation converting solid Lagrangian elements into SPH particle elements was added to the trabecular bone of the cervical spine segment in the CC_{MPS} model. The CC_{SPH} model included the anisotropic material models, the contacts, and the updated erosion criterion described in sections 3.1.2, 3.1.3, and 3.1.4.

The strain-based element erosion introduced in the CC_{Ani} model resulted in a loss of hard tissue material, particularly of the trabecular bone. As mentioned in section 2.5.5, the loss of hard tissue material in the cervical spine segment under compression resulted in a loss of both structural support and comminuted hard tissue material flow (Mattucci et al., 2019). The goal of the SPH implementation would be to mitigate the loss of trabecular bone material.

The SPH implementation was applied to the trabecular bone of the C5, C6, and C7 vertebrae. The implementation was achieved using the *DEFINE_ADAPTIVE_SOLID_TO_SPH card in LS-DYNA to adaptively transform the solid Lagrangian element of the trabecular bone into SPH particle elements upon erosion of the solid Lagrangian element (Figure 3.7). In the CC_{SPH} model, one SPH particle element was generated for each eroded solid Lagrangian element.

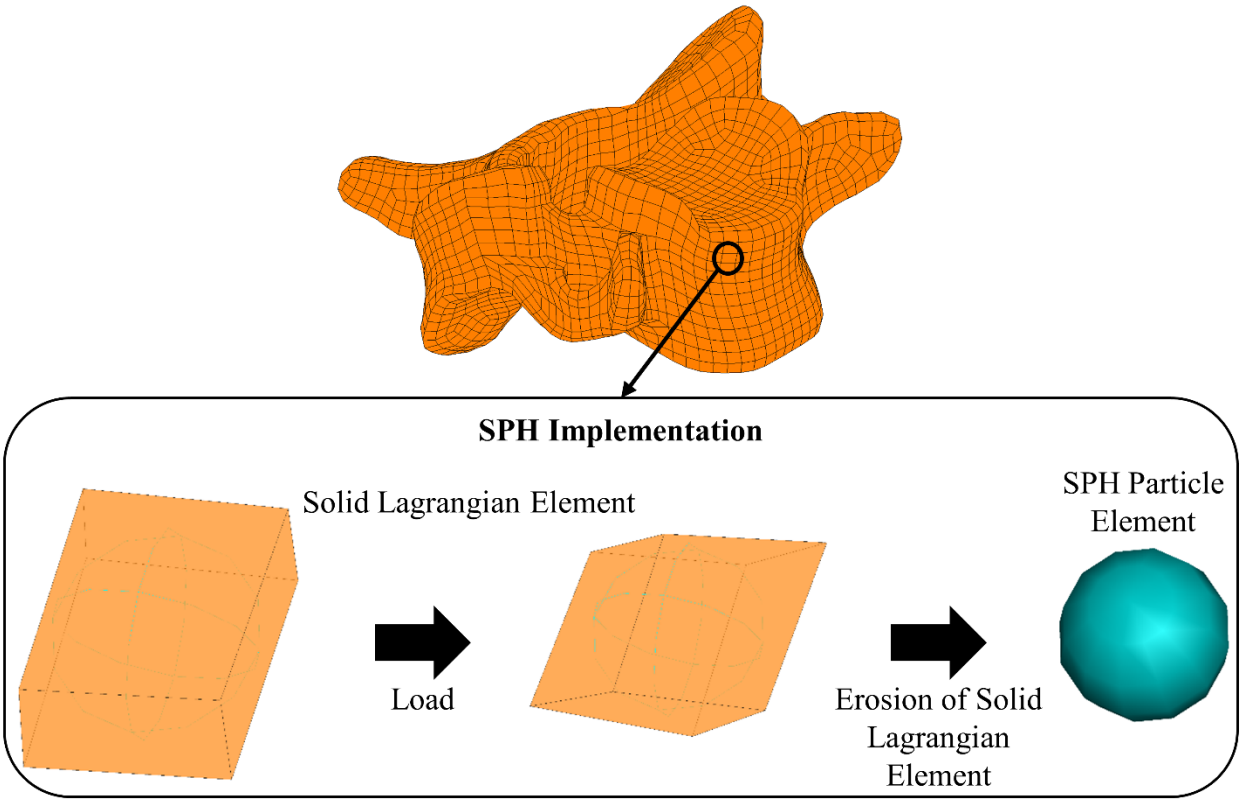


Figure 3.7: SPH implementation into the solid elements of the trabecular bone. The vertebra (top) shows the elements of the C6 vertebra. The schematic (bottom) shows the conversion of solid elements into SPH particle elements. The solid element is loaded. The solid element is transformed into an SPH particle element upon erosion of the solid element.

An elastic material model was assigned to the SPH particle elements to model the densified trabecular bone fragments in this initial investigation of implementing SPH into the trabecular bone. A linear elastic material model was determined to be suitable to represent the bone fragments in the CC_{SPH} model since the SPH particle elements would activate when the densification region became linear. Additionally, the transversely anisotropic density crushable foam material model assigned to the solid elements of the trabecular bone was not available for SPH elements in LS-DYNA.

A density, Young's modulus, and Poisson's ratio were the material properties defined for the elastic material model of the trabecular bone SPH elements (Table 3.5). The density of 1000 kg/m^3, also used for the anisotropic trabecular bone material model (Table 3.2), was based on the fresh bone density of trabecular bone measured experimentally before loading (Liu et al., 2013). The Young's modulus of 442 MPa was representative of the modulus from the linear section of the densification region of the single-element stress-strain response for the anisotropic trabecular bone material model (Figure 3.6). The Young's modulus of 442 MPa is also representative of the average modulus of the axial and transverse moduli of the transversely anisotropic density crushable foam material model of the trabecular bone (Table 3.2). Finally, a Poisson's ratio of 0.33 was selected out of consideration that the SPH particle elements would represent the densified crushed bone fragments of the trabecular bone. The anisotropic material model for the trabecular bone in the CC_{Ani} model before densification had a negligible Poisson's effect; however, the Poisson's ratio of foam had been reported to increase with the consolidation of collapsed pores (Koohbor et al., 2022). Thus, the average of the Poisson's ratios from the orthotopic elastic-plastic material model of the cortical bone in the CC_{Ani} model was used as the Poisson's ratio of the SPH particle elements (Table 3.2).

Table 3.5: Constitutive material model and material parameters assigned to the SPH elements of the trabecular bone in the SPH Model.

Tissue	Constitutive Material Model Description	LS-DYNA Material Model Name	Material Model Parameters	References
Trabecular Bone – SPH Elements	Elastic	*MAT_ELASTIC	ρ = 1000 kg/m^3 E = 442 MPa ν = 0.33	(Ashman et al., 1984; Khor, 2018; Liu et al., 2013)

Contact definitions were also added to prevent the generated SPH particle elements from penetrating the other cervical spine segment parts and the loading apparatus. As recommended by the LS-DYNA manual for eroding nodes-to-surface contacts, the SPH particle elements in the contacts were defined as a set of nodes on the slave side of the contact definition.

3.2 Evaluation of the SPH Implementation in the CC_{SPH} Model Against Experimental Targets

To evaluate the implementation of SPH, the models with and without the SPH implementation were assessed against the experimental results. The model with the SPH implementation was the CC_{SPH} model described in section 3.1.5, which included the SPH implementation, updated erosion criterion, added contacts, and anisotropic material models described between sections 3.1.2 and 3.1.5. The model without the SPH implementation was the CC_{MPS} model described in section 3.1.4, which included the updated erosion criterion, added contacts, and anisotropic material models described between sections 3.1.2 and 3.1.4. The force-displacement response, hard tissue damage pattern, and occlusion results of the CC_{SPH} model and the CC_{MPS} model were compared against the results reported in the central compression experimental test performed by Carter (Carter, 2002).

3.2.1 Force-Displacement Response

In the experimental tests, displacement and force values were measured and reported. The displacement applied to the specimen was measured according to the displacement of the hydraulic ram. The force in the specimen was measured from a load cell located at the bottom of the experimental setup.

The displacement and force values from the CC_{SPH} model and the CC_{MPS} model were measured from the part of the loading apparatus in the model corresponding to where the experimental values were measured. The displacement applied to the cervical spine segment in the model was taken by measuring the displacement in the downward direction (*z*-direction) of the rigid part of the top potting. The values for the force in the segment were measured using a section plane in the post-processing software (LS-PrePost, LST, Livermore, CA). The section plane was positioned through the center of the load cell part in the coronal plane (*x*-*y* plane) (Figure 3.8). The force in the direction of the longitudinal axis (*z*-direction) was measured at this section plane. The force values were filtered using a SAE CFC 600 filter with a cutoff frequency of 1000 Hz. This filter was selected to match the filtering applied to the data from the experimental test.

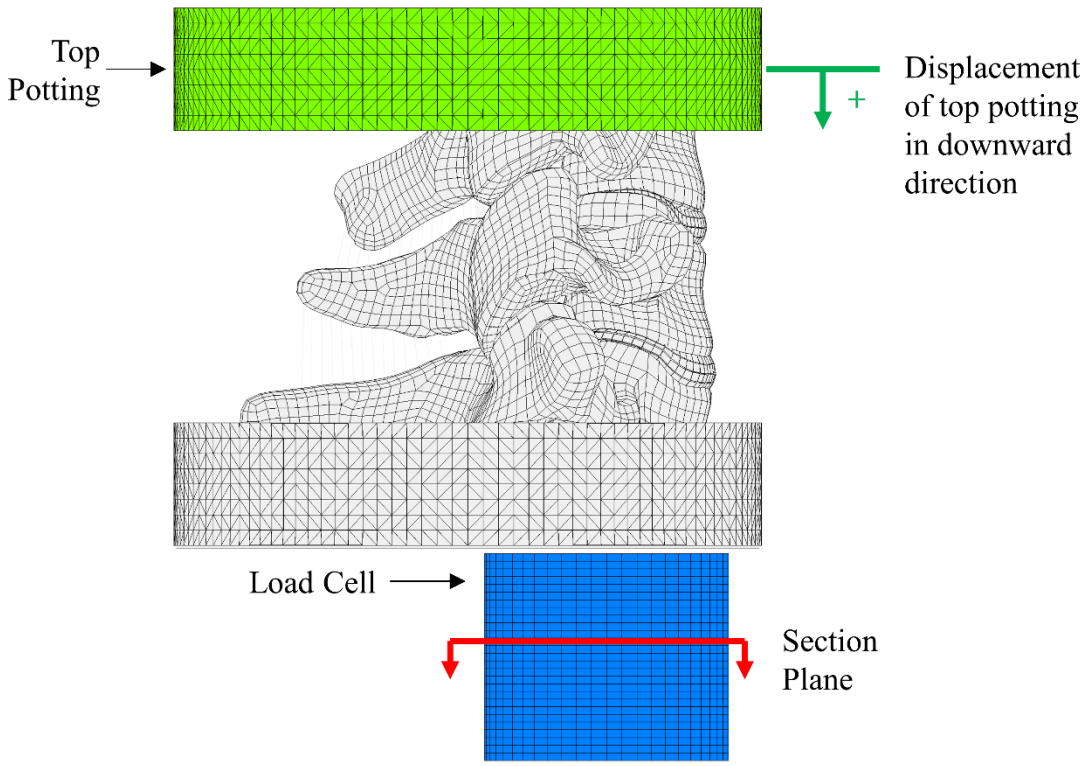


Figure 3.8: Sagittal view of the CC model with labels to indicate where the displacement and force values are measured. The displacement is measured as the displacement of the top potting. The green arrow indicates the direction of positive displacement. The force is measured at the load cell. The red arrow indicates to location of the section plane used to measure the force in the model.

The force and displacement values were used to compare the force-displacement responses of the CC_{SPH} model and the CC_{MPS} model to the force-displacement responses from the experimental tests. The experimental central compression force-displacement curves selected for comparison were from specimens #10 (C5-C6-C7 segment from 30 year old male) and #40 (C5-C6-C7 segment from 41 year old male) (Carter, 2002). Experimental specimens #10 and #40 were selected for comparison since both specimens matched the sex, age, and segment level of the CC_{SPH} model and the CC_{MPS} model. Both experimental specimens were C5-C6-C7 male specimens in the young age group of less than 50 years old. Additionally, the peak displacements applied to these specimens were similar to the maximum displacement of the displacement input curve applied to the model.

To obtain a single value to assess the overall force increase of the force-displacement responses, the energy associated with each force-displacement response curve was calculated. The energy calculation was performed by calculating the area under the force-displacement curve between 0 mm of displacement and the maximum displacement.

The energy was calculated using the following equation.

$$\text{Energy} = \sum_{i=1}^{n} \left(\frac{f_{i+1} + f_i}{2} \right) (dz_{i+1} - dz_i)$$

Where the variables were:

i = time step

f = force at time step

n = total time steps between 0 mm and maximum displacement

dz = displacement at time step

3.2.2 Hard Tissue Failures Predicted in FE Model Compared to Reported Tissue Damage from Experiments

In the experimental central compression tests (Carter, 2002), injury patterns were recorded according to the damage visually observed at different hard and soft tissue locations of each experimental specimen. Across the eight central compression experimental specimens, hard tissue injury was reported at the vertebral body, pedicle, articular pillar, lamina, and spinous process. The five locations where tissue injury was reported experimentally were used to guide the tissue failure assessment in the model. The comparison of tissue failures in the model to the experimental results was limited to comparing the structures with failure and not the extent of failure since the experimental results reported whether or not each location was injured.

The failure of only the hard tissue locations was the focus of the evaluation of the model simulation results since the aim of this project was to enhance hard tissue fracture. Additionally, the work in this project sought to investigate occlusion in the spinal canal. In this cervical spine segment model under central compression, occlusion was driven by hard tissue injury and fracture. Thus, the hard tissue locations where injury was reported experimentally were checked for failure in the model. To assess hard tissue failure in the model, failure was considered to have occurred at the hard tissue location if at least one element, with a mesh size of approximately 1.4 mm, at the location was eroded by the end of the simulation. The presence of erosion was used as an objective criterion to determine failure; however, one eroded element was not necessarily indicative of macroscopic damage that might be equivalent to damage that would be determined by visual inspection during the experimental tests. Thus, determining injury based on the presence of erosion may be slightly misleading.

In the experimental tests, the anterior and posterior vertebral bodies were the only locations where hard tissue injury was observed in all experimental specimens subjected to the central compression loading. Thus, the presence of hard tissue failure in the vertebral body of the model was the comparison of interest when comparing the results of the models to the experimental results.

3.2.3 Spinal Canal Occlusion

To evaluate the flow of hard tissue material into the spinal canal space in the CC_{SPH} model and the CC_{MPS} model, occlusion was expressed as a percent change in the two-dimensional area within the spinal canal occupied by intruding hard tissue material. A positive percent change was indicative of an increase in the area occupied by hard tissue material and a decrease in the spinal canal area. Conversely, a negative percent change indicated a decrease in the area occupied by hard tissue within the spinal canal space.

In the experimental work (Carter, 2002), occlusion of the spinal canal was measured using the SCOT, as described in section 2.4.4. To ensure the measurement of occlusion in the model was comparable and compatible with the experimental measurements, the evaluation of occlusion in the model was based on three considerations: the vertebral level from which occlusion was measured, the plane in which occlusion was measured, and the quantity represented by the measure of occlusion. First, the occlusion in the model was determined from the whole middle C6 vertebra since this is where much of the hard tissue failure was reported in the experimental and model results. Second, occlusion was measured from a superior-inferior view in the coronal plane of the vertebra with the spinal canal visible. The superior-inferior view allowed for the monitoring of hard tissue material movement in the coronal plane, corresponding to the direction of material movement causing the SCOT tubing to narrow in the experimental work. Third, the amount of hard tissue material displacing into the spinal canal space was quantified in terms of a two-dimensional area in the coronal plane. The calculated percent occlusion would then represent the increase in the two-dimensional area occupied by material intruding into the spinal canal relative to the neutral spine position at the beginning of the simulation.

Thus, to calculate percent occlusion throughout the simulation, the initial location and area of the spinal canal space at the beginning of the simulation was determined in phase one, while the area of material intrusion and corresponding percent occlusion was determined in phase two (Figure 3.9). In phase one, a rectangle was defined around the spinal canal space in the superior-inferior view of the whole C6 vertebra (Figure 3.9, steps 1 and 2). The area within the rectangle occupied by solid, shell, and SPH particle elements of the hard tissue was calculated using an image processing program (ImageJ) (Figure 3.9, step 3). At each subsequent time step, the rectangle from phase one was applied to the superior-inferior view of the whole C6 vertebra and the area occupied by hard tissue elements was calculated (Figure 3.9, steps 4 to 6). The percent increase in occupied area at each time step relative to the area calculated from phase one was the percent occlusion, representing the increase in hard tissue material inside the spinal canal space. The two-phase approach to calculating the occlusion in the simulation will be referred to in this thesis as the Rectangle Method.

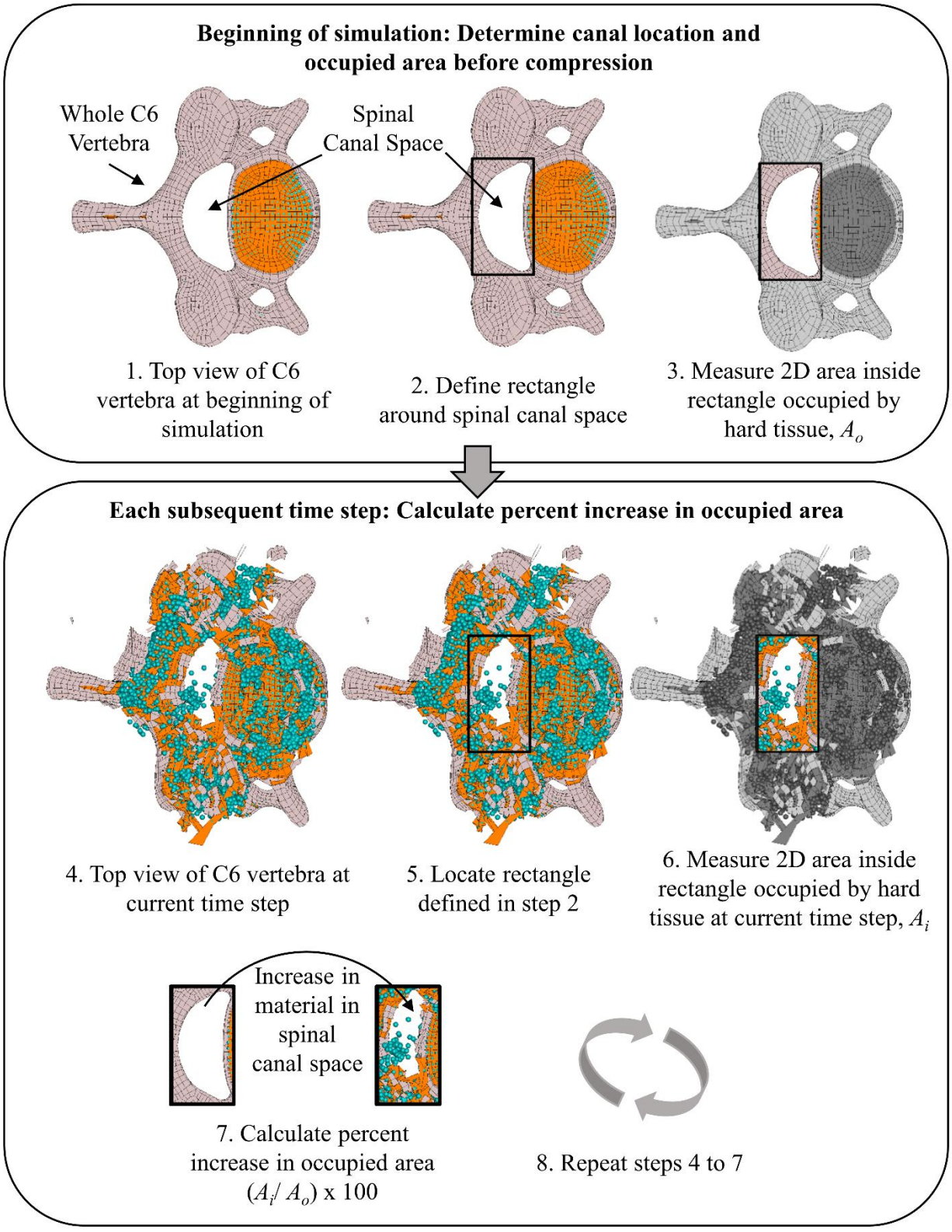


Figure 3.9: Schematic of the steps in the Rectangle Method used to calculate percent occlusion in the model. The images of the C6 vertebra shown steps 4 to 7 are an examples of the percent occlusion calculation method for the last time step of the CC_{SPH} model.

The equation to calculate the percent occlusion at each time step is as follows:

$$Percent\ Occlusion_{Area} = \frac{A_i}{A_o} \times 100$$

Where:

$Percent\ Occlusion_{Area}$ = calculated percent occlusion at the current time step

A_o = "occupied area within the rectangle" at the beginning of the simulation (t = 0 ms)

A_i = "occupied area within the rectangle" at the current time step

From the values of percent occlusion measured at each time step of the model, the percent occlusion was plotted as a function of time. The occlusion responses for the CC_{SPH} model and the CC_{MPS} model were compared. Additionally, the maximum occlusion was taken as the maximum occlusion measured across all time steps in the simulation. The maximum occlusion of the CC_{SPH} model and the CC_{MPS} model were compared to the experimental maximum occlusions.

3.3 Investigation of the Effect on the Force-Displacement Response with Varied Number of SPH Particles Generated Upon Erosion

A study was conducted to investigate how the force-displacement response was influenced by varying the number of SPH particles generated for each eroded solid Lagrangian element. The number of SPH particle elements generated for each solid element by the conversion in LS-DYNA was determined by the *nq* parameter. For hexahedral elements, such as the solid trabecular elements in the CC_{SPH} model, the generated SPH particles were evenly distributed in an *nq* x *nq* x *nq* configuration within the hexahedral element. Thus, the *nq* parameter determined the number of SPH particle elements along the length, width, and depth of the hexahedral element. The CC_{SPH} model used an *nq* value of 1 so that one solid Lagrangian element would transform into one SPH particle element upon erosion of the solid element. In the investigation in this section, the value of the *nq* parameter in the CC_{SPH} model was increased to 2 (CC_{NQ2}) and to 3 (CC_{NQ3}) (Figure 3.10). Thus, one solid element would transform into 8 SPH particles in the CC_{NQ2} model and 27 SPH particles in the CC_{NQ3} model. The force-displacement responses of the CC_{SPH} model, CC_{NQ2} model, and CC_{NQ3} model were compared. To evaluate the force-displacement responses using a single value, the energy for each force-displacement response up to a selected displacement was calculated and compared. The selected displacements were determined based on the displacement before a simulation reached an error termination.

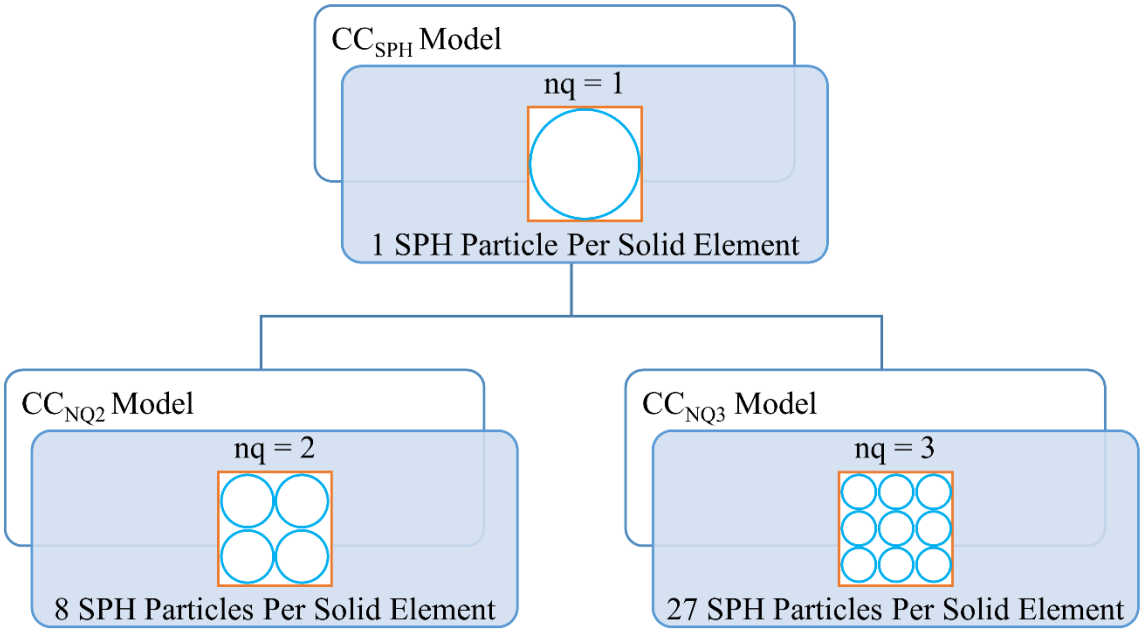


Figure 3.10: Overview of simulation configuration names included in the investigation of increasing the number of SPH particles generated for each solid element. Each diagram shows a two-dimensional illustration of the configuration of SPH particles generated in LS DYNA.

3.4 Parametric Study: Investigating Model Response Under Varied Impact Severity, Material Parameters, and Eccentric Loading

The CC_{SPH} model was used in the parametric study, primarily to investigate the effect of varying certain parameters on the measured occlusion in the model (Figure 3.11). In this section, each parameter that was investigated will be described. Additionally, the model output that was evaluated will be explained.

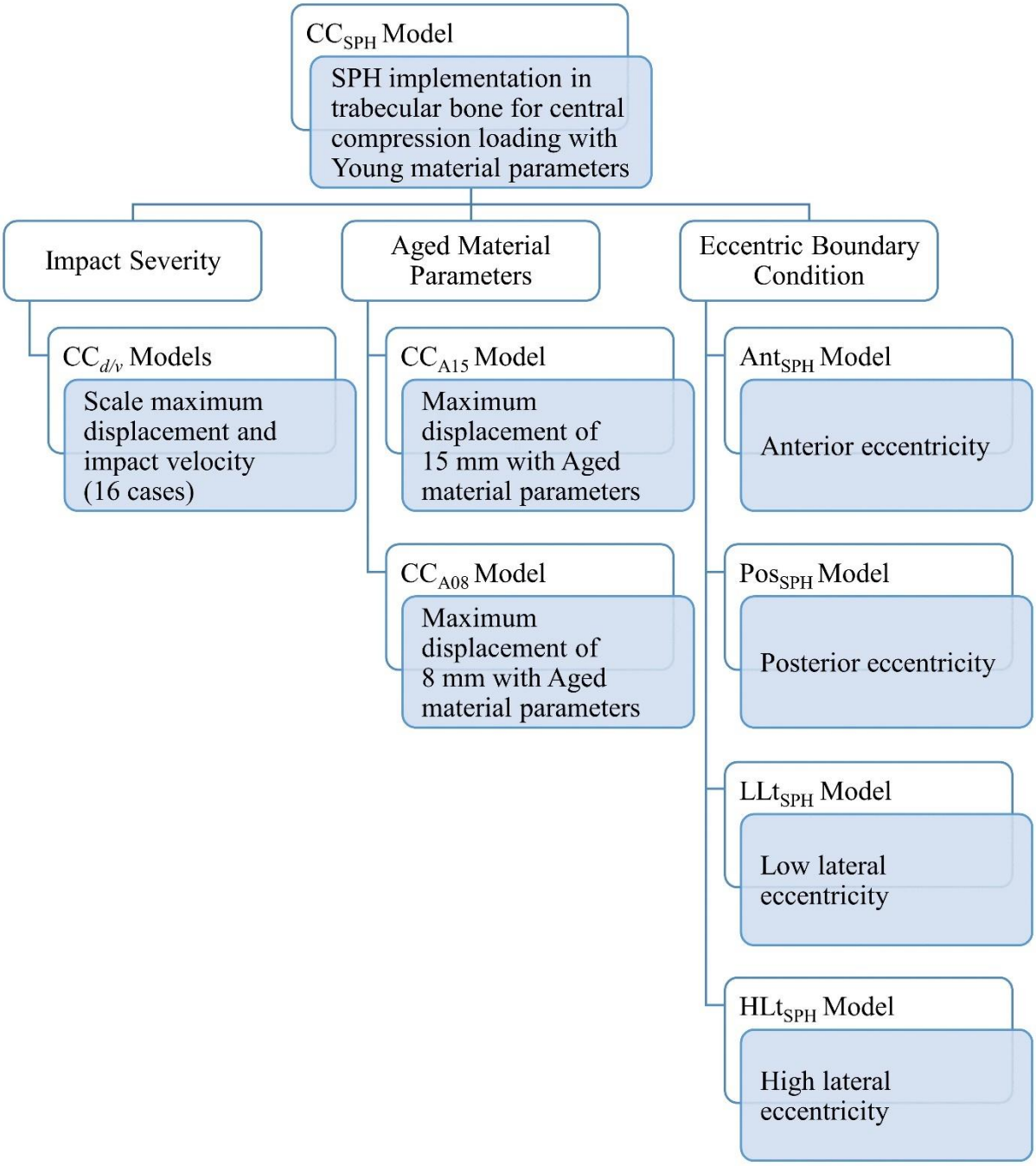


Figure 3.11: Overview of parameters investigated for the parametric study using the cervical spine model as developed for the CC$_{SPH}$ model.

3.4.1 Investigating the Effect of Varying Maximum Velocity and Maximum Displacement on Spinal Canal Occlusion

Vertebral fractures can occur from various impact scenarios and conditions which result in various impact severities experienced at the segment level in the cervical spine. The experimental central compression test applied maximum displacements between 8.3 mm to 15.7 mm in compression to achieve maximum velocities of between 0.8 m/s to 1.5 m/s (Carter, 2002). These ranges of maximum displacements and velocities were selected to be within the range of displacements and velocities that would result in hard tissue injury at a 2-FSU segment level as determined by literature (Carter, 2002).

The targeted maximum displacements and maximum velocities for the impact severity parametric study were based on the experimental maximum displacements and maximum velocities for the central compression cases (Figure 3.12). From the experimental values, four target maximum displacement and group maximum velocities were selected. The target maximum displacements were 8.3 mm, 10.0 mm, 12.6 mm, and 15.0 mm. The target maximum velocities were 0.8 m/s, 1.0 m/s, 1.2 m/s, and 1.4 m/s. The sixteen combinations of target maximum displacements and maximum velocities were applied to the CC_{SPH} model and run as the impact severity parametric study cases.

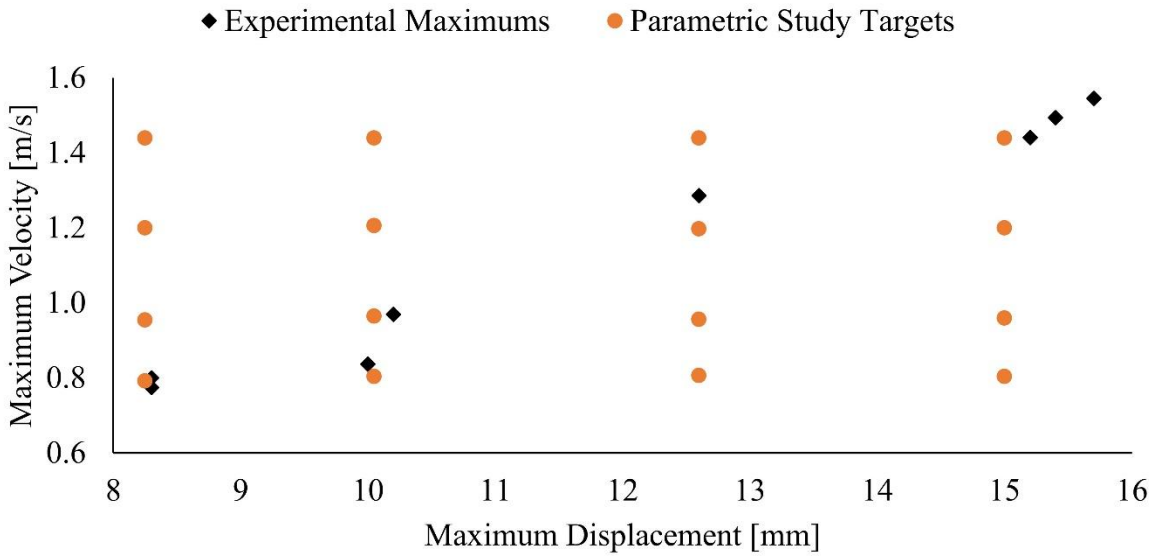


Figure 3.12: Each black diamond point shows the maximum displacement and maximum velocity measured for a central compression experimental specimen. The orange circle points show the maximum displacement and maximum velocity for each case run in the impact severity investigation in the parametric study.

The case names of the sixteen combinations of maximum displacements and maximum velocities are shown in Figure 3.13.

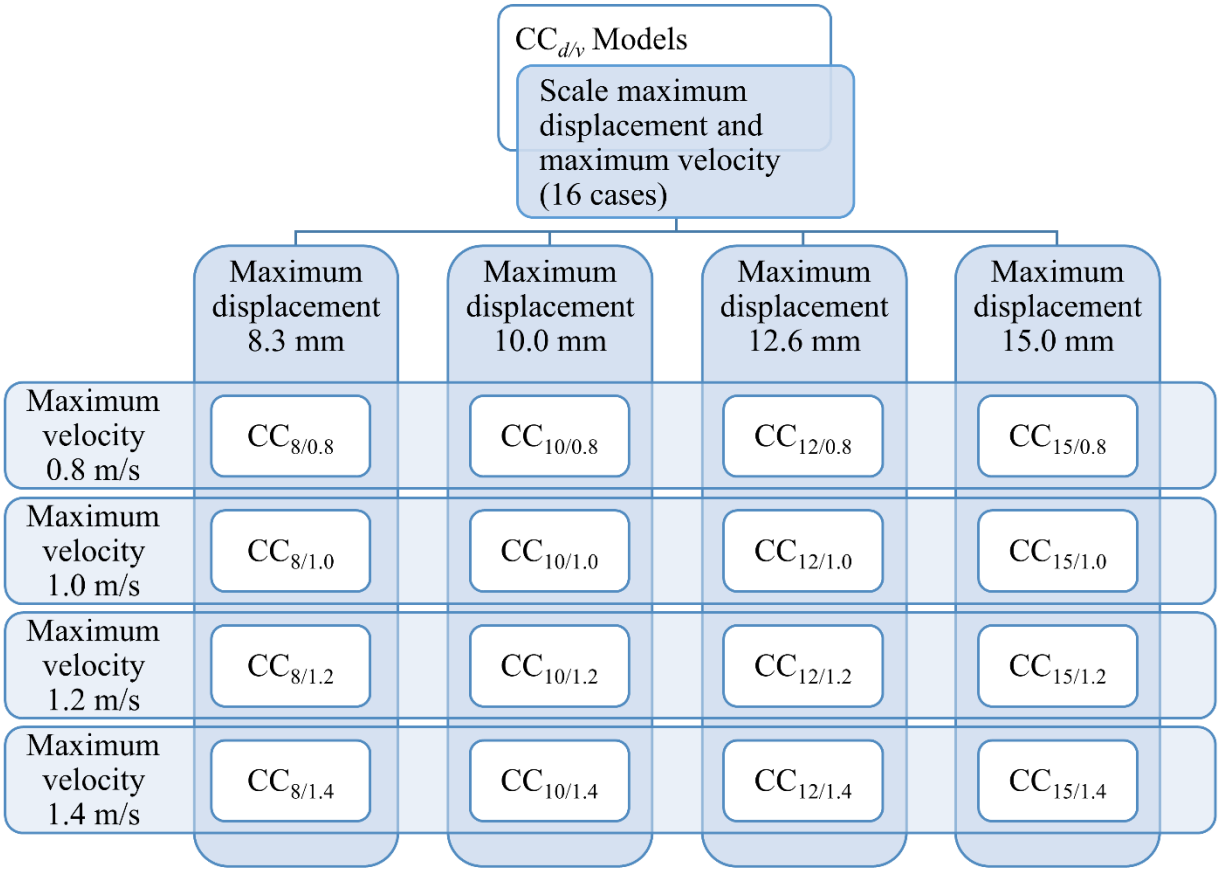


Figure 3.13: Case names for each combination of maximum displacement and maximum velocity run for the impact severity parametric study.

Varying the maximum displacement and maximum velocity in the model was achieved by scaling the displacement input to the top potting of the CC_{SPH} model. Central compression was applied to the cervical spine segment through the displacement of the top potting of the model. The downward motion of the top potting was defined using a displacement-time input curve. Thus, to vary the maximum displacement applied in the model, a scale factor was applied to the displacement values of the displacement-time input curve. Likewise, to vary the maximum velocity in the model, a scale factor was applied to the time values of the displacement-time curve.

The peak occlusion, determined as the maximum occlusion across all time steps in the simulation, was plotted against both the maximum displacement and maximum velocity to observe the effect of varying the maximum displacement and maximum velocity on the occlusion in the spinal canal.

Additionally, the maximum occlusions of four model cases and four experimental specimens with the closest matching maximum velocity and displacement combinations were compared. Specifically, the $CC_{8/1.4}$ model matched an experimental specimen with a maximum velocity of 0.8 m/s and a maximum displacement of 8.3 mm. The $CC_{10/1.2}$ model matched an experimental specimen with a maximum velocity of 1.0 m/s and a maximum displacement of 10.2 mm. The $CC_{12/1.0}$ model matched an experimental specimen with a maximum velocity of 1.3 m/s and a maximum displacement of 12.6 mm. The $CC_{15/0.8}$ model matched an experimental specimen with a maximum velocity of 1.4 m/s and a maximum displacement of 15.2 mm.

3.4.2 Comparison of Occlusion and Force-Displacement Response Using Aged Material Parameters for the Hard Tissues

To investigate the influence of young and aged hard tissue material parameters on the model response, the CC_{SPH} model using young hard tissue material parameters was run with aged hard tissue material parameters and the responses were compared. The CC_{SPH} model used hard tissue material parameters representative of a young age group of younger than 50 years old. For this parameter of the parametric study, hard tissue material parameters representing the aged age group of older than 70 years old was implemented into the cervical spine specimen of the CC_{SPH} model (Khor, 2018) (Table 3.6). Additionally, the material properties of the SPH particle elements were adjusted to reflect the material properties of the aged material parameters. The lower values of the hard tissue material parameters for the aged age group corresponded to the lower strength and stiffness seen in hard tissues as the bone mineral density decreases with age (Tanoto et al., 2024; Zioupos, 2001).

Table 3.6: Constitutive material models and key material parameters for the anisotropic hard tissue material models developed by Khor for the aged age group of older than 70 years old (Khor, 2018).

Tissue	Constitutive Material Model Description	LS-DYNA Material Model Name	Material Model Parameters	References
Trabecular Bone	Transversely Anisotropic Density Crushable Foam	*MAT_ TRANSVERSELY _ANISOTROPIC_ CRUSHABLE_ FOAM	E_1 = 344 MPa E_2 = 138.8 MPa ρ = 1000 kg/m^3 G = 132 MPa K = 287 MPa	(Khor, 2018; Liu et al., 2013; Mosekilde et al., 1987)
Cortical Bone	Orthotropic Elastic-Plastic	*MAT_ORTHO_ ELASTIC_ PLASTIC	E_1 = 17.325 GPa E_2 = 10.095 GPa ρ = 2000 kg/m^3 σ_y = 200.86 MPa ν_{12} = 0.35 ν_{23} = 0.42 ν_{31} = 0.222	(Ashman et al., 1984; Khor, 2018; Reilly and Burstein, 1975; Tang et al., 2015)

The material model with aged material parameters for the hard tissues also included a strain-based element erosion criterion (Table 3.7). The failure strain values from the material model developed by Khor were based on reported ultimate strains from experimental testing (Khor, 2018; Liu et al., 2013; Mosekilde et al., 1987). In the current work, a minimum principal strain erosion criterion was added to the erosion criterion for the solid elements of the trabecular bone in a process similar to the one described in section 3.1.4. The added minimum principal strain erosion criterion for the aged material parameters was defined at a strain of 1.2 in compression (Figure 3.14). The selected strain allowed for the solid Lagrangian element to transform into an SPH particle element in the linear section of the densification region. The SPH particle elements would therefore represent the densified crushed hard tissue fragments.

Table 3.7: Principal strains, in terms of true strain, of the strain-based erosion criterion applied to the hard tissue material models with aged material parameters (Khor, 2018).

Part Name	Minimum Principal Strain	Maximum Principal Strain	References
Trabecular Bone	-0.9*	0.0733	(Khor, 2018; Liu et al., 2013; Mosekilde et al., 1987)
Cortical Bone	-0.0205	0.0233	(Khor, 2018; Reilly and Burstein, 1975)

*Based on strain where linear densification region of single element stress-strain response begins.

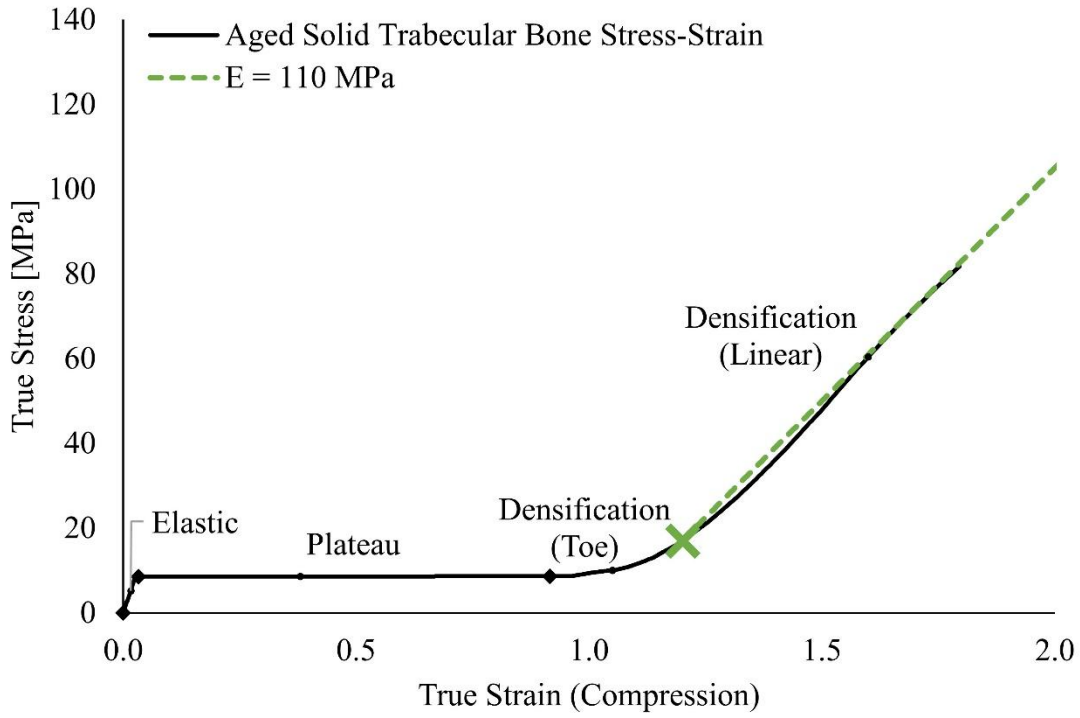


Figure 3.14: Stress-strain response of a single element simulation using the trabecular bone material model developed by Khor (Khor, 2018; Liu et al., 2013; Mosekilde et al., 1985; Sanyal et al., 2012). The *x*-axis shows the true strain in compression. The *y*-axis shows the true stress in compression. The "X" indicates where the erosion of the solid Lagrangian element occurs.

The SPH particle elements for the trabecular bone were also assigned an elastic material model with material properties of density, Young's modulus, and Poisson's ratio (Table 3.8). The density of 1000 kg/m^3, based on experimentally measured values, matched the density of the aged anisotropic material model of the trabecular bone. The Young's modulus of 110 MPa was the modulus in the linear section of the densification region of the single-element stress-strain response for the aged anisotropic material model of the trabecular bone. Finally, the Poisson's ratio of 0.33 was the average Poisson's ratio of the orthotopic elastic-plastic material model assigned to the shell elements of the aged cortical bone.

Table 3.8: Constitutive material models and key material properties assigned to the SPH elements of the aged trabecular bone.

Tissue	Constitutive Material Model Description	LS-DYNA Material Model Name	Material Model Parameters	References
Trabecular Bone – SPH Elements	Elastic Plastic	*MAT_ELASTIC	ρ = 1000 kg/m^3 E = 241 MPa ν = 0.33	(Ashman et al., 1984; Khor, 2018; Liu et al., 2013)

The response under central compression using the aged material model and properties was assessed for a displacement input with a maximum displacement of 8 mm (CC_{A08} model) and with a maximum displacement of 15 mm (CC_{A15} model) (Figure 3.15). The maximum displacement of 8 mm allowed for comparison of the model with aged material properties to the response of experimental specimen #12, the experimental specimen with similar age and sex. Experimental specimen #12 was also a male specimen in the aged age group of older than 70 years old. The maximum displacement of 15 mm allowed for comparison of the model responses using the young and aged material properties. The responses of the models were evaluated against experimental force-displacement response and maximum occlusion.

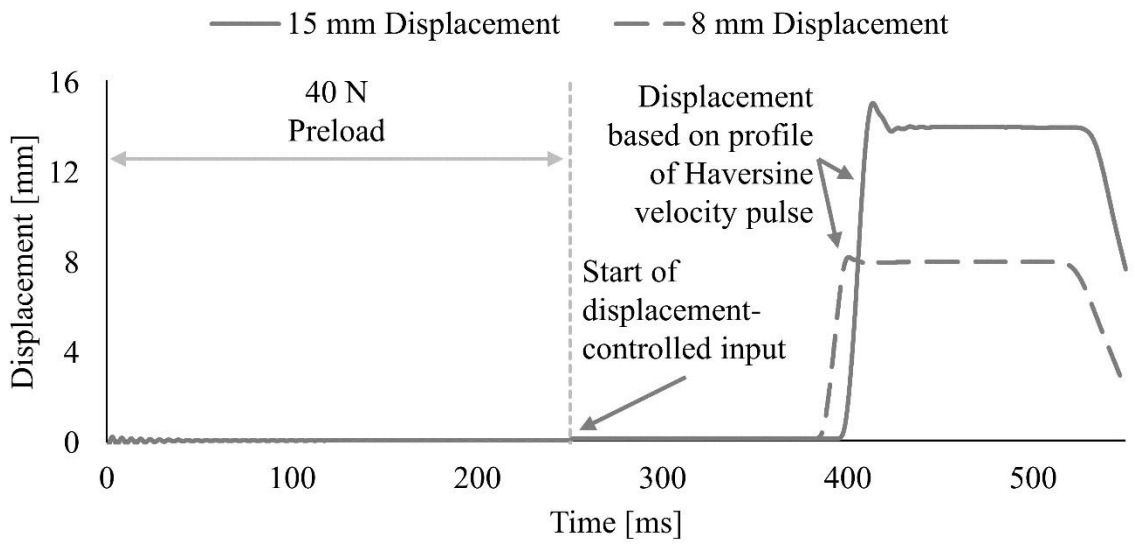


Figure 3.15: The displacement vs time graph shows the displacement of the top potting with maximum displacements of 15 mm in compression (CC_{A15}) and of 8 mm in compression (CC_{A08}). A 40 N preload was applied between 0 ms and 250 ms. After 250 ms, a displacement-controlled input was applied in the downward direction (compression). The grey dashed curve shows the displacement input with a maximum displacement of 15 mm. The light grey curve shows the displacement input with a maximum displacement of 8 mm.

3.4.3 Investigating the Effect of Eccentric Boundary Conditions on Spinal Canal Occlusion

To investigate the effect of eccentric loading on the occlusion of the spinal canal, four eccentric cases were run. The anterior and posterior eccentric cases were based on the experimental setup from Carter (Carter, 2002). The low lateral and high lateral eccentric cases were based on the experimental test setup from Van Toen (Van Toen, 2013; Van Toen et al., 2014a, 2014b). The experimental setups for eccentric loading had been recreated in a finite element model by Khor (Khor, 2018). In summary, a 45 N preload was first applied to the C5 superior endplate with a direction vector based on the geometric centroid of the C5 superior endplate. The preload was followed by an eccentric displacement-controlled input at 250 ms in the simulation. The eccentricity in the model was achieved by applying the boundary conditions to the bearing of the loading apparatus above the specimen (Figure 3.16). The location of the bearing from the geometric centroid of the inferior (C6-C7) IVD determined the type of eccentricity for each case. The bearing was 18 mm anterior of the geometric centroid of the C6-C7 IVD in the anterior eccentric case (Ant model) and 18 mm posterior of the geometric centroid of the C6-C7 IVD in the posterior eccentric case (Pos model). The top of the loading apparatus with the bearing was rotated 90 degrees for the lateral eccentric cases. The bearing was then positioned 0.3 mm lateral of the geometric centroid of the C6-C7

IVD for the low lateral eccentric case (LLt model) and 40.9 mm lateral of the geometric centroid of the C6-C7 IVD for the high lateral eccentric case (HLt model).

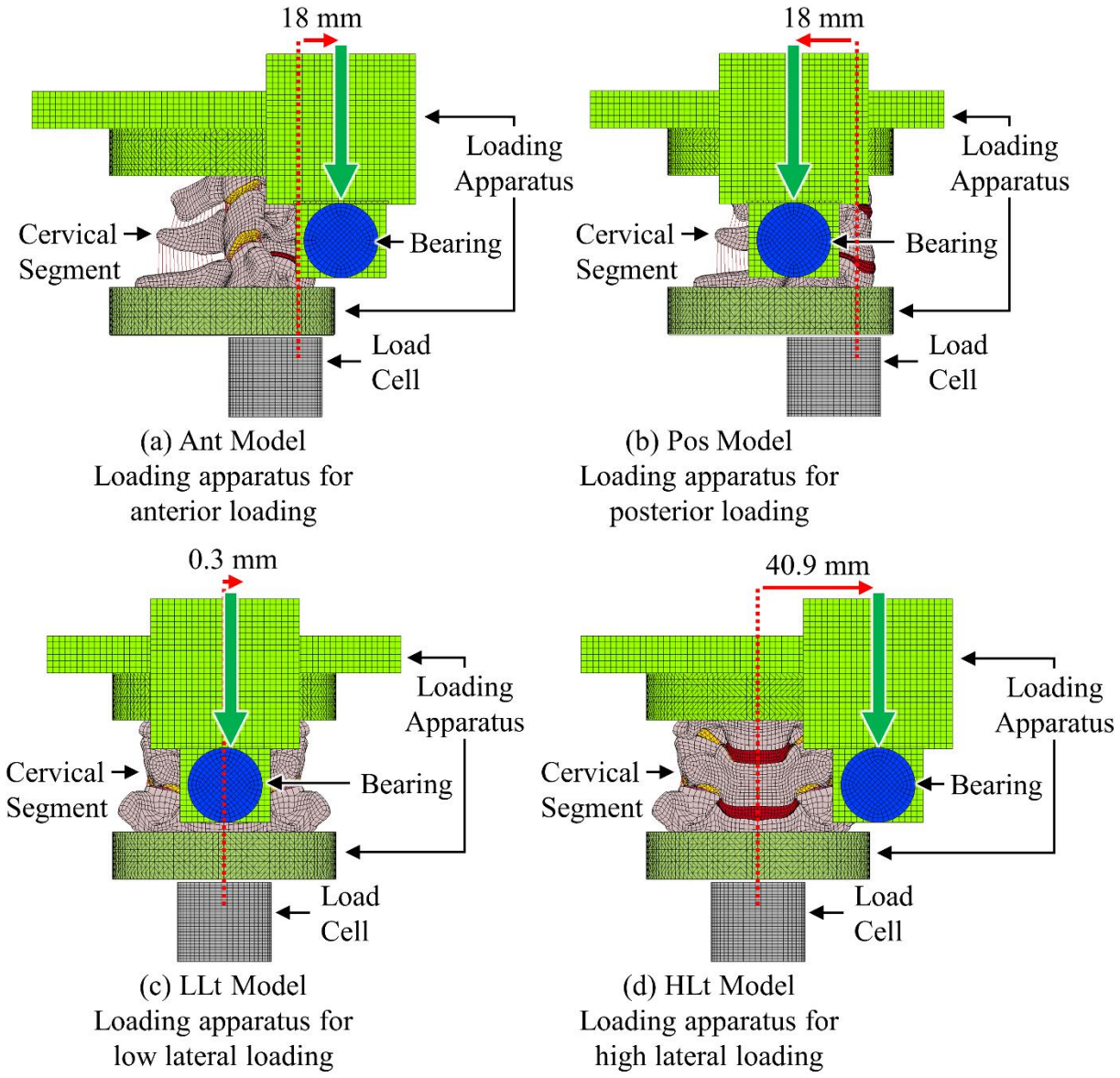


Figure 3.16: Model setups used for the (a) anterior, (b) posterior, (c) low lateral, and (d) high lateral eccentric cases in the parametric study. The red dashed lines indicate the location of the geometric centroid of the C6-C7 intervertebral disc. The green arrows indicate the location of the bearing where the displacement-controlled input was applied. The labels above the red arrows indicate the horizontal distance between the geometric centroid of the C6-C7 disc and the bearing where the displacement-controlled input was applied. The light and dark green parts indicate the loading apparatus. The blue parts indicate the bearing of the loading apparatus. The grey parts indication the load cell.

The cervical spine segment in the Ant_{SPH} model, Pos_{SPH} model, LLt_{SPH} model, and HLt_{SPH} model was the segment used in the CC_{SPH} model. Thus, to assess the four cases of eccentricity with the SPH implementation, the peak occlusions were compared to the average peak occlusions reported in the experimental data.

Chapter 4
Results

4.1 Model Enhancements to the FE Motion Segment Model: GHBMC Segment to SPH Implementation

The force-displacement responses from the central compression of a C5-C6-C7 segment model were used to evaluate the model response as changes were progressively implemented into the cervical spine segment, from the segment extracted from the GHBMC M50 model to the implementation of SPH into the trabecular bone. This section describes the force-displacement responses of the CC_{PlK}, CC_{Ani}, CC_{Con}, CC_{MPS}, and CC_{SPH} models.

4.1.1 Plastic Kinematic Material Model for Hard Tissues: CC_{PlK} Model

The force-displacement response of the CC_{PlK} model displayed an initial stiffness region, a decrease in force, and then a plateau until the maximum displacement (Figure 4.1). The initial stiffness region in the CC_{PlK} model corresponded to the compression of the intervertebral discs and the rotation of the C6 vertebra (Figure 4.2). The global maximum force of 4.9 kN was reached at 2.7 mm of displacement in compression (Point PlK1, Figure 4.1). The force then decreased abruptly to 1.2 kN at 3.2 mm of displacement with widespread erosion in the vertebral body of the C6 vertebra (Point PlK2, Figure 4.1). By 3.2 mm of displacement, 1141 solid elements had eroded in the C6 vertebral body, corresponding to 14.8% of the total number of solid elements in the C6 vertebra. Once elements eroded in the vertebral body of the C6 vertebra, continued compression resulted in interpenetration between the inferior and superior solid elements of the C6 vertebral body. The force increased to 1.7 kN at 3.6 mm of displacement as the intervertebral discs began to bulge into the cavity of the C6 vertebral body created by eroded elements (Point PlK3, Figure 4.1). Between 3.6 mm and 15.0 mm of displacement, the force plateaued around 1.3 kN. At 10.2 mm and 1.9 kN, interpenetration began between the C6 and C7 articular pillars after erosion in the inferior C6 articular pillar (Point PlK4, Figure 4.1). At 10.9 mm and 1.6 kN, interpenetration between the C5-C6 and the C6-C7 intervertebral discs began (Point PlK5, Figure 4.1). A force of 0.8 kN was reached at the maximum displacement of 15.0 mm (Point PlK6, Figure 4.1).

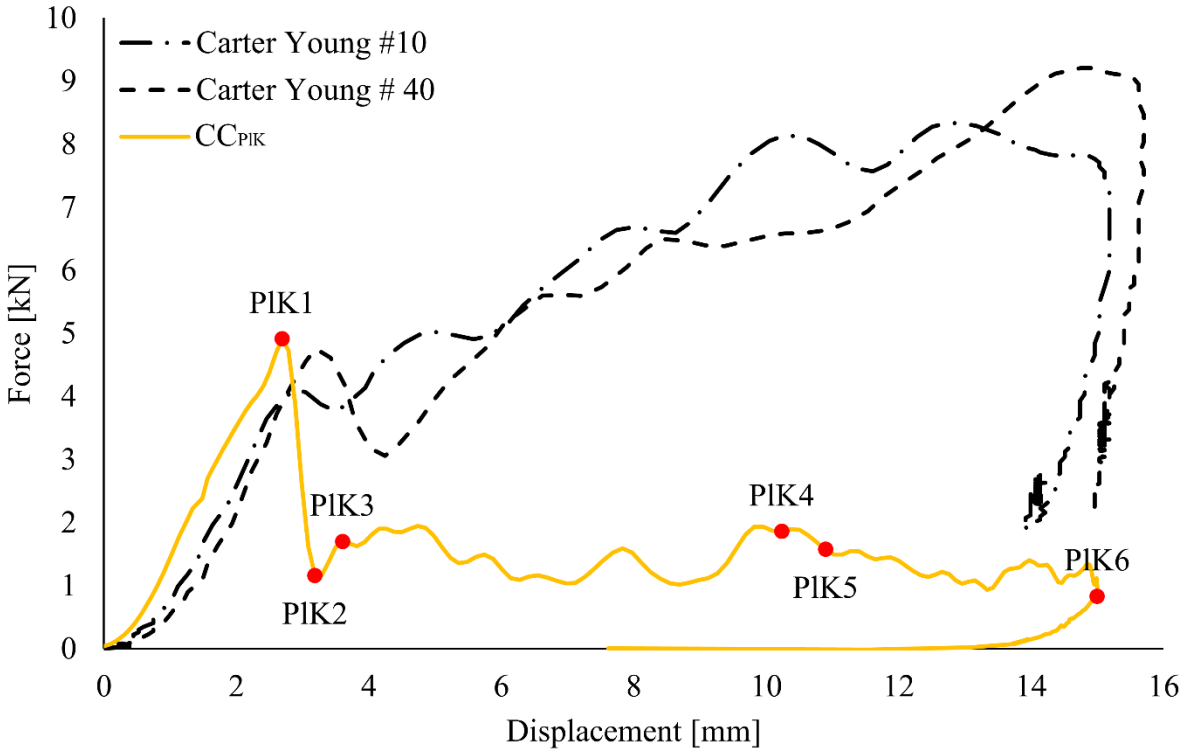


Figure 4.1: Force-displacement responses of the experimental specimen and of the CC_{PIK} model. The black dashed curves show the experimental responses (Carter et al., 2002; Rycman et al., 2023). The yellow curve shows the force-displacement response of the CC_{PIK} model.

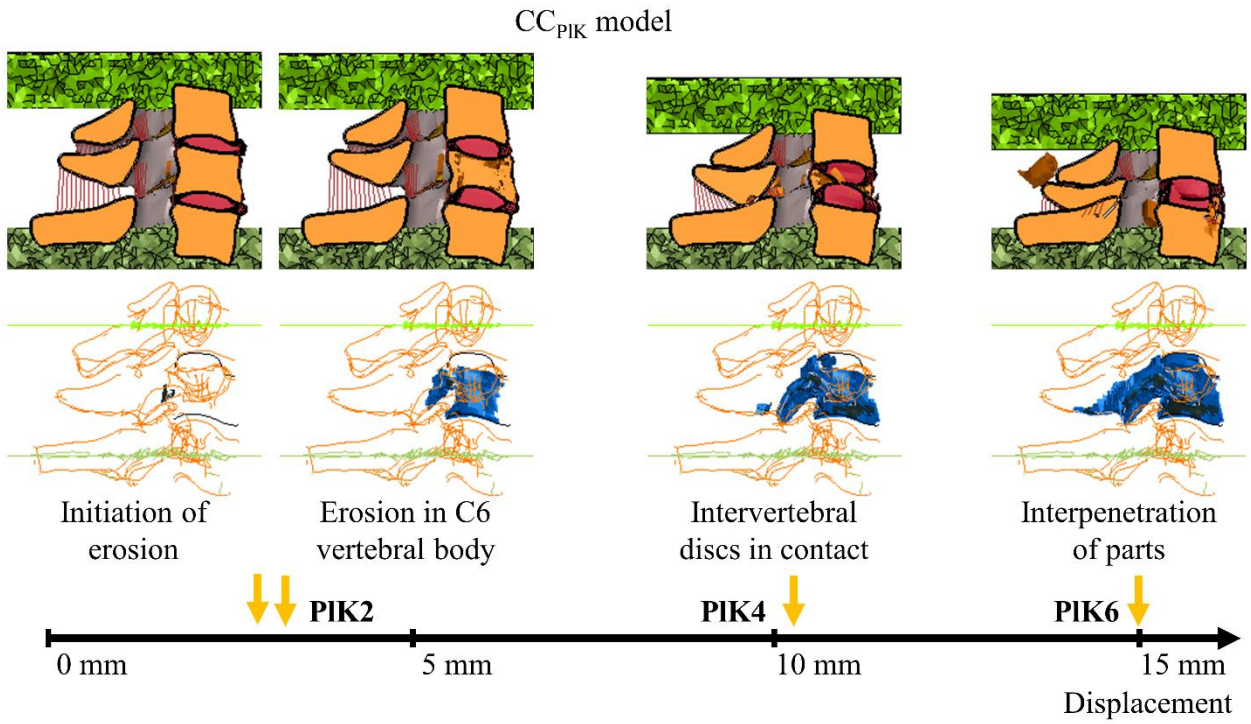


Figure 4.2: Section views in the midsagittal plane (top) and hard tissue erosion patterns (bottom) for the CC_{PIK} model during loading. In the section views, the light orange parts represent the solid elements of the trabecular bone, the purple-grey parts represent the shell elements of the cortical bone, the red parts represent the intervertebral discs, and the green parts represent the potting. In the erosion pattern images, the blue shaded region indicates the eroded hard tissue elements.

4.1.2 Anisotropic Material Model for Hard Tissues: CC_{Ani} Model

The implementation of the anisotropic material model for the hard tissues resulted in a more gradual failure of hard tissue elements, leading the force to increase after initial erosion and fracture in the articular pillars and pedicles.

The force-displacement response of the CC_{Ani} model showed a similar initial stiffness region to the CC_{PIK} model in the first 1.5 mm of displacement as the intervertebral discs were compressed (Figure 4.3). The force-displacement response of the CC_{Ani} model then increased to a local maximum of 3.3 kN at 2.1 mm of displacement (Point Ani1, Figure 4.3). The local maximum at 2.1 mm corresponded to the point of initial failure when the onset of element erosion began with the erosion of solid trabecular elements in the left articular pillar of the C6 vertebra (Figure 4.4). The force-displacement response then decreased to 2.3 kN at 2.5 mm of displacement as the pedicles of the C6 vertebra fractured and as the C6 vertebral body rotated (Point Ani2, Figure 4.3). Between 2.5 mm to 4.7 mm of displacement, the force increased to 4.8 kN (Point Ani3, Figure 4.3). As the force increased with continued compression, erosion progressed in the articular pillar of the C6 vertebra. Between 4.7 mm and 6.8 mm, the force decreased to 3.5 kN

(Point Ani4, Figure 4.3). The force decrease occurred with erosion progression in the inferior C6 articular pillars and in the inferior C5 vertebral body. The inferior C6 articular pillars eroded as the articular pillars, laminae, and spinous process of the C6 vertebra were pushed in the posterior direction with compression of the segment. Erosion of the inferior C5 vertebral body occurred as the C5-C6 intervertebral disc bulged upward. The deformation of the intervertebral discs and erosion of the C5 vertebral body also allowed for rotation of the C6 vertebral body. Between 6.8 mm and 10.8 mm, the force increased to 5.1 kN as continued compression led to interpenetration between the C5-C6 intervertebral disc and C5 vertebral body, the C6 articular pillar and C7 articular pillar, and the superior-anterior edge of the C6 vertebral body and intervertebral disc (Point Ani5, Figure 4.3). Erosion also began in the vertebral body of the C7 vertebral body. Between 10.8 mm and 12.9 mm, the force decreased and increased again to 5.0 kN with continued interpenetration, primarily between the C5 vertebral body, the C5-C6 intervertebral disc, and the C6 vertebral body (Point Ani6, Figure 4.3). Between 12.9 mm and 14.5 mm, the force decreased to 2.4 kN with continued erosion in the C6 spinous process and interpenetration between the C5 vertebral body and C5-C6 intervertebral disc, the C6 and C7 spinous processes, and the C6 and C7 articular pillars (Point Ani7, Figure 4.3). At the maximum displacement of 15.0 mm, the force was 1.6 kN.

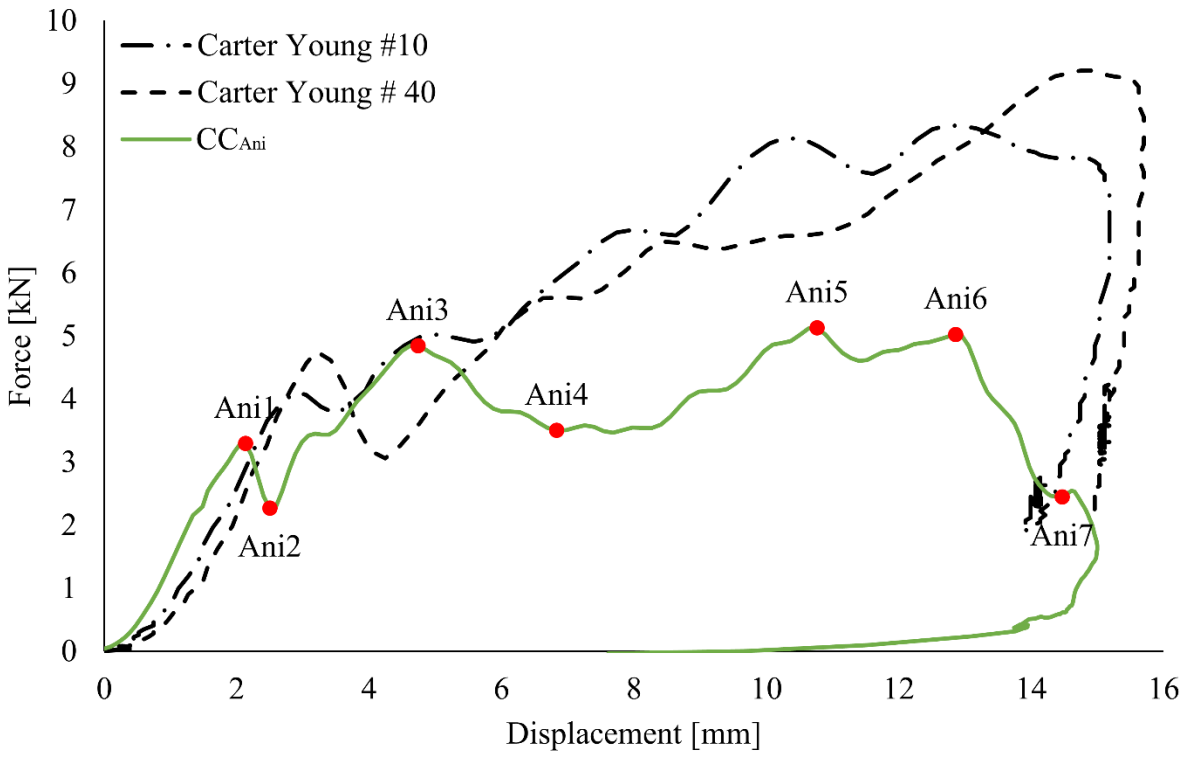


Figure 4.3: Force-displacement responses of the experimental specimen and of the CC_{Ani} model. The black dashed curves show the experimental responses (Carter et al., 2002; Rycman et al., 2023). The light green curve shows the force-displacement response of the CC_{Ani} model.

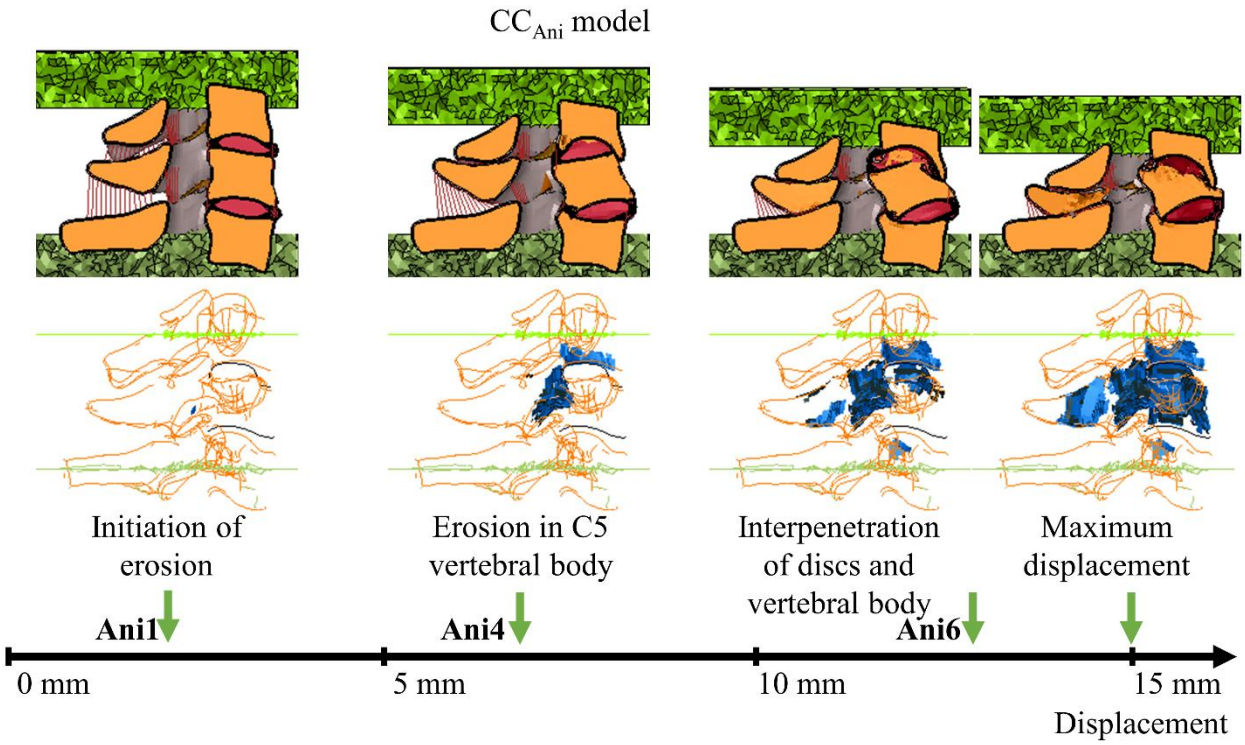


Figure 4.4: Section views in the midsagittal plane (top) and hard tissue erosion patterns (bottom) for the CC_{Ani} model during loading. In the section views, the light orange parts represent the solid elements of the trabecular bone, the purple-grey parts represent the shell elements of the cortical bone, the red parts represent the intervertebral discs, and the green parts represent the potting. In the erosion pattern images, the blue shaded region indicates the eroded hard tissue elements.

4.1.3 Added Contact Definitions to Account for Erosion and to Allow for Ligament to Intervertebral Disc Contact: CC_{Con} Model

The addition of contacts in the CC_{Con} model allowed the contact definitions to account for the erosion of hard tissue elements and allowed for contact between the ALL, PLL, and intervertebral discs. The added contact definitions resulted in an increase in the force response after erosion initiation in the vertebral bodies.

The point of the initial failure in the CC_{Con} model at 3.2 kN at 2.0 mm of displacement occurred with the onset of the element erosion in the left articular pillar and pedicle of the C6 vertebra (Point Con1, Figure 4.5) (Figure 4.6). The force decreased to 2.3 kN at 2.3 mm of displacement as the pedicles of the C6 vertebra fractured and as the C6 vertebral body rotated (Point Con2, Figure 4.5). As compression continued to 4.7 mm of displacement, the force increased to 5.8 kN as elements of the intervertebral discs, inferior C5 vertebral body, and superior C7 vertebral body compressed and deformed (Point Con3, Figure

4.5). Between 4.7 mm to 6.0 mm of displacement, the force increased to 5.9 kN before decreasing to 5.3 kN (Point Con4, Figure 4.5). The increase in force occurred with the onset of erosion in the C5 and C7 vertebral bodies. The decrease in force occurred with erosion progression in the inferior C6 articular pillars and C5 vertebral body. As erosion progressed, the articular pillars, laminae, and spinous process of the C6 vertebra moved posteriorly, and the C5-C6 intervertebral disc bulged upward into the C5 vertebral body. From 6.0 mm to 8.1 mm of displacement, the force increased to the global maximum of 6.2 kN (Point Con5, Figure 4.5). The increase in force occurred with erosion progression in the inferior C5 vertebral body, the superior C7 vertebral body, and the inferior C6 articular pillars. From 8.1 mm to 12.1 mm, the force decreased to 2.7 kN as fracture initiated and propagated across the C6 vertebral body (Point Con6, Figure 4.5). Fracture initiation began with erosion in the superior-anterior edge of the C6 vertebral body as the C5 vertebral body pushed the C5-C6 intervertebral disc into the C6 vertebral body. Fracture then propagated with erosion progression spreading from the anterior to the posterior side of the vertebral body. As the C6 vertebral body fractured, the articular pillars, laminae, and spinous process continued to be pushed in the posterior direction. From 12.1 mm to the maximum displacement of 15.0 mm, the force plateaued as the C6 vertebral body was further compressed and as erosion progressed in the spinous process of the C6 vertebra (Point Con7, Figure 4.5).

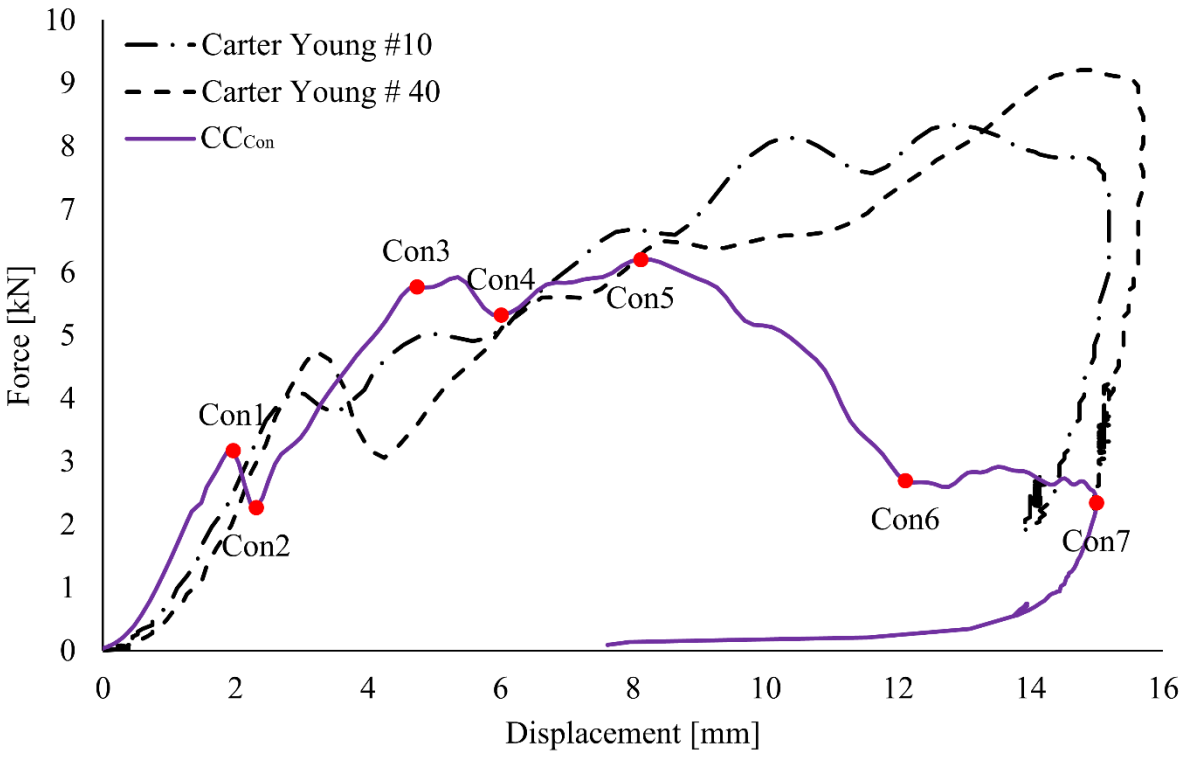


Figure 4.5: Force-displacement responses of the experimental specimen and of the CC_{Con} model. The black dashed curves show the experimental responses (Carter et al., 2002; Rycman et al., 2023). The purple curve shows the force-displacement response of the CC_{Con} model.

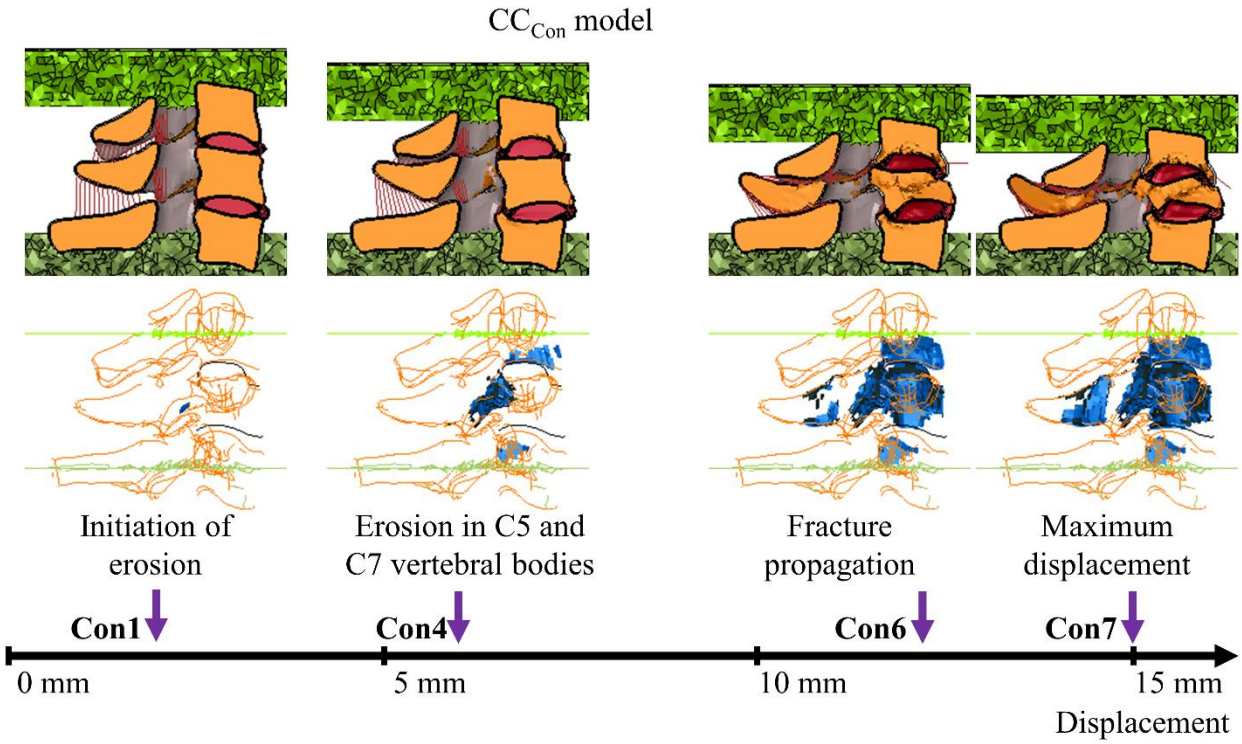


Figure 4.6: Section views in the midsagittal plane (top) and hard tissue erosion patterns (bottom) for the CC_{Con} model during loading. In the section views, the light orange parts represent the solid elements of the trabecular bone, the purple-grey parts represent the shell elements of the cortical bone, the red parts represent the intervertebral discs, and the green parts represent the potting. In the erosion pattern images, the blue shaded region indicates the eroded hard tissue elements.

4.1.4 Addition of Minimum Principal Strain to Erosion Criterion of Trabecular Bone: CC_{MPS} Model

The addition of the minimum principal strain to the erosion criterion of the trabecular bone was to model compressive failure; however, the addition of the minimum principal strain did not have a large influence on the force-displacement response.

The point of initial failure in the CC_{MPS} model occurred as 3.2 kN and 2.0 mm of displacement as the first elements eroded in the left articular pillar and pedicle of the C6 vertebra (Point MPS1, Figure 4.7) (Figure 4.8). The force decreased to 2.3 kN at 2.3 mm of displacement as the pedicles of the C6 vertebra fractured and the C6 vertebral body rotated (Point MPS2, Figure 4.7). With continued compression to 4.6 mm of displacement, the force increased to 5.7 kN as the elements of the intervertebral discs, C5 vertebral body, and C7 vertebral body deformed (Point MPS3, Figure 4.7). The onset of erosion also occurred in the inferior C5 vertebral body. From 4.6 mm to 5.2 mm of displacement, the force increased to 6.0 kN with

erosion progression in the inferior C5 vertebral body and upward bulging of the C5-C6 intervertebral disc into the C5 vertebral body (Point MPS4, Figure 4.7). From 5.2 mm to 6.3 mm of displacement, the force decreased to 5.3 kN as erosion progressed in the inferior C6 articular pillar, the C5 vertebral body, and the C7 vertebral body (Point MPS5, Figure 4.7). With erosion in the C6 articular pillars, the articular pillars, laminae, and spinous process of the C6 vertebra were pushed in the posterior direction. With erosion in the inferior C5 vertebral body and the superior C7 vertebral body, the intervertebral discs pushed into the C5 and C7 vertebral bodies. From 6.3 mm to 8.3 mm, the force increased to the global maximum of 6.2 kN (Point MPS6, Figure 4.7). As the force increased, compression of the segment pushed the C6 articular pillar in the inferior direction. The C5-C6 intervertebral disc was also pushed into the inferior C5 vertebral body, resulting in erosion. From 8.3 mm to 9.3 mm, the force decreased to 5.8 kN before increasing to 6.1 kN (Point MPS7, Figure 4.7). The change in force occurred with posterior motion of the C6 articular pillars, laminae, and spinous process, rotation of the C6 vertebral body, and downward motion of the C6-C7 disc into the C7 vertebral body. From 9.3 mm to 11.8 mm, the force decreased to 3.0 kN with the initiation and propagation of fracture in the C6 vertebral body (Point MPS8, Figure 4.7). The initiation of fracture began with erosion in the superior-anterior edge of the C6 vertebral body as the C5-C6 intervertebral disc was pushed into the C6 vertebral body. Fracture propagated with erosion progression toward the posterior side of the C6 vertebral body. Between 11.8 mm and 12.1 mm, the force decreased to a local minimum of 2.7 kN (Point MPS9, Figure 4.7). From 12.1 mm to the maximum displacement of 15.0 mm, the force reached 2.1 kN as erosion progressed in the C6 vertebral body, the inferior C6 spinous process, and the inferior C6 articular pillars (Point MPS10, Figure 4.7).

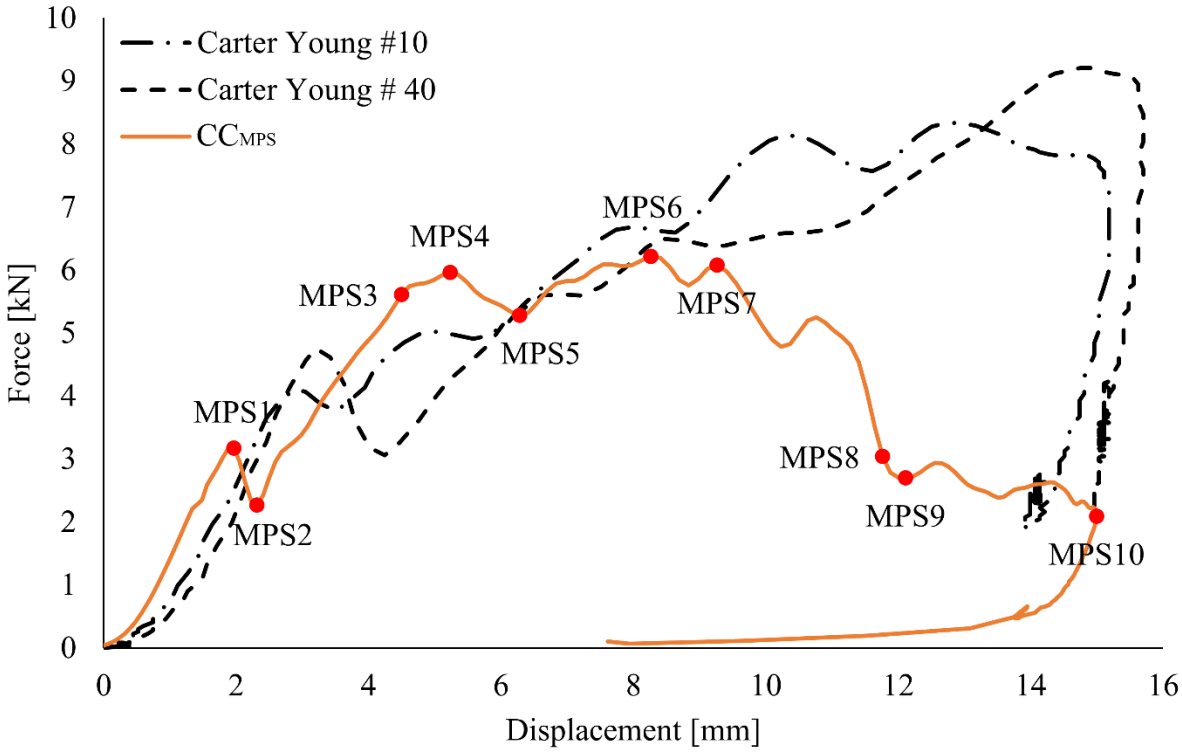


Figure 4.7: Force-displacement responses of the experimental specimen and of the CC$_{MPS}$ model. The black dashed curves show the experimental responses (Carter et al., 2002; Rycman et al., 2023). The orange curve shows the force-displacement response of the CC$_{MPS}$ model.

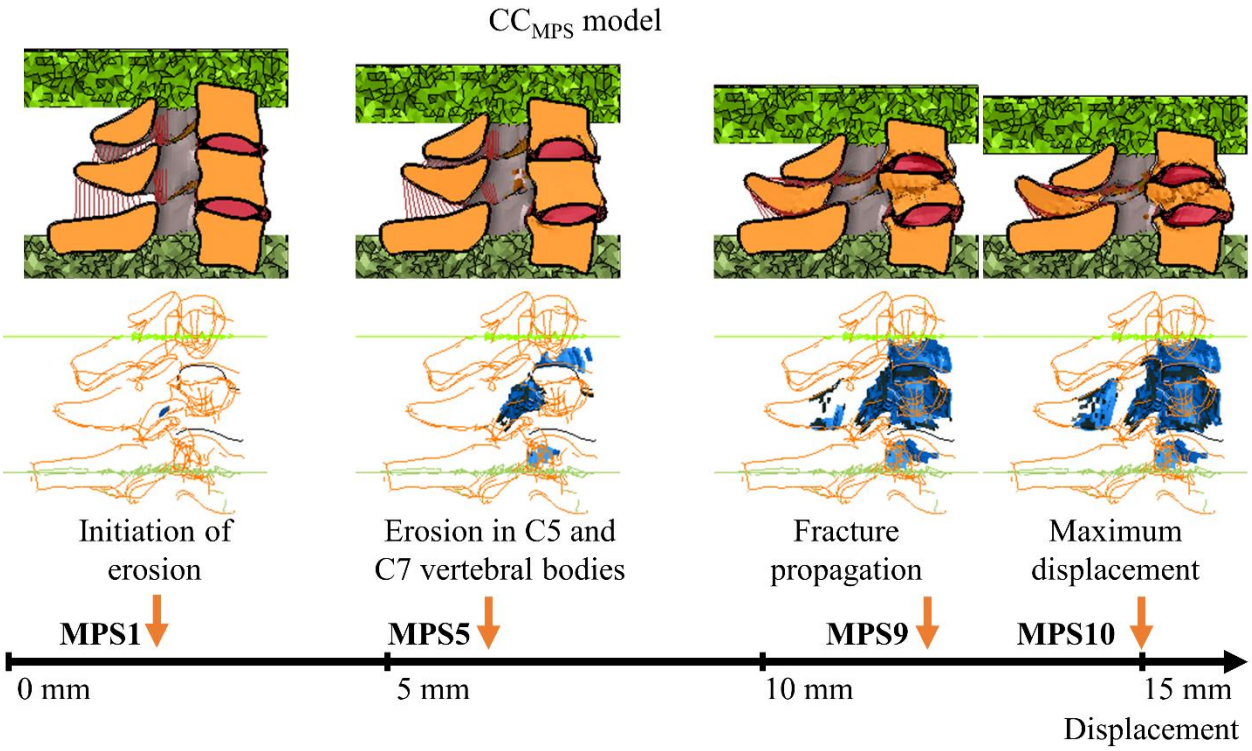


Figure 4.8: Section views in the midsagittal plane (top) and hard tissue erosion patterns (bottom) for the CC_{MPS} model during loading. In the section views, the light orange parts represent the solid elements of the trabecular bone, the purple-grey parts represent the shell elements of the cortical bone, the red parts represent the intervertebral discs, and the green parts represent the potting. In the erosion pattern images, the blue shaded region indicates the eroded hard tissue elements.

4.1.5 Implementation of SPH to Trabecular Bone: CC_{SPH} Model

The addition of the SPH implement to transform solid elements to SPH elements upon erosion allowed for the overall increase in the force response.

In the initial stiffness region of the CC_{SPH} model, the force increased as the intervertebral discs deformed. The point of initial failure occurred at 3.2 kN and 2.0 mm of displacement, corresponding to the onset of element erosion in the left articular pillar and pedicle of the C6 vertebra (Point SPH1, Figure 4.9) (Figure 4.10). The force then decreased to 2.3 kN at 2.3 mm of displacement as the C6 pedicles fractured and the C6 vertebral body rotated (Point SPH2, Figure 4.9). Between 2.3 mm and 4.7 mm of displacement, the force increased to 6.0 kN as the discs continued to deform and bulge into the C5 and C7 vertebral bodies (Point SPH3, Figure 4.9). The onset of erosion in the C5 inferior vertebral body occurred at 4.4 mm. From 4.7 mm to 8.4 mm, the force increased to 7.8 kN (Point SPH4, Figure 4.9). As the force increased, the C5-C6 intervertebral disc bulged into the inferior C5 vertebral body as erosion progressed in the C5 vertebral body. At 5.9 mm of displacement, the onset of erosion began in the superior C7 vertebral body,

allowing the C6-C7 intervertebral disc to push into the C7 vertebral body. From 8.4 mm to 9.5 mm of displacement, the force decreased to 6.7 kN with rotation of the C6 vertebral body (Point SPH5, Figure 4.9). As the C6 vertebral body rotated, fracture initiation began as the C5-C6 intervertebral disc was pushed into the superior-anterior edge of the C6 vertebral body. From 9.5 mm to 11.5 mm of displacement, the force decreased to 5.7 kN as fracture began to propagate across the C6 vertebral body (Point SPH6, Figure 4.9). Fracture propagation continued until 12.3 mm of displacement as the force increased to 6.2 kN (Point SPH7, Figure 4.9). After fracture propagation, the force further increased until the global maximum of 7.9 kN at 14.6 mm of displacement (Point SPH8, Figure 4.9). The continued force increase occurred as erosion continued in the vertebral body, pedicles, and spinous process of the C6 vertebral. At the maximum displacement of 15.0 mm, the force was 6.7 kN (Point SPH9, Figure 4.9).

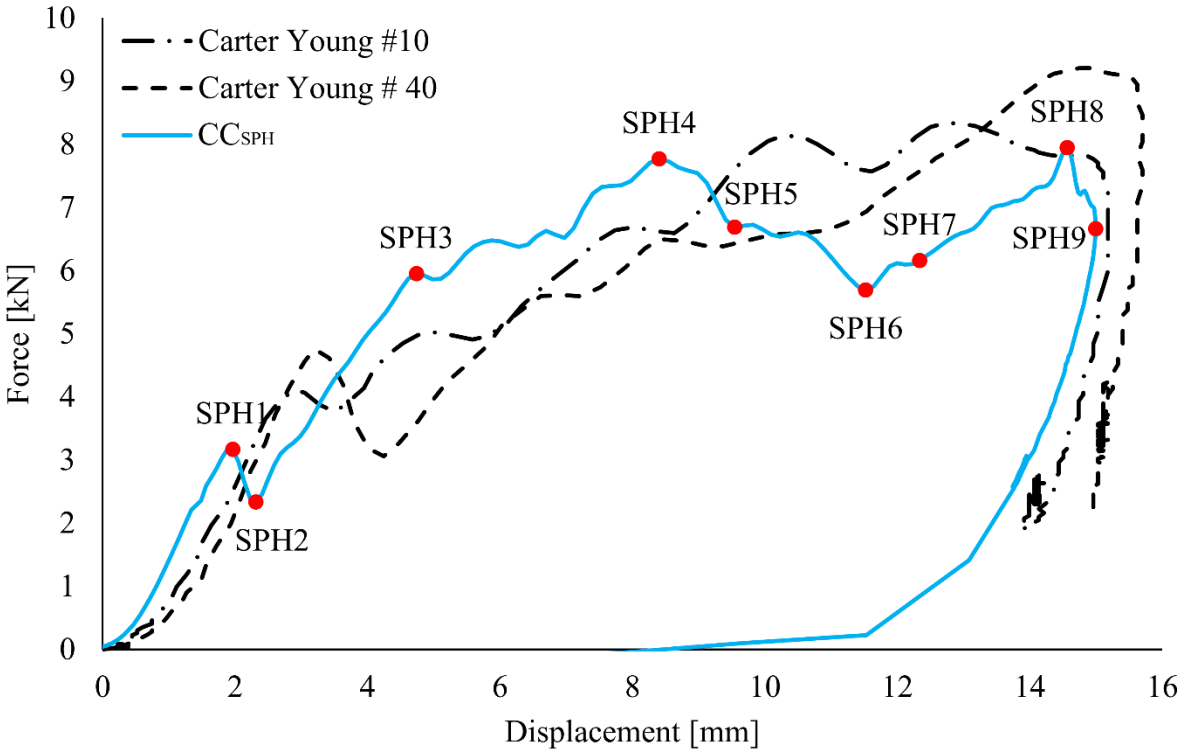


Figure 4.9: Force-displacement responses of the experimental specimen and of the CC_{SPH} model. The black dashed curves show the experimental responses (Carter et al., 2002; Rycman et al., 2023). The light blue curve shows the force-displacement response of the CC_{SPH} model.

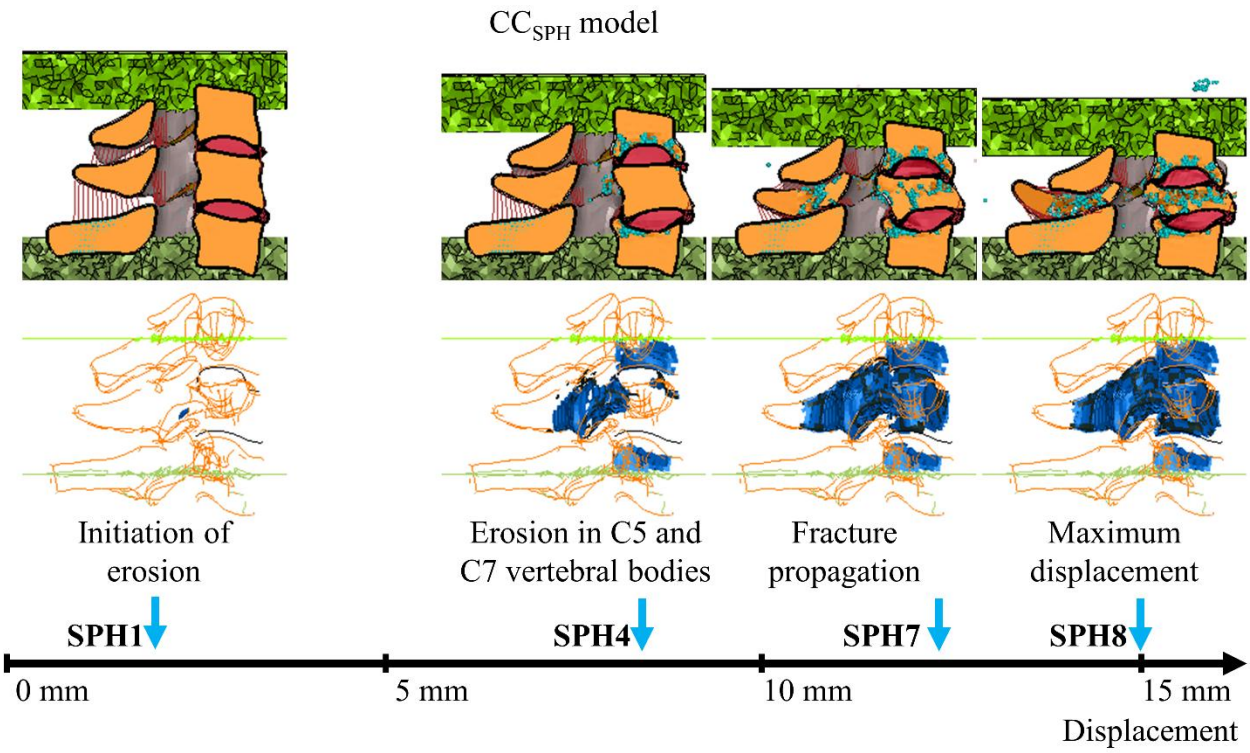


Figure 4.10: Section views in the midsagittal plane (top) and hard tissue erosion patterns (bottom) for the CC_{SPH} model during loading. In the section views, the light orange parts represent the solid elements of the trabecular bone, the purple-grey parts represent the shell elements of the cortical bone, the red parts represent the intervertebral discs, and the green parts represent the potting. In the erosion pattern images, the blue shaded region indicates the eroded hard tissue elements.

4.2 Evaluation of the SPH Implementation in the CC_{SPH} Model Against Experimental Targets

To evaluate the implementation of SPH into the trabecular bone, the force-displacement response, injury pattern, and spinal canal occlusion of the CC_{MPS} model and the CC_{SPH} model were compared and assessed against results from the experiments. The CC_{MPS} model was considered the model without the SPH implementation, and the CC_{SPH} model was considered the model with the SPH implementation.

4.2.1 Force-Displacement Response

The CC_{MPS} model and the CC_{SPH} model had the same point of initial failure when the onset of element erosion began in the left articular pillar and pedicle of the C6 vertebra (Point A, Figure 4.11). The force-displacement responses continued to be similar in the first 4.5 mm of displacement until the onset of erosion in the C5 vertebral body. The force-displacement responses of the CC_{MPS} and the CC_{SPH} models first diverged at 5.2 mm when erosion progressed in the inferior C6 articular pillar and inferior C5 vertebral body (Point B, Figure 4.11). At 5.2 mm in the CC_{MPS} model, the articular pillar was pushed in

the posterior direction. The posterior movement of the articular pillar with compression of the segment was accompanied by erosion in the inferior C6 articular pillar (Point B to Point C, Figure 4.12). In the CC_{SPH} model, the C6 articular pillar was not pushed in the posterior direction. Instead, the articular pillar was pushed in the anterior direction until fracturing at 9.7 mm of displacement (Point B to Point D, Figure 4.12). The force-displacement responses of the CC_{MPS} model and the CC_{SPH} model continued to diverge with fracture propagation in the C6 vertebral body. The force-displacement response of the CC_{MPS} model decreased during fracture propagation (Point C to Point E, Figure 4.11), while the force-displacement response of the CC_{SPH} model demonstrated a sustained force during fracture propagation (Point D to Point F, Figure 4.11). After 12.3 mm of displacement, the force-displacement response of the CC_{SPH} model further diverged from the response of the CC_{MPS} model as the segment compressed and as erosion continued.

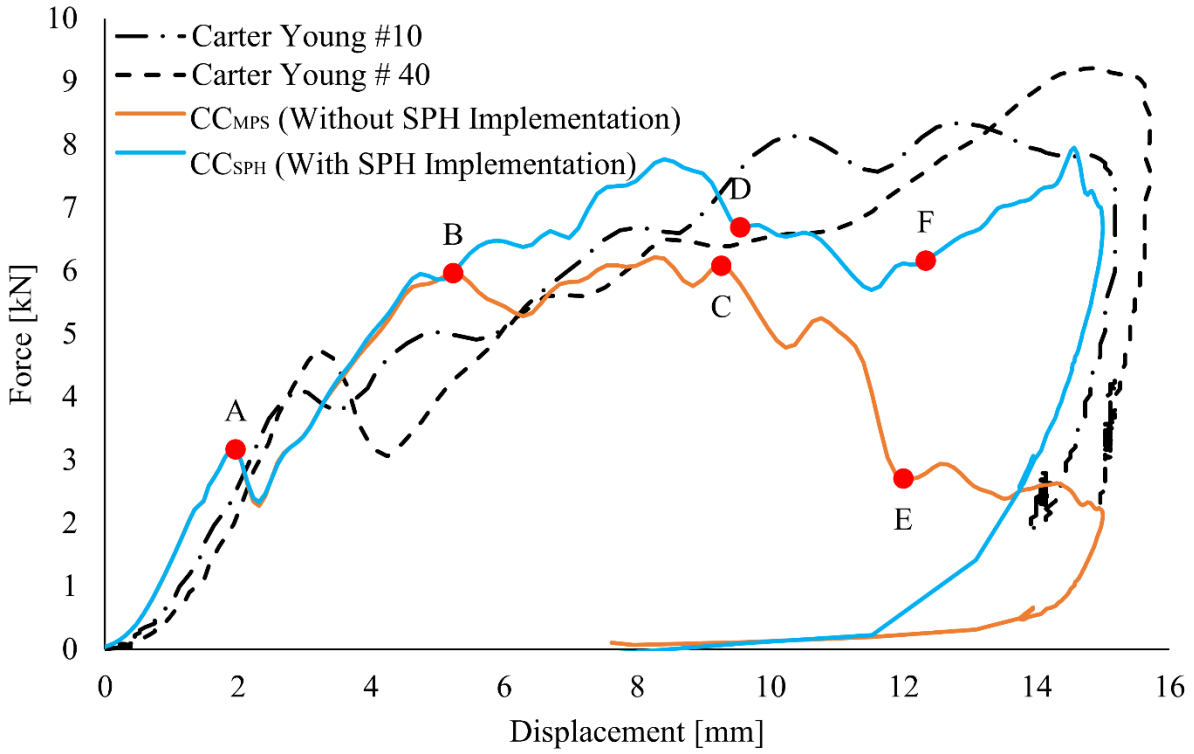


Figure 4.11: Force-displacement responses of the experimental specimen, the CC_{MPS} model and the CC_{SPH} model. The black dashed curves show the experimental responses (Carter et al., 2002; Rycman et al., 2023). The orange curve shows the force-displacement response of the CC_{MPS} model without the SPH implementation. The light blue curve shows the force-displacement response of the CC_{SPH} model with the SPH implementation.

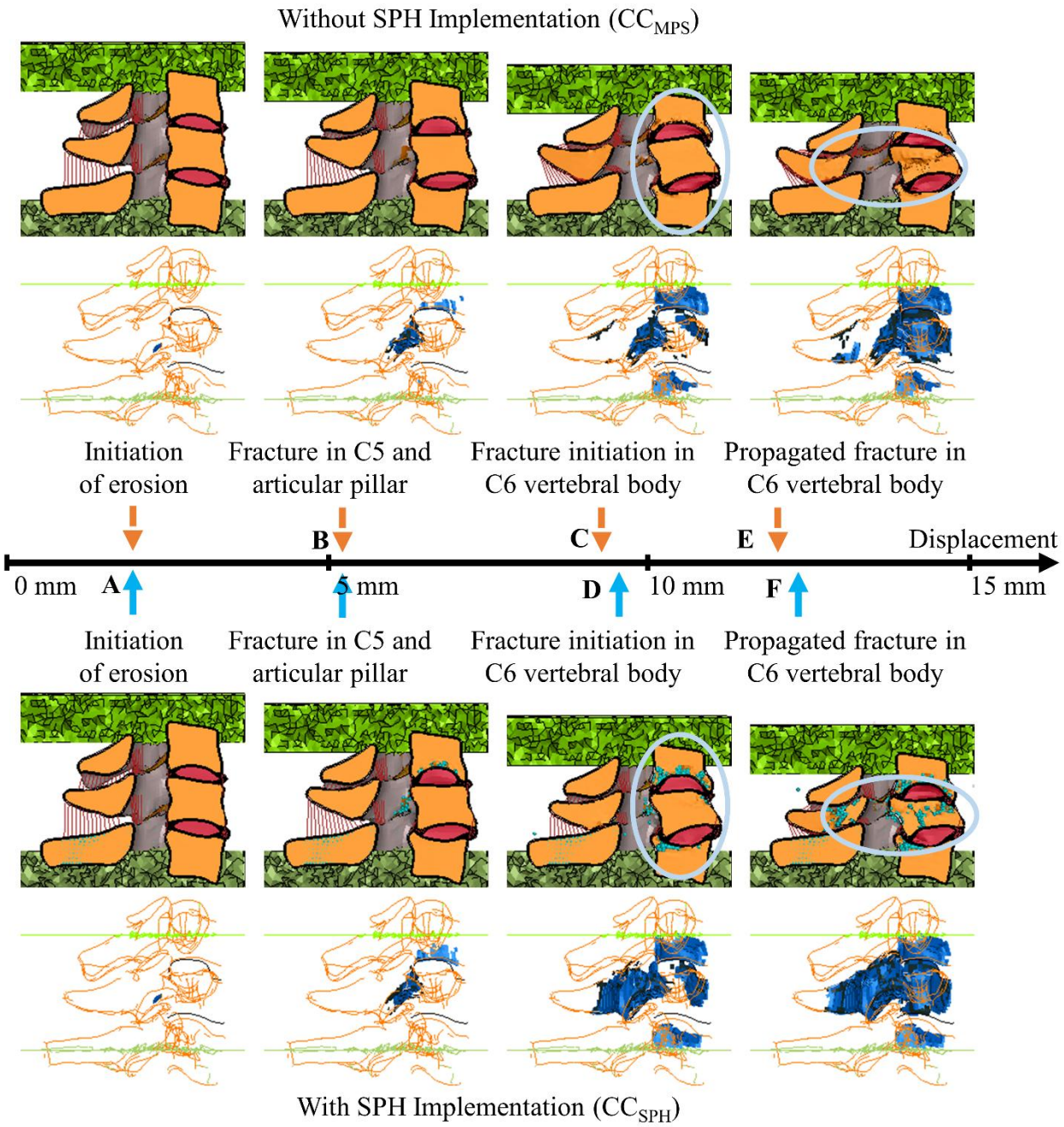


Figure 4.12: Eroded elements and section views in the sagittal plane of the CC_{MPS} model without the SPH implementation (top) and the CC_{SPH} model with the SPH implementation (bottom). The points correspond to the points in Figure 4.11. Point A is at 2.0 mm, point B is at 5.2 mm, point C is at 9.3 mm, point D is at 9.5 mm, point E s at 12.0 mm, and point F is at 12.3 mm. The blue regions indicate eroded elements of the hard tissues in the vertebrae. In the sagittal plane section views, the orange parts indicate the solid elements of the trabecular bone, the cyan spheres indicate the SPH particle elements, the dark purple part indicate the shell elements of the cortical bone, the red parts indicate the intervertebral discs, and the light and dark green parts indicate the top and bottom potting. The light blue circles at points C and D indication the differences in the intrusion of the intervertebral discs into the C5 and C7 vertebral bodies. The light blue circles at points E and F indication the differences in displacement of hard tissue material into the spinal canal space.

4.2.2 Hard Tissue Failures Predicted in FE Model Compared to Reported Tissue Damage from Experiments

Hard tissue elements were observed to have eroded in all locations of the vertebra in both the CC_{MPS} model and the CC_{SPH} model, differing from the frequency of injury patterns observed experimentally (Table 4.1). Both the CC_{MPS} and the CC_{SPH} models had widespread erosion in the anterior and posterior vertebral bodies (Figure 4.13). The C6 vertebra in the CC_{MPS} model had elements that eroded in the pedicles, articular pillars, laminae, and spinous process. The eroded elements in the articular pillars were on the anterior side. Additionally, erosion was considered to have occurred in the laminae and spinous process; however, the erosion was only in the posterior laminae and the anterior spinous process. In the CC_{SPH} model, erosion also occurred in the pedicles, articular pillars, laminae, and spinous process. Unlike the CC_{MPS} model, the erosion was more widespread throughout the articular pillars and laminae of the CC_{SPH} model.

Table 4.1: Reported injury patterns in the experimental specimens (Carter, 2002). The values in the Experimental Specimen row indicate the number of specimens out of the eight total central compression specimens with injury reported at each hard tissue location. The structures evaluated were the AVB (anterior vertebral body), PVB (posterior vertebral body), RPED (right pedicle), LPED (left pedicle), RAP (right articular pillar), LAP (left articular pillar), RLAM (right lamina), LLAM (left lamina), and SP (spinous process).

	Hard Tissue Vertebra Location								
	AVB	PVB	RPED	LPED	RAP	LAP	RLAM	LLAM	SP
# Experimental Specimens with damage out of 8 total specimens	8	8	3	1	3	3	3	2	2

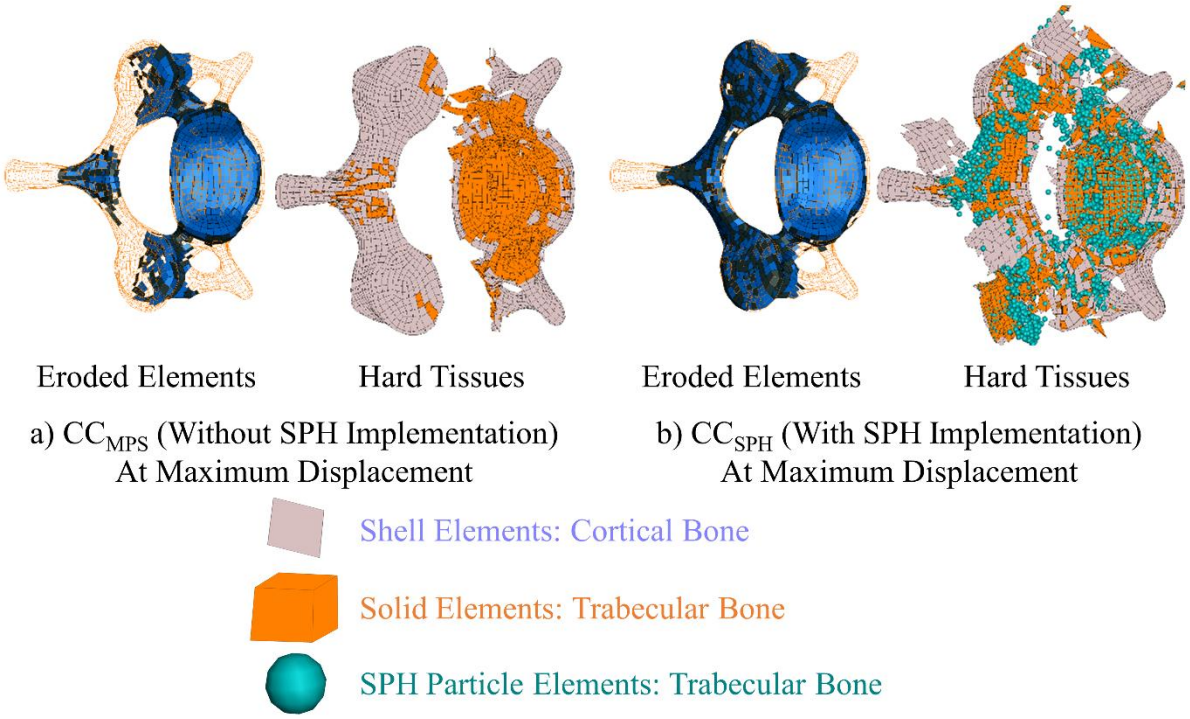


Figure 4.13: Eroded elements and superior views of the hard tissues of the whole C6 vertebra. In the images of eroded elements, the blue shaded regions indicate eroded solid and shell hard tissue elements. In the superior views of the hard tissues, the orange elements indicate the solid elements of the trabecular bone, the light purple elements indicate the shell elements of the cortical bone, and the cyan spheres indicate the SPH particle elements of the trabecular bone.

4.2.3 Spinal Canal Occlusion

The CC_{MPS} model and the CC_{SPH} model had a similar percent occlusion of the spinal canal up to 402.6 ms in the simulation, corresponding to a displacement of 4.2 mm (Figure 4.14). As the segment was loaded, the percent occlusion of the CC_{MPS} model and the CC_{SPH} model increased to 1.4% at 400.4 ms, corresponding to 2.0 mm of displacement. From 400.4 ms to 400.9 ms, corresponding to a compression from 2.0 mm to 2.4 mm of displacement, the percent occlusion of the CC_{MPS} model and the CC_{SPH} model increased to 10.2%. Between 400.9 ms and 403.8 ms, corresponding to a compression from 2.4 mm to 5.6 mm in displacement, the percent occlusions increased to 12.3% for the CC_{MPS} model and 11.0% in the CC_{SPH} model.

After 403.8 ms, corresponding to 5.6 mm in displacement, the percent occlusions diverged, with the CC_{MPS} model showing a sharp decrease in percent occlusion and the CC_{SPH} model showing a sharp increase in percent occlusion. At 410.6 ms, corresponding to 14.0 mm of displacement, the spinal canal space of the CC_{MPS} model increased, reaching a minimum percent occlusion of -26.0%. In contrast, the

spinal canal space of the CC_{SPH} model decreased, reaching a percent occlusion of 52.0% at 410.6 ms and 14.0 mm in displacement. At 413.6 ms in the simulation, the segment was compressed to the maximum displacement of 15.0 mm. The CC_{MPS} model had a percent occlusion of -23.5% and the CC_{SPH} model had a percent occlusion of 46.2%. During the holding phase, the displacement was held constant. The percent occlusions of both models also plateaued with average percent occlusions of -22.7% for the CC_{MPS} model and 46.3% for the CC_{SPH} model. During the unloading phase, both models also demonstrated an increase in percent occlusion. At the end of the simulation at 7.6 mm of displacement, the CC_{MPS} model reached a percent occlusion of -9.5% and the CC_{SPH} model reached a percent occlusion of 65.6%.

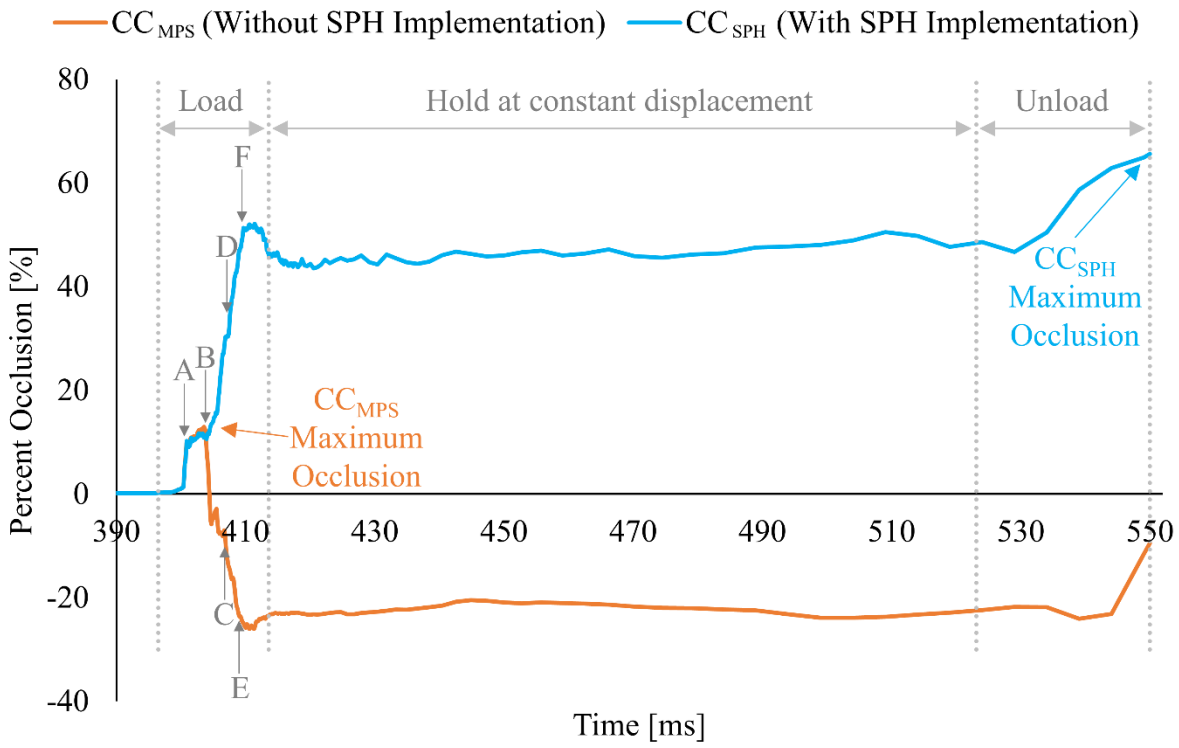


Figure 4.14: Percent occlusion of the spinal canal at the level of the C6 vertebra as a function of time in the simulation. The orange curve shows the percent occlusion of the CC_{MPS} model without the SPH implementation. The light blue curve shows the percent occlusion of the CC_{SPH} model with the SPH implementation. The light grey dotting lines indicate the beginning and ends of the loading phase, the holding phase, and the unloading phase. The letter labels correspond to the points in Figure 4.11.

The maximum occlusion of the CC_{MPS} model of 13.0% occurred at 403.6 ms and 5.4 mm of displacement. The maximum occlusion was measured during the loading phase before the sharp change in percent occlusion. After the maximum occlusion, the percent occlusion in the CC_{MPS} model decreased to a negative value as the articular pillars, laminae, and spinous process displaced away from the spinal canal space (Figure 4.15). The CC_{SPH} model reached a maximum percent occlusion of 65.6% at the end of the simulation after the unloading phase. The average maximum occlusion of the age and sex-matched experimental specimen was 69%. The percent difference of the maximum occlusions measured in the models in comparison to the experimental average was 136.7% for the CC_{MPS} model and 5.0% for the CC_{SPH} model (Figure 4.16).

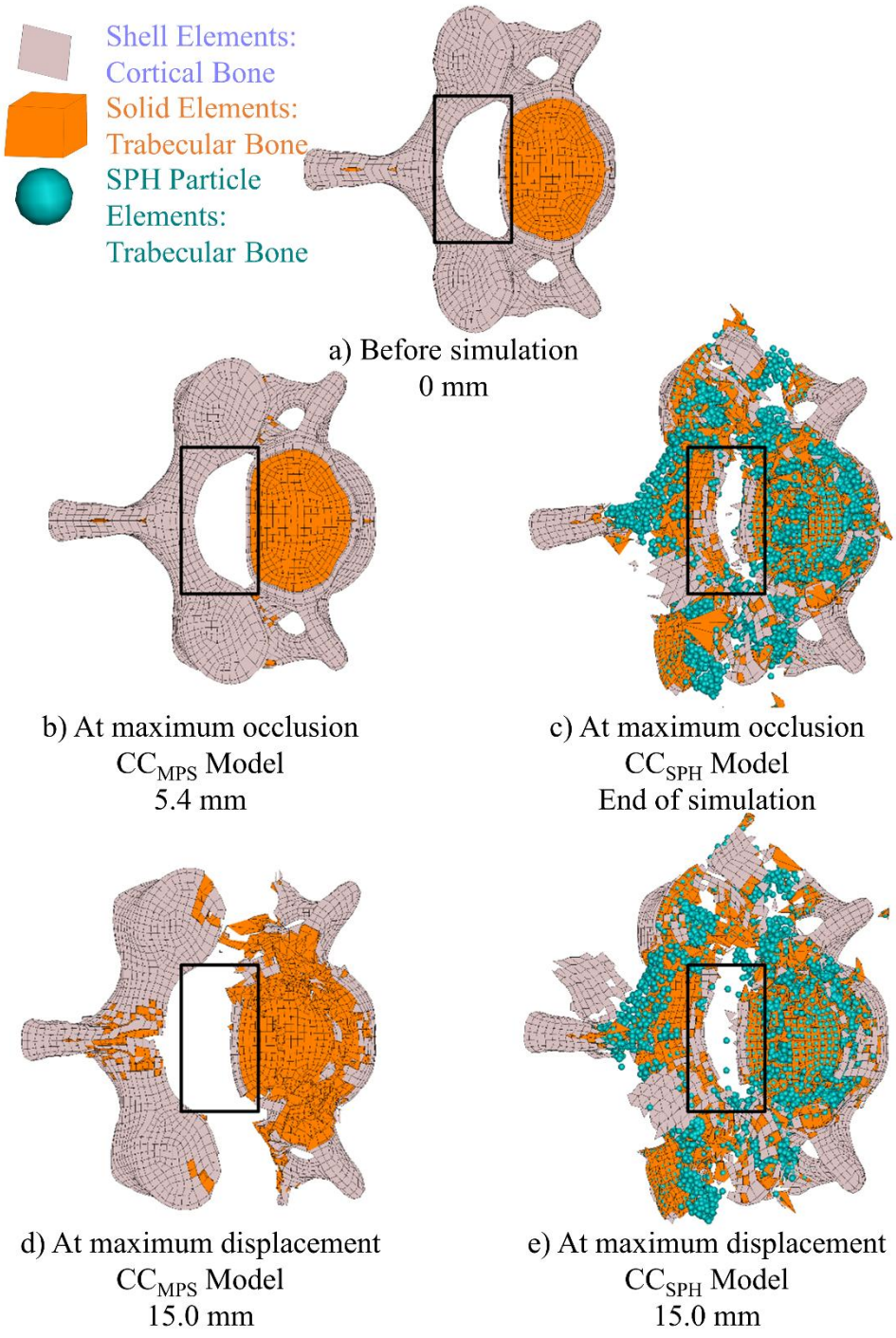


Figure 4.15: Superior views of the hard tissues of the whole C6 vertebra. The black rectangles indicate the area used to measure the percent occlusion. The orange elements represent the solid elements of the trabecular bone. The light purple elements represent the shell elements of the cortical bone. The cyan spheres indicate the SPH particle elements of the trabecular bone.

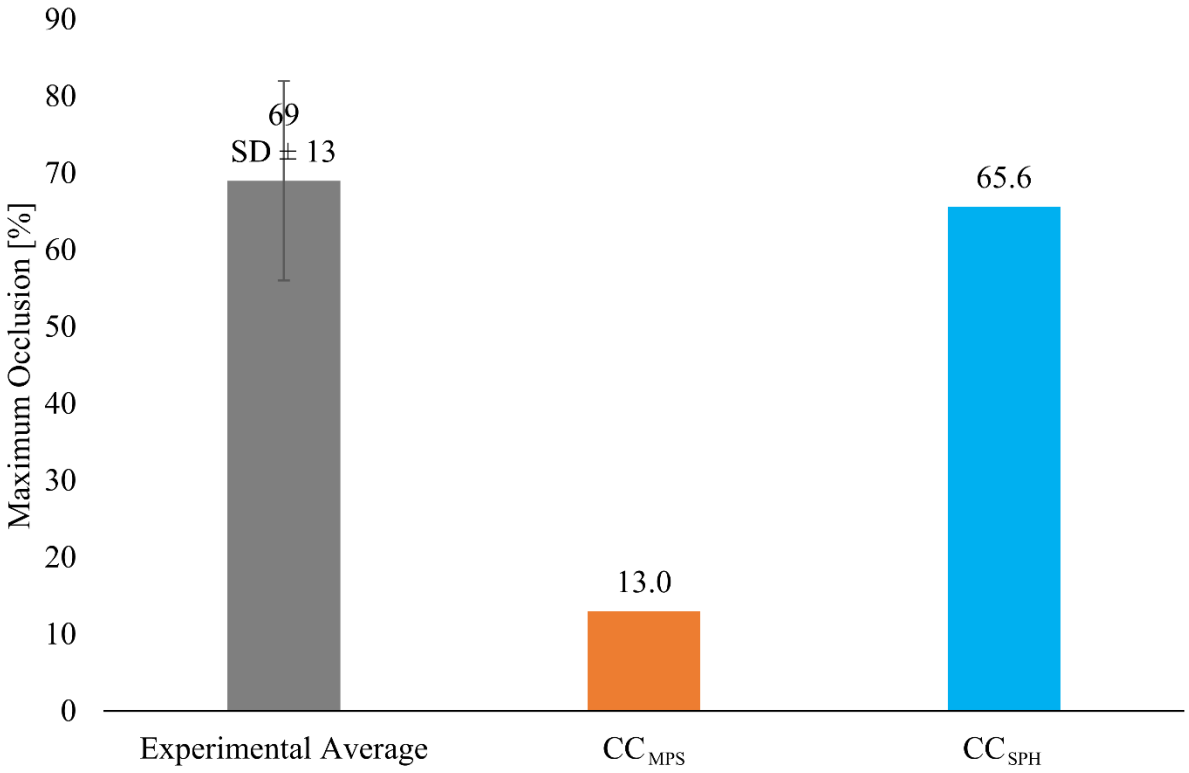


Figure 4.16: Maximum percent occlusions of the experiments and models. The maximum percent occlusion and standard deviation (SD) for the Experimental Average are for the age and sex-matched experimental specimens. The maximum percent occlusion for the CC_{MPS} model is for the model without the SPH implementation. The maximum percent occlusion for the CC_{SPH} model is for the model with the SPH implementation.

4.3 Investigation of the Effect on the Force-Displacement Response with Varied Number of SPH Particles Generated Upon Erosion

The force-displacement responses of the CC_{NQ2} model and the CC_{NQ3} model demonstrated a similar force-displacement response to the CC_{SPH} model up to 4.5 mm of displacement (Figure 4.17). Between 4.5 mm and the maximum displacement of 15.0 mm, the response of the CC_{NQ2} model continued to show a similar trend with similar forces to the CC_{SPH} model. The CC_{NQ3} model experienced numerical instabilities and, therefore, did not follow a similar force-displacement response to the CC_{SPH} model.

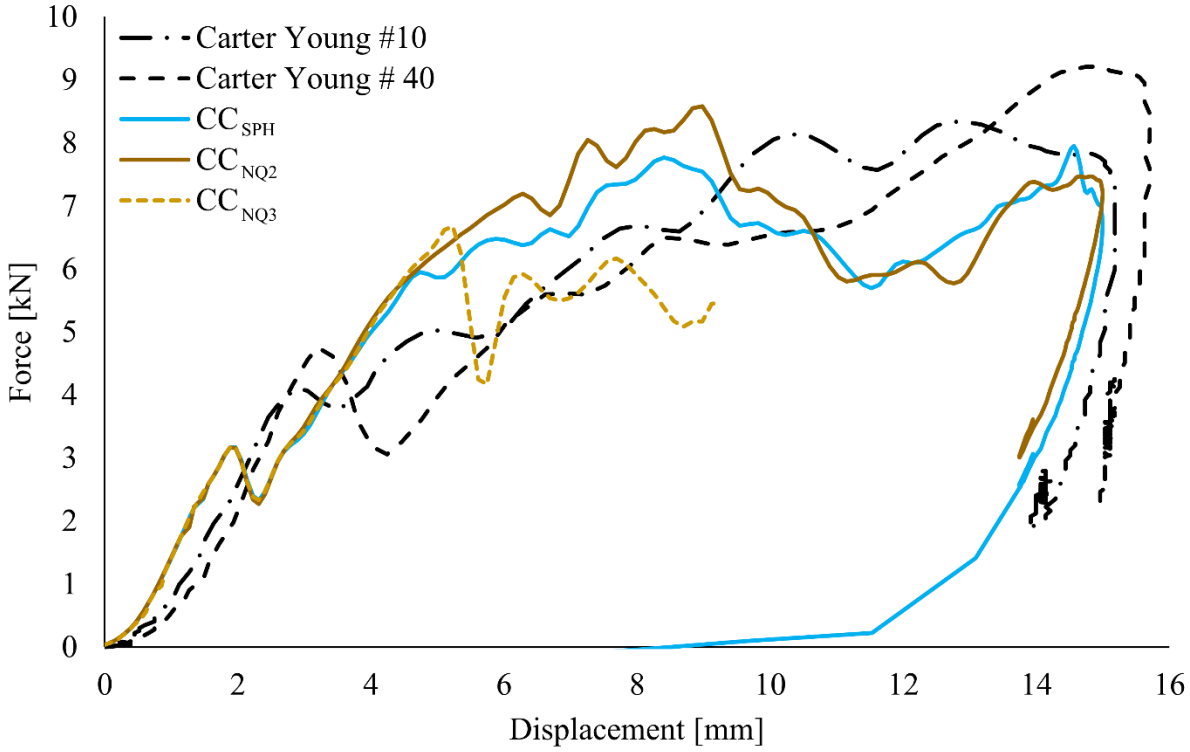


Figure 4.17: Force-displacement responses of the experiments and models. The black dashed curves indicate the force-displacement responses of the central compression age and sex-matched specimen. The light blue curve indicates the force-displacement response of the CC_{SPH} model with the SPH implementation. The brown curve and dashed brown curve indicate the responses of the CC_{NQ2} model and the CC_{NQ3} model where the number of SPH elements generated for each eroded solid element in the trabecular bone is increased.

The CC_{NQ2} model had a force-displacement response with a trend similar to the response of the CC_{SPH} model throughout loading. The CC_{NQ2} model showed a force increase between 4.5 mm and 9.0 mm, a force decrease between 9.0 mm and 11.1 mm, and a force increase from 11.1 mm to 14.0 mm of displacement.

The CC_{NQ3} model ended with an error termination at 9.3 mm of displacement. At 5.2 mm of displacement, the force of the CC_{NQ3} model showed a decrease to 4.2 kN, below the force-displacement responses of the CC_{SPH} model and CC_{NQ2} model responses. The subsequent force of the CC_{NQ3} model increased to 5.9 kN at 6.1 mm of displacement, but continued to remain below the forces of the CC_{SPH} model and the CC_{NQ2} model until the error termination at 9.3 mm of displacement.

4.4 Parametric Study: Investigating Model Response Under Varied Impact Severity, Material Parameters, and Eccentric Loading

This section includes the results from the models used to evaluate the effects of varying impact severity, using aged hard tissue material parameters, and applying eccentric boundary conditions. The effect of varying impact severity was investigated using the maximum percent occlusion in the spinal canal (section 4.4.1). The models using aged hard tissue parameters were evaluated using the force-displacement responses and maximum percent occlusion in the spinal canal (section 4.4.2). The models using eccentric boundary conditions were evaluated from measurements of the maximum percent occlusion (section 4.4.3).

4.4.1 Investigating the Effect of Varying Maximum Velocity and Maximum Displacement on Spinal Canal Occlusion

The maximum values corresponding to the experimental specimens and models with different maximum displacements and velocities are plotted in Figure 4.18.

The maximum percent occlusions of the experiments and models are plotted against the maximum displacements in Figure 4.18a. At a maximum displacement of 8.2 mm, the maximum occlusions were between 9.0% and 23.5% for the four cases with different maximum velocities. At a maximum displacement of 10.0 mm, the maximum occlusions were between 13.6% and 29.9%. At a maximum displacement of 12.6 mm, the maximum occlusions were between 10.4% and 71.5%. At a maximum displacement of 15.0 mm, the maximum occlusions were between 25.5% and 76.5%.

The maximum percent occlusions are plotted against the maximum velocities in Figure 4.18b. At a maximum velocity of 0.8 m/s, the maximum occlusions were between 9.0% and 76.5%. At a maximum velocity of 1.0 m/s, the maximum occlusions were between 11.2% and 25.5%. At a maximum velocity of 1.2 m/s, the maximum occlusions were between 10.4% and 64.0%. At a maximum velocity of 1.4 m/s, the maximum occlusions were between 13.4% and 76.2%.

The maximum occlusions reported in the experiments were between 48% and 82%.

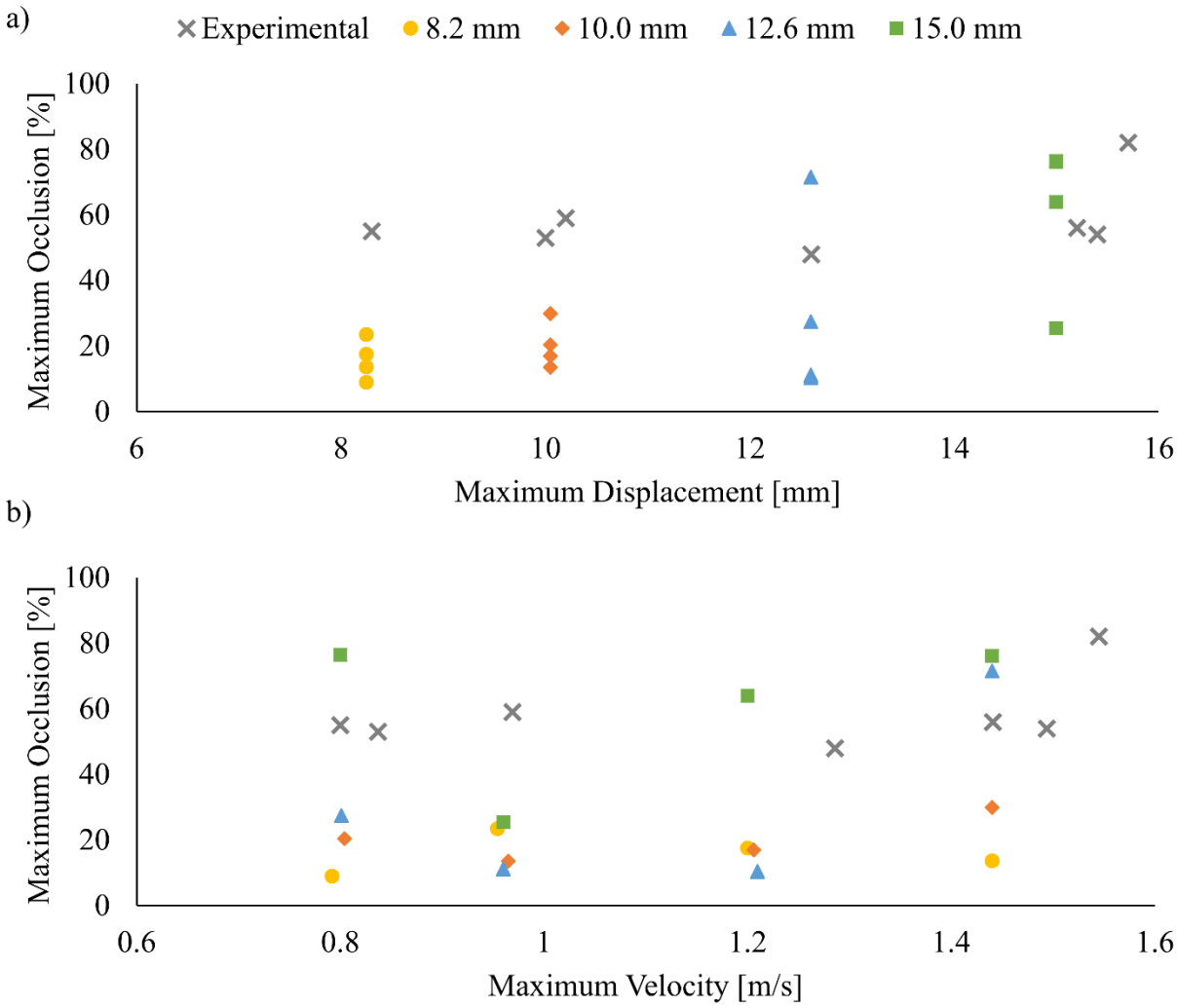


Figure 4.18: The maximum percent occlusions from the experiments and models with varying maximum displacements and maximum velocities. The maximum percent occlusion plotted as a function of (a) the maximum displacement and (b) maximum velocity.

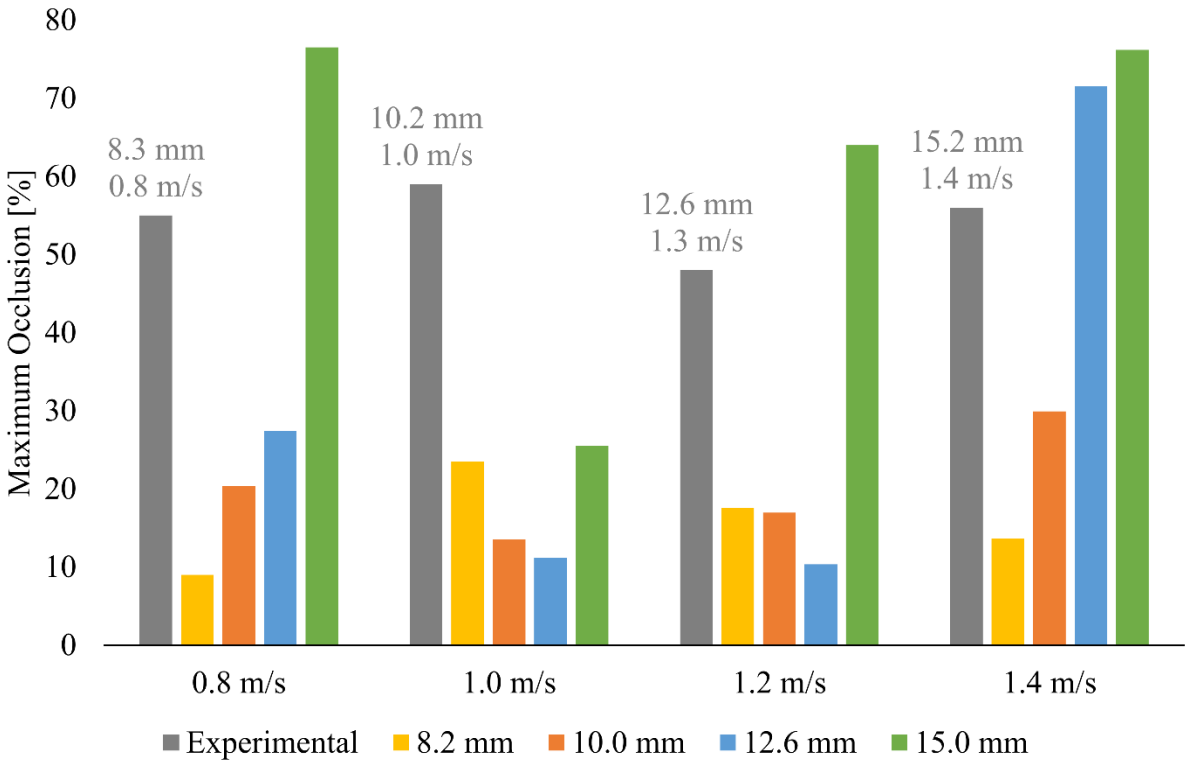


Figure 4.19: The maximum percent occlusions from the experiments and models with varying maximum displacements and maximum velocities. The grey bars indicate the maximum percent occlusions for the four experimental specimens with maximum displacement and maximum velocity combinations that most closely match a maximum displacement and maximum velocity combination in a model. The groups of bars increase in maximum velocity along the x-axis.

The maximum occlusions of four experimental cases and the four models with the closest maximum displacements and velocities are shown in Figure 4.20. The percent differences of the models in comparison with the experimental specimen for each maximum velocity and displacement group were 83.6% for the 8.2 mm and 0.8 m/s group, 77.0% for the 10.0 mm and 1.0 m/s group, 78.4% for the 12.6 mm and 1.2 m/s group, and 36.0% for the 15.0 mm and 1.4 m/s group.

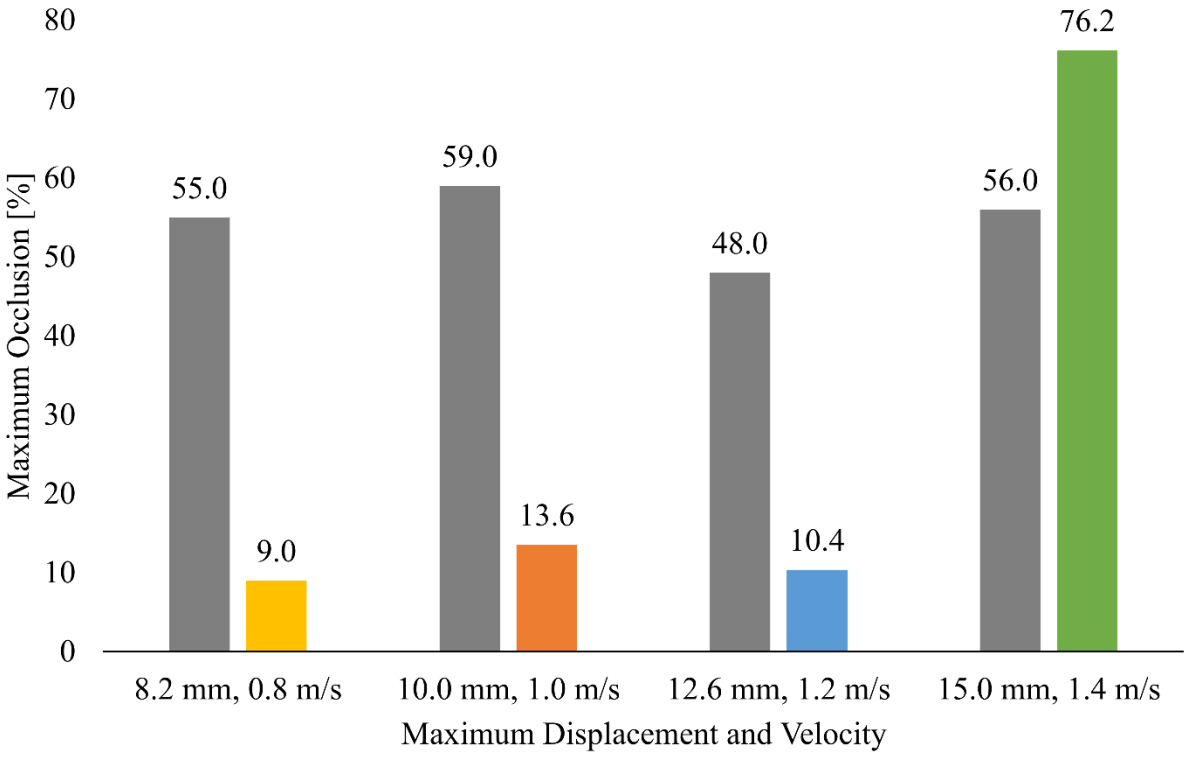


Figure 4.20: Maximum percent occlusions for the experiments and models with matching maximum displacement and maximum velocity combinations.

4.4.2 Comparison of Occlusion and Force-Displacement Response Using Aged Material Parameters for the Hard Tissues

The CC_{A08} model showed an initial stiffness region, an increase in force, and a force decrease before the unloading phase at 8.1 mm of displacement. The point of initial failure occurred at the local maximum at 2.1 kN and 1.8 mm of displacement (Point A08-1, Figure 4.21). From 1.8 mm to 2.0 mm, the force decreased to 1.7 kN as the pedicles of the C6 vertebra fractured and as the C6 vertebral body rotated (Point A08-2, Figure 4.21). From 2.0 mm to 6.0 mm of displacement, the force increased from 1.7 kN to 4.7 kN as erosion began in the C6 spinous process, the inferior C6 articular pillars, the center of the inferior C5 vertebral body, and the center of the superior C7 vertebral body (Point A08-3, Figure 4.21). The erosion in the vertebral bodies occurred as the intervertebral discs bulged directly into the C5 and C7

vertebral bodies. From 5.9 mm to 7.5 mm of displacement, the force decreased to 3.6 kN as the C5-C6 intervertebral disc pushed down into the superior-anterior edge of the C6 vertebral body (Point A08-4, Figure 4.21). As the superior-anterior edge of the C6 vertebral body eroded, the C6 vertebral body rotated. Between 7.5 mm and 8.0 mm, the force increased to 3.9 kN as erosion continued in the superior-anterior corner of C6 vertebral body (Point A08-5, Figure 4.21). At the maximum displacement of 8.1 mm, the force was 3.6 kN (Point A08-6, Figure 4.21).

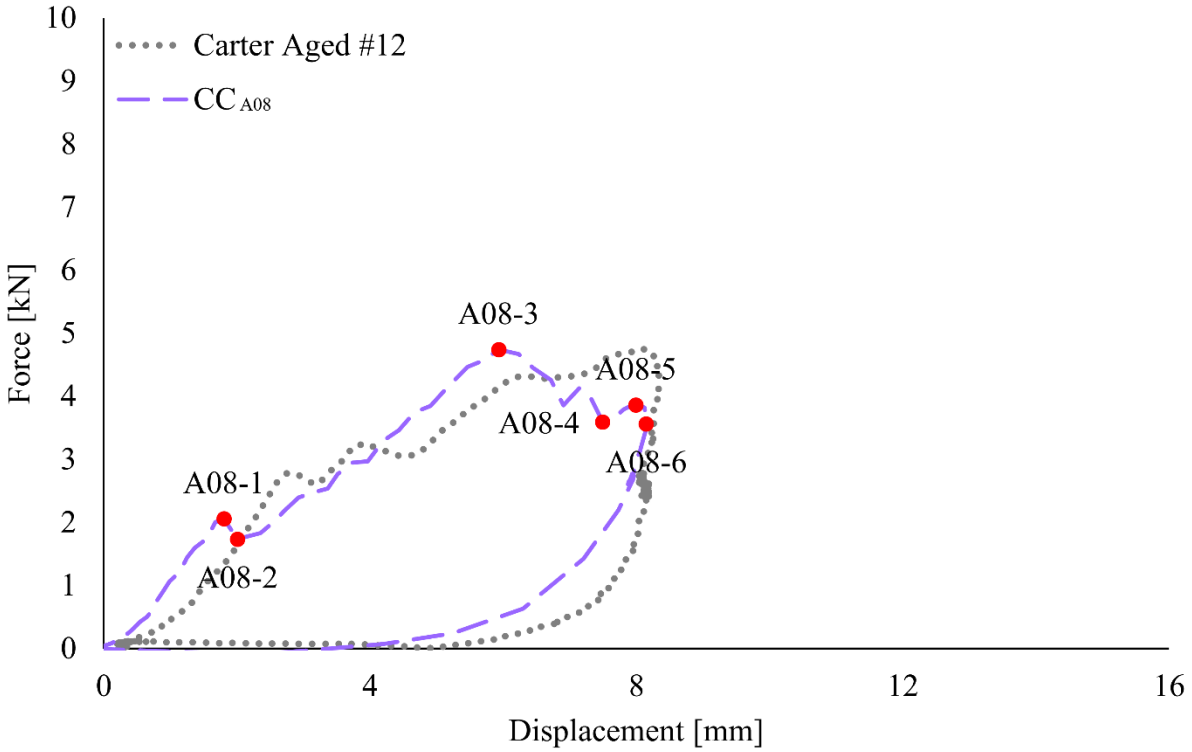


Figure 4.21: Force-displacement responses of the experimental specimen and of the CC_{A08} model. The grey dotted curve shows the experimental response (Carter, 2002). The light purple dashed curve shows the force-displacement response of the CC_{A08} model.

With a maximum displacement of 15.0 mm, the force-displacement response of the CC_{A15} model displayed an initial stiffness region, a force increase, a plateau in force, and then a decrease in force as the segment was unloaded. The force increased in the initial stiffness region as the intervertebral discs were compressed and deformed. The point of initial failure occurred at 2.0 kN at 1.8 mm of displacement as erosion began in the articular pillars of the C6 vertebra (Point A15-1, Figure 4.22). Between 1.8 mm and 2.1 mm of displacement, the force decreased to 1.7 kN as the C6 pedicles fractured and the C6 vertebral body rotated (Point A15-2, Figure 4.22). From 2.1 mm to 5.9 mm of displacement, the force increased to 4.7 kN as erosion progressed from the center of the inferior C5 vertebral body and superior C7 vertebral body (Point A15-3, Figure 4.22). The erosion in the C5 and C7 vertebral bodies was also accompanied by

the bulging of the intervertebral discs into the center of the inferior C5 vertebral body and superior C7 vertebral body. Erosion progression also occurred in the C6 articular pillars.

After 5.9 mm in the CC_{A15} model, the force plateaued until the end of the loading phase. At 7.8 mm, the force reached 4.5 kN as the C5-C6 intervertebral disc pushed into the superior-anterior edge of the C6 vertebral body, resulting in erosion in the C6 vertebral body (Point A15-4, Figure 4.22). As the segment was compressed, erosion occurred in the superior-anterior corner of the C6 vertebral body eroded. The intervertebral discs no longer pushed into the C5 or C7 vertebral body. Erosion also progressed in the inferior articular pillar and spinous process of the C6 vertebra. From 7.8 mm to 8.4 mm of displacement, the force decreased from 4.5 kN to 3.6 kN as the C6 vertebral body rotated and as material failed in the superior-anterior corner of the C6 vertebral body directly below the C5-C6 disc (Point A15-5, Figure 4.22). From 8.4 mm to 11.5 mm of displacement, the force plateaued as erosion progressed through the rest of the superior C6 vertebral body (Point A15-6, Figure 4.22). The spinous process of the C6 vertebra also fractured. From 11.5 mm to 14.7 mm of displacement, the force increased from 3.8 kN to 5.1 kN (Point A15-7, Figure 4.22). With continued compression, erosion only progressed in the C6 vertebral body. At the maximum displacement of 15.0 mm, the force was 4.6 kN (Point A15-8, Figure 4.22).

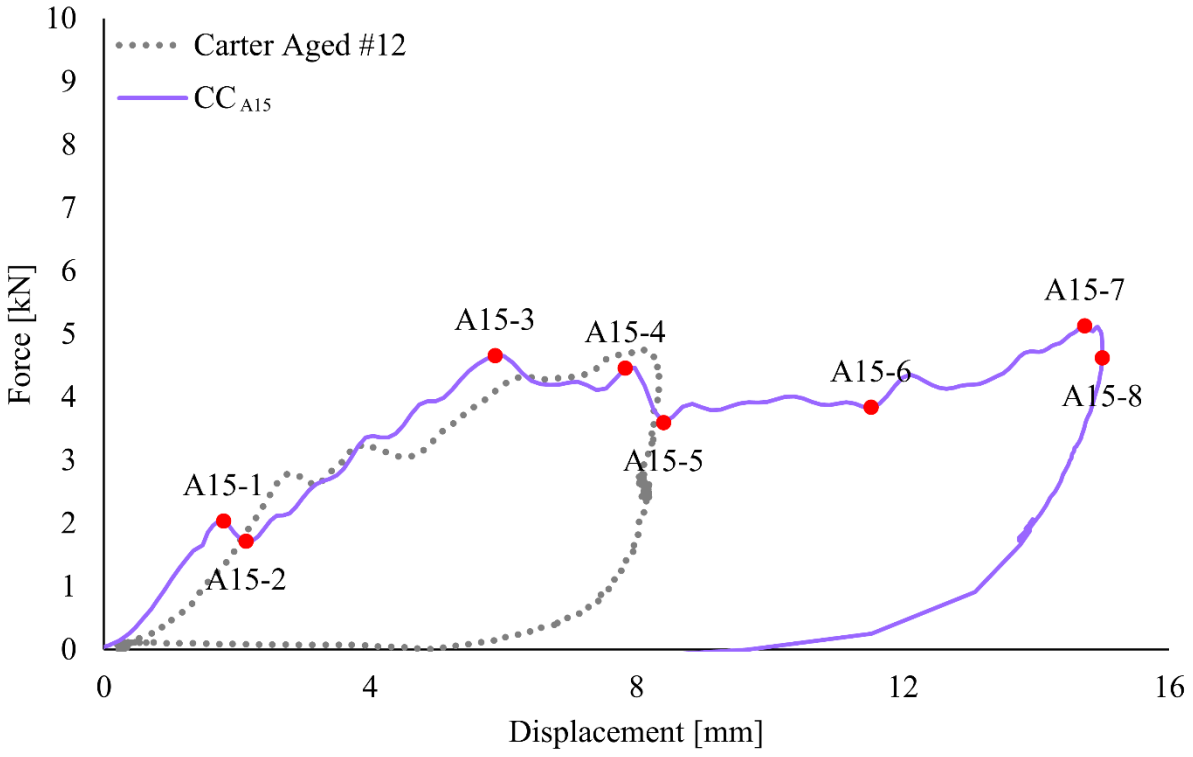


Figure 4.22: Force-displacement responses of the experimental specimen and of the CC_{A15} model. The grey dotted curve shows the experimental response (Carter, 2002). The light purple curve shows the force-displacement response of the CC_{A15} model.

The maximum occlusion in the spinal canal was 20.8% in the CC_{A08} model and 90.1% in the CC_{A15} model (Figure 4.23). The maximum occlusion of the age and sex-matched specimen was 55%. Thus, the occlusion of the CC_{A08} model was 90.1% lower than the experimental occlusion and the occlusion of the CC_{A15} model was 48.4% greater.

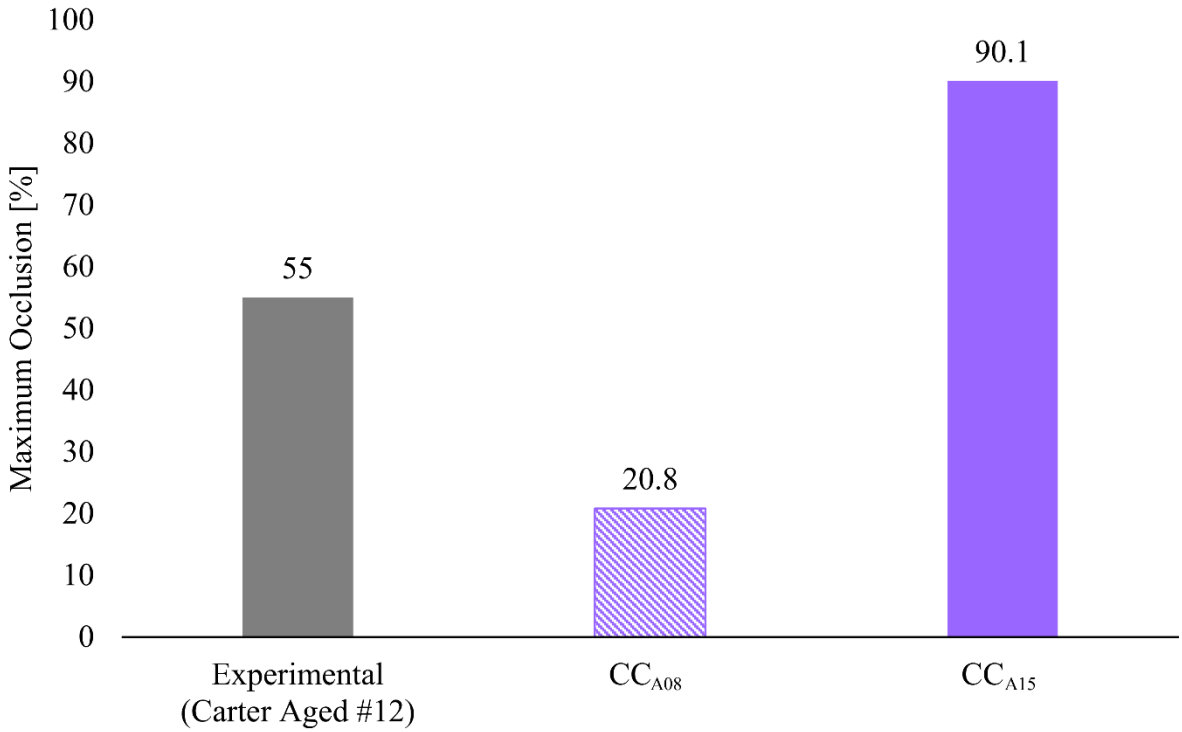


Figure 4.23: The maximum percent occlusions for the experimental and models with aged material parameters.

The maximum occlusion in the CC_{A08} model was measured at 7.9 mm in the holding phase. The maximum occlusion in the CC_{A15} model was measured at 13.9 mm in the holding phase (Figure 4.24). With widespread erosion and crushing of the C6 vertebra, hard tissue material was displaced into the spinal canal space.

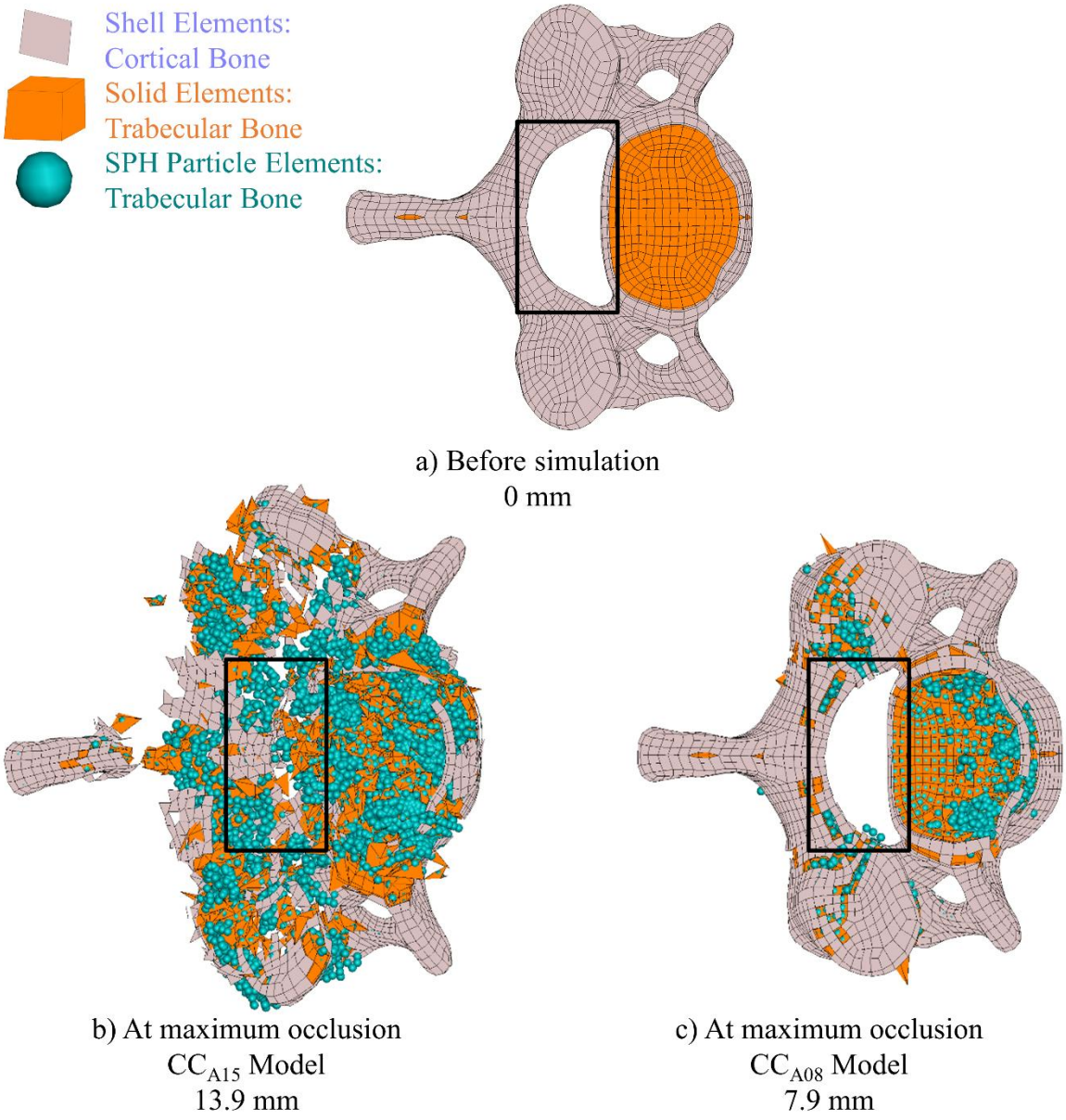


Figure 4.24: Superior views of the hard tissues of the whole C6 vertebra for the CC_{A15} model and CC_{A08} model with aged hard tissue material parameters. The black rectangles indicate the area used to measure the percent occlusion. The orange elements represent the solid elements of the trabecular bone. The light purple elements represent the shell elements of the cortical bone. The cyan spheres represent the SPH particle elements of the trabecular bone.

4.4.3 Investigating the Effect of Eccentric Boundary Conditions on Spinal Canal Occlusion

The maximum occlusions of the experiments and models for central compression, posterior eccentricity, anterior eccentricity, low lateral eccentricity, and high lateral eccentricity are shown in Figure 4.25. The maximum occlusions for the experiments are the average maximum percent occlusions across the specimens of all ages and sexes. The maximum percent occlusions measured in the model at the level of the C6 vertebra were 65.6% for the CC_{SPH} model, 47.6% in the Ant_{SPH} model, 74.8% in the Pos_{SPH} model, 40.5% in the LLt_{SPH} model, and 21.8% in the HLt_{SPH} model. The percent difference of each impact type in comparison to the experimental average was 11.1% for the CC_{SPH} model, 22.0% for the Pos_{SPH} model, 26.7% for the LLt_{SPH} model, and 21.4% for the $HLat_{SPH}$ model.

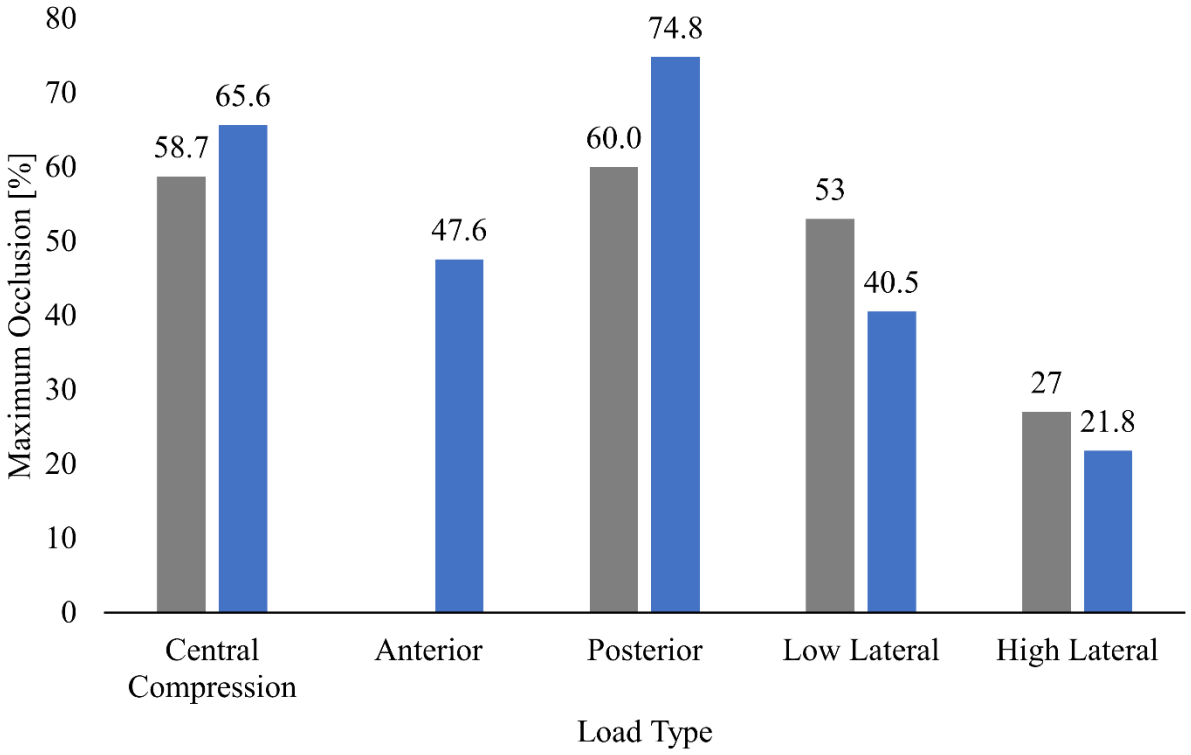


Figure 4.25: Maximum percent occlusion for the experiments and models under central compression and eccentric loading. The grey bars represent the average maximum values reported in the experiments for central compression and posterior eccentricity (Carter, 2002) and for low and high lateral eccentricity (Van Toen et al., 2014b). The blue bars represent the maximum percent occlusion from the models measured at the level of the C6 vertebra.

When maximum occlusion occurred, the occlusion of the spinal canal at the level of the C6 vertebra increased as the laminae displaced into the spinal canal space of the Ant_{SPH} model and the HLt_{SPH} model

(Figure 4.26). The displacement of the vertebral body into the spinal canal space resulted in an increase in occlusion for the Pos_{SPH} model and the LLt_{SPH} model.

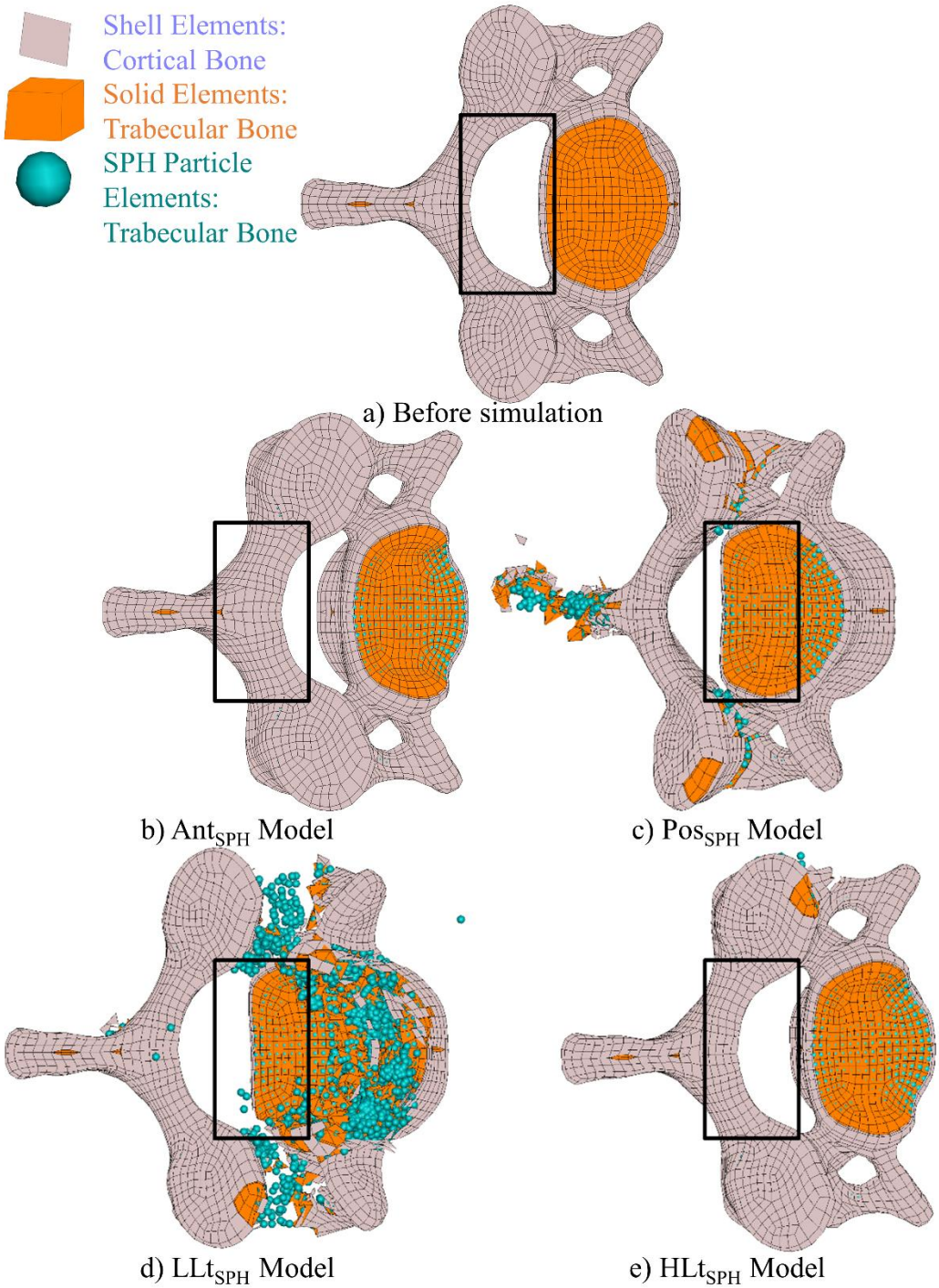


Figure 4.26: Superior views of the hard tissues of the whole C6 vertebra for eccentric loading. The black rectangles indicate the area used to measure the percent occlusion. The orange elements represent the solid elements of the trabecular bone. The light purple elements represent the shell elements of the cortical bone. The cyan spheres represent the SPH particle elements of the trabecular bone.

Chapter 5
Discussion

The aim of this study was to improve the predictive capabilities of cervical spine finite element models to predict compressive loading and fracture progression. Previous studies (DeWit and Cronin, 2012; Khor, 2018) have shown that contemporary finite element models of a functional spinal unit can predict loading prior to fracture, but the force and energy after initiation of fracture are lower than reported in experimental data. Owing to element erosion to model failure in contemporary models, material and energy were lost as failure progressed. In the current study, it was proposed to introduce SPH particle elements after element erosion to preserve material and load carrying capability for post-fracture simulation. The conversion of eroded solid Lagrangian trabecular bone elements to SPH particle elements was numerically stable and the analysis ran to completion under aggressive prescribed displacement boundary conditions. SPH is a meshless method that conserves mass and is conducive to simulating large deformations (de Vaucorbeil and Hutchinson, 2020; Liu and Liu, 2010). Converting eroded elements to SPH resulted in continued structural support and post-fracture material flow. The continued structural support with the SPH implementation was found to better represent the experimental results demonstrating continued increase in load with large-scale fracture. Furthermore, the SPH implementation allowed for modelling of material flow and occlusion during the simulation. Thus, the implementation of SPH to the central compression model provided a response that was in better agreement with the experimental force-displacement, energy, and occlusion experimental results.

The specific discussion is presented below in terms of model enhancements (section 5.1), model assessment using experiments (section 5.2) and SPH particle dependency (section 5.3), and finally the parametric study including boundary conditions, specimen age, and load eccentricity (section 5.4).

5.1 Model Enhancements to the FE Motion Segment Model: GHBMC Segment to SPH Implementation

Five models were developed with progressive enhancements, starting from the segment extracted from the GHBMC model to the segment with the implementation of SPH. The force-displacement responses were used to observe the effect of each added enhancement.

5.1.1 Plastic Kinematic Material Model for Hard Tissues: CC_{PIK} Model

The CC_{PIK} model was run using the C5-C6-C7 segment directly extracted from the GHBMC M50 model to establish a baseline force-displacement response before evaluating the subsequent progression of model enhancements. Overall, the CC_{PIK} model ran stably to the end of the simulation and predicted hard tissue

loading and fracture onset in agreement with the experimental data. However, after fracture initiation, the model underpredicted the force due to element erosion creating gaps in the model and no longer supporting load, demonstrating a limitation of traditional erosion-based failure modelling. Specifically, the CC_{PIK} model demonstrated approximately linear loading in the initial stiffness region up to point P1K1 (Figure 5.1), at which point element erosion initiated, leading to a rapid decrease in force, followed by a plateau until the end of loading. With the onset of hard tissue element erosion, widespread element failure occurred rapidly, creating empty voids in the trabecular bone of the C6 vertebral body (Figure 5.1). The visible gaps resulted in the sudden loss of structural support within the vertebral body. The plateau in force following initial widespread erosion was due to the remaining peripheral trabecular material supporting a small amount of load. The erosion within the vertebral body also created new surfaces of trabecular bone. The new surfaces were not accounted for in the contact definitions of the CC_{PIK} model. Thus, calculations were not performed during the simulation to prevent the new surfaces from interpenetrating, or passing through, other parts of the model. Together, the sudden loss of material and absence of contacts between the newly generated surfaces from erosion resulted in the low plateau in force with continued compression. The absence of contacts for new surfaces also allowed the remaining fractured pieces of trabecular bone within the C6 vertebral body to move through the cortical bone and out of the vertebra. With no contacts or material between the C5-C6 and C6-C7 intervertebral discs, further compression of the segment also pushed the intervertebral discs together.

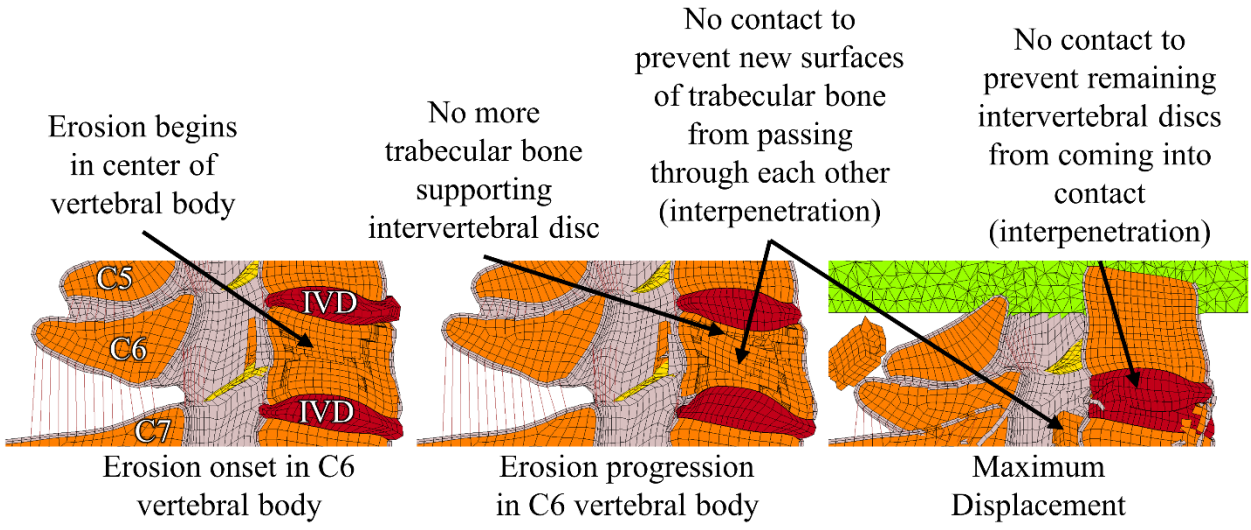


Figure 5.1: Midsagittal section view of the CC_{PIK} model showing the onset of erosion in the C6 vertebra, the abrupt loss in hard tissue material in the C6 vertebra, and the interpenetration between hard tissues and intervertebral discs.

5.1.2 Anisotropic Material Model for Hard Tissues: CC_{Ani} Model

The improved material constitutive models and parameters used for the cortical and trabecular bone in the CC_{Ani} model enabled representation of the anisotropy of bone and the mechanical characteristics of trabecular bone, improving upon the linear isotropic elastic-plastic material models used in the CC_{PlK} model. The anisotropic material models had different material properties in two orthogonal directions to better represent the way trabeculae and osteons are aligned in the bone with increased strength in the primary direction of loading. As such, the cortical and trabecular bone moduli in the transverse directions in the CC_{Ani} model were lower than in the CC_{PlK} model. Furthermore, the crushable foam constitutive model used for the trabecular bone in the CC_{Ani} model allowed the crush plateau and densification regions to be modelled. The crush plateau of the foam model allowed for more element deformation in the segment model before hard tissue failure.

The improved anisotropic material models in the CC_{Ani} model led to the lower force at the point of initial failure, a more gradual progression of element erosion, and a higher force plateau compared to the force-displacement response of the CC_{PlK} model. The anisotropic material model in the CC_{Ani} model with a lower transverse modulus and updated failure criterion allowed for more progressive failure of the hard tissue elements. At the point of initial failure, the displacement at which the first hard tissue element eroded, the hard tissue elements of the CC_{Ani} model experienced higher strains, particularly in the anterior-posterior direction in the articular pillars of the C6 vertebra. In addition, the increased element deformation in the CC_{Ani} model resulted in fracture occurring in different vertebral locations and a more gradual progression of hard tissue erosion. Although the first element to erode was in the inferior C6 articular pillar for both the CC_{PlK} model and CC_{Ani} model, subsequent fracture, denoted by widespread erosion, occurred in different locations. Element deformation, primarily in the C5 and C7 vertebral bodies, permitted the C6 vertebral body to rotate (Figure 5.2). The rotation of the C6 vertebral body led to fracture in the C6 pedicles. In contrast, the vertebrae of CC_{PlK} model did not rotate after the point of initial failure. Strain in the CC_{PlK} model was therefore concentrated in the C6 vertebral body, resulting in abrupt and widespread erosion. The sudden loss of hard tissue material, represented by widespread erosion, would not have occurred in the experimental specimens. The deformation of hard tissue elements and rotation of the C6 vertebral body in the segment of the CC_{Ani} model also allowed for gradual progression of hard tissue failure, demonstrated by the smaller force decrease after the point of initial failure compared to the CC_{PlK} model. The gradual progression of hard tissue element failure and the foam material model of the trabecular bone also resulted in the force-displacement response of the CC_{Ani} model increasing and plateauing at a higher force than in the CC_{PlK} model (Figure 5.2). Since the trabecular bone elements failed progressively in the CC_{Ani} model, more hard tissue was available to provide structural

support in the vertebral bodies during compression, leading to the higher plateau in the force-displacement response of the CC_{Ani} model. Despite the stiffer material properties of the CC_{PlK} model, the force plateaued at a lower force due to the void left in the C6 vertebral body after abrupt element erosion. Although the overall higher force of the CC_{Ani} model was in better agreement with the experimental force-displacement response than the CC_{PlK} model, the force of the CC_{Ani} model plateaued below the experimental force.

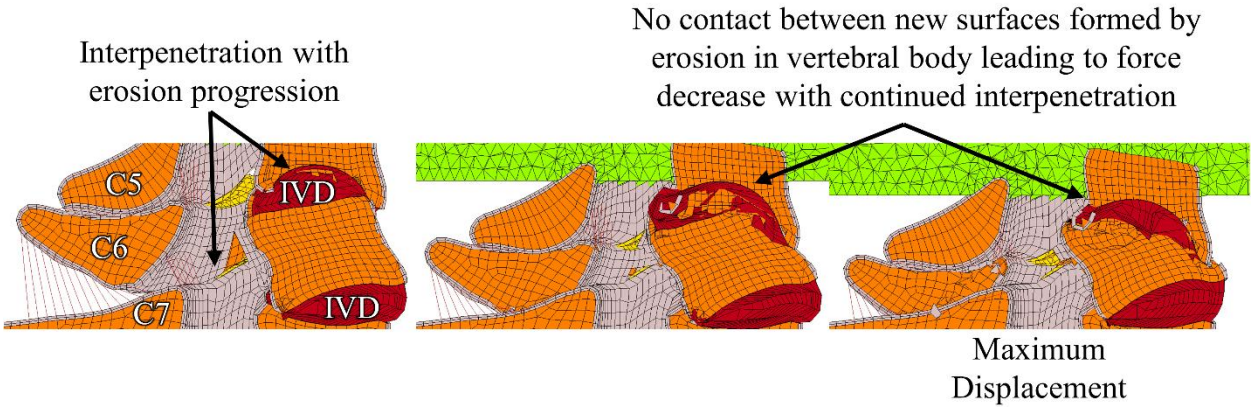


Figure 5.2: Midsagittal section view of the CC_{Ani} model showing the interpenetration at the inferior C6 articular pillar and inferior C5 vertebral body with erosion.

The contact surface definitions from the GHBMC segment in the CC_{PlK} model did not account for element erosion and allowed for interpenetration between parts as elements eroded, contributing to a loss of force in the CC_{Ani} model. As the hard tissue elements failed, particularly of the trabecular bone, new surfaces were formed in the model. The contact definitions of the CC_{Ani} model did not check for penetration at new surfaces formed due to erosion. Thus, the new surfaces were allowed to push through other parts in the model as the segment continued to be compressed (Figure 5.2). As the C5 vertebral body pushed through the C5-C6 intervertebral disc, a dip occurred in the force plateau. After the plateau, the force decreased as continued compression of the segment resulted in the C5 vertebral body penetrating into the C5-C6 intervertebral disc and the C6 vertebral body. In addition, the C6 articular pillar penetrated into the C7 articular pillar. The interpenetration between parts due to the absence of contact definitions between newly created surfaces formed after erosion led to the loss in force.

5.1.3 Added Contact Definitions to Account for Erosion and to Allow for Ligament to Intervertebral Disc Contact: CC_{Con} Model

In the CC_{Con} model, eroding contacts were defined to account for the formation of new surfaces during erosion, resulting in an increase in segment force post fracture. The effect of the new contact definitions resulted in a force increase after the point of initial failure (Figure 5.3), increasing to a plateau at a higher force than the CC_{Ani} model. The higher force in the CC_{Con} model was due to the eroding contact definitions that prevented the inferior C6 articular pillars from pushing through the C7 articular pillars with erosion in the C6 articular pillars (Figure 5.3). After the force increase, the force plateau in the CC_{Con} model did not exhibit the decrease in force shown by the CC_{Ani} model due to the eroding contact definitions preventing the interpenetration of the C5 vertebral body into the C5-C6 intervertebral disc. After the force plateau, the force of the CC_{Con} model decreased with widespread erosion and fracture propagation in the C6 vertebral body. Although the force increase in the CC_{Con} model was not sustained as failure progressed, the decrease in force corresponded to the loss of hard tissue material and structural support in the vertebral bodies instead of interpenetration between elements. However, a consequence of including eroding contacts was that the compute time increased by approximately 1.5 times compared to the CC_{Ani} model.

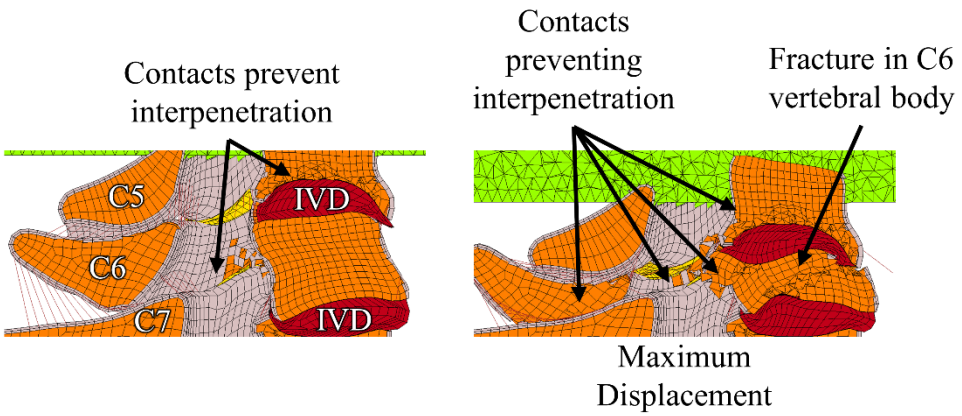


Figure 5.3: Midsagittal section view of the CC_{Con} model showing the contacts preventing interpenetration at the inferior C6 articular pillar and inferior C5 vertebral body.

Owing to penetrations between the ligaments and intervertebral disks, a contact was added between the ALL and PLL and the intervertebral discs, but it did not have a substantial effect on preventing the discs from displacing past the ligaments. This outcome was attributed to existing initial penetration between the ligament tension-only elements and the shell and solid elements of the intervertebral disc. Thus, additional penetration of the vertebral bodies and intervertebral discs past the ligaments was not prevented due to the nature of the contact formulation in LS-DYNA, and the added contact was expected to have

minimal affect. The displacement of the intervertebral disc past the ligaments was particularly noticeable at the ALL. In the future, alternate definitions of the ligaments (i.e. using shell elements) should be considered.

5.1.4 Addition of Minimum Principal Strain to Erosion Criterion to Trabecular Bone: CC_{MPS} Model

A minimum principal strain criterion was included to support the subsequent implementation of SPH discussed in the following section (section 5.1.5). Prior to the implementation of SPH, the CC_{MPS} model with the addition of a minimum principal strain to the erosion criterion of the anisotropic material model for the trabecular bone did not result in a substantial change in force-displacement response. Overall, the force-displacement response showed a similar trend to the response of the CC_{Con} model. The CC_{MPS} model and CC_{Con} model had the same point of initial failure and force increase up to the force plateau and had similar fracture patterns (Figure 5.4). Additionally, in the CC_{Con} model with only a maximum principal strain criterion, 0.28% of the trabecular bone elements, representing 57 solid elements, reached or exceeded a minimum principal strain of 0.9. Thus, the small percentage of additional trabecular elements expected to fail with the modified criterion was expected to have minimal effect on the force-displacement response.

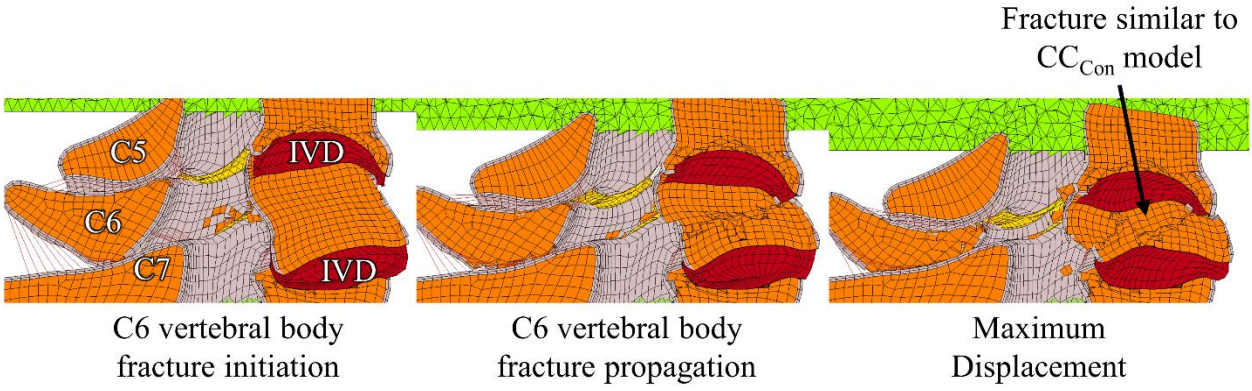


Figure 5.4: Midsagittal section view of the CC_{MPS} model showing the fracture initiation and propagation in the C6 vertebral body.

5.1.5 Implementation of SPH for Trabecular Bone: CC_{SPH} Model

The implementation of SPH in the CC_{SPH} model was intended to represent the comminuted bone material and provide structural support to the segment following element erosion, resulting in the overall increase in force throughout loading in the force-displacement response (Figure 5.5). The initial stiffness region up to the point of first element erosion was similar to the responses of the CC_{Ani}, CC_{Con}, and CC_{MPS} models.

However, while the previous models showed a decrease or plateau in force with erosion progression in the articular pillars and vertebral bodies, the CC_{SPH} model showed an overall force increase, with force values consistently higher than the CC_{Ani}, CC_{Con}, and CC_{MPS} models until the end of loading, attributed to the representation of the comminuted material. The higher force of the CC_{SPH} model was due to the activation of SPH particle elements in the articular pillars and vertebral bodies (Figure 5.5) due to erosion of solid Lagrangian trabecular bone elements. The response of the CC_{SPH} model in comparison to the CC_{MPS} model and the experimental responses is further discussed in section 5.2.1. The implementation of SPH also approximately doubled the compute time compared to the CC_{MPS} model.

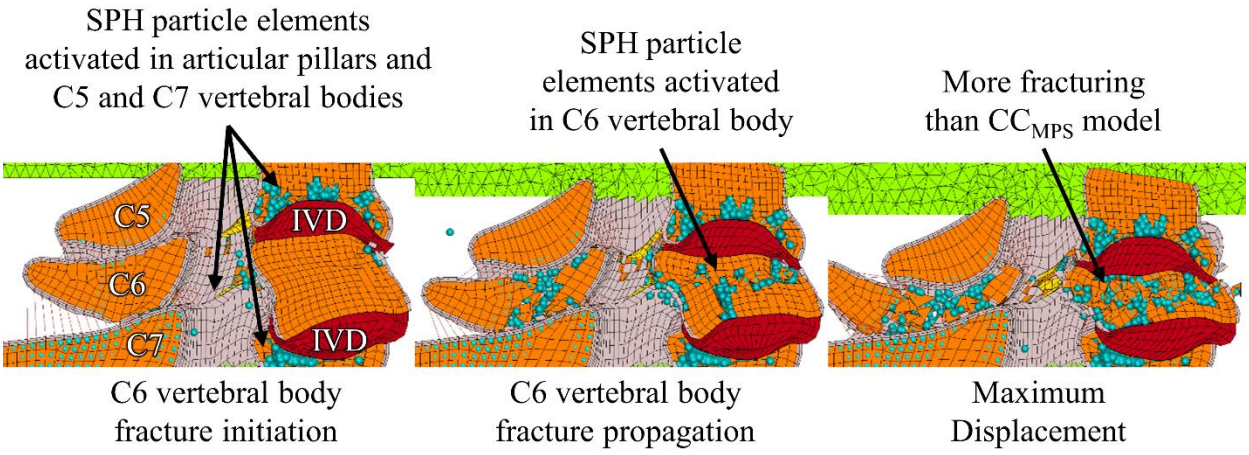


Figure 5.5: Midsagittal section view of the CC_{SPH} model showing the fracture initiation and propagation in the C6 vertebral body.

5.2 Evaluation of the SPH Implementation in the CC_{SPH} Model Against Experimental Targets

To evaluate the implementation of SPH in the trabecular bone, the CC_{SPH} model with the SPH implementation was compared to the CC_{MPS} model without the SPH implementation. The CC_{SPH} model and the CC_{MPS} model were evaluated using the force-displacement response, reported hard tissue damage, and the occlusion measured from the experiment.

5.2.1 Force-Displacement Response

The overall increase in force of the CC_{SPH} model was in better agreement with the trend of the experimental force-displacement responses compared to the CC_{MPS} model.

The force-displacement responses of the CC_{MPS} model and the CC_{SPH} model were similar prior to widespread erosion in the hard tissues of the segment. The CC_{MPS} model and CC_{SPH} model had the same initial stiffness region leading to the same point of initial failure at 3.2 kN and 2.0 mm of displacement in

compression, as expected and confirming that the SPH did not affect response prior to element erosion. The force and displacement where the first element eroded were the same in both the CC_{MPS} model and the CC_{SPH} model since the models would be the same before the activation of SPH particle elements. After the point of initial failure, the force-displacement responses of the CC_{MPS} model and the CC_{SPH} model remained similar since the location of erosion had minimal influence on the load bearing regions of the segment. A force decrease was observed as fracture in the pedicles of the C6 vertebra allowed the C6 vertebral body to rotate. The rotation of the C6 vertebral body observed in the model was enabled by fracture in the pedicles allowing the vertebral body to displace away from the rest of the vertebra, and due to fracture in the C5 and C7 vertebral bodies allowing the intervertebral discs to uncompress in the intervertebral joints. The erosion and deformation in the C5 and C7 vertebral bodies provided more space for the intervertebral discs to deform, subsequently allowing the superior face of the C6 vertebral body to displace posteriorly and the inferior face of the C6 vertebral body to displace anteriorly. The amount of rotation seen in the C6 vertebral body in the CC_{MPS} model and the CC_{SPH} model may be more than the experimental specimens would have shown due to the lack of constraints from tissues surrounding the vertebral column. For example, an ALL with a three-dimensional structure may contribute to providing resistance against the rotation in the vertebral body. The beam elements representing the ALL in the model may not have provided the same amount of resistance or containment as a three-dimensional structure. After vertebral body rotation, the force-displacement responses increased with element deformation in the intervertebral discs and in the C5 and C7 vertebral bodies. The trend of the force increasing after the first local maxima, the point where hard tissue failure initiates in the model, agreed with the trend in the experimental responses; however, the force in the CC_{MPS} model and CC_{SPH} model increased above the force of the experimental responses. The differences between the initial stiffness region, point of initial failure, and subsequent force increase in the model and experimental responses may be attributed to factors such as the different compliances in the loading apparatus, potting, and segment as well as different initial segment positions.

After 5.2 mm of displacement in compression, the force-displacement responses of the CC_{MPS} model and the CC_{SPH} model began to diverge with the onset of erosion in the load bearing regions of the inferior C5 vertebral body, the superior C7 vertebral body, and the inferior C6 articular pillars. In the CC_{MPS} model, erosion signified a loss of hard tissue material as the force plateaued, whereas erosion in the CC_{SPH} model corresponded to activation of SPH particle elements to preserve hard tissue material, allowing the force to increase. Thus, the higher force-displacement response of the CC_{SPH} model in comparison to the CC_{MPS} model illustrated the structural support provided by preserving hard tissue material rather than removing elements in the articular pillars and vertebral bodies. As elements eroded, the force-displacement response

of the CC_{MPS} model decreased below the experimental responses, while the response of the CC_{SPH} model increased above the experimental responses.

The force-displacement responses of the CC_{MPS} model and the CC_{SPH} model further diverged with fracture progression in the C6 vertebral bodies. During fracture propagation of the CC_{MPS} model (Figure 4.11, Point C to Point E), erosion of the solid trabecular bone elements in the C6 vertebral body led to a decrease in force. In contrast, the CC_{SPH} model showed an overall force increase from the onset of fracture in the C6 vertebral body until the end of loading. Although the force decreased with initial fracture in the C6 vertebral body and spinous process in the CC_{SPH} model, the force-displacement response showed an overall increase in force with continued compression and crushing of the fractured material. The overall increase in force throughout loading of the CC_{SPH} model was in agreement with the trend of the experimental force-displacement responses.

The difference between the CC_{MPS} model and the CC_{SPH} model can be demonstrated by the energy, calculated as the area under the force-displacement response (Figure 5.6). Before the onset of erosion in the C5 and C7 vertebral bodies (Figure 4.11, up to Point B), the energy of the CC_{MPS} model was 17.6 J and the energy of the CC_{SPH} model was 17.8 J, representing a percent difference of 0.9%. The energy associated with the CC_{MPS} model and the CC_{SPH} model were similar up to this point since erosion was not yet widespread. Before the initialization and propagation of fracture in the C6 vertebral body, the energy of the CC_{MPS} model was 41.2 J and the energy of the CC_{SPH} model was 48.0 J, representing a percent difference of 15.2%. The difference in energy up to this point was primarily attributed to erosion in the C5 and C7 vertebral bodies, where 6.1% of the solid trabecular elements in the C5 and C7 vertebrae eroded in the CC_{MPS} model. At the maximum displacement, the energy of the CC_{MPS} model was 61.3 J and the energy of the CC_{SPH} model was 83.1 J, representing a percent difference of 30.3%. The difference in energy at the maximum displacement was primarily attributed to element erosion representing fracture propagation in the C6 vertebral body, with 30.1% of the solid trabecular elements in the C6 vertebra eroding in the CC_{MPS} model.

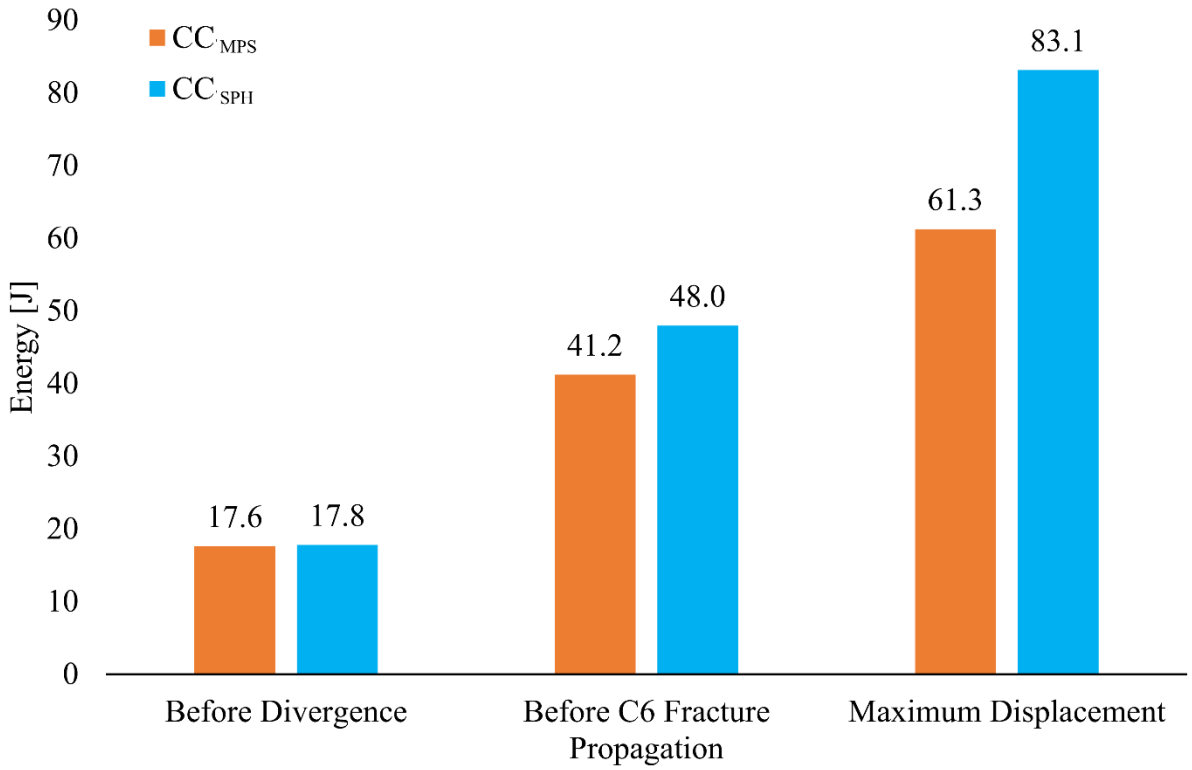


Figure 5.6: Energy from the force-displacement responses of the CC_{MPS} model and the CC_{SPH} model calculated before divergence (between 0.0 mm and 5.2 mm), before C6 fracture propagation (between 0.0 mm and 9.3 mm), at maximum displacement (between 0.0 mm and 15.0 mm).

At the maximum displacement, the average energy from the two age and sex-matched experimental specimens was 86.4 J (Figure 5.7). The percent difference between the CC_{MPS} model and the CC_{SPH} model compared to the average energy of the experimental responses was 34.1% and 3.9%, respectively. The structural support provided by the SPH implementation in the CC_{SPH} model resulted in an overall increasing force-displacement response that was in better agreement with the experimental force-displacement responses.

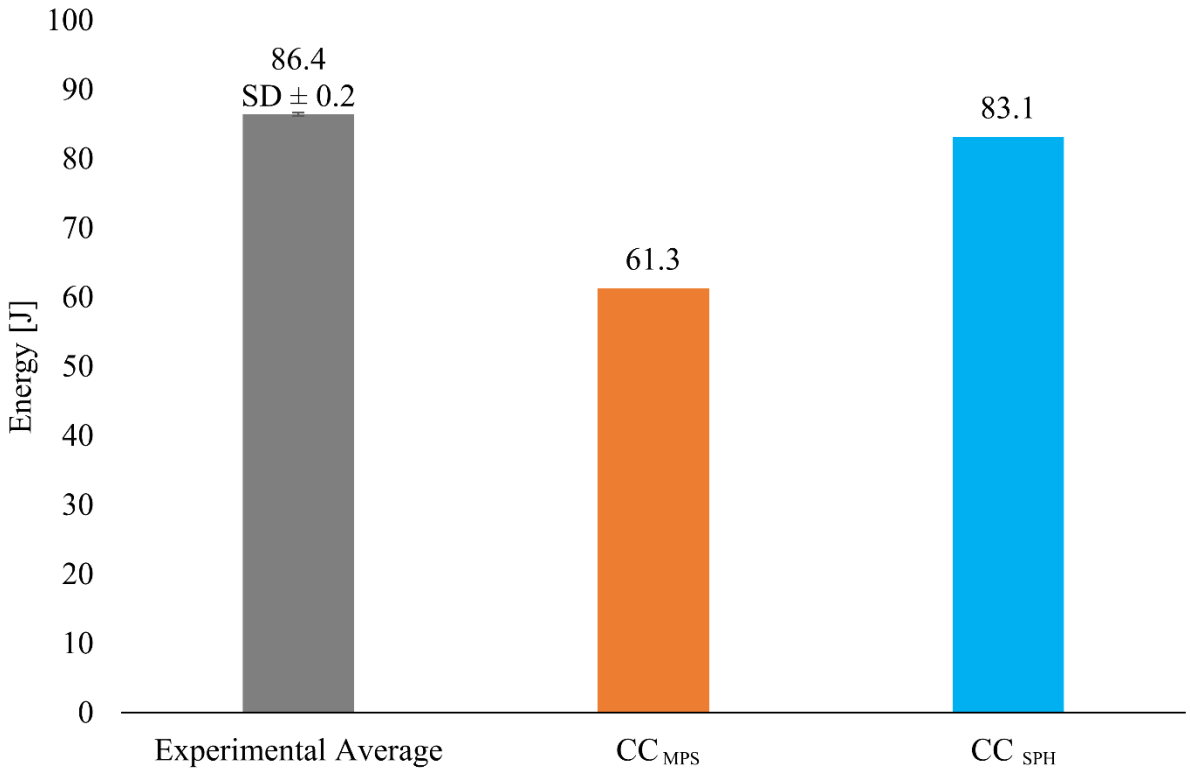


Figure 5.7: Energy from the force-displacement responses of the experiments and models calculated between 0.0 mm and 15.0 mm. The experimental average and corresponding standard deviation (SD) are from the age and sex-matched experimental specimen showing improved correspondence between the CC_{SPH} model and experiment.

The comparison of energy between the CC_{MPS} model and the CC_{SPH} model illustrated the importance of the SPH implementation in providing structural support as the vertebrae fractured during compression. The vertebral structures in the model that contributed the most to supporting load in the segment were the vertebral bodies. Thus, as erosion became more widespread in the vertebral bodies, more hard tissue material was lost in the load bearing regions of the segment in the CC_{MPS} model. As material was lost in the CC_{MPS} model, the force in the CC_{SPH} model correspondingly increased and diverged from the CC_{MPS} model. The increase in force of the CC_{SPH} model over the CC_{MPS} model grew as fracture became more widespread in the vertebral bodies, illustrating the importance of SPH in providing the structural support lost due to element erosion during compression.

5.2.2 Hard Tissue Failures Predicted in FE Model Compared to Reported Tissue Damage from Experiments

Damage in the FE model was determined based on the presence of eroded elements in each vertebral structure. While this method of evaluation may not be equivalent to the experimental method of evaluating injury based on macroscopic tissue damage, it provided an objective way to evaluate whether a structure was considered injured in the model.

Based on the damage observed across all eight experimental specimens undergoing central compression loading, it was expected that hard tissue damage should be present in the vertebral bodies. It was also expected that hard tissue damage could occur in the right pedicle, articular pillars, and right lamina as three of the eight experimental specimens were reported to have damage in these structures. Hard tissue damage in the left pedicle, left lamina, and spinous process occurred less often.

Using an evaluation method for the models by determining hard tissue damage based on the presence of erosion, damage was determined to be present in all structures for both the CC_{MPS} model and the CC_{SPH} model. Since damage occurred in all structures of the models, the model results differed from the expected injury locations based on experimental results.

Furthermore, the CC_{SPH} model showed more widespread erosion compared to the CC_{MPS} model. In the CC_{SPH} model, erosion was widespread throughout the vertebral body, pedicles, articular pillars, and laminae. In the CC_{MPS} model, there was less hard tissue injury, denoted by the erosion pattern, in the posterior structures of the C6 vertebra. The posterior articular pillars and laminae did not have as much hard tissue damage compared to the CC_{SPH} model since the articular pillars, laminae, and spinous process of the CC_{MPS} model were displaced in the posterior direction during compression. Since the articular pillars, laminae, and spinous process of the CC_{SPH} model were not displaced posteriorly, these structures were crushed during compression leading to more hard tissue damage. In addition, the implementation of SPH to preserve material in the segment of the CC_{SPH} model also led to more material needing to fit in the same space. At maximum displacement, 30.1% of the solid trabecular elements had eroded in the C6 vertebra of the CC_{MPS} model. In comparison, 55.6% of the solid trabecular elements had eroded in the C6 vertebra of the CC_{SPH} model. More elements reached the failure strain thresholds in the CC_{SPH} model due to the material preserved in the segment. Thus, when the segment was compressed to the same displacement, there was more hard tissue material in the CC_{SPH} model that needed to fit in the same space, resulting in the elements experiencing higher strains in the CC_{SPH} model and, correspondingly, more element failure.

One of the differences between the hard tissue damage patterns in the models and experiments was that the erosion patterns in both the CC_{MPS} model and the CC_{SPH} model were symmetric, whereas the reported experimental injury patterns suggested asymmetry in injury locations. The more symmetric result from the models was expected since the geometry and properties of the segment model were symmetric. Likewise, asymmetry in the injury of the experimental specimens would also be expected as real specimens would not be perfectly symmetric. Thus, for example, while the right pedicle and right lamina were more likely to be injured than the left pedicle and left lamina based on the experimental results, the model would be unlikely to predict different injuries in the right and left sides of the specimen.

The higher compliance between the potting and segment in the experimental set-up may have also contributed to fewer injured locations in the hard tissue of the experimental specimens. During compression in the experimental tests, the vertebra may have been allowed to rotate or displace more, resulting in less hard tissue injury at the same displacement.

5.2.3 Spinal Canal Occlusion

The implementation of SPH to preserve fractured hard tissue material allowed for modelling the flow of comminuted or fractured material into the spinal canal. The increase of material occluding the spinal canal under compression agreed with experimental tests where compression of vertebral segments was reported to produce occlusion of the spinal canal. Without the SPH implementation in the CC_{MPS} model, the fractured material displaced away from the spinal canal, leading the measured percent occlusion to decrease, contrary to the experimental data. With the SPH implementation in the CC_{SPH} model, fractured material was pushed into the spinal canal, resulting in the increase in measured percent occlusion, increasing with compression displacement as noted in the experiments.

Without the SPH implementation in the CC_{MPS} model, a loss of structural support in the articular pillars allowed the spinous process to displace away from the spinal canal space, leading to a decrease in the measured percent occlusion. The initial decrease in occlusion in the CC_{MPS} model corresponded to the start of erosion progression in the inferior C6 articular pillars. The load between articular pillars was transferred through the contact points between the inferior C5 to superior C6 facet joint cartilages and the inferior C6 and superior C7 facet joint cartilages. The erosion and corresponding loss of trabecular bone material in the C6 articular pillars affected the load path between facet joint cartilages. As the segment was compressed, the loss of articular pillar material resulted in the articular pillars of the C6 vertebra being pushed in the posterior direction. Consequently, the laminae and spinous process of the C6 vertebra were also displaced in the posterior direction away from the spinal canal. The posterior motion of the

articular pillars, laminae, and spinous process lead the occlusion of the CC_{MPS} model to decrease to negative values of measured percent occlusion.

In contrast, the SPH implementation meant the activated SPH particle elements in the C6 vertebra of the CC_{SPH} model were able to provide structural support during widespread fracture in the articular pillars. Hard tissue material was, therefore, preserved in the articular pillars during fracture. As the segment was compressed, the articular pillars of the CC_{SPH} model were instead displaced downward. The spinous process in the CC_{SPH} model was displaced 5.5 mm closer to the spinal canal space compared to the CC_{MPS} model.

In the CC_{MPS} model and the CC_{SPH} model, the superior half of the C6 vertebral body was pushed into the spinal canal space, contributing to an increase in the percent occlusion. As the segment was compressed, the C6 vertebral body rotated before undergoing fracture initiation and propagation. The initial rotation and subsequent fracture of the C6 vertebral body resulted in material occluding the spinal canal space. Once the vertebral body fractured, bone fragments, represented by the SPH particle elements, were allowed to displace into the spinal canal. Thus, the implementation of SPH allowed for simulating the movement of bone fragments. The maximum occlusion of the CC_{SPH} model was 5% percent different from the experimental average of the age and sex-matches specimen, in better agreement compared to the CC_{MPS} model with a 137% difference from the experimental average.

Although the percent occlusion of the CC_{SPH} model was similar to the experimental occlusion, there were some limitations to the method of measuring occlusion in the model. In the experiments, the tubing of the SCOT used to measure occlusion provided a measure of the impingement into the space within the spinal canal. In the model, the occlusion was evaluated within a two-dimensional rectangle enclosing the entire spinal canal space. Thus, the occlusion was based on the change in a selected area containing the spinal canal. Furthermore, the initial rectangular area of interest used for the model evaluation initially contained hard tissue material. The size of the area of interest in the model and the fact that the area of interest initially contained hard tissue material resulted in a measurement more sensitive to the displacement of hard tissue material away from the area of interest. In the experiments, the displacement of the spinous process away from the tubing of the SCOT would not affect the measured occlusion since the SCOT would only measure the impingement of tissues onto the tubing. As demonstrated with the CC_{MPS} model, the displacement of the spinous process away from the spinal canal space in the model evaluation resulted in a decrease in percent occlusion to a negative value, indicating a widening of the spinal canal space.

5.3 Investigation of the Effect on the Force-Displacement Response with Varied Number of SPH Particles Generated Upon Erosion

When a Lagrangian element was eroded, it could be converted to a single or multiple SPH particles. A first investigation quantified the effect of increasing the number of SPH particles from 1 (CC_{SPH}) to 8 (CC_{NQ2}). The force-displacement response of the CC_{SPH} model and the CC_{NQ2} model were similar, demonstrating good agreement in the model response when one solid trabecular bone element was converted to one or to eight SPH particle elements (Figure 5.8).

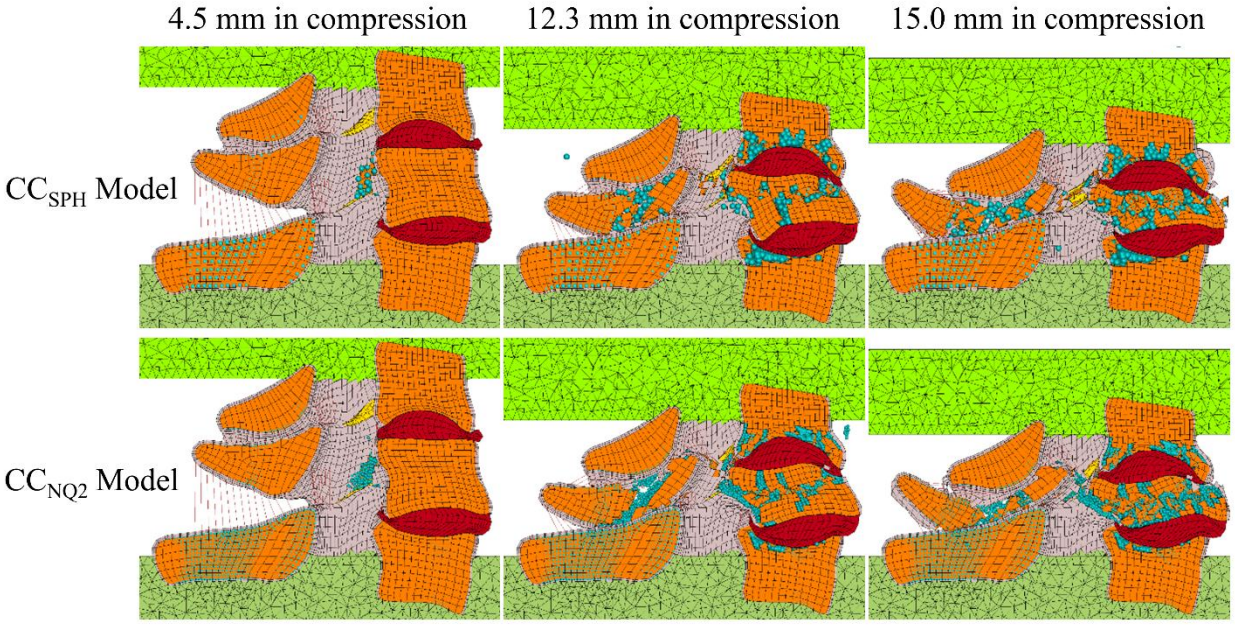


Figure 5.8: Midsagittal section plane views of the CC_{SPH} model and the CC_{NQ2} model. The models show similar fracture patterns with fracture at the pedicles at 4.5 mm, fracture propagation at 12.3 mm, and crushing of hard tissue material at the maximum displacement of 15.0 mm.

Increasing to the CC_{NQ3} model, 27 particles were generated for each eroded Lagrangian element. The force-displacement response of the CC_{NQ3} model was numerically unstable with a decrease in force after 5.2 mm of displacement and an error termination at 9.3 mm of displacement. The decrease in the force of the CC_{NQ3} model corresponded to the onset of fracture in the C6 vertebral body of the CC_{NQ3} model. The higher concentration of SPH particles in the CC_{NQ3} model resulted in a lower calculated area of influence for each particle. The increased number of SPH particles, resulting in a smaller area of influence around each particle, allowed the activated SPH particle elements to be compressed more closely into gaps in the segment and to escape the segment. The escaped SPH particles no longer influenced the subsequent fracture and no longer carried load during compression. Additionally, with the increased number of SPH particle elements generated for each solid element, the direction of fracture (erosion) of solid elements

appeared to more closely follow the vertical direction of the solid element mesh. The direction of eroded solid elements progressing vertically first occurred in the inferior C5 vertebral body, leading to less overall fracture in the C5 vertebral body and consequently earlier rotation of the C6 vertebral body. The earlier rotation of the C6 vertebral body then led to earlier fracture propagation in the C6 vertebral body where vertical erosion progression along the mesh of the solid trabecular elements was seen again. The numerical instability with the higher number of generated SPH particle elements in the CC_{NQ3} suggested a need for compatibility between the SPH size and the solid element size (Figure 5.9).

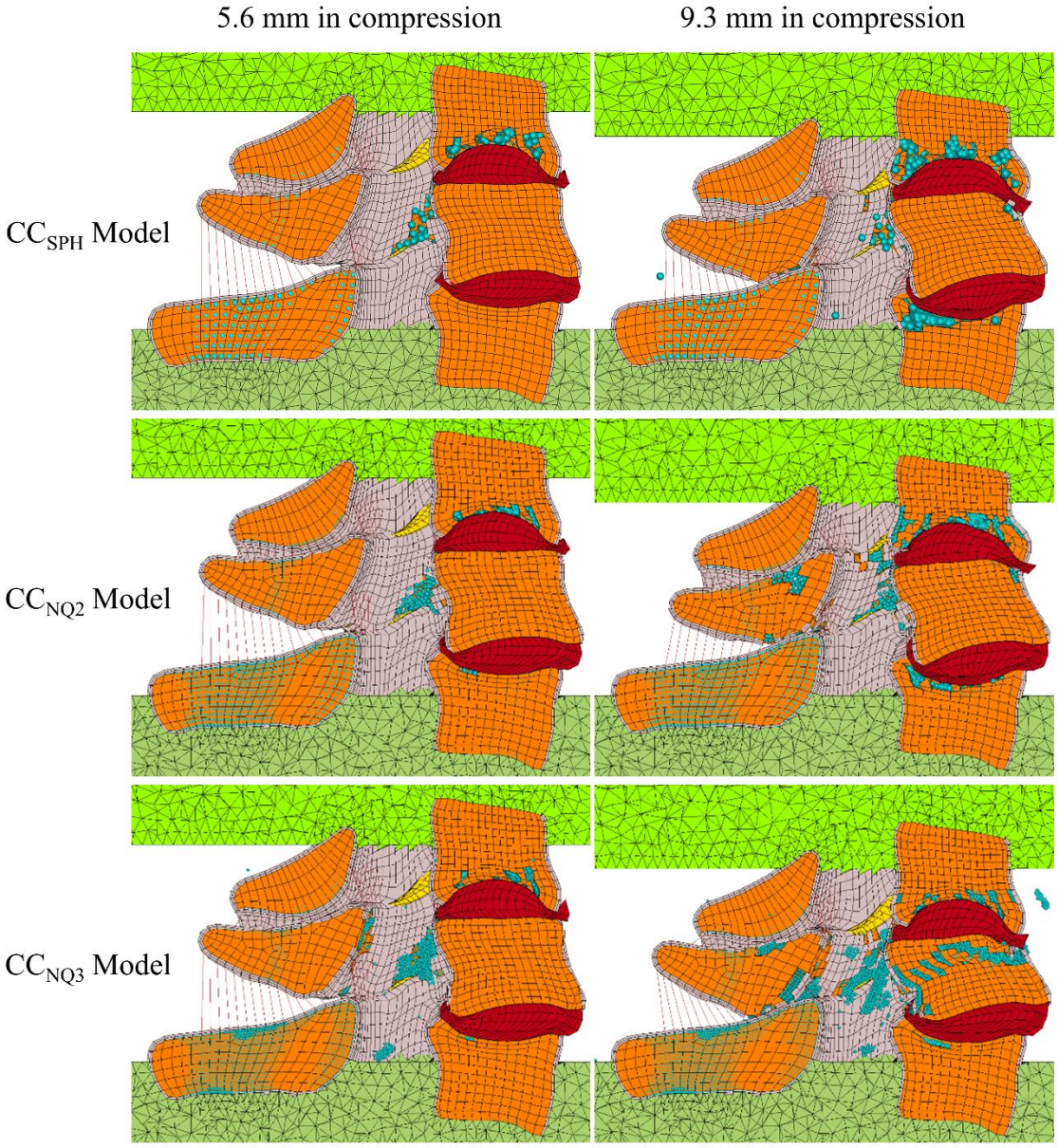


Figure 5.9: Midsagittal section plane views of the CC_{SPH} model, the CC_{NQ2} model, and the CC_{NQ3} model. At 5.6 mm, there was a sharp increase in the force-displacement response of the CC_{NQ3} model. At 9.3 mm, the CC_{NQ3} model reached an error termination.

Between 0 mm and 9.3 mm, where the CC_{NQ3} model experienced an error termination, the energy of the CC_{SPH} model was 46.1 J, the energy of the CC_{NQ2} model was 49.0 J, and the energy of the CC_{NQ3} model was 13.7 J (Figure 5.10). The energy of the CC_{NQ2} model was 6.2% greater than the CC_{SPH} model, while the energy of the CC_{NQ3} model was 108.3% less than the energy of the CC_{SPH} model.

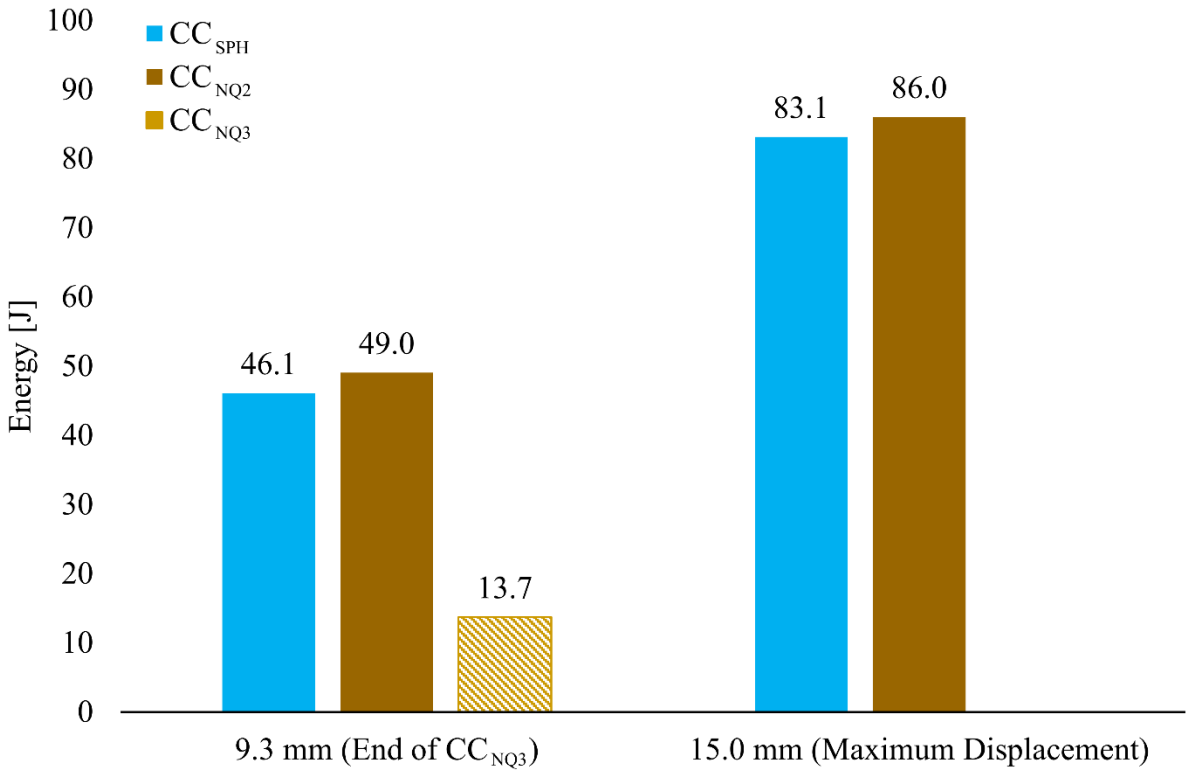


Figure 5.10: The energy of the force-displacement responses of the models where the number of SPH particles generated for each solid element in the trabecular bone is increased. The energy was calculated between 0.0 mm and 9.3 mm and between 0.0 mm and 15.0 mm.

5.4 Parametric Study: Investigating Model Response Under Varied Impact Severity, Material Parameters, and Eccentric Loading

In the parametric study, sixteen cases were run with varied impact severity (varying maximum displacements and velocities) (section 5.4.1), two cases were run with aged hard tissue material parameters (section 5.4.2), and four cases were run with eccentric boundary conditions (section 5.4.3). For all cases, the maximum percent occlusions were compared to the experimental results. The energy of the force-displacement responses for the cases with aged hard tissue material parameters were also compared to experimental results.

5.4.1 Investigating the Effect of Varying Maximum Velocity and Maximum Displacement on Spinal Canal Occlusion

Sixteen cases were run with maximum displacements between 8.2 mm and 15.0 mm and maximum velocities between 0.8 m/s and 1.44 m/s (Figure 5.11). The ranges of maximum velocities and displacements were based on the range applied experimentally, which were based on the maximum velocities and displacements expected to generate injury in the experimental specimen. The range only included injurious impact conditions and resulted in similar maximum percent occlusions across the eight experimental specimens. Most experimental specimens had a maximum percent occlusion between 48% and 59%, with one experimental specimen having a maximum percent occlusion of 82%.

For the sixteen cases run, the maximum percent occlusion was more dependent on the maximum displacements rather than the maximum velocity (Figure 5.11). Between the cases at the four difference maximum velocities between 0.8 m/s and 1.44 m/s, there did not seem to be a trend in the range or averages of the maximum percent occlusions measured at difference maximum displacements in compression. Between the cases at the four maximum displacements between 8.2 mm and 15.0 mm, the range and largest maximum percent occlusion at 8.2 mm and 10.0 mm were smaller than at 12.6 mm and 15.0 mm. Sagittal section views of the models in each group of maximum displacements showed that at 12.6 mm and 15.0 mm, fracture had propagated across the entire C6 vertebral body in the simulations at all velocities. At 10.0 mm, fracture propagation had progressed part way across the C6 vertebral body. At 8.2 mm, fracture initiation had begun in the C6 vertebral body without fracture propagation. Thus, the maximum displacements in compression applied to the segment affected the degree of completion of fracture propagation in the C6 vertebral body. Although the occlusions of the models did not show an increasing or decreasing trend as the maximum displacements were varied from 8.2 mm to 15.0 mm in compression, the range of maximum occlusions was smaller at lower maximum displacements. The smaller range and lower values of occlusion at lower maximum displacements illustrated that the higher maximum displacements leading to complete fracture propagation introduced the potential of higher occlusion in the spinal canal. Thus, more compression allowed for more hard tissue failure, which in turn increased the potential for hard tissue material to be displaced into the spinal canal.

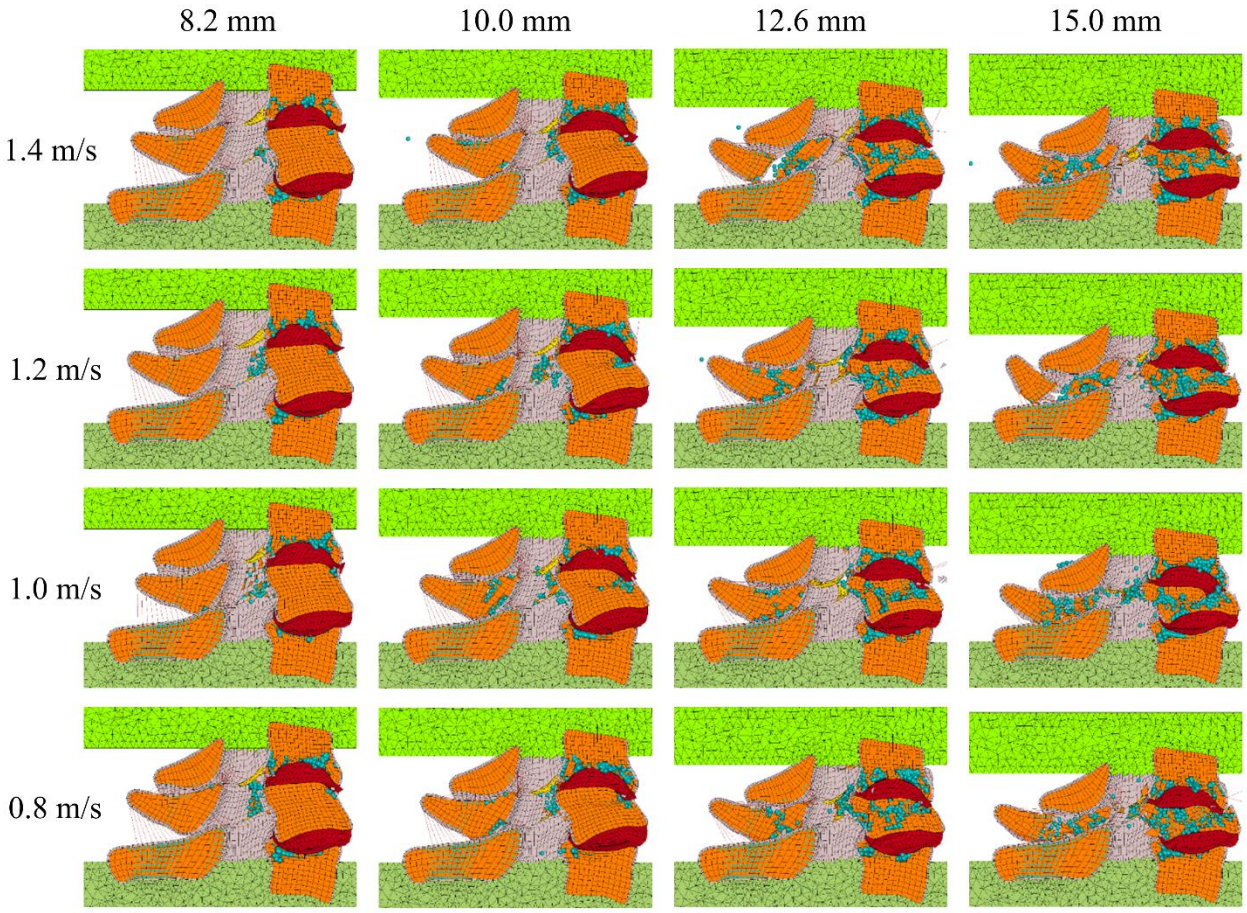


Figure 5.11: Midsagittal section views showing the models with varying maximum velocities and maximum displacements. Each image shows the model at the maximum displacement. The maximum displacements increase from left to right. The maximum velocities decrease from top to bottom. More visible SPH particles (cyan spheres) corresponds to larger amounts of damage.

Overall, the model underpredicted occlusion of the spinal canal at the lower maximum displacements, below 15 mm in compression, when compared to the experimentally reported values for maximum occlusion. Specifically, the maximum occlusions of the $CC_{15/1.4}$ and $CC_{15/1.2}$ models, with maximum displacements of 15 mm and maximum velocities of 1.4 m/s and 1.2 m/s, were within the 95% confidence interval of the mean maximum occlusions reported experimentally. The $CC_{15/0.8}$ and $CC_{12/1.4}$ models had maximum occlusions outside the 95% confidence interval but below the highest maximum occlusion reported experimentally. The maximum occlusions of the remaining model cases were below both the 95% confidence interval and smallest maximum occlusion reported experimentally. Furthermore, when the $CC_{8/1.4}$, $CC_{10/1.2}$, $CC_{12/1.0}$, and $CC_{15/0.8}$ models were compared to the experimental specimens with the closest matching combination of maximum velocity and maximum displacement, the models underpredicted occlusion at maximum velocities below 1.4 m/s and maximum displacements below 15.0 mm (Figure 4.20).

One factor leading to the underprediction of maximum occlusions by the model was the dependence of the occlusion on maximum displacement in the model. Since the models predicted more dependence of the maximum occlusion on the maximum displacement applied in compression, the maximum occlusions predicted by the model at 15 mm were generally within the experimental range. Conversely, the cases in the model with lower maximum displacements predicted occlusions below the experimental range. A second factor influencing the underprediction of maximum occlusions by the model was the direction the spinous process was displaced and the method which spinal canal occlusion was evaluated in the model. Of the sixteen cases, there were more cases where the spinous process appeared to be displaced away from the spinal canal than there were cases where the spinous process visibly displaced into the spinal canal (Figure 5.12). While the displacement of the spinous process away from the spinal canal would not affect the measured occlusion in the experiments, the method of evaluating the model would have resulted in a decrease in occlusion as the spinal canal space increased. The maximum occlusion measured in the model, therefore, did not always account for occlusion of hard tissue from the vertebral body into the spinal canal.

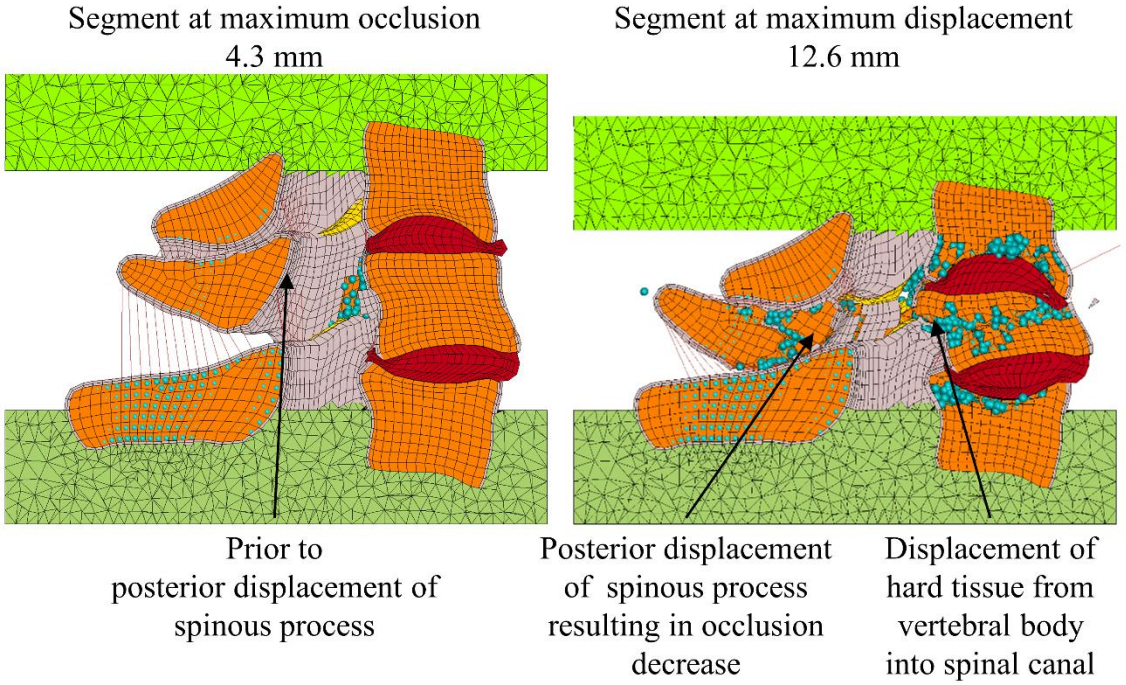


Figure 5.12: Midsagittal section view of the $CC_{12/1.2}$ model, compressed to a maximum displacement of 12.6 mm at a maximum velocity of 1.2 m/s. The section views show the segment when the maximum occlusion was measured according to the Rectangle method (left) and the segment at the maximum displacement of 12.6 mm (right). Since the spinous process displaced in the posterior direction for the $CC_{12/1.2}$ model, the maximum occlusion occurred before reaching maximum displacement.

The combinations of maximum velocity and displacement in the sixteen model cases were selected to include all combinations of maximum velocity and displacement within the experimental range. The combinations in the parametric study therefore included more combinations of maximum velocity and displacement than applied experimentally and may differ from combinations that would have been measured from a C5-C6-C7 segment under head-first loading or other compressive impacts to the whole spinal column. The cases in this parametric study were an investigation into the results of the numerical simulation using the ranges of the maximum velocities and displacements applied experimentally using a displacement-controlled input profile.

5.4.2 Comparison of Occlusion and Force-Displacement Response Using Aged Material Parameters for the Hard Tissues

Bone generally demonstrates a decrease in strength with age. For example, changes in the lattice structure of the trabeculae reduce its ability to carry load (Mosekilde et al., 1987). It was, therefore, expected that the force-displacement response would be lower with aged material parameters compared with the young material parameters.

The overall force-displacement response of the CC_{A08} model, the segment with aged material and the SPH implementation compressed to a maximum displacement of 8.0 mm, was in agreement with the trend and force of the response from the age and sex-matched experimental specimen. The force of the CC_{A08} model initially increased as SPH was activated to provide structural support in the articular pillars of the C6 vertebra and in the vertebral bodies of the C5 and C7 vertebrae. The force then decreased with the onset of fracture in the superior C6 vertebral body and with rotation of the C6 vertebral body. However, the energy of the CC_{A08} model was similar to the energy of the age and sex-matched experimental specimen (Figure 5.13). The experimental energy was 23.4 J. The energy of the CC_{A08} model was 23.5 J, equivalent to a 0.5% difference when compared to the experimental energy. Thus, the overall force-displacement response and energy of the model was in agreement with the experimental results. A limitation of this comparison was having only one experimental specimen. Additionally, of the 7720 solid trabecular bone elements forming the C6 vertebra, 26.8% eroded. Thus, it was also expected that not as much hard tissue would be lost due to erosion and there would have been less activated SPH particle elements as well.

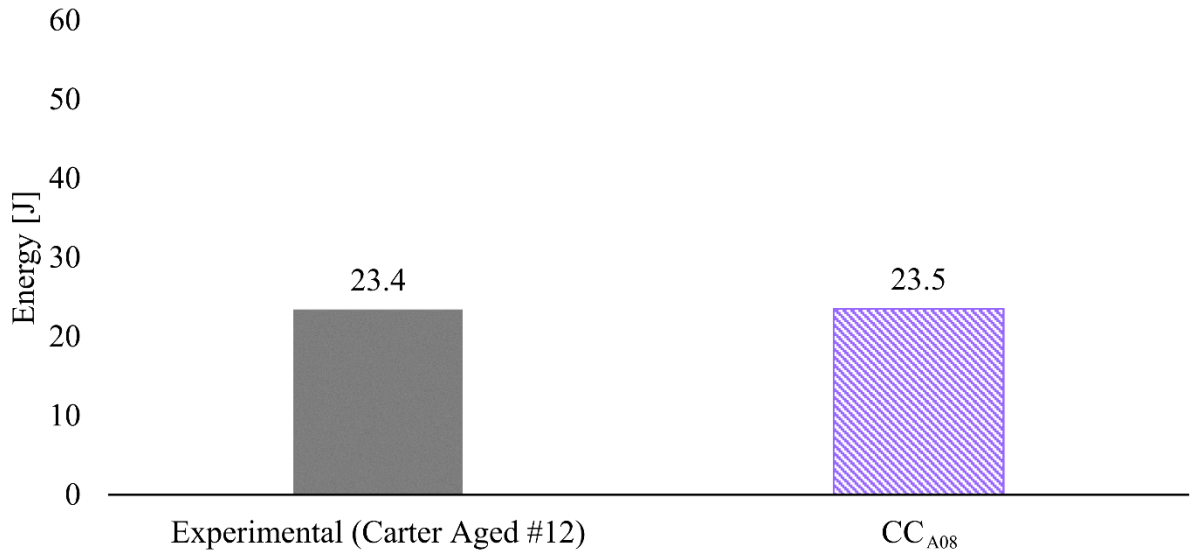


Figure 5.13: The energy of the aged experimental specimen (solid gray) and the CC_{A08} model (striped purple) with aged hard tissue material parameters compressed to a maximum displacement of 8.0 mm.

The occlusion of the CC_{A08} model was lower than the occlusion from the experimental specimen. The underprediction of occlusion of the model using the aged hard tissue parameters was a result of the failure progression in the model. Due to the lower strength and failure strain thresholds of the aged hard tissue material parameters, the erosion in the C6 vertebral body began in the superior-anterior edge (Figure 5.14). As the segment was compressed, the intervertebral disc loaded the C6 vertebral body, resulting in failure of the hard tissue material directly below it. At the maximum displacement of 8.1 mm, the hard tissue material that failed was on the anterior side of the vertebral body, opposite to the spinal canal location, and therefore did not lead to increased occlusion in the spinal canal.

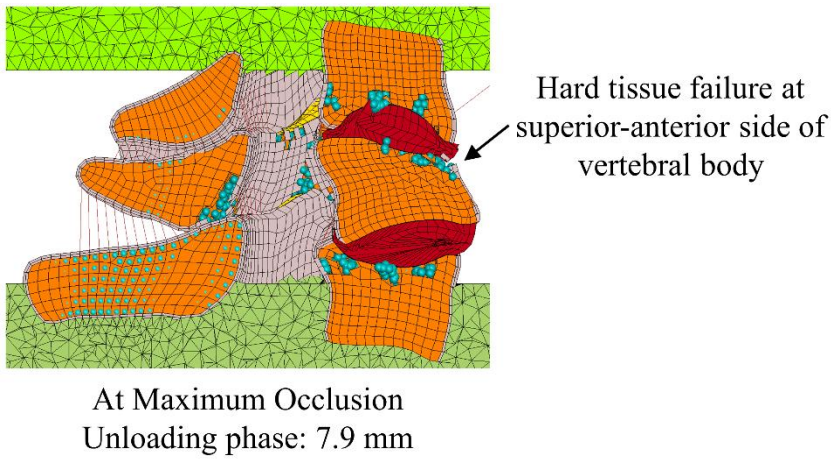


Figure 5.14: A midsagittal section view showing the CC_{A08} model at the maximum percent occlusion. The maximum occlusion was measured during the unloading phase.

Considering higher displacement up to 15 mm, the CC_{A15} model demonstrated a similar increase in force as the CC_{A08} model with a subsequent force plateau up to 15.0 mm of displacement. In comparison to the CC_{SPH} model using the young material parameters for the hard tissues, the CC_{A15} model with the aged hard tissue material parameters had a lower force owing to the lower material failure properties in the aged model. Similarly, the energy corresponding to the area under the force-displacement response of the CC_{A15} model was 44.7% lower than the CC_{SPH} model (Figure 5.15). Additionally, when looking at the fracture pattern in the C6 vertebra of the CC_{A15} model, the progression of material failure differed in comparison to the CC_{SPH} model (Figure 5.16). In the CC_{SPH} model, after rotation of the C6 vertebral body, fracture initiated in the superior-anterior edge of the vertebral body before propagating through the middle of the vertebral body. A difference in trabecular failure was expected since the trabecular bone weakens with age; however, vertebral fractures that are typically expected due to aging depend on the changes in multiple structures of the spinal column, not just the hard tissues (Adams and Dolan, 2011). In the CC_{A15} model, the lower strength of the hard tissue elements allowed hard tissue failure in the vertebral body to initiate at a lower displacement in compression. Thus, when fracture progression began in the CC_{A15} model with the aged hard tissue material parameters, the C6 vertebral body was less rotated and there was more vertical space in the segment for the vertebral bodies and intervertebral discs. Both factors lead to fracture progressing down from the superior surface of the vertebral body rather than diagonally across the vertebral body in both the CC_{A08} model and the CC_{A15} model.

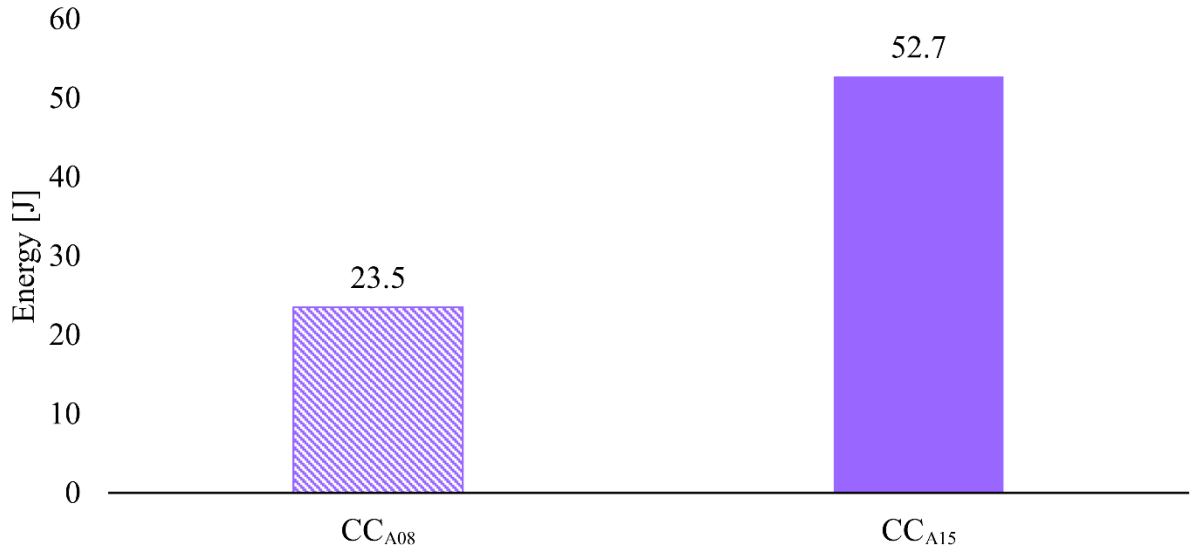


Figure 5.15: The energy of the CCA08 model (stripped purple) with aged hard tissue material parameters compressed to a maximum displacement of 8.0 mm and the CC_{A15} model (solid purple)with the aged hard tissue material parameters compressed to a maximum displacement of 15.0 mm.

When comparing the maximum percent occlusion between young and aged models for a maximum displacement of 15.0 mm, the occlusion was greater with the aged hard tissue material parameters (Figure 4.23). With the aged material parameters in the CC_{A15} model, the lower stress-strain relationship and failure strains resulted in more hard tissue erosion. The increase in erosion and, therefore, activated SPH particle elements allowed more material from both the spinous process and vertebral body to be pushed into the spinal canal.

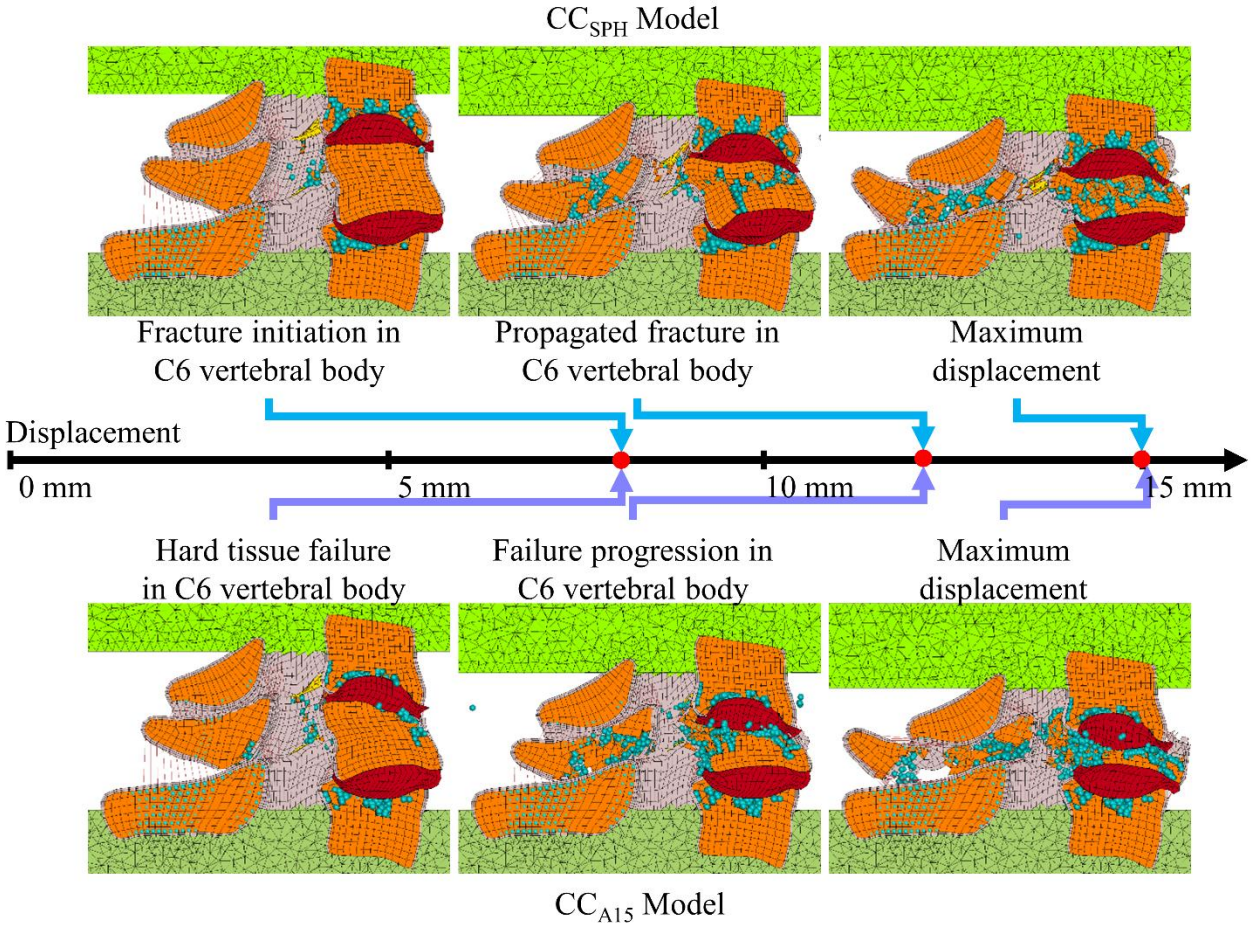


Figure 5.16: Midsagittal section views showing the CC_{SPH} model (top) and the CC_{A15} model (bottom) at 8.1 mm, 12.1 mm, and 15.0 mm of displacement. In the CC_{SPH} model with the young hard tissue material parameters, fracture initiated and propagated across the C6 vertebral body. In the CC_{A15} model with the aged hard tissue material parameters, hard tissue material failure progressed from the superior to inferior sides of the C6 vertebra.

5.4.3 Investigating the Effect of Eccentric Boundary Conditions on Spinal Canal Occlusion

The measured percent occlusions for the models with eccentric loading agreed with the trends of the maximum occlusions measured experimentally. In both the experimental and model measurements, the highest occlusion was seen in the posterior eccentric loading case. The second, third, and fourth highest occlusion values were seen in the central compression, low lateral, and high lateral loading cases, respectively (Figure 4.25).

With eccentric loading, the occlusion from the C6 vertebra of the segment model measured using the Rectangle Method was primarily attributed to the displacement and rotation of the C6 vertebra. Recall that with the Rectangle Method, occlusion was measured based on the two-dimensional area from the superior view of the C6 vertebra, so that vertebral motion into the tracked area of interest would be measured as an increase in occlusion. Thus, the measured increase in occlusion, in the case of eccentric compression of the segment, did not necessarily indicate intrusion of bone fragments into the spinal canal.

With an anterior eccentric compression applied in the Ant_{SPH} model, the maximum occlusion measured was lower than in the CC_{SPH} model with a central compression loading. Anterior eccentric compression, resulting in flexion of the segment, led the C6 vertebra of the Ant_{SPH} model to displace and rotate relative to its original position before loading. The laminae and spinous process, therefore, moved into the rectangle of the Rectangle Method leading to an increase in the measured occlusion. The occlusion measured only from a superior view of the Ant_{SPH} model did not reflect the amount of comminuted material displaced into the spinal canal or the amount of hard tissue fractured. However, it would be expected that an anterior eccentric compression would result in less occlusion of the spinal canal since the anterior side of the vertebral body would experience more compression. Fractured hard tissue on the anterior side of the vertebral body would not be pushed into the spinal canal space.

The Pos_{SPH} model, with posterior eccentric compression, had a higher maximum occlusion than the CC_{SPH} model. The occlusion of the Pos_{SPH} model measured using the Rectangle Method increased due to rotation of the C6 vertebra leading the vertebral body to rotate into the rectangle, but similar to the Ant_{SPH} model, the increase in occlusion did not reflect the amount of narrowing of the spinal canal space at the level of the C6 vertebra. Although the spinous process fractured in the Pos_{SPH} model, bone fragments from the spinous process did not contribute to the measured occlusion. SPH particle elements from fracture in the articular pillars and posterior vertebral body, but primarily the articular pillars, did displace into the spinal canal. However, it was still the rotation of the vertebral body which mainly contributed to the occlusion measured by the Rectangle Method.

The maximum occlusion measured from the LLt_{SPH} model, under low lateral eccentric compression, was lower than the maximum occlusion of the CC_{SPH} model and higher than the maximum occlusions from both the Ant_{SPH} model and the Pos_{SPH} model. Unlike the Ant_{SPH} model and the Pos_{SPH} model, the vertebral body of the LLt_{SPH} model did fracture. Subsequent compression resulted in the displacement of hard tissue material from the C6 vertebral body into the spinal canal, contributing to an increase in occlusion. Additionally, the lateral boundary conditions led to displacement of the C6 vertebra in the transverse plane, further contributing to an increase in occlusion. Despite hard tissue fracture and displacement of the C6 vertebra, the maximum occlusion of the LLt_{SPH} model was lower than the CC_{SPH} model due to the posterior displacement of the spinous process following fracture at the pedicles of the C6 vertebra. The maximum occlusion was also lower than the Ant_{SPH} model and the Pos_{SPH} model since hard tissue fracture and the boundary conditions resulted in no overall rotation of the C6 vertebra of the LLt_{SPH} model, which was what led to higher measured occlusion in the Ant_{SPH} model and the Pos_{SPH} model.

The HLt_{SPH} model had a lower maximum occlusion than the CC_{SPH} model and the other eccentric compression cases. Since no hard tissue fracture occurred in the HLt_{SPH} model, no bone fragments displaced into the spinal canal. Thus, only the displacement and rotation of the C6 vertebra contributed to spinal canal occlusion as the laminae displaced into the rectangle. The maximum occlusion using the Rectangle Method was measured during unloading as the segment was in flexion. Since the amount of flexion experienced by the HLt_{SPH} model was less than the Ant_{SPH} model, the C6 vertebra also did not rotate as much, hence the lower measure occlusion. Similar to the Ant_{SPH} model, the occlusion reported using the Rectangle Method did not indicate narrowing of the spinal canal during loading of the HLt_{SPH} model.

The main limitation of using the Rectangle Method on a superior view of the C6 vertebra when measuring the spinal canal occlusion during eccentric loading was that the method does not capture changes in the spinal canal space with displacement or rotation of the vertebra (Figure 5.17). During eccentric loading of the experimental specimen, bending of the spinal canal space did not necessarily result in narrowing of the spinal canal, which would have been a phenomenon the SCOT would have better quantified since the tubing of the SCOT would bend with the spinal canal. Conversely, the occlusion measured from the superior view of the C6 vertebra in the Rectangle Method did not represent the narrowing of the spinal canal space available for the spinal cord. Instead, the value of occlusion was more reflective of the rotation and displacement of the C6 vertebra, regardless of whether hard tissue injury occurred or whether bone fragments displaced into the spinal canal.

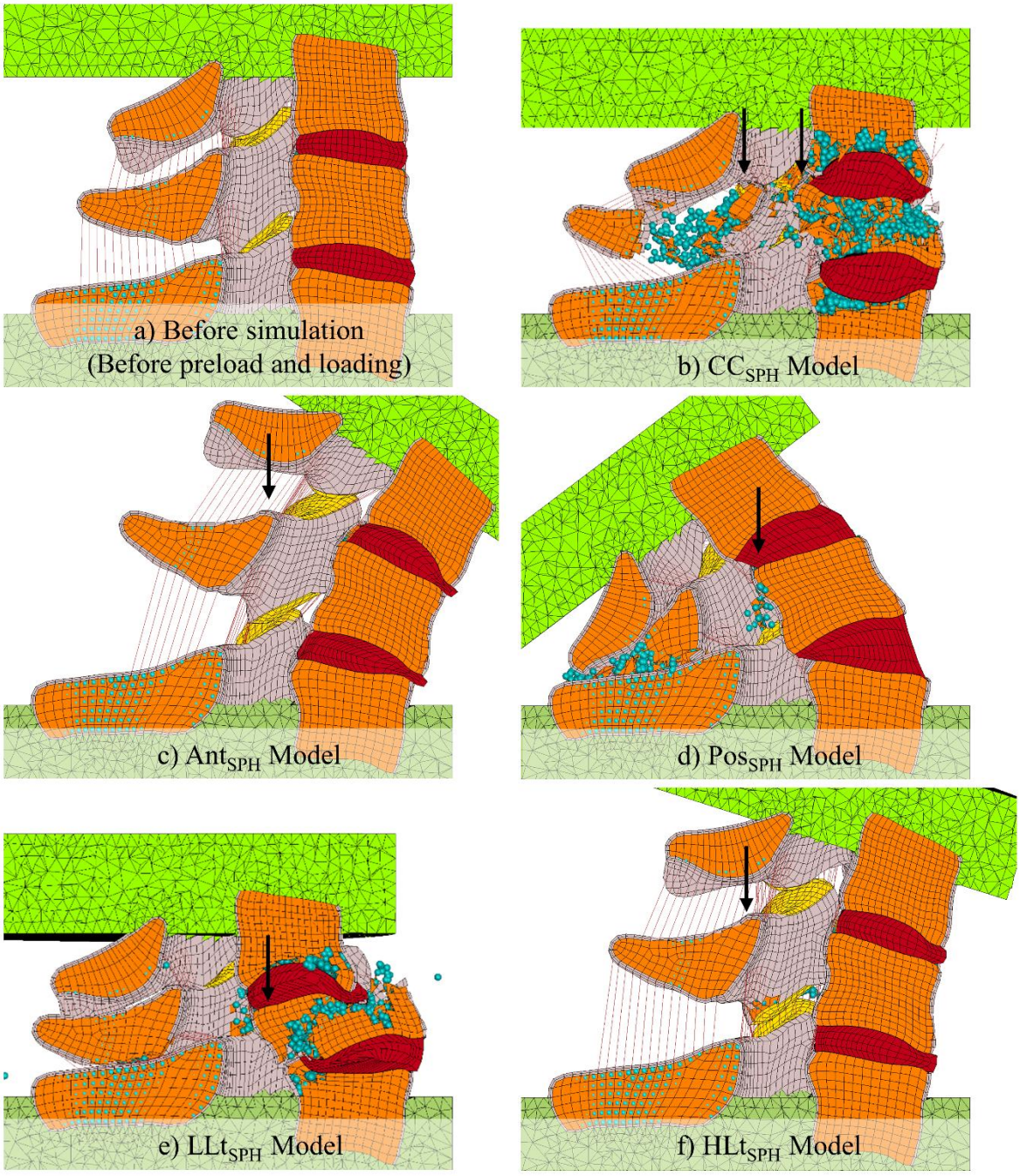


Figure 5.17: Midsagittal section views of a) the model with no loading and b) the CC$_{SPH}$ model, c) the Ant$_{SPH}$ model, d) the Pos$_{SPH}$ model, e) the LLt$_{SPH}$ model, and f) the HLt$_{SPH}$ model at the maximum percent occlusion, as measured by the two-dimensional area from the superior view of the C6 vertebra. The black vertical arrows indicate the regions of the C6 vertebra that would be considered to have occluded the spinal canal area using the Rectangle Method.

The maximum occlusions measured by the Rectangle Method overestimated the contribution of vertebral displacement and rotation to changes in the spinal canal geometry while not considering the effect of the relative positions of adjacent vertebrae on the spinal canal geometry. In the Ant_{SPH} model, the anterior displacement and rotation of the C6 vertebra resulted in a 47.6% measure of occlusion; however, the sagittal view of the segment did not show tissue displacement into the spinal canal space (Figure 5.17c). Additionally, in the midsagittal plane, the anterior and posterior boundaries of the spinal canal appear to leave space for a spinal cord. In the Pos_{SPH} model, the posterior displacement and rotation of the C6 vertebra resulted in a measured 74.8% occlusion. Although hard tissue fracture occurred, the displacement of the C6 vertebral body into the rectangle was not a result of widespread fracture in the vertebral body. Furthermore, the sagittal view of the segment showed that the midsagittal diameter of the canal narrowed as the C6 vertebral body moved closer to the anterior side of the C7 spinous process (Figure 5.17d). The narrowing of the spinal canal due to the relative positions between vertebrae during eccentric loading was also not captured from an evaluation of only the C6 vertebra. In the LLt_{SPH} model, a 40.5% occlusion was measured due to the displacement of hard tissue from the C6 vertebral body into the spinal canal. While the LLt_{SPH} model did show hard tissue failure in the C6 vertebral body, the sagittal view of the segment also showed narrowing of the spinal canal as the C6 vertebral body was pushed toward the C7 spinous process (Figure 5.17e). Thus, canal changes due to the relative positions of the C6 and C7 vertebrae in both the LLt_{SPH} model and the Pos_{SPH} model were not captured using the Rectangle Method to evaluate the two-dimensional canal area from the superior view of the C6 vertebra. In the HLt_{SPH} model, a 21.8% occlusion was measured as the entire C6 vertebra rotated anteriorly, but as with the Ant_{SPH} model, the sagittal view of the HLt_{SPH} model showed no hard tissue fracture or hard tissue displacement into the spinal canal.

Thus, the Rectangle Method was more appropriate for measuring the occlusion of the spinal canal during central compression loading, but it did not consider the canal changes resulting from eccentric loading. While a two-dimensional evaluation of the spinal canal space in the midsagittal plane may be more suitable for anterior and posterior eccentric compression, the midsagittal plane would also not capture all changes in the spinal canal space during lateral eccentric compression. As such, methods such as using a spinal cord or a surrogate spinal cord in the model to capture the three-dimensional changes in the spinal canal would be more applicable in measuring occlusion from both central and eccentric compression. Additionally, a spinal cord or surrogate spinal cord would evaluate the space occupied by the spinal cord and therefore would provide quantities more relevant to investigating spinal cord injury.

5.5 Limitations and Future Work

The geometry of the FE segment model was from a specific human male subject and may have differed in geometry compared to the experimental specimens. A previous study compared the C5-C6-C7 segment from the GHBMC model to the geometry, alignment, and orientation of the experimental specimens (Khor, 2018). Comparisons of the C5-C6-C7 experimental specimens to the segment from the GHBMC M50 model showed differences in vertebral body depths, intervertebral disc heights, and Bezier angles. The segment from the GHBMC model had a lower spinal curvature than the experimental specimens in the Carter (2002) study (Khor, 2018). The differences in geometries could lead to differences in the responses of the model and is an area for future investigation.

Only the hard tissue material parameters were varied for the CC_{A08} model and the CC_{A15} model to represent an aged segment. Other material and geometry changes were not considered. Data on properties such as the bone density of the experimental specimens was not reported, and therefore, was not implemented into the hard tissue material model of the segment. Other changes such as disc degeneration were also not considered when comparing the segment model to the aged experimental specimens. Future work may consider further material properties and geometries representative of a broader range of specimens with various ages, sexes, or geometries.

The SPH implementation in LS-DYNA that converted Lagrangian continuum elements into SPH particle elements is currently only available for solid elements. Thus, the implementation of SPH in this work was only applied to the trabecular bone. Although material from the cortical bone was also lost due to element erosion, it was assumed that the amount of material lost would have been small compared to the amount of material lost during element erosion in the trabecular bone since trabecular bone accounts for most of the volume in the vertebra.

The endplates in the model were meshed with shell elements of uniform thickness. It has been reported that the superior endplates are usually thinner than the inferior endplates, and future work should consider enhancing the geometries of the endplates. In addition, modelling endplate thickness variations, including a failure criterion for the endplates, and modelling the flow of marrow and fat in the trabecular bone in future work might help improve the modelling of burst fractures.

The aim of this study was to investigate the implementation of SPH as a means of improving the modelling of hard tissue failure in compression loading; however, the failure of other tissues in the segment is also important and may contribute to the response of the segment. Although the material properties and failure of the ligaments are well documented, less work has been done on endplate failure and disc response which should be investigated further.

The segment model used in this project did not include all the tissues that may have been present in the experimental specimens. For example, the absence of the periosteum, connective tissues, and bone marrow, as well as the simplified ligament geometry in the segment model may have influenced the movement of the vertebrae and bone fragments. Bone marrow and other fluid-like substances in the trabecular bone which may have influenced the fracture and movement of bone fragments in the experimental specimens were not included in the model but were considered, in part, through the SPH implementation. The periosteum, connective tissue, and ligaments in the experimental specimen may have provided support and containment around the fractured hard tissues and vertebrae. In the model, the absence of surrounding tissues to provide containment may have allowed the SPH particle elements and other fractured hard tissue elements to displace more easily into or toward the spinal canal. Elements in the model moving toward the spinal canal would have contributed to higher values of occlusion. On the other hand, the absence of surrounding tissues around vertebral structures such as the articular pillar may have made it easier for trabecular bone material to be pushed away from the spinal canal. At the articular pillars, movement of the hard tissues outward away from the load path during compression may have contributed to a loss in force. Additionally, the posterior movement of the articular pillar also contributed to a decrease in occlusion in the cases where the laminae and spinous process moved in the posterior direction.

Comparisons of the model responses to the experimental responses were limited by the number of experimental specimens available for comparison. For example, the CC_{SPH} model was representative of an average male of less than 50 years old. Of the eight experimental specimens undergoing central compression loading, only two specimens were male and less than 50 years old. Additionally, only one specimen was male and older than 70 years old for comparison to the CC_{A08} model. It is recommended that additional experimental segment compression tests be conducted including high-speed x-ray imaging and quantification of the damaged materials.

Chapter 6
Conclusion

The overall aim of the work in this thesis was to enhance the modelling of hard tissue fracture, primarily in the trabecular bone, to improve the post-fracture response of a C5-C6-C7 finite element model of a cervical spine segment extracted from the GHBMC M50 v6-0 model and loaded under compression. Previously, hard tissue fracture was modelled using strain-based element erosion where trabecular and cortical bone elements were removed from the simulation upon failure. While element erosion allowed for the prediction of fracture initiation in the segment, the removal of elements resulted in a loss of structural support with continued compression. Thus, the work in this thesis aimed to mitigate the loss of material through the implementation of SPH, where one solid Lagrangian trabecular bone element would be converted into one SPH particle element upon erosion of the solid element.

Prior to the implementation of SPH, three model enhancements were progressively implemented and the resulting changes in the force-displacement response under central compression were investigated. The segment and apparatus set-up was based on an experimental central compression test by Carter where spinal canal occlusion was measured using the SCOT, consisting of a tube fitted into the spinal canal space. The initial FE segment extracted from the GHBMC model simulated fracture under compression using strain-based element erosion, but it overpredicted the initial fracture force and underpredicted the force with subsequent compression and fracture. The first model enhancement replaced the plastic kinematic material models of the hard tissues with anisotropic material models developed by Khor. The anisotropic material models improved the prediction of fracture initiation and allowed for a higher post-fracture force plateau; however, the model still demonstrated a loss in force post fracture due to interpenetration of parts and the loss of material during erosion. The second model enhancement was the addition of eroding contact definitions to prevent parts from penetrating through each other as new surfaces were formed during erosion progression. The eroding contact definitions allowed the segment to continue carrying load after fracture, resulting in a further increase in the force plateau after fracture initiation. The third model enhancement was the addition of a minimum principal strain criterion to the erosion criterion of the anisotropic material model of the trabecular bone. Although the minimum principal strain criterion did not have much effect on the force-displacement response, the criterion was added to allow the trabecular elements to fail under compression, preparing the model for the upcoming SPH implementation.

Following the three model enhancements, SPH was implemented into the trabecular bone and evaluated using the force-displacement response, hard tissue damage patterns, and spinal canal occlusions. The

responses of the model with the SPH implementation were compared against the model without the SPH implementation and against age and sex-matched experimental specimens. The force-displacement response of the model with the SPH implementation showed more of a force increase over the model without the SPH implementation with more compression and hard tissue erosion, demonstrating the added support provided by the implementation of SPH in the segment. The SPH implementation also resulted in a force-displacement response in better agreement with the trend and energy of the experimental specimens, where the energy was calculated as the area under the force-displacement response up to the maximum displacement. The models, both with and without the implementation of SPH, predicted damage in all hard tissue regions. The spinal canal occlusion in the model was determined using the Rectangle Method, calculating the change in two-dimensional area occupied by hard tissue material within a rectangular area of interest around the spinal canal space of a superior-inferior view of the C6 vertebra. Using the Rectangle Method for evaluation, the model with the SPH implementation had higher occlusion than the model without the SPH implementation and was also in better agreement with experimentally reported occlusion due to preserved material in the model allowing hard tissue to displace into the spinal canal.

When the number of SPH elements generated per solid element was increased from one to eight, the force-displacement responses were similar. However, increasing the number of SPH particles generated per solid element to 27 particles resulted in an eventual decrease in force as erosion progressed and in numerical instability. When 27 SPH particles were generated per solid element, the area of influence around each SPH particle correspondingly decreased, allowing SPH particles to escape the segment more easily. Additionally, fracture in the vertebral bodies appeared to travel vertically, following the direction of the solid element mesh. The instability of the model with higher number of SPH particles suggested a required compatibility between the size of the solid element and the number of generated SPH particles for each solid element.

Finally, using the segment with all model enhancements including the SPH implementation, a parametric study was conducted for three parameters: impact severity, aged hard tissue material parameters, and eccentricity of loading. To vary the impact severity parameter, the same displacement profile was scaled to achieve maximum displacements and maximum velocities matching the range applied experimentally. Generally, the amount of hard tissue fracture in the C6 vertebral body of the FE segment model demonstrated a greater dependence on the maximum displacement applied in compression rather than the maximum velocity. A greater amount of fractured hard tissue in the C6 vertebra at higher maximum displacements, in turn, meant a higher potential for greater occlusion. Thus, the model underpredicted occlusion at lower displacements in comparison to the experimental results. When the hard tissue material

parameters were adjusted to represent an aged age group of greater than 70 years old, the model demonstrated a force-displacement increase similar to the age and sex-matched experimental specimen. At 15 mm of displacement in compression, the force-displacement response of the FE segment model with aged hard tissue material parameters was lower than with young hard tissue material parameters, where the young material parameters were representative of an age group younger than 50 years old. Additionally, more hard tissue fracture occurred with the aged hard tissue material parameters resulting in a higher occlusion than in the model with young hard tissue material parameters. Finally, the values of maximum occlusion for eccentric compression of the FE model demonstrated a similar trend to the experimental results, where the cases ordered from highest to lowest maximum occlusion were the posterior eccentric case, the central compression case, the low lateral eccentric case, and the high lateral eccentric case. However, measurement of occlusion for eccentric compression using the Rectangle Method was influenced by rotation and displacement of the C6 vertebra instead of the displacement of fractured hard tissue into the spinal canal. Vertebral body fracture in the FE segment model was primarily seen in the central compression and low lateral eccentric case, spinous process fracture was seen in the central compression, low lateral eccentric, and posterior eccentric cases, and little to no erosion was observed in the anterior eccentric and high lateral cases.

Two of the limitations of this work include the number of experimental specimens available for evaluating the model responses and the method which occlusion was evaluated in the FE segment model. Thus, the first recommendation for future work is additional experimental segment compression tests with additional quantification of damaged material. The second recommendation for future work is the implementation of a spinal cord into the canal of the FE segment model to quantify changes in the canal geometry and deformation of the spinal cord in order to investigate spinal cord injury. In conclusion, the implementation of SPH was able to help preserve trabecular bone material to provide structural support and model the flow of fractured material in the segment under compression.

Letter of Copyright Permission

ELSEVIER LICENSE

TERMS AND CONDITIONS

Dec 12, 2024

This Agreement between Sophia Ngan ("You") and Elsevier ("Elsevier") consists of your license details and the terms and conditions provided by Elsevier and Copyright Clearance Center.

License Number	5926700499689
License date	Dec 12, 2024
Licensed Content Publisher	Elsevier
Licensed Content Publication	Journal of the Mechanical Behavior of Biomedical Materials
Licensed Content Title	Experimental study of cancellous bone under large strains and a constitutive probabilistic model
Licensed Content Author	V. Kefalas,D.A. Eftaxiopoulos
Licensed Content Date	Feb 1, 2012
Licensed Content Volume	6
Licensed Content Issue	n/a
Licensed Content Pages	12
Start Page	41
End Page	52
Type of Use	reuse in a thesis/dissertation
Portion	figures/tables/illustrations
Number of figures/tables/illustrations	1
Format	both print and electronic
Are you the author of this Elsevier article?	No
Will you be translating?	No

Title of new work	Multi-Physics Smoothed Particle Hydrodynamics Implementation to Enhance Vertebral Fracture Prediction in a Finite Element Model of a Lower Cervical Spine Segment Under Compression
Institution name	University of Waterloo
Expected presentation date	Dec 2024
Portions	Figure 1
The Requesting Person / Organization to Appear on the License	Sophia Ngan
Requestor Location	Sophia Ngan 200 University Ave W Waterloo, ON N2L3G1 Canada
Publisher Tax ID	GB 494 6272 12
Total	0.00 CAD
Terms and Conditions	

References

Adams, M.A., Dolan, P., 2011. Biomechanics of vertebral compression fractures and clinical application. Arch Orthop Trauma Surg 131, 1703–1710. https://doi.org/10.1007/s00402-011-1355-9

Algahtany, M., McFaull, S., Chen, L., Zhang, S., Saarela, O., Alqahtani, F., Cusimano, M.D., 2021. The Changing Etiology and Epidemiology of Traumatic Spinal Injury: A Population-Based Study. World Neurosurgery 149, e116–e127. https://doi.org/10.1016/j.wneu.2021.02.066

Arhiptsov, K., Marom, G., 2021. Numerical models of spinal cord trauma: The effect of cerebrospinal fluid pressure and epidural fat on the results. Journal of Neurotrauma 38, 2176–2185. https://doi.org/10.1089/neu.2021.0065

Ashman, R.B., Cowin, S.C., Van Buskirk, W.C., Rice, J.C., 1984. A continuous wave technique for the measurement of the elastic properties of cortical bone. Journal of Biomechanics 17, 349–361. https://doi.org/10.1016/0021-9290(84)90029-0

Baigi, V., Azadmanjir, Z., Khormali, M., Ghodsi, Z., Dashtkoohi, M., Sadeghi-Naini, M., Naghdi, K., Khazaeipour, Z., Abdi, M., Harrop, J.S., Rahimi-Movaghar, V., 2024. Comparison of Traumatic Spinal Fracture Patterns Between Motorcyclists and Occupants of Other Nonheavy Motor Vehicles: A Report from the National Spinal Cord and Column Injury Registry of Iran. World Neurosurgery 189, e177–e183. https://doi.org/10.1016/j.wneu.2024.06.014

Bambach, M.R., Grzebieta, R.H., McIntosh, A.S., Mattos, G.A., 2013. Cervical and thoracic spine injury from interactions with vehicle roofs in pure rollover crashes. Accident Analysis & Prevention 50, 34–43. https://doi.org/10.1016/j.aap.2012.10.006

Barker, J., Cronin, D.S., 2022. Muscle Activation Affects Kinematic Response and Injury Risk in Non-Traditional Oblique Impact Scenarios Assessed with a Head and Neck Finite Element Model. SAE International Journal of Transportation Safety 10.

Barker, J.B., Cronin, D.S., 2020. Multilevel Validation of a Male Neck Finite Element Model With Active Musculature. Journal of Biomechanical Engineering 143. https://doi.org/10.1115/1.4047866

Barker, J.B., Cronin, D.S., Nightingale, R.W., 2017. Lower Cervical Spine Motion Segment Computational Model Validation: Kinematic and Kinetic Response for Quasi-Static and Dynamic Loading. Journal of Biomechanical Engineering 139. https://doi.org/10.1115/1.4036464

Basafa, E., Otake, Y., Kutzer, M.D., Armiger, R.S., Armand, M., 2012. A Particle-Based Model for Prediction of Cement Diffusion During Osteoporotic Hip Augmentation Surgery: Theory and Validation. Presented at the ASME 2010 International Mechanical Engineering Congress and Exposition, American Society of Mechanical Engineers Digital Collection, pp. 381–390. https://doi.org/10.1115/IMECE2010-38978

Boakye-Yiadom, S., Cronin, D.S., 2018. On the importance of retaining stresses and strains in repositioning computational biomechanical models of the cervical spine. International Journal for Numerical Methods in Biomedical Engineering 34, e2905. https://doi.org/10.1002/cnm.2905

Camacho, D.L., Nightingale, R.W., Robinette, J.J., Vanguri, S.K., Coates, D.J., Myers, B.S., 1997. Experimental Flexibility Measurements for the Development of a Computational Head-Neck Model Validated for Near-Vertex Head Impact. Presented at the 41st Annual Stapp Car Crash Conference, p. 973345. https://doi.org/10.4271/973345

Carter, D.R., Hayes, W.C., 1977. The compressive behavior of bone as a two-phase porous structure. JBJS 59, 954.

Carter, J.W., 2002. Compressive cervical spine injury: the effect of injury mechanism on structural injury pattern and neurologic injury potential (Thesis).

Carter, J.W., Ku, G.S., Nuckley, D.J., Ching, R.P., 2002. Tolerance of the cervical spine to eccentric axial compression. Stapp Car Crash J 46, 441–459. https://doi.org/10.4271/2002-22-0022

Carter, J.W., Mirza, S.K., Tencer, A.F., Ching, R.P., 2000. Canal Geometry Changes Associated With Axial Compressive Cervical Spine Fracture. Spine 25, 46.

Chang, D.G., Tencer, A.F., Ching, R.P., Treece, B., Senft, D., Anderson, P.A., 1994. Geometric changes in the cervical spinal canal during impact. Spine (Phila Pa 1976) 19, 973–980. https://doi.org/10.1097/00007632-199404150-00017

Chawla, A., Mukherjee, S., Mohan, D., Jain, S.S., 2005. Validation of the Cervical Spine Model in THUMS. Presented at the 19th International Technical Conference on the Enhanced Safety of Vehicles (ESV).

Chen, Z., He, Y., Gu, Y., Su, B., Ren, Y., Liu, Y., 2021. A novel method for numerical simulation of the interaction between level ice and marine structures. J Mar Sci Technol 26, 1170–1183. https://doi.org/10.1007/s00773-021-00799-w

Ching, R.P., Watson, N.A., Carter, J.W., Tencer, A.F., 1997. The Effect of Post-Injury Spinal Position on Canal Occlusion in a Cervical Spine Burst Fracture Model. Spine 22, 1710.

Chiu, A.K., Pease, T.J., Prakash, H., Oster, B.A., Smith, R.A., Sahlani, M., Ratanpal, A.S., Amin, I., Scalea, T.M., Bivona, L.J., Jauregui, J.J., Cavanaugh, D.L., Koh, E.Y., Ludwig, S.C., 2024. The changing epidemiology of traumatic spine injuries: a trends analysis of 26 years of patients at a major level 1 trauma center in the United States. The Spine Journal 24, 1561–1570. https://doi.org/10.1016/j.spinee.2024.05.009

Cloake, T., Bastien, C., Hardwicke, J., Venetsanos, D.T., Sturgess, C.N., 2021. A critique of the THUMS lower limb model for pedestrian impact applications: 13th European LS-DYNA Conference 2021.

Cooper, D.M.L., Kawalilak, C.E., Harrison, K., Johnston, B.D., Johnston, J.D., 2016. Cortical Bone Porosity: What Is It, Why Is It Important, and How Can We Detect It? Curr Osteoporos Rep 14, 187–198. https://doi.org/10.1007/s11914-016-0319-y

Corrales, M.A., Cronin, D.S., 2021. Importance of the cervical capsular joint cartilage geometry on head and facet joint kinematics assessed in a Finite element neck model. Journal of Biomechanics 123, 110528. https://doi.org/10.1016/j.jbiomech.2021.110528

Cronin, D.S., 2021. ME 720 Course Notes.

Currey, J.D., 1984. Effects of Differences in Mineralization on the Mechanical Properties of Bone. JSTOR, Series B, Biological Sciences 304, 509–518.

Dalstra, M., Huiskes, R., Odgaard, A., van Erning, L., 1993. Mechanical and textural properties of pelvic trabecular bone. Journal of Biomechanics 26, 523–535. https://doi.org/10.1016/0021-9290(93)90014-6

de Vaucorbeil, A., Hutchinson, C.R., 2020. A new total-Lagrangian smooth particle hydrodynamics approximation for the simulation of damage and fracture of ductile materials. International Journal for Numerical Methods in Engineering 121, 2227–2245. https://doi.org/10.1002/nme.6306

DeWit, J.A., Cronin, D.S., 2012. Cervical spine segment finite element model for traumatic injury prediction. Journal of the Mechanical Behavior of Biomedical Materials 10, 138–150. https://doi.org/10.1016/j.jmbbm.2012.02.015

Eckersley, C.P., Nightingale, R.W., Luck, J.F., Bass, C.R., 2019. The role of cervical muscles in mitigating concussion. Journal of Science and Medicine in Sport 22, 667–671. https://doi.org/10.1016/j.jsams.2019.01.009

Fraser, K., 2014. Adaptive Smoothed Particle Hydrodynamics Neighbor Search Algorithm for Large Plastic Deformation Computational Solid Mechanics.

Gayzik, F.S., Moreno, D.P., Geer, C.P., Wuertzer, S.D., Martin, R.S., Stitzel, J.D., 2011. Development of a Full Body CAD Dataset for Computational Modeling: A Multi-modality Approach. Ann Biomed Eng 39, 2568. https://doi.org/10.1007/s10439-011-0359-5

Gibson, L.J., 1985. The mechanical behaviour of cancellous bone. Journal of Biomechanics 18, 317–328. https://doi.org/10.1016/0021-9290(85)90287-8

Gibson, L.J., Ashby, M.F., 1997. Cellular Solids: Structure and Properties, 2nd ed, Cambridge Solid State Science Series. Cambridge University Press, Cambridge. https://doi.org/10.1017/CBO9781139878326

Gingold, R.A., Monaghan, J.J., 1977. Smoothed particle hydrodynamics: theory and application to non-spherical stars. Monthly Notices of the Royal Astronomical Society 181, 375–389. https://doi.org/10.1093/mnras/181.3.375
Goldstein, S.A., 1987. The mechanical properties of trabecular bone: Dependence on anatomic location and function. Journal of Biomechanics, F. Gaynor Evans Anniversary Issue on Bone Biomechanics 20, 1055–1061. https://doi.org/10.1016/0021-9290(87)90023-6
Gray, H., 1918. Anatomy of the Human Body Archives, 20th ed. Philadelphia: Lea & Febiger; Bartleby.com.
Hamilton, W.J. (Ed.), 1976. Textbook of Human Anatomy. Palgrave Macmillan UK, London. https://doi.org/10.1007/978-1-349-06486-1
Hansen, U., Zioupos, P., Simpson, R., Currey, J.D., Hynd, D., 2008. The Effect of Strain Rate on the Mechanical Properties of Human Cortical Bone. Journal of Biomechanical Engineering 130. https://doi.org/10.1115/1.2838032
He, Q.-G., Chen, X., Chen, J.-F., 2020. Finite element-smoothed particle hydrodynamics adaptive method in simulating debris cloud. Acta Astronautica 175, 99–117. https://doi.org/10.1016/j.actaastro.2020.05.056
Hobson, S.L., Eisenberg, J.M., 2024. Subaxial cervical spine fractures. Seminars in Spine Surgery, Cervical Trauma 36, 101099. https://doi.org/10.1016/j.semss.2024.101099
Hong, J., Cha, H., Park, Y., Lee, S., Khang, G., Kim, Y., 2007. Elastic Moduli and Poisson's Ratios of Microscopic Human Femoral Trabeculae, in: Jarm, T., Kramar, P., Zupanic, A. (Eds.), 11th Mediterranean Conference on Medical and Biomedical Engineering and Computing 2007, IFMBE Proceedings. Springer, Berlin, Heidelberg, pp. 274–277. https://doi.org/10.1007/978-3-540-73044-6_68
Huiskes, R., Rietbergen, B.V., 2005. Chapter 4 Biomechanics of Bone, in: Basic Orthopaedic Biomechanics and Mechano-Biology. Lippincott Williams & Wilkins, Philadelphia.
Hung, T.-K., Lin, H.-S., Bunegin, L., Albin, M.S., 1982. Mechanical and neurological response of cat spinal cord under static loading. Surgical Neurology 17, 213–217. https://doi.org/10.1016/0090-3019(82)90284-1
Iwamoto, M., Kisanuki, Y., Watanabe, I., Furusu, K., Miki, K., Hasegawa, J., 2002. Development of a Finite Element Model of the Total Human Model for Safety (THUMS) and Application to Injury Reconstruction. Presented at the 2002 International Research Council on Biomechanics of Injury Conference, Munich, Germany.
Iwamoto, M., Nakahira, Y., Kimpara, H., 2015. Development and Validation of the Total HUman Model for Safety (THUMS) Toward Further Understanding of Occupant Injury Mechanisms in Precrash and During Crash. Traffic Injury Prevention 16, S36–S48. https://doi.org/10.1080/15389588.2015.1015000
Jackson, A.B., Dijkers, M., DeVivo, M.J., Poczatek, R.B., 2004. A demographic profile of new traumatic spinal cord injuries: Change and stability over 30 years. Archives of Physical Medicine and Rehabilitation 85, 1740–1748. https://doi.org/10.1016/j.apmr.2004.04.035
John, J., Iraeus, J., Klug, C., Svensson, M., Linder, A., 2020. VIVA+ Open Human Body Models for Virtual Testing. Presented at the automotive CAE Grand Challenge, Hanau, Germany.
John, J., Klug, C., Kranjec, M., Svenning, E., Iraeus, J., 2022. Hello, world! VIVA+: A human body model lineup to evaluate sex-differences in crash protection. Frontiers in Bioengineering and Biotechnology 10.
Johnson, G.R., Stryk, R.A., 2003. Conversion of 3D distorted elements into meshless particles during dynamic deformation. International Journal of Impact Engineering 28, 947–966. https://doi.org/10.1016/S0734-743X(03)00012-5
Kala, J., Husek, M., 2016. Improved Element Erosion Function for Concrete-Like Materials with the SPH Method. Shock and Vibration 2016. https://doi.org/10.1155/2016/4593749
Keaveny, T.M., Hayes, W.C., 1993. A 20-Year Perspective on the Mechanical Properties of Trabecular Bone. Journal of Biomechanical Engineering 115, 534–542. https://doi.org/10.1115/1.2895536

Keaveny, T.M., Morgan, E.F., Niebur, G.L., Yeh, O.C., 2001. Biomechanics of Trabecular Bone. Annual Review of Biomedical Engineering 3, 307–333. https://doi.org/10.1146/annurev.bioeng.3.1.307
Kefalas, V., Eftaxiopoulos, D.A., 2012. Experimental study of cancellous bone under large strains and a constitutive probabilistic model. Journal of the Mechanical Behavior of Biomedical Materials 6, 41–52. https://doi.org/10.1016/j.jmbbm.2011.10.006
Keyak, J.H., 2001. Improved prediction of proximal femoral fracture load using nonlinear finite element models. Medical Engineering & Physics 23, 165–173. https://doi.org/10.1016/S1350-4533(01)00045-5
Khor, F., 2018. Computational Modeling of Hard Tissue Response and Fracture in the Lower Cervical Spine under Compression Including Age Effects (Master Thesis). University of Waterloo.
Khor, F., Cronin, D., Carter, J., 2018. Hard Tissue Failure of an Aged Lower Cervical Spine Segment Model in Compression Loading with Anterior-Posterior Eccentricity. Presented at the 2018 Injury Biomechanics Symposium.
Khor, F., Cronin, D., Van Toen, C., 2017. Lower Cervical Spine Hard Tissue Injury Prediction in Axial Compression, in: IRCOBI Conference Proceedings. Presented at the 2017 International Research Council on Biomechanics of Injury (IRCOBI).
Klenerman, L., 2015. Human Anatomy: A Very Short Introduction. Oxford University Press. https://doi.org/10.1093/actrade/9780198707370.001.0001
Koohbor, B., Youssef, G., Uddin, K.Z., Kokash, Y., 2022. Dynamic Behavior and Impact Tolerance of Elastomeric Foams Subjected to Multiple Impact Conditions. J. dynamic behavior mater. 8, 359–370. https://doi.org/10.1007/s40870-022-00340-z
Krueger, H., Noonan, V.K., Trenaman, L.M., Joshi, P., Rivers, C.S., 2013. The economic burden of traumatic spinal cord injury in Canada. Chronic Dis Inj Can 33, 113–122.
Kulper, S.A., Fang, C.X., Ren, X., Guo, M., Sze, K.Y., Leung, F.K.L., Lu, W.W., 2018. Development and initial validation of a novel smoothed-particle hydrodynamics-based simulation model of trabecular bone penetration by metallic implants. Journal of Orthopaedic Research 36, 1114–1123. https://doi.org/10.1002/jor.23734
Lenehan, B., Boran, S., Street, J., Higgins, T., McCormack, D., Poynton, A.R., 2009. Demographics of acute admissions to a National Spinal Injuries Unit. Eur Spine J 18, 938–942. https://doi.org/10.1007/s00586-009-0923-y
Li, S., Abdel-Wahab, A., Demirci, E., Silberschmidt, V.V., 2014. Penetration of cutting tool into cortical bone: Experimental and numerical investigation of anisotropic mechanical behaviour. Journal of Biomechanics 47, 1117–1126. https://doi.org/10.1016/j.jbiomech.2013.12.019
Li, S., Zahedi, A., Silberschmidt, V., 2017. Numerical Simulation of Bone Cutting: Hybrid SPH-FE Approach, in: Numerical Methods and Advanced Simulation in Biomechanics and Biological Processes. https://doi.org/10.1016/B978-0-12-811718-7.00010-1
Lindahl, O., 1976. Mechanical Properties of Dried Defatted Spongy Bone. Acta Orthopaedica Scandinavica 47, 11–19. https://doi.org/10.3109/17453677608998966
Liu, J.F., Shim, V.P.W., Lee, P.V.S., 2013. Quasi-static Compressive and Tensile Tests on Cancellous Bone in Human Cervical Spine, in: Prorok, B.C., Barthelat, F., Korach, C.S., Grande-Allen, K.J., Lipke, E., Lykofatitits, G., Zavattieri, P. (Eds.), Mechanics of Biological Systems and Materials, Volume 5, Conference Proceedings of the Society for Experimental Mechanics Series. Springer, New York, NY, pp. 109–118. https://doi.org/10.1007/978-1-4614-4427-5_16
Liu, M.B., Liu, G.R., 2010. Smoothed Particle Hydrodynamics (SPH): an Overview and Recent Developments. Archives of Computational Methods in Engineering 17, 25–76. https://doi.org/10.1007/s11831-010-9040-7
Lucy, L.B., 1977. A numerical approach to the testing of the fission hypothesis. The Astronomical Journal 82, 1013–1024. https://doi.org/10.1086/112164
Mattos, G.A., Mcintosh, A.S., Grzebieta, R.H., Yoganandan, N., Pintar, F.A., 2015. Sensitivity of Head and Cervical Spine Injury Measures to Impact Factors Relevant to Rollover Crashes. Traffic Injury Prevention 16, S140–S147. https://doi.org/10.1080/15389588.2015.1012585

Mattucci, S., 2011. Strain Rate Dependent Properties of Younger Human Cervical Spine Ligaments (Master Thesis). University of Waterloo.
Mattucci, S., Speidel, J., Liu, J., Kwon, B.K., Tetzlaff, W., Oxland, T.R., 2019. Basic biomechanics of spinal cord injury — How injuries happen in people and how animal models have informed our understanding. Clinical Biomechanics, SI: Central Nervous System (CNS) Injury Biomechanics 64, 58–68. https://doi.org/10.1016/j.clinbiomech.2018.03.020
McElhaney, J.H., 1966. Dynamic response of bone and muscle tissue. Journal of Applied Physiology 21, 1231–1236. https://doi.org/10.1152/jappl.1966.21.4.1231
Mosekilde, Li., Mosekilde, Le., Danielsen, C.C., 1987. Biomechanical competence of vertebral trabecular bone in relation to ash density and age in normal individuals. Bone 8, 79–85. https://doi.org/10.1016/8756-3282(87)90074-3
Mosekilde, Lis, Viidik, A., Mosekilde, Leif, 1985. Correlation between the compressive strength of iliac and vertebral trabecular bone in normal individuals. Bone 6, 291–295. https://doi.org/10.1016/8756-3282(85)90317-5
Müller, C.W., Otte, D., Decker, S., Stübig, T., Panzica, M., Krettek, C., Brand, S., 2014. Vertebral fractures in motor vehicle accidents–a medical and technical analysis of 33,015 injured front-seat occupants. Accident Analysis & Prevention 66, 15–19. https://doi.org/10.1016/j.aap.2014.01.003
National Spinal Cord Injury Statistical Center, 2023. THE 2023 ANNUAL STATISTICAL REPORT COMPLETE PUBLIC VERSION for the SPINAL CORD INJURY MODEL SYSTEMS.
Nightingale, R.W., Sganga, J., Cutcliffe, H., Bass, C.R. 'Dale,' 2016. Impact responses of the cervical spine: A computational study of the effects of muscle activity, torso constraint, and pre-flexion. Journal of Biomechanics 49, 558–564. https://doi.org/10.1016/j.jbiomech.2016.01.006
Nuckley, D.J., Van Nausdle, J.A., Eck, M.P., Ching, R.P., 2007. Neural space and biomechanical integrity of the developing cervical spine in compression. Spine (Phila Pa 1976) 32, E181-187. https://doi.org/10.1097/01.brs.0000257527.22080.d7
Östh, J., Brolin, K., Svensson, M.Y., Linder, A., 2016. A Female Ligamentous Cervical Spine Finite Element Model Validated for Physiological Loads. Journal of Biomechanical Engineering 138. https://doi.org/10.1115/1.4032966
Östh, J., Mendoza-Vazquez, M., Linder, A., Svensson, M., Brolin, K., 2017a. The VIVA OpenHBM Finite Element 50th Percentile Female Occupant Model: Whole Body Model Development and Kinematic Validation, in: Conference Proceedings International Research Council on the Biomechanics of Injury, IRCOBI. Presented at the 2017 International Research Council on the Biomechanics of Injury Conference, IRCOBI 2017, Antwerp, pp. 443–466.
Östh, J., Mendoza-Vazquez, M., Sato, F., Svensson, M.Y., Linder, A., Brolin, K., 2017b. A female head–neck model for rear impact simulations. Journal of Biomechanics 51, 49–56. https://doi.org/10.1016/j.jbiomech.2016.11.066
Panjabi, M.M., Kifune, M., Wen, L., Arand, M., Oxland, T.R., Lin, R.M., Yoon, W.S., Vasavada, A., 1995. Dynamic canal encroachment during thoracolumbar burst fractures. J Spinal Disord 8, 39–48.
Praxis Spinal Cord Institute, 2023. Rick Hansen Spinal Cord Injury Registry: A look at Spinal Cord Injury in Canada in 2021.
Praxis Spinal Cord Institute, 2021. A look at Traumatic Spinal Cord Injury in Canada in 2019 [WWW Document]. Praxis Spinal Cord Institute. URL https://praxisinstitute.org/rhscir-2019-annual-report-a-look-at-traumatic-spinal-cord-injury-in-canada-in-2019/ (accessed 12.15.22).
Raynak, G.C., Nuckley, D.J., Tencer, A.F., Ching, R.P., 1998. Transducers for Dynamic Measurement of Spine Neural-Space Occlusions. Journal of Biomechanical Engineering 120, 787–791. https://doi.org/10.1115/1.2834895
Reilly, D.T., Burstein, A.H., 1975. The elastic and ultimate properties of compact bone tissue. Journal of Biomechanics 8, 393–405. https://doi.org/10.1016/0021-9290(75)90075-5
Reilly, D.T., Burstein, A.H., Frankel, V.H., 1974. The elastic modulus for bone. Journal of Biomechanics 7, 271–275. https://doi.org/10.1016/0021-9290(74)90018-9

Rho, J.-Y., Kuhn-Spearing, L., Zioupos, P., 1998. Mechanical properties and the hierarchical structure of bone. Medical Engineering & Physics 20, 92–102. https://doi.org/10.1016/S1350-4533(98)00007-1

Roaf, R., 1960. A STUDY OF THE MECHANICS OF SPINAL INJURIES. The Journal of Bone & Joint Surgery British Volume 42-B, 810–823. https://doi.org/10.1302/0301-620X.42B4.810

Robin, S., 2001. HUMOS: HUMAN MODEL FOR SAFETY - A JOINT EFFORT TOWARDS THE DEVELOPMENT OF REFINED HUMAN-LIKE CAR OCCUPANT MODELS. Presented at the PROCEEDINGS OF 17TH INTERNATIONAL TECHNICAL CONFERENCE ON THE ENHANCED SAFETY OF VEHICLES. CD ROM.

Ru, K., Swati, R.F., Zeng, H., Khan, Z., Chen, Z., Qian, A., Hu, L., 2024. Chapter 3 - The whole bone mechanical properties and modeling study, in: Qian, A., Hu, L. (Eds.), Bone Cell Biomechanics, Mechanobiology and Bone Diseases. Academic Press, pp. 53–94. https://doi.org/10.1016/B978-0-323-96123-3.00012-9

Russell, C.M., Choo, A.M., Tetzlaff, W., Chung, T.-E., Oxland, T.R., 2012. Maximum Principal Strain Correlates with Spinal Cord Tissue Damage in Contusion and Dislocation Injuries in the Rat Cervical Spine. Journal of Neurotrauma 29, 1574–85. https://doi.org/10.1089/neu.2011.2225

Rycman, A., McLachlin, S., Cronin, D.S., 2022. Comparison of numerical methods for cerebrospinal fluid representation and fluid–structure interaction during transverse impact of a finite element spinal cord model. International Journal for Numerical Methods in Biomedical Engineering 38, e3570. https://doi.org/10.1002/cnm.3570

Rycman, A., Ngan, S., Carter, J., Cronin, D.S., 2023. Short communication: Assessment of Spinal Cord Tissue Deformation During Central Compression and Fracture in a Functional Spinal Unit Finite Element Model, in: IRCOBI Conference Proceedings. Presented at the 2023 International Research Council on Biomechanics of Injury (IRCOBI).

Saari, A., Itshayek, E., Cripton, P.A., 2011. Cervical spinal cord deformation during simulated head-first impact injuries. Journal of Biomechanics 44, 2565–2571. https://doi.org/10.1016/j.jbiomech.2011.06.015

Sanyal, A., Gupta, A., Bayraktar, H.H., Kwon, R.Y., Keaveny, T.M., 2012. Shear strength behavior of human trabecular bone. Journal of Biomechanics 45, 2513–2519. https://doi.org/10.1016/j.jbiomech.2012.07.023

Singh, A., Tetreault, L., Kalsi-Ryan, S., Nouri, A., Fehlings, M.G., 2014. Global prevalence and incidence of traumatic spinal cord injury. CLEP 6, 309–331. https://doi.org/10.2147/CLEP.S68889

Spinal Cord Injury BC, 2020. About Spinal Cord Injury. Spinal Cord Injury BC. URL https://sci-bc.ca/info-centre/spinal-cord-injury/ (accessed 12.15.22).

Stein, D.M., Kufera, J.A., Ho, S.M., Ryb, G.E., Dischinger, P.C., O'Connor, J.V., Scalea, T.M., 2011. Occupant and Crash Characteristics for Case Occupants With Cervical Spine Injuries Sustained in Motor Vehicle Collisions. Journal of Trauma and Acute Care Surgery 70, 299. https://doi.org/10.1097/TA.0b013e3181f8aa91

Sun, J., Rojas, A., Bertrand, P., Petit, Y., Kraenzler, R., Arnoux, P.J., 2012. Investigation of Motorcyclist Cervical Spine Trauma Using HUMOS Model. Traffic Injury Prevention 13, 519–528. https://doi.org/10.1080/15389588.2012.656857

Tang, A., Pawar, J., Bridge, C., King, R., Kakarmath, S., Harris, M., Khurana, B., 2021. Traumatic cervical spine fracture patterns on CT: a retrospective analysis at a level 1 trauma center. Emerg Radiol 28, 965–976. https://doi.org/10.1007/s10140-021-01952-z

Tang, T., Ebacher, V., Cripton, P., Guy, P., McKay, H., Wang, R., 2015. Shear deformation and fracture of human cortical bone. Bone 71, 25–35. https://doi.org/10.1016/j.bone.2014.10.001

Tanoto, H., Fan, H., Ha, D., Ambrose, C.G., Klineberg, E.O., Zhou, Y., 2024. Quantifying the relation between aging-related trabecular bone microstructure and mechanical properties with digital volume correlation approach. Extreme Mechanics Letters 73, 102265. https://doi.org/10.1016/j.eml.2024.102265

Thollon, L., Arnoux, P.-J., Kayvantash, K., Cavallero, C., Brunet, C., 2002. Human injury evaluation using HUMOS RADIOSS finite element model, in: IRCOBI Conference.
Thurman, D.J., Burnett, C.L., Beaudoin, D.E., Jeppson, L., Sniezek, J.E., 1995. Risk factors and mechanisms of occurrence in motor vehicle-related spinal cord injuries: Utah. Accident Analysis & Prevention 27, 411–415. https://doi.org/10.1016/0001-4575(94)00059-U
Tokura, S., Niwa, K., 2017. Evaluation of Debris Modeling Technique on Failure Simulation of Concrete Structures. Presented at the 11th European LS-DYNA Conference 2017, Salzburg, Austria.
Tran, N.T., Watson, N.A., Tencer, A.F., Ching, R.P., Anderson, P.A., 1995. Mechanism of the burst fracture in the thoracolumbar spine. The effect of loading rate. Spine (Phila Pa 1976) 20, 1984–1988. https://doi.org/10.1097/00007632-199509150-00004
Tropiano, P., Thollon, L., Arnoux, P.J., Huang, R.C., Kayvantash, K., Poitout, D.G., Brunet, C., 2004. Using a Finite Element Model to Evaluate Human Injuries Application to the HUMOS Model in Whiplash Situation. Spine 29, 1709. https://doi.org/10.1097/01.BRS.0000135840.92373.5C
Van Toen, C.Y., 2013. Biomechanics of cervical spine and spinal cord injury under combined axial compression and lateral bending loading. University of British Columbia. https://doi.org/10.14288/1.0072137
Van Toen, C.Y., Carter, J.W., Oxland, T.R., Cripton, P.A., 2014a. Moment Measurements in Dynamic and Quasi-Static Spine Segment Testing Using Eccentric Compression are Susceptible to Artifacts Based on Loading Configuration. Journal of Biomechanical Engineering 136. https://doi.org/10.1115/1.4028817
Van Toen, C.Y., Melnyk, A.D., Street, J., Oxland, T.R., Cripton, P.A., 2014b. The effect of lateral eccentricity on failure loads, kinematics, and canal occlusions of the cervical spine in axial loading. Journal of Biomechanics 47, 1164–1172. https://doi.org/10.1016/j.jbiomech.2013.12.001
WHO, 2024. Spinal cord injury [WWW Document]. URL https://www.who.int/news-room/fact-sheets/detail/spinal-cord-injury (accessed 5.17.24).
Wilcox, R.K., Boerger, T.O., Allen, D.J., Barton, D.C., Limb, D., Dickson, R.A., Hall, R.M., 2003. A Dynamic Study of Thoracolumbar Burst Fractures. JBJS 85, 2184.
Wilcox, R.K., Boerger, T.O., Hall, R.M., Barton, D.C., Limb, D., Dickson, R.A., 2002. Measurement of canal occlusion during the thoracolumbar burst fracture process. Journal of Biomechanics 35, 381–384. https://doi.org/10.1016/S0021-9290(01)00180-4
Wishart, J.M., Need, A.O., Horowitz, M., Morris†, H.A., Nordin, B.E.C., 1995. Effect of age on bone density and bone turnover in men. Clinical Endocrinology 42, 141–146. https://doi.org/10.1111/j.1365-2265.1995.tb01854.x
Wu, D., Isaksson, P., Ferguson, S.J., Persson, C., 2018. Young's modulus of trabecular bone at the tissue level: A review. Acta Biomaterialia 78, 1–12. https://doi.org/10.1016/j.actbio.2018.08.001
Zhu, Q., Lane, C., Ching, R.P., Gordon, J.D., Fisher, C.G., Dvorak, M.F., Cripton, P.A., Oxland, T.R., 2008. Translational constraint influences dynamic spinal canal occlusion of the thoracic spine: An in vitro experimental study. Journal of Biomechanics 41, 171–179. https://doi.org/10.1016/j.jbiomech.2007.06.030
Zioupos, P., 2001. Ageing Human Bone: Factors Affecting its Biomechanical Properties and the Role of Collagen. J Biomater Appl 15, 187–229. https://doi.org/10.1106/5JUJ-TFJ3-JVVA-3RJ0